Universidad del País Vasco Euskal Herriko Unibertsitatea

POLYMAT

# SYNTHESIS, STRUCTURE, CRYSTALLIZATION AND CONFINEMENT OF ISODIMORPHIC PBS-*ran*-PCL COPOLYESTERS

***Maryam Safari***

***Ph.D. Thesis***

Polymer Science and Technology Department

Faculty of Chemistry

San Sebastian, 2020

eman ta zabal zazu

Universidad del País Vasco

Euskal Herriko Unibertsitatea

# SYNTHESIS, STRUCTURE, CRYSTALLIZATION AND CONFINEMENT OF ISODIMORPHIC PBS-*ran*-PCL COPOLYESTERS

***By***

***Maryam Safari***

***Supervisor***

***Prof. Alejandro J. Müller***

Polymer Science and Technology Department

Faculty of Chemistry

San Sebastian, 2020

# Table of Contents

# *Chapter I:*

# *Aim and Structure of the Thesis*

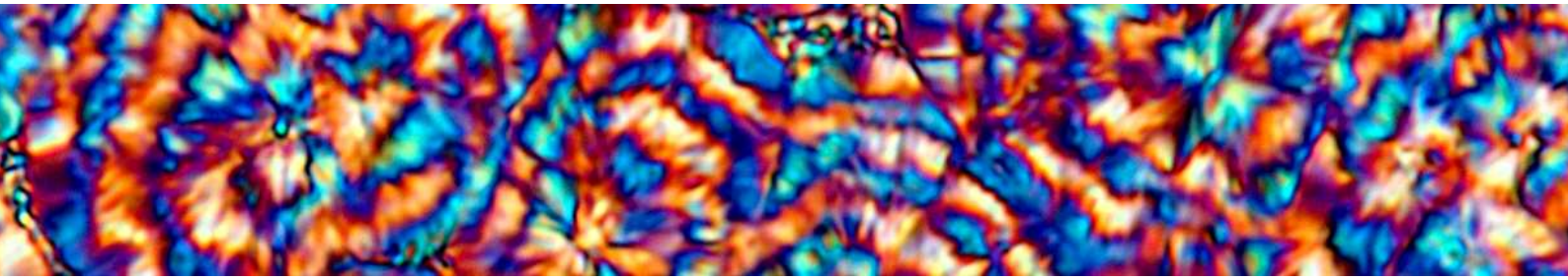

# Table of Contents

## 1.1. INTRODUCTION

Polymers have arrived to be indispensable materials due to their versatility in structure and properties. Nowadays, a world without polymers cannot be conceived because these materials are present in the development of all new and modern technologies. On the other hand, the concern about environmental problems and limitation of fossil sources has motivated the investigation of new polymeric materials and the innovation of technologies based on renewable and biodegradable compounds. Although the challenge is great, many efforts have been made to attain such objectives [1-2].

The biobased polymers are attract the attention of scientist due to their biodegradability and biocompatibility and their prospective in different fields including packaging, coating, tissue engineering, drug delivery system and many more. Each of these applications demands materials with specific physical, chemical, mechanical and degradation properties to provide efficient therapy [3-5].

The term biopolymer is used for those polymer that are biobased, biodegradable, or both, and they are commonly differentiated in three main groups: i) Biobased or partially biobased non-biodegradable polymers such as biobased PE, PP, or PET, ii) polymers that are both biobased and biodegradable, such as PLA and PHA or PBS, and iii) polymers that are based on fossil resources and are biodegradable, such as PBAT [4, 6-7].

Among these group, the family of aliphatic polyesters is one of the most attractive because of their biodegradability and biocompatibility [8-9]. They have attracted considerable attention and numerous research works have been published dealing with biodegradable aliphatic polyesters. Unfortunately, these kinds of biopolymers do not usually fulfill all the mechanical requirements needed and they are also characterized by a high crystallinity which limits their biodegradation rate. Therefore, in order to tailor these properties, the synthesis of random copolyesters

with biobased comonomers has been done to obtain versatile random copolymers [10]. Copolymerization has been used to limit their degree of crystallization and improve their physical properties to extend their applications in the biodegradable polymer market. Additionally, some works showed that through the variation of the copolymer composition thermal properties could be controlled without significant loss of crystalline properties.

Among polymer nanostructures, one dimensional nanostructure has become one of the most promising since "tailored polymer one dimensional nanostructures" can be easily synthesized by replication of AAO hard templates. AAO template is an attractive low cost mold composed of cylindrical nanopores characterized by narrow distribution of diameter and length of pores. Confinement within an AAO template can radically alter polymer crystallization. At one extreme, subdividing the crystallizable material into nanoscale requires the generation of one (homogeneous) nucleus per pore to fully crystallize the specimen. The subsequent development of polymer infiltration methods allowed preparing the desired one dimensional polymer nanostructures [11-15].

Taking into account the necessity to study of the crystallization behavior of random copolymers because of its strong correlation with biodegradation rates, mechanical properties and applications [16-20]. The work of this thesis is focused on two main topics; in the first part, the morphology, crystallization behavior, and properties of isodimorphic PBS-*ran*-PCL random copolymer, with two crystalline phases at pseudo-eutectic point, were studied in Chapter 4-8. The second part comprises Chapter 9-10 and contains a study of the morphology and crystallization behavior of the nanofiber polyesters and isodimorphic copolymers.

## 1.2. AIMS OF THIS THESIS

The aim of this thesis is to study the structure, morphology and thermal properties, as well as crystallization kinetics of biodegrable poly(butylene succinate-

*ran*-caprolactone) isodimorphic random copolyester in bulk and under confinement position.

In particular the aims are:

- *To determine the isodimorphism model of the PBS-ran-PCL random copolyesters with three different molecular weight.*
- *To analyze the rate-dependent behavior of PBS-ran-PBA at compositions close to the eutectic point and at pseudo-eutectic point.*
- *To determine the influence of the molecular weight on the structural thermal properties of the copolymers.*
- *Perform detailed isothermal studies of the nucleation kinetics, spherulitic growth rates and overall crystallization kinetics by DSC and PLOM techniques.*
- *To study the mechanical properties of PBS-ran-PCL isodimorphic random copolyester.*
- *Fabrication of AAO templates.*
- *Fabrication of polyester nanostructures using AAO template and studying their crystallization behavior and their crystal orientation under confined position.*
- *To carry out new studies on isodimorphic random copolymer properties under confinement.*

## 1.3. STRUCTURE OF THE THESIS

The PhD work has been divided into ten chapters.

- In ***chapter 1***, a general introduction is presented, which describes the origin of this work.
- In ***chapter 2***, also some concepts related to the synthesis of polymers and to the study of morphology and crystallization of materials have been written, with the intention of a better understanding of concepts used throughout the thesis.
- In ***Chapter 3***, we summarized the synthesis of BSxCLy copolyesters with three different molecular weight (low, high, ultra-high) using different types of catalysts and synthesis methods. Furthermore, the main experimental techniques and the conditions used are also included.

- ***Chapter 4*** describes the characterization of LMw-PBS-*ran*-PCL obtained by organo-catalyzed polymerization.
- In ***Chapter 5***, the synthesis and characterization of HMw-PBS-*ran*-PCL obtained by metallic catalyst and comparing their proberties with LMw-PBS-*ran*-PCL.
- ***Chapter 6*** discusses the detailed isothermal studies of the nucleation kinetics, spherulitic growth rates and overall crystallization kinetics studied by DSC and PLOM techniques.
- In ***Chapter 7***, the mechanical properties of VHMw-PBS-*ran*-PCL is investigated.
- ***Chapter 8*** discusses the polymer properties under confinement position, deals with the study of selected polymers, PBS and PBA homopolyesters within AAO template.
- ***Chapter 9*** shows the crystallization, morphology and properties of the HMw-PBS-*ran*-PCL copolyesters under confinement position.
- Finally, ***Chapter 10*** is a section of appendix that complements what is shown in chapters 4 to 9. Finally, a list of publications and a summary of the content of this thesis are also included.

## 1.4. REFERENCES

1. Gandini, A., Polymers from renewable resources: a challenge for the future of macromolecular materials. *Macromolecules* **2008,** *41* (24), 9491-9504.

2. Luckachan, G. E.; Pillai, C., Biodegradable polymers-a review on recent trends and emerging perspectives. *Journal of Polymers and the Environment* **2011,** *19* (3), 637-676.

3. Nair, L. S.; Laurencin, C. T., Biodegradable polymers as biomaterials. *Progress in polymer science* **2007,** *32* (8-9), 762-798.

4. Gross, R. A.; Kalra, B., Biodegradable polymers for the environment. *Science* **2002,** *297* (5582), 803-807.

5. Vroman, I.; Tighzert, L., Biodegradable polymers. *Materials* **2009,** *2* (2), 307-344.

6. Díaz, A.; Katsarava, R.; Puiggalí, J., Synthesis, properties and applications of biodegradable polymers derived from diols and dicarboxylic acids: From polyesters to poly (ester amide) s. *International journal of molecular sciences* **2014,** *15* (5), 7064-7123.

7. Vilela, C.; Sousa, A. F.; Fonseca, A. C.; Serra, A. C.; Coelho, J. F.; Freire, C. S.; Silvestre, A. J., The quest for sustainable polyesters–insights into the future. *Polymer Chemistry* **2014,** *5* (9), 3119-3141.

8. Vert, M.; Li, S.; Spenlehauer, G.; Guérin, P., Bioresorbability and biocompatibility of aliphatic polyesters. *Journal of materials science: Materials in medicine* **1992,** *3* (6), 432-446.

9. Albertsson, A.-C.; Varma, I. K., Aliphatic polyesters: synthesis, properties and applications. In *Degradable Aliphatic Polyesters*, Springer: 2002; pp 1-40.

10. Ki, H.; Park, O. O., Synthesis, characterization and biodegradability of the biodegradable aliphatic–aromatic random copolyesters. *Polymer* **2001,** *42* (5), 1849-1861.

11. Michell, R. M.; Blaszczyk-Lezak, I.; Mijangos, C.; Müller, A. J., Confined crystallization of polymers within anodic aluminum oxide templates. *Journal of Polymer Science Part B: Polymer Physics* **2014,** *52* (18), 1179-1194.

12. Müller, A. J.; Arnal, M. L.; Lorenzo, A. T., Crystallization in nano-confined polymeric systems. *Handbook of polymer crystallization* **2013,** *1*.

13. Michell, R. M.; Blaszczyk-Lezak, I.; Mijangos, C.; Mueller, A. J., Confinement effects on polymer crystallization: From droplets to alumina nanopores. *Polymer* **2013,** *54* (16), 4059-4077.

14. Martin, J.; Mijangos, C., Tailored polymer-based nanofibers and nanotubes by means of different infiltration methods into alumina nanopores. *Langmuir* **2008,** *25* (2), 1181-1187.

15. Michell, R. M.; Mueller, A. J., Confined crystallization of polymeric materials. *Progress in Polymer Science* **2016,** *54*, 183-213.

16. Pérez-Camargo, R. A.; Arandia, I.; Safari, M.; Cavallo, D.; Lotti, N.; Soccio, M.; Müller, A. J., Crystallization of isodimorphic aliphatic random copolyesters: Pseudo-eutectic behavior and double-crystalline materials. *European Polymer Journal* **2018,** *101*, 233-247.

17. Iwata, T.; Doi, Y., Crystal structure and biodegradation of aliphatic polyester crystals. *Macromolecular chemistry and physics* **1999,** *200* (11), 2429-2442.

18. Young, R. J.; Lovell, P. A., *Introduction to polymers*. CRC press: 2011.

19. Schultz, J. M., *Polymer crystallization: the development of crystalline order in thermoplastic polymers*. Amer Chemical Society: 2001.

20. Bassett, D. C., *Principles of polymer morphology*. CUP Archive: 1981.

# *Chapter II:*

# *General Aspects on Polymerization and Polymer Crystallization of Investigated Materials*

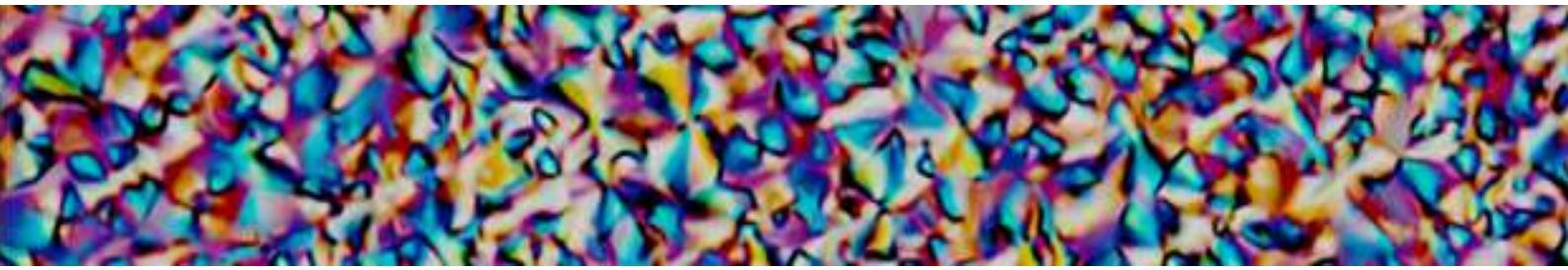

# Table of Contents

## 2.1. INTRODUCTION

A great variety of synthetic polymers became available on the industrial scale in 20th century. Robust technology base is petro-chemistry, developing in the 1950s. Exploitation of oil, gas as fossil raw materials for the chemical industry and polymer production greatly improved cost-effectiveness and simplified manufacturing of macromolecular materials. Since then the attractive combination of low cost with facile processing and innovation represents the key feature of plastics. The demand for polymer is driven by growth in end use markets, such as packaging, automotive, infrastructure, transport rails, and telecommunication mainly from developing economies [1-2].

The word polyester represents a wide quantity of polymers containing a group ester in the repeating unit. Since the pioneers experiments made in the 1930's, the applications of the polyesters have been incredible extended, including engineering plastics, high performance and biodegradable materials, etc. It is mainly possible due to the diversity of the monomer structures, making enormous advances in the improvement of their properties. Nevertheless, these advances triggered consequences respecting to the environment. In this context, the polymeric industry is awareness about ecological problems and the scarcity of fossil stocks. Consequently, the pursuit of natural origin alternatives begins to be essential for the fabrication of compounds with optimized properties [3-5].

Biobased polymer industry is one of the markets with a higher growth [3-5]. Many projects around the world have proposed the use of different natural-origin monomers [6-10]. Actually, there is an expectation that the biobased production of them will be close to 12 millions of tons by the year 2020 [11-12]. There are success stories and very promising development, but failures and serious problems also exist that a detailed investigation helps to overcome these weaknesses.

In nanotechnology applications, reduced dimensions confine polymer crystallization to sizes that are of the same order of magnitude as individual lamellar crystals. The confinement of polymer systems can occur in one dimension (lamellae in ultrathin films and nanolayers), two dimensions or three dimensions (dropletsor spheres in block copolymer and blends) [13-14]. One dimensional (1D) polymer nanostructures have attracted much attention due to their unique properties and many potential applications in areas such as sensors, transistors, separation, storage, and photovoltaic cells [15].

## 2.2. POLYESTER

Polyesters are one of the most important and most used polycondensation polymers and are derived from dicarboxylic acids and diols. Polyester is a polymer class containing ester functional group on polymeric main chain [16-17].

Recent researches have indicated that using of polyester polymer processed into various forms, e.g., fibers, filament, fabric, composites, resins, dendrimers, films, sheets, and membranes in different fields, such as textile, automotive, medical, electronic, and construction applications, attracts worldwide interest. Polyester is also extensively used as packaging materials, such as bottle/containers. The polymerization of polyester could be carried out as polycondensation, ring-opening polymerization, and polyaddition processes.

Furthermore, polyester could be recycled by physical (mechanical) or chemical (hydrolysis, methanolysis, and glycolysis reactions) methods. Recycled polyester could be used for packaging, construction parts, pipes, tanks, geotextiles, nonwoven, carpets, etc. It is expected to run out of crude oil reserves at World in 2043. Thus, recycling of petroleum-based polymers is crucial. In addition, effectively recycling of polyester will give rise to lessen carbon dioxide emission and thus global warming [16-17].

Polyester can be classified into two groups: thermoplastic polyesters and thermoset (unsaturated polyester, polyester resin) polyesters. Thermoplastic polymers could be categorized as linear aromatic polyesters (fiber- and film-forming polyesters), elastomers (block copolyesters), liquid crystal polyester, engineering plastics, poly(hydroxyl alkanoates) and aliphatic polyesters [16]. According to the composition of their main chain, polyesters can be aliphatic, Semi-aromatic, or aromatic [18].

### 2.2.1. Aliphatic Polyesters

Aliphatic polyesters are among the most used biodegradable polymers in medical applications and have been extensively investigated in the past. Ester linkages are frequently encountered in nature and hence it is expected that synthetic polymers containing such linkages and an appropriate structure would be environmentally degradable [19].

The aliphatic polyesters, developed initially, were of low molecular mass with poor mechanical properties. The dihydroxy-terminated poly(alkylene alkanoates) found applications in the production of polyurethane or as plasticizers in PVC. In the 1960s poly(L-lactide), PLLA, was proposed as a biocompatible, biodegradable, and bioresorbable material (a material that degrades and is further resorbed in vivo). Homopolymers and copolymers of lactide and glycolide form the basis of surgical sutures, drug delivery devices, and other body implants [19].

In the present work, two biodegradable aliphatic polyester (PBS and PCL) are synthesized and characterized.

#### 2.2.1.1. Poly (ε-caprolactone), PCL

Polycaprolactone (PCL) is a polymer composed of hexanoate repeat units, included in the class of aliphatic polyesters. Industrially, ε-Caprolactone (ε-CL) is produced by the oxidation of cyclohexanone by peracetic acid [20]. PCL is one of the earliest biopolymers, as it was synthesized in 1930. [21] The repetitive molecular unit of

PCL consists of five nonpolar methylene groups and a single relatively polar ester group [22]. PCL is strongly hydrophobic, semicrystalline, highly soluble at room temperature, and has a good solubility in a wide range of organic solvents such as N,N-Dimethylformamide, tetrahydrofuran, dichloromethane, acetone, chloroform [23].

PCL has the following chemical composition $(C_6H_{10}O_2)_n$. As semicrystalline polymer, PCL exhibits a glass transition around -60 °C and a melting temperature ranging between 59 and 64 °C [24-26]. Because of these, PCL can be easily processed at relatively low temperatures into wide range of forms such as nanospheres, nanofibers and foams. Due to its very low glass transition temperature, PCL is a very flexible and elastic polymer, with high elongation at break ( > 700 %) but low tensile strength (around 23 MPa) [24].

PCL has been thoroughly investigated for its peculiar mechanical properties, miscibility with a large range of other polymers, and biodegradability. Indeed, owing to its native biocompatibility and biodegradability, PCL has been extensively studied for the preparation of controlled drug delivery systems by several formulations of polymers or copolymers. Moreover, its permeability to a wide range of drugs enabled uniform drug distribution in the matrix, assuring a long-term release-up to several months-by a degradation mechanism. Owing to a markedly slow degradation rate, PCL has been largely used for the preparation of long-term implants and scaffolds able to reproduce the natural extracellular matrix, thus supporting the three-dimensional (3D) cell culture in tissue engineering and repair. Hence, PCL has also been certified as FDA approved (Food and Drug Administration, USA) and CE registered mark (European Community) for use in a large number of drug-delivery and medical devices, even though surprisingly few have been commercialized or widely translated to clinical studies.

Early studies on the crystallization behavior of PCL have adopted dilatometry and optical microscopy. The crystalline growth of PCL was spherulitic and the crystallization exhibited a time dependent nucleation. Clear Maltese cross has

been observed for PCL at low supercooling. But as the crystallization temperature decreases, spherulites with banding are formed for low molecular weight PCL. The crystallization behavior of PCL also depends on the molecular weight and the structural topology of chains. Applying the Avrami fitting to the crystallization kinetics data predicted a 3D dimensional growth with instantaneous nucleation, since the Avrami index of PCLs were around 3 [27-29].

#### 2.2.1.2. Poly (butylene succinate), PBS

PBS is a biodegradable aliphatic polyester with the chemical formula $(C_8H_{12}O_4)_n$, commercially available since 1993. It is a polymer of wide industrial interest, used for production of mulching films, compostable bags, nonwoven sheets and textiles, as well as catering products and foams. PBS is classified as a "green" polymer, generally synthesized through polycondensation of 1,4-butanediol and succinic acid, with both monomers produced from short-term renewable sources. Succinic acid can be attained from carbohydrates through fermentation with consumption of carbon dioxide, advantageously contributing to carbon sequestration, and 1,4-butanediol can be produced through hydrogenation and reduction of succinic acid. PBS can also be synthesized via a "greener" route like enzymatic catalysis, using a lipase catalyst, Candida Antarctica, physically adsorbed within a macroporous resin [30-31].

Biodegradability and compostability also contribute to the attractiveness of PBS. Biodegradation of PBS chains is initiated by hydrolysis of ester bonds, leading to the formation of water-soluble fragments. These short PBS chain segments can be assimilated by microorganisms and finally changed into eco-friendly products, that is, carbon dioxide, water and biomass. Given the many interesting properties of PBS, as for example a melting point similar to low density polyethylene, tensile strength close to polypropylene, stiffness between low density and high density polyethylene, and the variety of possible applications, including the production of biomedical materials,

biodegradable agricultural film, packaging, etc., it can be predicted that PBS resins will constitute a large market in few years [30-31].

PBS is a crystallizable polymer with a crystallization ability ($X_c$) in the range 35–45%. As such, its properties strongly depend on the crystal fraction and morphology. Crystal's modifications have a monoclinic unit cell that includes two repeating units. Crystal growth usually occurs via heterogeneous nucleation, but can also be initiated by homogeneous nucleation at temperatures below 7 °C. Experimental data on both the nucleation and crystallization kinetics of PBS are available in a wide temperature range, from the glass transition temperature $T_g$ around -35 °C to temperatures close to the melting point. The melting behavior of PBS has also received attention, due to the presence of multiple endotherms, which arise from melting of crystals of low stability and subsequent recrystallization of the unstable melt occurring during heating. The equilibrium melting temperature, $T_m°$, was estimated to be 127.5 °C if determined with the Hoffman-Weeks approach, and 146.5 °C if calculated with Gibbs-Thomson equation [30-32].

## 2.3. COPOLYESTERS

Copolymers synthesis offers the ability to alter the properties of homopolymers in a desired direction by the introduction of the appropriately chosen second repeating unit. In this way, the desired properties of two different homopolymers are combined in a single copolymer. The magnitudes of properties, such as crystallinity, flexibility, crystallization and melting temperature, as well as glass transition temperature are generally altered, and even the directions of these changes can be selected depending on whether statistical, alternating or block copolymers are involved [33].

The most commonly produced copolymers, due to their versatility and simplicity are the random copolymers, in which the final properties are generally in between the properties of the parent components or co-monomers.

### 2.3.1. Random copolyesters

Random copolymers are those in which the probability of finding a given constitutional repeating unit at any given site is independent of the nature of the adjacent position. The term "random copolymer" is occasionally used for copolymers with the additional restriction that the constitutional repeating units are present in equal amounts. Therefore, random copolymers are a special case of statistical copolymers, in which statistical laws, e.g., Markovian statistics (i.e., first- or second-order) are obeyed. Although, it is worth noting that random copolymers obeys Bernoullian statistics (i.e., zero-order Markovian statistics) [33].

Random copolymerization is a simple synthetic strategy of combining the properties of two distinct homopolymers. It provides random covalent links between different comonomers, therefore ensuring total melt miscibility, at variance with the typical immiscible polymer blends. Their thermal and mechanical properties can be tailored by changing the composition of the copolymer.

This work deals with the synthesis and crystallization behavior of random copolyesters, which are very important polymeric materials due to the fact that many of them can be biobased and biodegradable. Their hydrolytic degradation rates strongly depend on their chemical structure, degree of crystallinity and morphology. Their morphology and crystallinity can also influence their mechanical properties, permeability to gases and thermal stability.

The crystallization of random copolymers is a complex function of the chemical structure of the repeating units involved, molar ratio of comonomers and molecular weight. In general, the crystallization of random copolymers depends on whether the crystalline phase is pure or if the co-units enter into the crystallite, either in equilibrium or as a defect. This is reflected on both the crystallization and in the subsequent melting, generating three different behaviours, in copolymers with crystallizable parent components.

Scheme 2.1 represents the three general ways in which random copolymers can crystallize, as deduced from the trends of how the thermal transitions vary as a function of copolymer composition. The thermal transitions represented as examples in Scheme 2.1 are those typically determined by non-isothermal Differential Scanning Calorimetry (DSC) experiments. In addition, for the sake of clarity, cartoons of how the comonomeric units are located into the crystal lattice in these three crystallization models are also shown.

#### 2.3.1.1. Isomorphic random copolyesters

When two crystallizable repeating units meet strict molecular requirements, the copolymers can crystallize in the same crystal lattice, in the entire composition range. In other words, the two comonomeric units along the chain can co-crystallize regardless of composition. Therefore, the two comonomers can be considered miscible in the crystalline state. This case is referred to in Scheme 2.1 as total inclusion of comonomers in a single crystal lattice or isomorphic behaviour (see the corresponding cartoon (Isomorphism) at the right of the Scheme 2.1). Thermal and structural properties, such as melting temperatures and lattice parameters, typically show linear dependence on composition (see Scheme 2.1).

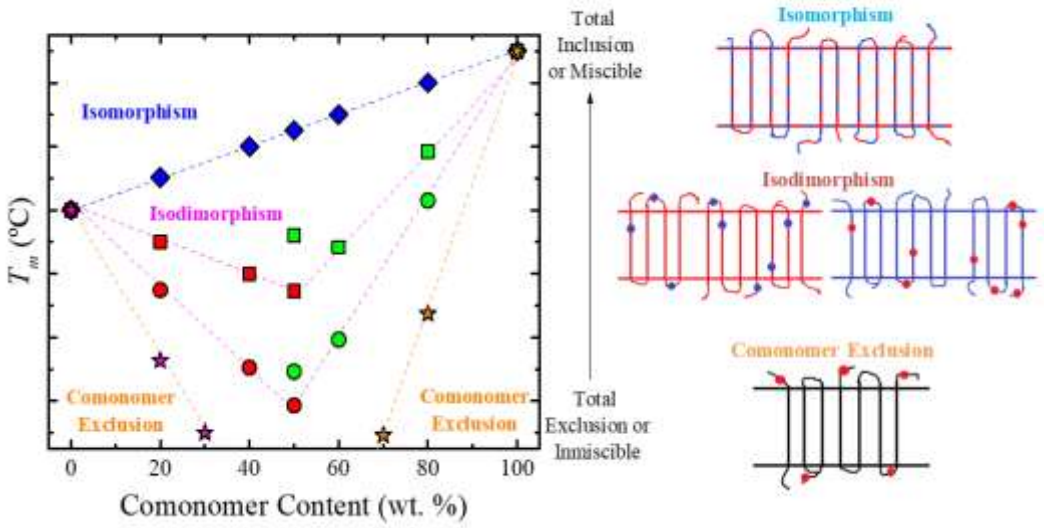


***Scheme 2.1.*** *Schematic representation of the different melting temperature, Tm, trends as a function of comonomer content (left). Cartoons of the models of the different crystallizations modes (right) described on the left* [34].

### 2.3.1.2. Isodimorphic random copolyesters

The concept of isomorphism in the polymer field was first considered by Natta et al.[35]. According to Allegra and Bassi [36], the requirements to observe macromolecular isomorphism in random copolymers are: (i) approximately same shape, volume and compatible conformations of the different monomer units, (ii) analogous chain conformation, lattice symmetry and dimensions of the crystalline phase of the "parent" homopolymers, (iii) total miscibility in the melt of the comonomers and (iv) similar rate of crystallization of the two parent homopolymers. As a result, a total inclusion of both comonomers in the crystalline lattice occurs, and the composition of the crystal perfectly reflects the one of the polymer chain. Because of the specific conditions to be met, only four random copolyesters have been reported to exhibit isomorphic crystallization: poly (hexamethylene gluarate-ran-hexamethylene azelate) (P(HG-ran-HA)) [37], poly (ε-caprolactone-*ran*-2-oxepane-1,5-

dione) (P(CL-*ran*-OPD)) [38], poly (ε-caprolactone-*ran*-ω-pentadecalactone) (P(CL-ran-PDL)),[39] and poly (butylene succinate-*ran*-butylene fumarate) (P(BS-*ran*-BF)) [40].

When the two homopolymers (A and B) do not share a common crystalline structure, but they still have similar repeating units, an isodimorphic behavior of the random copolymers (A-*ran*-B) constituted by the respective repeating units can result. A partial inclusion of comonomer A in the unit cell of homopolymer B crystals is typically observed for copolymers with composition rich in B units, and vice versa. However, the inclusion is only partial, i.e., the concentration of comonomer A in the B crystals is lower than its concentration in the polymer chain. Since both comonomers can be hosted in the crystals of the majority component (comonomer A in the B crystals, and comonomer B in the A crystals), a "pseudo-eutectic" trend of the thermal properties (melting and crystallization temperatures, as well as their enthalpies) is obtained ((see the Tm as function of comonomer composition (left) and the corresponding cartoon (isodimorphic case) at the right of the Scheme 2.1).

As represented in Scheme 2.1, isodimorphic copolymers are characterized by a homopolymer-A-rich crystalline phase in one side of the pseudo-eutectic region and a homopolymer-B-rich crystalline phase on the other side of the eutectic region. While isodimorphic copolymers can still crystallize in the entire composition range, the melting temperature of the two crystalline phases is depressed by the presence of the included second comonomer, until a minimum value is reached for an intermediate composition. As will be show below, recently, three phases have been found at the eutectic region, i.e., mixed amorphous phase, homopolymer-A-rich crystalline phase and homopolymer-B-rich crystalline phase. This is the reason behind the double data points represented at the eutectic composition in Scheme 2.1. More precisely, the term pseudo-eutectic point or pseudo-eutectic region should be preferred, since the three phases are not in thermodynamic equilibrium. Hence, at the pseudo-eutectic region the copolymers can display double crystalline superstructural morphologies.

According to the literature, there are no general rules that can unambiguously predict if a copolymer will display isodimorphism or not. In fact, even in those cases where the comonomers have similar chemical structures and are miscible in the amorphous phase, the possibility of forming a mixed crystalline unit cell, or in other words the efficiency of comonomer inclusion, is not easily determined. In spite of this, some features affecting isodimorphic behavior have been highlighted in the literature. For instance, a homopolymer with a large unit cell is expected to include more easily a comonomer whose respective homopolymer presents a smaller unit cell [41]. Also, a comonomer with an even number of methylene groups in the repeating unit will most likely include similar even CH2 comonomers in its unit cell, and exclude those with odd number of carbon atoms in their chemical structure [42-43]. These empirical rules, related to the miscibility of the comonomers in the crystalline state are not always strictly obeyed. However, below the important rules for this chapter are going to be described.

Scheme 2.1 show two curves for the isodimorphic case from top to bottom, representing different degrees of inclusion of the comonomers in the homopolymer crystal lattice. With a higher degree of inclusion, the crystallization/melting behavior deviates less from the isomorphic case. In contrast, when the comonomer units are largely excluded from the crystals, even though the copolymer may still able to crystallize in all compositions, the thermal response will be closer to that of a copolymer characterized by a complete rejection of the co-units to the amorphous phase, discussed in the following.

In this work, we consider that in order to determine whether random copolyesters are isodimorphic, the points indicated on Scheme 2.2 should be met.

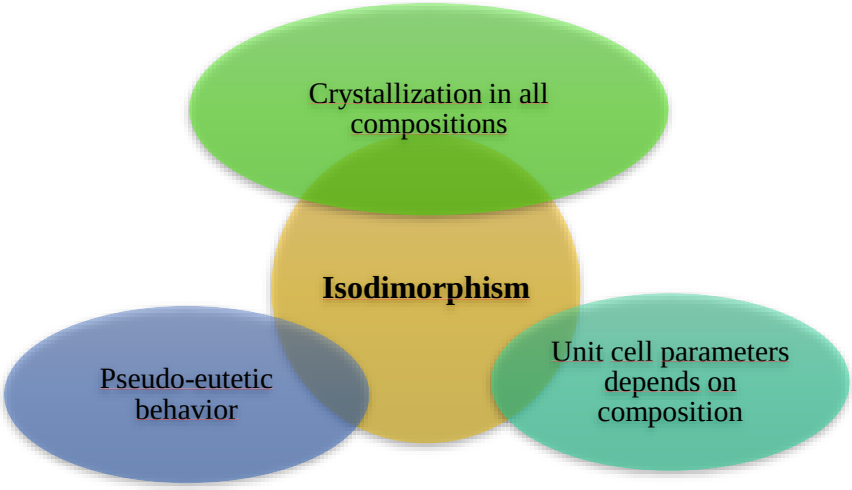


***Scheme 2.1.*** *Schematic representation of the criteria followed in this work to determine the isodimorphic character of random copolyesters.*

Scheme 2.2 shows that when a random copolyester is able to crystallize in all the composition range, with a pseudo-eutectic behaviour in the $T_m$ *versus* comonomer content curve, and with changes in the unit cell parameters with composition, then it can be considered isodimorphic. The different evidences of isodimorphism could be obtained by Differential scanning calorimetry (DSC) characterization which can efficiently highlight the pseudo-eutectic feature of the thermal transitions, as well as the crystallization in all the compositions. Deeper information is obtained by Wide and Small Angle X-Ray Scattering (WAXS/SAXS), since the partial inclusion of the minority co-unit in the crystalline unit cell (*i.e.*, note that such inclusion leads to changes in the unit cell parameters) of the major component affects the structure and morphology at different levels. Others techniques that can provide useful information are: infrared spectroscopy (FT-IR), Polarized Light Optical Microscopy (PLOM) and nuclear magnetic resonance (NMR) [34].

The above described criteria, with the suitable techniques, were used in four different copolyesters in the present work. It is important to remark that such criteria have been applied in previous works, by Arandia et al. [44], Safari et al. [45-46], and Pérez-Camargo et al. [47]. As we mentioned above, there are some factors that can

influence in some of the features of the isodimorphic behaviour. For instance, the chemical structure of the comonomers strongly influence in the position of the eutectic point.

In general, since both comonomers are semicrystalline, the position of the eutectic point is determined by the competition on the crystallization of both comonomers, whereas the miscibility reflects the compatible extent of comonomer in each crystal lattice [48].

#### 2.3.1.3. Random copolymers with complete exclusion

When comonomer B is completely rejected from the crystalline structure of the major component (comonomer A) (see the corresponding cartoon (comonomer exclusion) at the right of the Scheme 2.1), the transition temperatures and enthalpies are strongly depressed as the content of comonomer B increases in the random copolymer, and there exists a range of copolymer compositions where the copolymer remains completely amorphous. Random copolymers with complete exclusion, where symmetrical compositions do not crystallize are very common and constitute the most commonly reported case in the literature.

## 2.4. Methods of copolymerization

Among years, several methods for the synthesis of polyesters have been developed, optimizing the process and enhancing their properties. In this thesis, the polycondensation polymerization of polyesters, enzymatic polymerization and the ring opening polymerization of polyesters will be explored for the synthesis of copolyesters derived from Succinic acide, caprolactone, and buthane diol monomers and are presented as follows.

### 2.4.1. Melt polymerization by Polycondensation

Polyesters can be obtained by stoichiometric stepwise reaction between difunctional reactants with the formation of low molecular weight and condensates

byproducts. Typically, polyesterifications reactions include two steps: 1) esterification with a diol and 2) polycondensation to synthesize of polymers. It is necessary to maintain a proper end group stechiometry and to removal the condensates products in order to obtain high molecular weights [49]. These reactions are performed using an acid or using a dimethyl ester with an excess of 3:1 mol of diol. Vacuum is commonly applied in the second step in order to remove the condensate (water or methanol) and resulting high molecular weights. An organometallic catalyst, such as metal salts and oxides is used with temperatures in a range of 160-290 °C [50-51]. Many commercial aliphatic and aromatic polyesters, i.e. PET or PBT are produced by this method.

### 2.4.2. Ring Opening Polymerization (ROP)

ROP is an excellent polymerization method of synthesis for the preparation of polymers using cyclic monomers, which can be opened by both enthalpical and entropical ways [52]. Even though this method has been used for the polymerization of many products, the use in lactones is scarcely explored [51]. Ring sizes between 2 and 8 atoms may be polymerized due to the loss of enthalpy associated with the loss of ring strain. In this thesis, polymerization via ROP had applied for polymerization of ε-caprolactone.

### 2.4.3. Enzymatic polymerization by ROP

Enzymes can be used for polymerization by ROP. Enzymes are proteins which exhibits a high catalytic efficiency. Lipases are reported to be good catalysts for melt polycondensation [53] and ring opening polymerization [54-55]. The best activity of the enzymes is in hydrophilic solvents, on the contrast, hydrophobic solvents such as DMSO or methanol lead to significant modifications in enzyme conformation and therefore to a dramatic decrease in the enzyme activity. The enzymatic synthesis of polyesters is used in the preparation of low-melting point polyesters, mainly aliphaticones when the polymerization temperature is not upper than maximum accepted by the enzyme. Lipases have been proved to be efficient for polymerizations

via ROP, especially, Candida Antarctica (CALB) that is widely used in many reaction with different cyclic oligomers and lactones [56].

## 2.5. POLYMER CRYSTALLIZATION

The study of crystallization in polymers has attracted much attention as thermal and mechanical properties of semicrystalline materials depend on the number, dimensions and organization of their crystalline structures. Although a polymer can crystallize during its polymerization reaction or from a solution, the crystallization of the polymer from the melt state is the most significant because of its similarity to most industrial processing techniques.

The study of crystallization in relation to temperature can be carried out in an isothermal way, in which the material is rapidly cooled from the melt and left crystallizing at a constant temperature, or in a non-isothermal way, in which the material is cooled at a controlled rate. Despite the fact that during industrial processes crystallization is mostly developed in a non-isothermal way, obtaining like that a large distribution of crystals with different thickness and thermal stability, not only are non-isothermal studies done, but also many studies under isothermal conditions are carried out which are after extrapolated to dynamic or non-isothermal processes.

Crystallization is the combination between nucleation and growth processes. The crystallization of a polymer can occur only in a limited range of temperatures; the glass transition temperature ($T_g$) which is the lower temperature limit and the melting temperature the upper limit. Below $T_g$, the mobility of the polymer chains is restricted while close to $T_m$ the nucleation process is inhibited. It is known that the nucleation rate ($\dot{N}$) and the growth rate ($G$) do not depend in the same way on the degree of supercooling. Generally, the maximum of $\dot{N}$ appears at higher supercooling (see Scheme 2.3 ), at these low temperatures the segmental mobility is reduced and this favors the nucleation rate generating a greater number of crystals of small size. On the other hand, at higher temperatures crystalline growth is favored and fewer nuclei are formed generating larger spherulites [57-61].

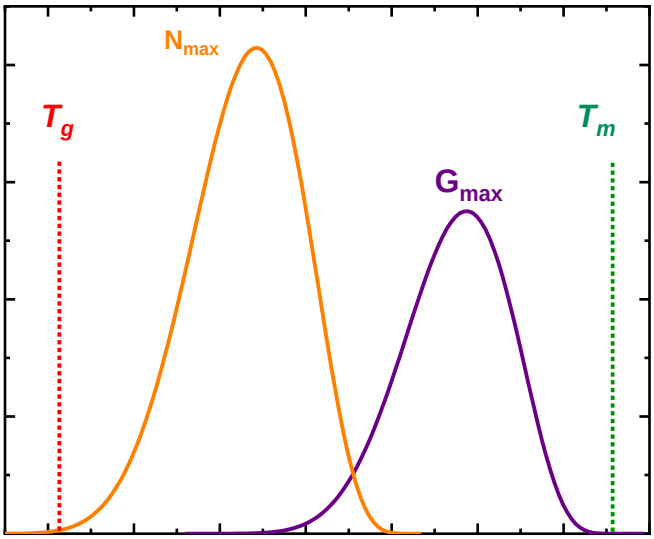


***Scheme 2.3**. Schematic representation of the nucleation rate and the crystalline growth rate (G) as a function of temperature. (Figure modified from reference [62])*

In this chapter, the fundamental processes involved in polymer crystallization are briefly summarized.

## 2.5.1. Crystal Morphology

### 2.5.1.2. Fringed micelle-model

In 1930 Herrmann reported the fringed-micelle model, which is presented schematized in Scheme 2.4 and is essentially based on a double phase system characterized by crystalline and amorphous regions [63]. It is essentially based on a two-phase system, characterized by crystalline and amorphous regions. The crystalline regions are composed by stacks of short lengths of different macromolecular chains, aligned parallel to each other. In contrast, the amorphous region is constituted by disordered sequences, which can be interconnected by two different ordered portions

of the chain. The key feature in this model is that one molecule participates in more than one crystallite since the molecular contour length (typically around 100 nm) is at least ten times longer than the experimentally measured size of crystallites. The model also explains the existence of fibrillary crystallites and predicts their growth direction normal to the chain axis [19]. The model easily accounts for the dissipation of molecular order from the crystalline to the amorphous regions. This model was able to explain, among others, the properties of hardness and flexibility based on the amorphous and crystalline percentages of the material, but it was not able to predict the optical properties.

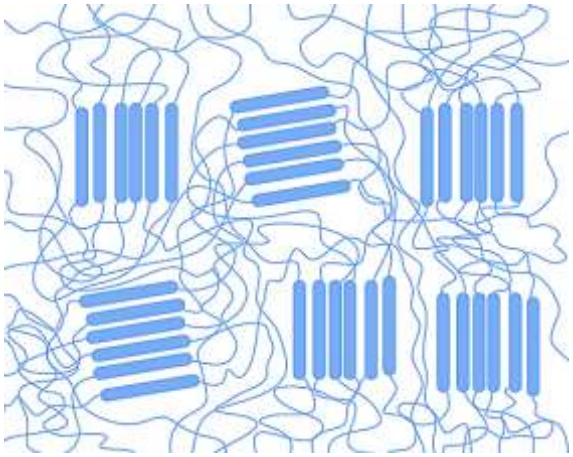

***Scheme 2.4.*** *The fringed-micelle model scheme [64].*

**2.5.2.2. Chain folded model**

In 1938, Storks introduced the concept of "chain-folding" since he concluded that the chains of the semicrystalline trans-polyisoprene had to fold when it crystallized [57]. Finally, in 1957 Keller [65] managed to obtain single crystals of polyethylene from a diluted xylene solution. The electron diffraction studies of the single crystals showed that the polymer chains had their axis placed perpendicularly to the single crystal base, which was explained by assuming that chains fold perpendicularly to the most extensive sides of the crystal. During the same year Fischer [66] and Till [67] also reported single polymeric crystals with very similar lamellar

morphologies to those reported by Keller. Therefore, the "folded-chain model" proposed by Keller (illustrated in Scheme 2.5) represented an important advance in the understanding of the organization of polymeric crystals obtained from solution [57].

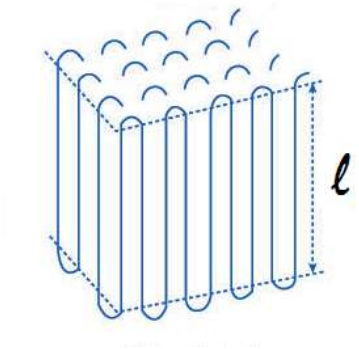


***Scheme 2.5**. Scheme of the concept of "chain-folding" proposed by Keller. (From reference [65])*

Keller reported that lamellae with folded chains are the fundamental unit of polymer morphology, which grow to form supramolecular structures such as spherulites, axialites and hedrites [57-59].

Kumaki et al. [68] were able to directly observe chain folds by torsional tapping atomic force microscopy in two-dimensional crystals of isotactic and syndiotactic poly(methyl methacrylate) in a Langmuir-Blodget film. One example of their observations can be appreciated in Figure 2.1. Similar results have been obtained by Hobbs et al. [69] in polyethylene.

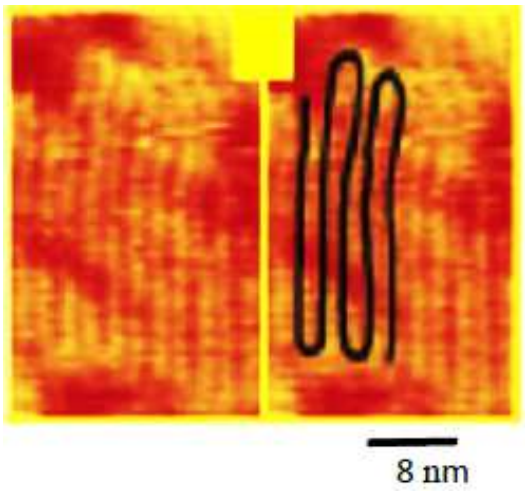


***Figure 2.1.*** *(Left) Torsional tapping atomic force image of a 2D layer of iPMMA crystallized in a Langmuir-Blodgett film by applying an extremely slow compression on the water surface where the material is deposited. (Right) Drawn in black on top of left image are some of the chain conformations observed, where chain folding is clearly appreciated. Kumaki et al.*

Flexible polymers capable to crystallize form spherically symmetric aggregates of radial lamellae known as spherulites. These structures appear as birefringent spheres which are observable by Polarized Light Optical Microscope (PLOM) and generally show characteristic extinction patterns called Maltese cross which are formed parallel and perpendicularly to the direction of polarization. If a sensitive tint plate is placed at 45° with respect to the polarization direction, distinct colours can be observed that not only enhanced contrast (as in Figure 2.2) but can also be used to determine the sign of the spherulites.

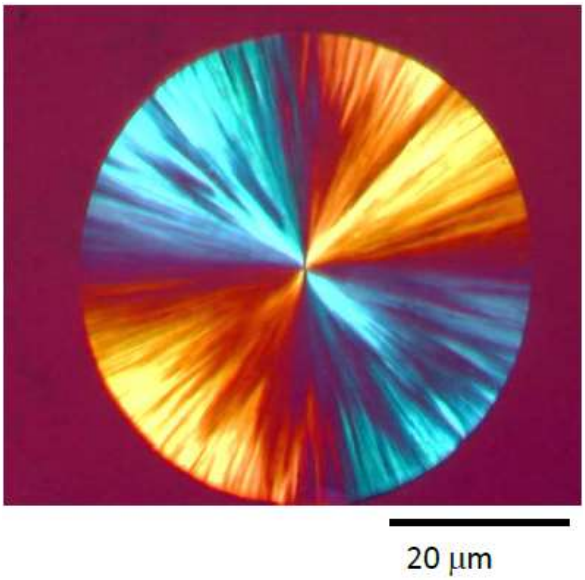


***Figure 2.2**. Spherulites of poly(lactic acid) (PLA) [14].*

Transmission electron microscopy (TEM) measurements in the internal areas of the spherulites, showed that they are constituted by lamellae (separated by amorphous interlamellar zones) which grow radially. Figure 2.3 shows TEM micrographs of poly(ε-caprolactone) single crystals grown from dilute solution and their corresponding electron diffraction patterns. Terraces with spiral growth starting at edge dislocation points are typical of solution grown single crystals. The degree of order in the crystals is apparent from the well-defined diffraction spots, hence the crystallinity degree is very high in these single crystals. More than 25 independent reflections can be obtained that fit well the orthorhombic unit cell reported for PCL with a = 0.747 nm, b = 0.498 nm, c (fiber axis) = 1.705-1.729 nm [70-71]. The c axis is oriented perpendicular to the single crystals basal surface.

The chains are arranged perpendicularly to the flat horizontal surface of the lamella and are therefore tangential to the spherulite and to the direction of growth (see Scheme 2.6) [57-59]. The thickness of typical lamellae in polymers vary from 50 to 400 Å. The primary lamellae (or mother lamellae) extend from the center to the end of the spherulite and along its growth axis new branches are formed by secondary lamellae (or daughter lamellae).

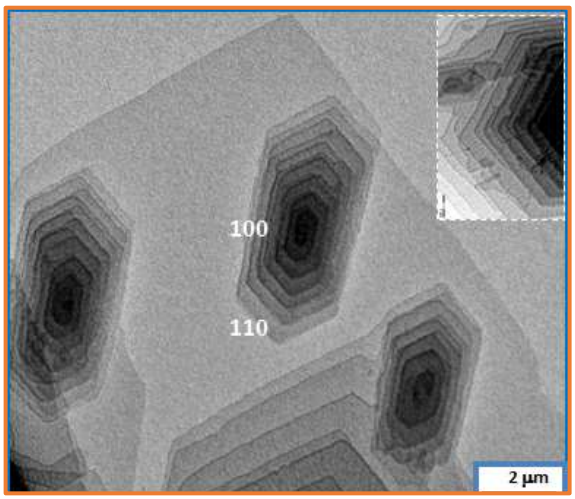


***Figure 2.3.*** *Poly (ε-caprolactone) single crystals grown from n-hexanol dilute solutions at 26 °C.*

From the point of view of spherulitic morphology, the model proposed by Mandelkern [58] in 1964 is currently accepted, in which three fundamental regions are defined (Scheme 2.7): the first corresponds to the crystalline region formed by lamellae; the second corresponds to the amorphous region with a totally disordered conformation and similar characteristics to those of the melt; and a third, the interfacial region, formed by chains which are also part of the lamellae and are in between this interfacial region.

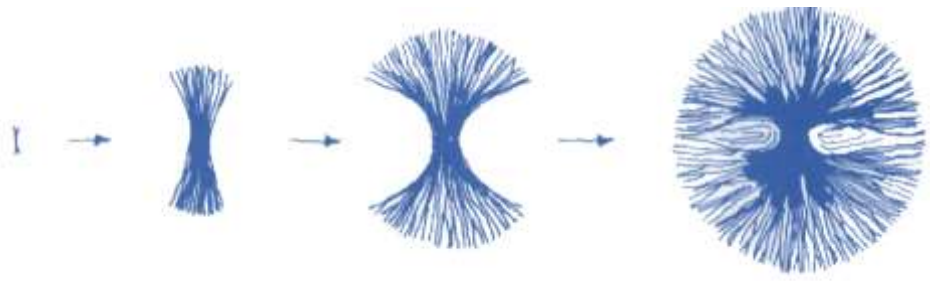

***Scheme 2.6****. A scheme indicating the growth process of spherulite initiated in lamellar sheafs* [72]*.*

The difference in size and morphology between the spherulites of different polymers will depend on the chemical nature, the molecular weight and its distribution, the crystallization conditions and the density of active nuclei present in the material.

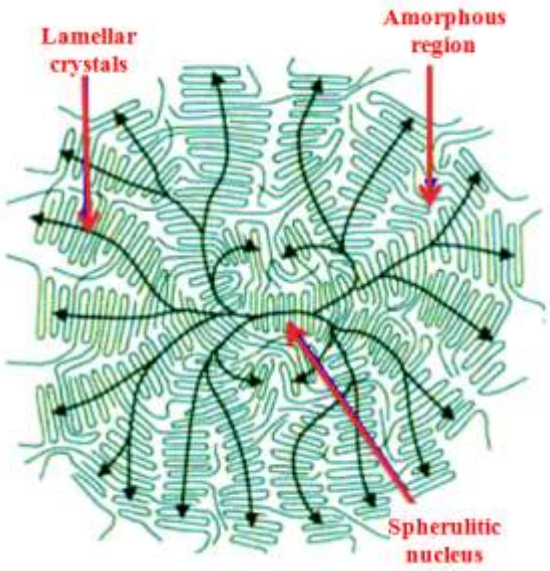


***Scheme 2.7.*** *Radial growth of spherulite in two dimensions. Amorphous and crystalline regions.*

Different techniques such as Wide Angle and Small Angle *X*-ray Scattering, Polarized Light Optical Microscopy, Phase-contrast Microscopy and even Transmission Electron Microscopy, are used to study these crystalline superstructures. In the present work, Polarized Optical Microscopy technique (PLOM) has mostly used since it provides a simple and useful way to directly visualize crystalline morphologies while determining spherulitic growth rates and nucleation density and kinetics.

### 2.5.2. Crystallization Kinetics

The crystallization in polymers can be defined as a first-order phase transformation of a supercooled liquid [3]. In the case of very low molecular weight molecules, they can crystallize almost immediately after reaching the equilibrium

melting point, but in the case of polymers, they are only able to crystallize at considerable high supercoolings. Polymer crystallization takes place at temperatures between the melting temperature ($T_m$) and the glass transition temperature ($T_g$). Starting from the melt, as temperature decreases the crystallization rate increases as the energetic barrier needed for phase transformation decreases, but as temperature is further decrease, the diffusion of molecular segments decreases and consequently reduces the crystallization rate. The lower the crystallization temperature the thinner the lamellar formed, i.e., they would be more metastable. This effect becomes more significant as the temperature approaches the glass transition. When polymers crystallize from the melt, as the crystallization temperature further decreases they crystallize first slowly, then more rapidly with a maximum crystallization rate, and finally slowly again following a bell shape trend [2-3.] On the other side, when they crystallize from the vitreous state, same phenomenon happens but in this case as temperature increases. Hence the high-temperature limit is controlled by the thermodynamic forces and the low-temperature limit by diffusion limitations of molecular segments.

Polymer crystallization involves primary crystallization, secondary crystallization and crystal reorganization processes. In order to better understand the kinetic analysis of the results which are presented along this PhD thesis work, below in the text some fundamental aspects of nucleation and crystal growth, will be presented and also the most important nucleation and growth theories will be discussed

**2.5.2.1. Primary Nucleation**

Nucleation is the first step in the formation of crystals in melt polymers. The process of crystal nucleation has been extensively described in the literature and its kinetics discussed in a large number of articles and books [58, 60, 73-77].

The first stage of primary nucleation involves both translational and rotational diffusion of crystallizable units with an appropriate orientation and position

which are able to develop a stable nucleus. This step is controlled by the free enthalpy change due to the phase transformation. At a nucleus critical size *r* *, the enthalpy barrier required to allow the nucleus growth is surpassed and from this point chains addition occurs irreversibly and the crystal begins the growth process.

Two nucleation mechanisms are known; homogeneous nucleation, when the formation of the nuclei occurs in the bulk phase, and heterogeneous nucleation, when the formation occurs on preexisting surfaces or heterogeneities. When nucleation goes through a homogeneous mechanism, intrinsically unstable particles (embryos) are formed in the melt because of thermal fluctuations. For those very small particles the decrease in free energy due to phase transition is exceeded by the increase in interfacial free energy. Regarding to the critical size of these particles, as the nucleation step is an active process associated with a free energy barrier to be overcome, there is a critical size separating these particles whose free energy of formation increases during growth from those whose energy decreases. If the size of embryos surpasses this critical value, they turns into kinetically stable aggregates (nuclei) of a growing crystal, otherwise, they disappear again [60, 78].

The critical radius of the sphere (*r**) associated with the free energy barrier is obtained following next equation [57] :

$$r^* = \frac{2\sigma T_m^\circ}{\Delta H^\circ \, \Delta T} \qquad \text{Eq. 2.1}$$

where $\Delta H^\circ$ is the enthalpy of fusion, $T_m^\circ$ is the melting temperature at the thermo-dynamic equilibrium, $\sigma$ is the specific free surface energy of the nucleus at the surface and $\Delta T$ represents supercooling defined as ($T_m^\circ$- $T_c$). Similarly, the free energy barrier which must be overcome in order to form stable aggregates is expressed by the following equation:

$$\Delta G^* = \frac{16\pi\sigma^3 {T_m^\circ}^2}{3\Delta {H^\circ}^2 \Delta T^2} \qquad \text{Eq. 2.2}$$

Equations 2.1 and 2.2 show that nucleation occurs more easily at lower crystallization temperatures since the free energy barrier associated with the process is smaller due to the nucleus critical size needed is also smaller.

The formation rate of crystalline nuclei which overcome the critical size and are able to grow is obtained by the following equation proposed by Turnbull and Fisher.[79] In which nucleation rate ($\dot{N}$), and temperature are related.

$$\dot{N} = N_0 e^{(\frac{E_D}{kT} - \frac{\Delta G^*}{kT})} \qquad \text{Eq. 2.3}$$

$\dot{N}$ is the nucleation rate, $E_D$ is the activation energy for the diffusion process and $\Delta G^*$ represents the free energy for the formation of an aggregate with critical dimensions.

The combination of equations 2.2 and 2.3 shows that during a controlled cooling from the molten state $\Delta G^*$ progressively decreases and therefore the nucleation process increases. At further temperature decreases the nucleation rate reaches a maximum value, and then decreases again with the approximation to the glass transition. One of the consequences of the temperature decrease is the viscosity increase which leads to a decrease of chains diffusion.

As explained before, nucleation can occur in different ways; the homogeneous nucleation, when nucleation process occurs in the bulk phase and nuclei are formed only by segments of polymer chains, and the heterogeneous nucleation, when nucleation occurs on preexisting surfaces or heterogeneities and impurities. Heterogeneous nucleation commonly occurs in polymers, since it is very difficult to produce pure polymer without any heterogeneities such as catalyst residues and solvent impurities. Furthermore, heterogeneous nucleation is

thermodynamically favored due to the presence of impurities allows heterogeneous nucleation to take place at smaller supercooling temperatures since the free energy barrier to be overcome will be smaller than forming new nuclei.

#### 2.5.2.2. Crystal Growth

Crystal growth occurs by secondary and tertiary nucleation. The initial step is the formation of secondary nuclei which is followed by a series of tertiary nucleation events [1]. The relationship of spherulitic growth rate (G), which involves the transport (diffusion) term and the secondary nucleation term, with temperature is similar to that of the primary nucleation. Due to both terms have an opposite temperature dependence behavior, as it is shown in Figure 2.4 the growth rate exhibits a maximum and follows a bell shape curve as function of the crystallization temperature (or supercooling). On the left side of the bell shape curve, at high supercooling the dominant term is the molecular transport (diffusion). The diffusion of the macromolecules to the growing front becomes very difficult as melt viscosity greatly increases as the temperature reaches the glass transition temperature, where growth rate decreases to zero. On the right side of the bell shape curve, at high crystallization temperatures, the growth rate is driven by thermodynamic forces of the secondary nucleation [80].

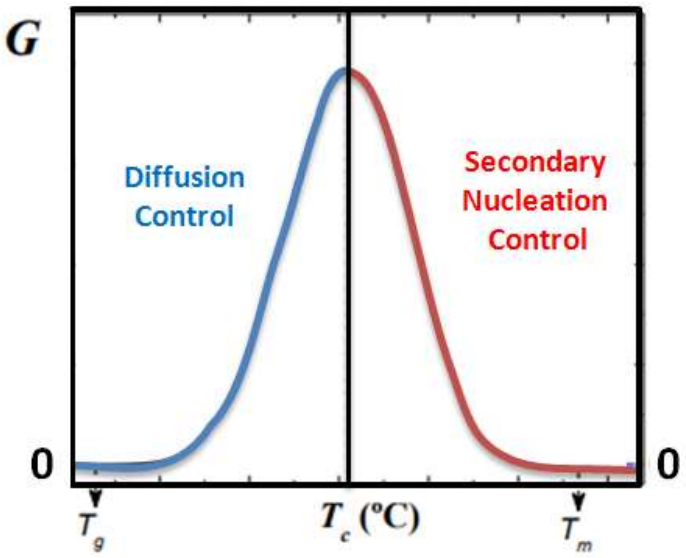


***Figure 2.4**. Crystal growth rate (G) as a function of the isothermal crystallization temperature.*

### 2.5.3. Polymer crystallization theories

Once nuclei are formed, their growth is affected by different factors such as structural regularity, plasticizers, molecular weight and flexibility. Several theories have been developed in order to explain polymer crystallization and the most important are divided by thermodynamic theories [81-82] and kinetics theories [57-60]. The former explain some characteristics about semicrystalline state such as the crystal thickness, however there is a general agreement which considers that kinetic factors control the growth rate and the morphology of polymers.

Kinetic theories are able to predict the temperature dependence with the growth rate, the initial crystal thickness ($l_c^*$), and other important morphological parameters. These theories also explain that the final state is the kinetically most favorable state. Furthermore, the growth rate varies with crystal thickness ($l_c$) and therefore the result on a of different crystal thicknesses distribution will depend on the relation between the crystallization rate and the crystal thickness at each particular temperature.

Depending on the different polymer crystallization theories, they can take into consideration the overall crystallization kinetics, which includes both primary nucleation and crystal growth contributions [78], or only the secondary nucleation (crystal growth). The most common theories among others are the Lauritzen and Hoffman (LH) model [13-14], which was developed to provide analytical expressions to quantify the energy barrier associated to the crystal growth, the Sadler and Gilmer theory [1,83], the Strobl mesomorphic precursors thesis,[60] and the "free growth" theory formulated by Göler and Sachs [2,84].

The last "free growth" theory formulated by Göler and Sachs is one of the first theories developed and the Avrami equation is one of its possible solutions. This theory also establishes that once a given nuclei is created, it grows unrestricted without the influence of others around that may have also been nucleated and could be growing within the same time [2,80, 85].

**2.5.3.1. Overall isothermal crystallization kinetics: The Avrami equation**

The Avrami equation describes how solids transform from one phase (state of matter) to another at constant temperature. The crystallization process occurs when polymers arrange into regular crystalline structures from an amorphous state, and as explained before in the text, the overall rate of crystallization involves two processes: the nucleation rate and the crystal growth rate [86]. One way to follow the crystallization kinetics has been developed through isothermal tests which are usually performed in a DSC. One of the most well-known theories used in order to study the isothermal overall crystallization kinetics is the Avrami model, which gives information about the variation of the crystalline content as a function of time at a constant crystallization temperature ($T_c$).

Avrami's model was proposed by Evans, Kolmogoroff and Avrami during the 1930s and 1940s, and it successfully describes the crystallization phenomenon of macromolecular chains [87-90], however, it does not give any detail of the molecular process involved in the nucleation and growth of polymeric crystals. The development

of Avrami's theory as well as its limits have been described in detail [57, 91], and it can be expressed as the following equation [85] :

$$1 - V_c = \exp(-k(t - t_0)^n) \qquad \text{Eq. 2.4}$$

where $V_c$ is the relative volumetric transformed fraction and $k$ the overall crystallization rate constant which includes contributions from both nucleation and growth. $n$ is the Avrami index, whose value depends on the mechanism of nucleation and on the dimensionality of crystal growth, $t$ is the experimental time and $t_0$ the induction time.

The induction time correction deals with the fact that a certain time may elapse before crystallization starts. In other words, once the isothermal crystallization temperature is reached, there is period of time in which there is not crystallization. This time is called the induction time. In mathematical terms, the Avrami equation is only defined when crystallization starts. Therefore, the experimental induction time must be subtracted from the absolute time [92].

One way to express $V_c$ as a funtion of mass fraction of the samples which crystallizes ($W_c$), is presented in equation 2.5;

$$V_c = \frac{W_c}{W_c + \left(\frac{\rho_c}{\rho_a}\right)(1 - W_c)} \qquad \text{Eq. 2.5}$$

where $W_c$ is the mass fraction of the sample, $\rho_c$ the density of a 100% crystalline sample and $\rho_a$ the density of 100% amorphous sample. $W_c$ is calculated from the following equation (equation 2.6), from the integration of the DSC experimental data measured during the isothermal crystallization [57] ;

$$W_c = \frac{\Delta H\ (t)}{\Delta H_{total}} \qquad \text{Eq. 2.6}$$

where $\Delta H(t)$ is the enthalpy variation as function of the time spent at a given crystallization temperature and $\Delta H_{total}$ is the maximum enthalpy value reached at the end of the isothermal crystallization process.

The Avrami constant (*k*) is used to provide a quantitative evaluation of the crystallization evolution since it includes the contribution of both nucleation and crystal growth events. It is directly related with the overall crystallization rate $1/t_{1/2}$ and follows next equation [78] :

$$K = \left(\frac{1}{t_{1/2}}\right)^n ln2 \qquad \text{Eq. 2.7}$$

where $1/t_{1/2}$ is the inverse of the half of the crystallization time (that can be considered an experimental measurement of the overall crystallization rate), and $t_{1/2}$ corresponds to the time needed to achieve 50% of the overall crystallization.

On the other hand, the Avrami index also determines the nucleation type and the crystal growth geometry according to *n* value, which is composed of two terms: [93]

$$n = n_d + n_n \qquad \text{Eq. 2.8}$$

$n_d$ represents the dimensionality of the growing crystals. This term only have integer values, 1, 2 or 3, corresponding to the formation of one, two and three dimensional entities. In the case of polymers the possible dimensions of the growing crystal are 2 or 3. They represent axialites (two dimensional lamellar aggregates) and spherulites (superstructural three dimensional aggregates), respectively.

The term $n_n$ represents the time dependence of the nucleation. This term has a range of values between 0 and 1, where zero corresponds to an instantaneous nucleation, and one to a sporadic nucleation. However, there are several cases where

nucleation is not purely instantaneous or purely sporadic and non-integer contributions to the Avrami index are obtained. Figure 2.5 represents the different combinations of both terms.

The crystallization rate can be expressed as the inverse of the half of the crystallization time, which is usually close to the time at which spherulites impinged on one another and it is usually close to the time where primary crystallization ends and secondary crystallization begins. It can also be defined as the time needed to achieve 50% of the overall crystallization, and it is calculated by equation 2.9:

$$\tau_{50\%} = \left(\frac{-\ln 0.5}{k}\right)^{1/n} = \left(\frac{0.69315}{k}\right)^{1/n} \qquad \text{Eq. 2.9}$$

In equation 2.9 it is assumed that at 50% of the conversion1-$V_c$ is equal to 0.5

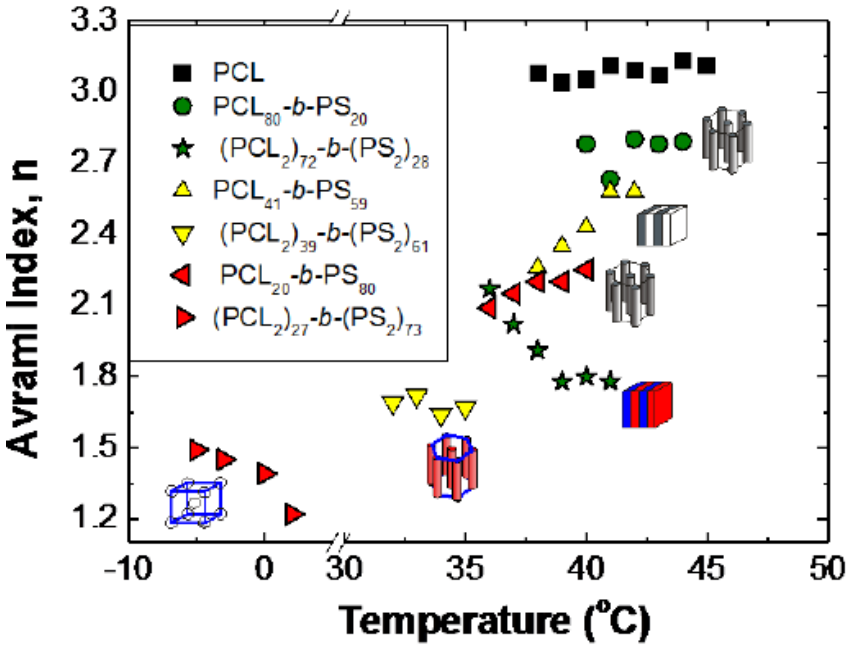

***Figure 2.5.*** *Avrami index values as a function of isothermal crystallization temperature for linear PCL-b-PS diblock copolymers and (PCL2)-b-(PS2) miktoarm star copolymers. Adapted from ref. 66. As the content of PCL decreases in the 3 linear PCL-b-PS copolymer samples, the morphology changes from PCL matrix (80% PCL) to PCL lamellae (41% PCL) to PCL cylinders (20% PCL). In the case of the 3 myktoarm copolymer samples, the morphology changes from PCL lamellae (72% PCL) to PCL cylinders (39% PCL) to PCL spheres (27% PCL)* [94]*.*

Therefore, the inverse of this time needed to achieve the 50% of the total transformation to the semi-crystalline state during the isothermal crystallization process ($1/\tau_{50\%}$) provides an experimental measure of the overall crystallization rate which includes both nucleation and growth. This value is determined experimentally from the isothermal crystallization at a given $T_c$, as shown in Figure 2.6a.

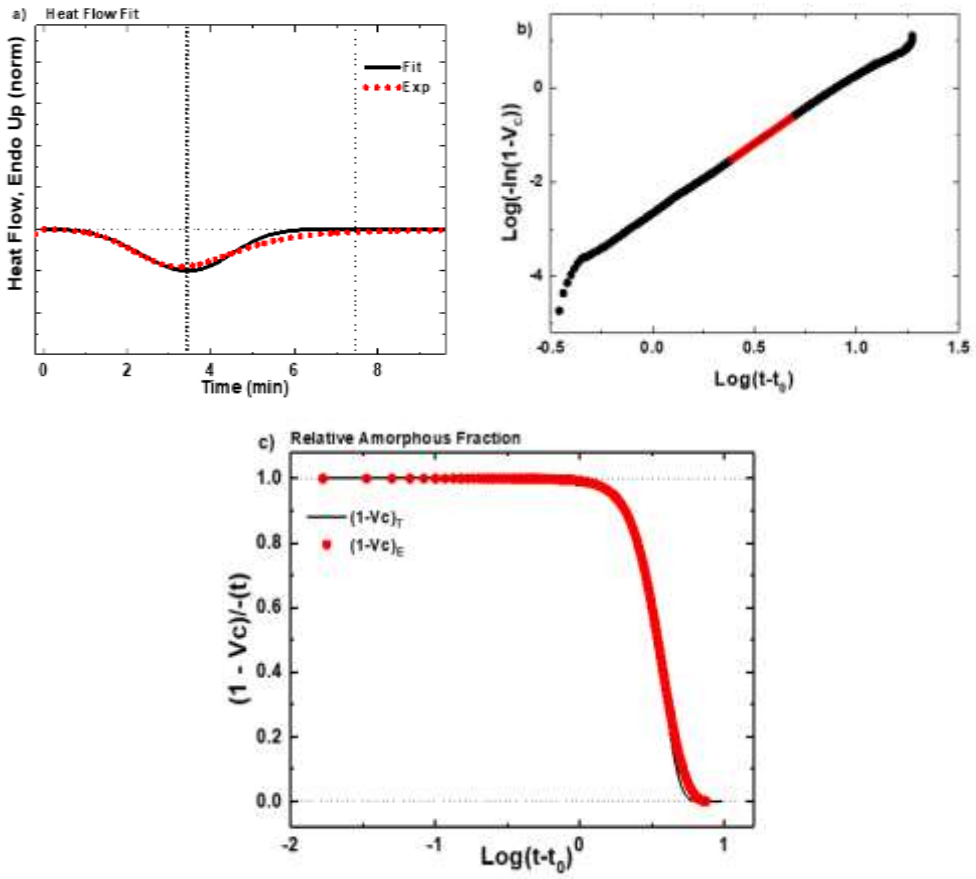


***Figure 2.6**. Avrami fits obtained by Origin: (a) Isothermal curve fit (b) Representation of the Avrami equation, (c) Untransformed relative amorphous fraction (1-$V_c$), as a function of time.*

After applying logarithmic properties to both sides, the following equation is obtained equation 2.10:

$$\log(-\ln(1 - V_c(t - t_o))c) = \log k + n \log(t - t_0) \qquad \text{Eq. 2.10}$$

Following this equation straight lines are obtained for each studied temperature and from the slopes the Avrami index are calculated. By using the Origin plug-in developed by Lorenzo et al. [85] , the Avrami fits are obtained. The Figure 2.6

shows an example of a representative fit of Avrami model and the Figure 2.6b the straight line previously mentioned in equation 2.10.

Figure 2.6a shows the Avrami fit to an isothermal crystallization curve obtained by DSC, while Figure 2.6b shows the untransformed relative amorphous fraction that indicates which percentage of transformation fits the equation. A good fit requires $R^2$ values larger than to 0.9990 according to the recommendations of Lorenzo et al. while the Avrami equation must be fitted up to 50% of transformation, as it assumes free growth of the superstructural entities.

**2.5.3.2. Overall isothermal crystallization kinetics: The Lauritzen-Hofmann equation**

The Lauritzen and Hoffman theory is one of the earliest theory derived to specifically model polymer chain crystallization based on a kinetic basis. [95] Although the theory has received much criticism lately, [95-100] it is still useful since its relatively simple analytical expression (Equation 2.11) can be used to fit experimental data over a wide supercooling range [99, 101-105]. The theory can be applied for both spherulitic growth rate (*i.e.*, experimental data obtained by PLOM) and overall crystallization rate (*i.e.*, data obtained by DSC). In the case of the spherulitic growth rate (*G (T)*), the LH equation can be expressed as a function of the supercooling ($\Delta T$) according to [95-96, 100, 106-107]:

$$G(T) = G_0 \exp\left(\frac{-U^*}{R\,(T_c - T_\alpha)}\right) exp\left(\frac{-K_g^G}{T_c \Delta T_f}\right) \qquad \text{Eq.2.11}$$

where $G_0$ is a pre-exponential growth rate constant. The first term is controlled by diffusion, and $U^*$ is the activation energy for the transport of the macromolecules to the growth front (a value of 1500 cal/mol is usually employed), $R$ is the gas constant, and $T_c$ is the isothermal crystallization temperature. $T_\alpha$ is the temperature at which chain mobility ceases, and it is usually taken as $T_g$- 30 (K). The second term is the secondary nucleation term where $\Delta T$ is the supercooling defined as $T_m^0$-$T_c$, with $T_m^0$ as the equilibrium melting point, which can be calculated according to the Hoffman-Weeks extrapolation (H-W) as is show below. The factor $f$ is a

temperature correction term equal to $2T_c/(T_c+T_m^0)$, and $K_g^G$ is a secondary nucleation constant that is proportional to the energy barrier for spherulitic growth.

The value of $K_g^G$ can be expressed as [95-96, 100, 106-107]:

$$K_g^G = \frac{jb_0\sigma\sigma_e T_m^0}{k\Delta h_f} \quad \text{Eq.2.12}$$

where *j* is determined by the operating regime (see below) and is equal to 4 for regime I and III and is taken as 2 for regime II; $b_0$ is the width of the chain, $\sigma$ is the lateral surface free energy, $\sigma_e$ is the fold surface free energy, *k* is the Boltzmann constant, and $\Delta h_f$ is the heat of fusion of a perfect crystal. The following equations allow the calculation of $\sigma$ (and therefore $\sigma_e$) and *q*, the work done by the chain to form a fold:

$$\sigma = 0.1\Delta h_f\sqrt{a_0 b_0} \quad \text{Eq.2.13}$$

$$q = 2a_0 b_0 \sigma_e \quad \text{Eq.2.14}$$

Where $a_0b_0$ is the cross-sectional area of the chain.

The Lauritzen and Hoffman theory analyzes the growth data according to the competition between the rate of deposition of secondary nuclei (*i*) and the rate of lateral surface spreading (*g*), resulting in three different regimes:

- *Regime I: occurs when i<<g and may be found at very low ΔT.*
- *Regime II: i is the order of g and occurs at moderate ΔT.*
- *Regime III: i>g and is found at very high ΔT.*

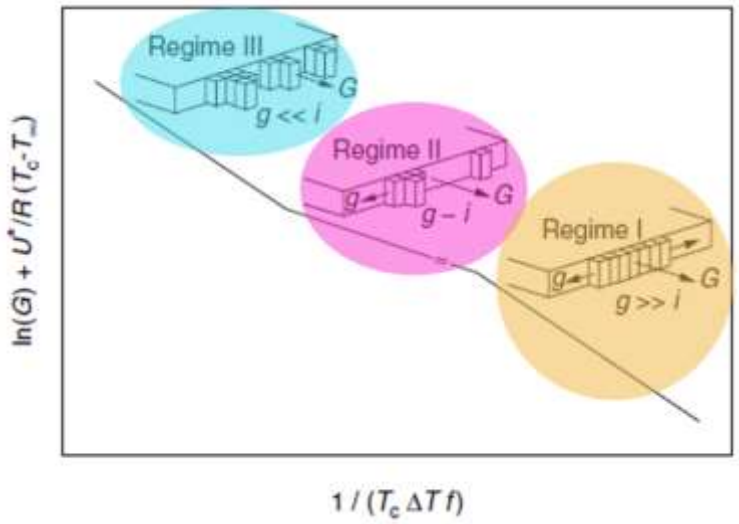


***Scheme 2.9.*** *Schematic representation of LH regimes [95].*

The overall crystallization kinetics (not only the spherulite growth rate) is determined by the contributions of both nucleation and growth. The L-H theory can be applied not only to the spherulites growth rate but also to the isothermal crystallization kinetics data collected by DSC. In the latter case, the Equation 2.17 is as follow:

$$\frac{1}{\tau_{50\%}}(T) = G_0^{\tau} exp\left(\frac{-U^*}{R(T_c - T_\alpha)}\right) exp\left(\frac{-K_g^{\tau}}{T\Delta T f}\right) \qquad \text{Eq.2.15}$$

Notice that the superscript $\tau$ is use to indicate that the parameters depend on the experimental data obtained by DSC, whereas the superscript *G* indicate that the parameters were obtained from the PLOM experimental data. The Equations 2.12 to 2.15 can be used with the DSC data.

The experimental data to apply the Lauritzen and Hoffman Theory can also be analyzed with the Origin ® plug in developed by Lorenzo et al. [85]. The plots generated are show in Figure 2.7

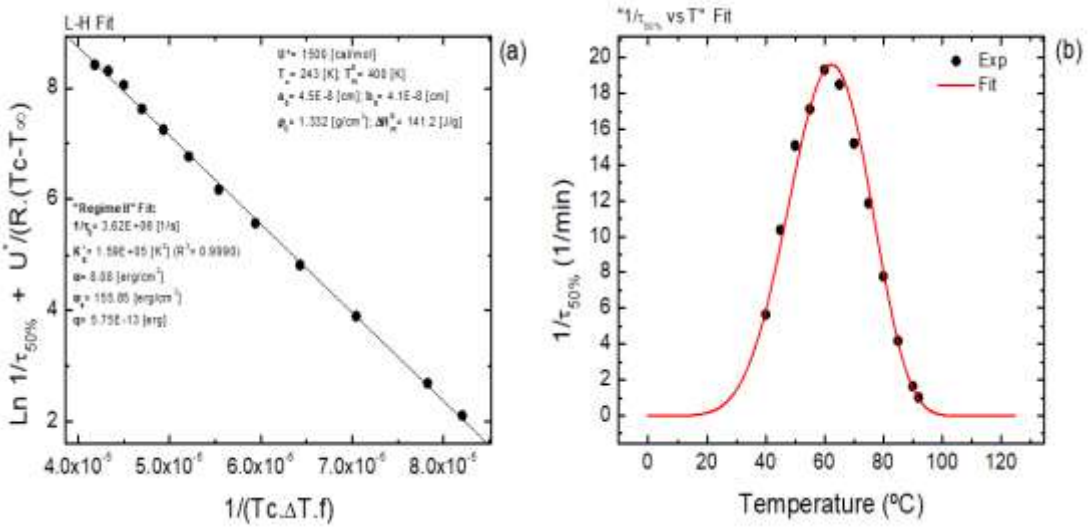


***Figure 2.7.*** *Lauiritzen and Hoffman plots obtained through the Origin plug in developed by Lorenzo et al.*[85].

It is worth noting that similar plots are obtained when the data from PLOM experiments is used. However, it is important to remark that the $K_g^G$ values should be lower than the $K_g^\tau$ ones, since the latter includes nucleation and growth, whereas the first includes only the spherulite growth.

## 2.6. CONFINED POLYMERIC MATERIALS

The interest in confined crystallization has greatly increased with the development andprogress of nanotechnology applications. Polymeric confined crystallization has been studied in droplets, ultrathin films, nanolayers, nanostructures from solutions, blends, copolymers, polymers infiltrated within AAO templates and nanocomposites.

Massuda et al. developed an experimental technique to prepare hexagonal nanoporous arrays of AAO templates [108]. The double anodization process consists in a first anodization where an irregular AAO layer is formed, afterwards this layer is removed and a second anodization is performed. The remains of the first anodization

act as seed for the growing of the new structures in a hexagonalarray [109-110]. Anodic aluminum oxide (AAO) templates consist of a dense array of cylindrical nanopores, that lay mutually parallel and perpendicular to the underlying Al substrate (Figure 2.8.a). Pores in AAO templates are arranged in well-ordered domains of close-packed hexagonal symmetry over 10–20 interpore distances, while on a larger scale, domains are randomly oriented. The pores grow originally blind (with closed ends), because a non-porous, constant thickness aluminum oxide layer, the barrier layer, separates the empty space of pores and the underlying Al substrate. However, both the barrier layer and the aluminum substrate may be easily etched so that through-hole nanomembranes are achieved [108, 111-113]. Figure 2.8-b and c shows SEM micrographs of typical AAO templates produced for this work.

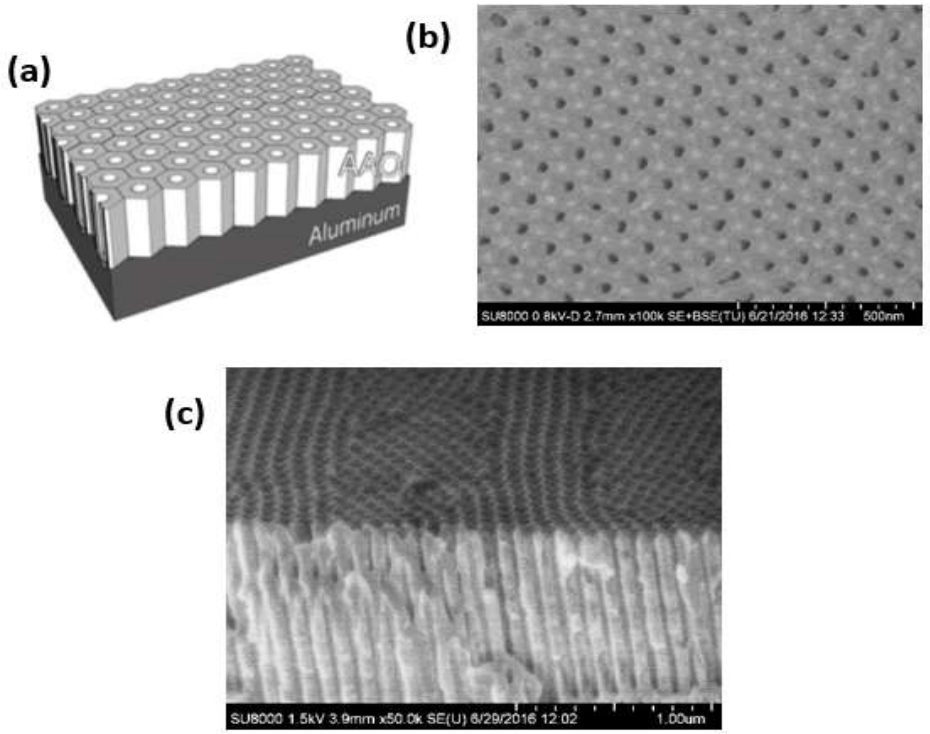


***Figure 2.8.*** *(a) Idealized structure of anodic porous alumina and a cross-sectional view of the anodized layer. SEM micrographs of AAO templates: (b) 35 nm top view, (c) 35 nm side view.*

### 2.6.1. Methods of preparation of polymer nanostructures using AAO templates

There are a few methods for the infiltration of polymeric samples within AAO templates. Depending on the process involved and conditions, polymer infiltration methods described above may be classified into two main groups: methods based on applied forces and methods based on wetting phenomena. As discussed in the preceding, the latter group of infiltration methods, by far the most common, is based on the wetting properties of liquids onto solid surfaces, and they have the peculiarity of being spontaneous. Depending on the process involved in the infiltration, three different methods can be considered: melt wetting, classified at the same type in complete wetting regime, known as precursor film method and partial wetting regime, known as capillary method, and solution wetting and other sophisticated methods. Figure 2.9 summarizes all the infiltration methods of polymers within AAO membranes. It is important to note that other methods of infiltration based on vacuum, rotation or a combination of different complex processes have also been reported to prepare polymer nanostructures [114-115].

In general, it is possible to obtain a continuous nanofibers, nantubes, and core-shell nanostructure among other unstable structures. Figure 2.10 shows some examples of obtained nanostructure using AAO templates.

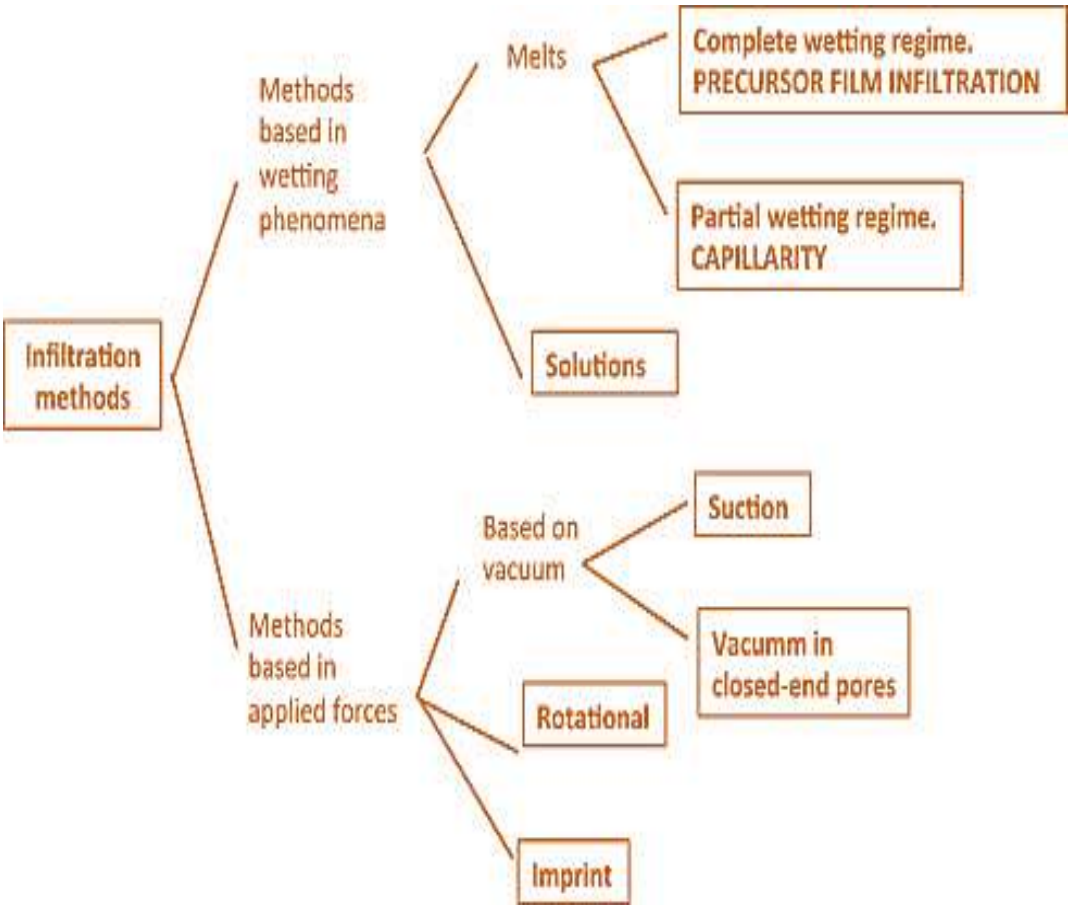


***Figure 2.9.*** *Summary of different infiltration methods of polymers within AAO templates [110].*

As a porous template, AAO present several features that set it apart from other templates when it comes to fabricate polymer nanostructures. Most important are:

*(1)AAO presents high flexibility regarding achievable pore diameters, pore lengths and interpore distances, that enables polymer nanomaterials with tailored dimensions;*

*(2) Nanopores are arranged in orderly fashion, that allows for the patterning of ordered polymer nanostructures;*

*(3) Pores in AAO are highly monodisperse in size and shape, that lead to the production of polymer nanostructures of high morphological quality;*

*(4) The template-based approach allow for the patterning of any polymer capable of being molten or in solution;*

*(5) AAO can be easily dissolved in acidic or alkaline without affecting the polymer nanostructures embedded into the pores, to obtain free polymer nanostructures.*

### 2.6.2. Crystallization within in AAO template

The crystallization of infiltrated polymers within AAO templates is an elegant way to study the effects of confinement on the nucleation and growth of isolated nanofibers. The crystallization can be studied by DSC since small sections of templates (with infiltrated polymer) can fit in the aluminum pans employed. Changing the size of them a nopores allows the study of the influence of spatial confinement without changing the molecular weight of the material. Additionally, it is possible to infiltrate almost any polymer. For these reasons, the crystallization of polymers within AAO templates has attracted much recent attention [13, 116].

In general, for almost all infiltrated polymeric materials, crystal orientation within the nanopores is a function of pore diameter. $T_c$ usually decreases and area function of pore size. When no pore interconnection remains, the crystallization occur at large supercoolings in heterogeneity free environments. Hence, the nucleation mechanism changes from heterogeneous to surface or homogeneous nucleation. The crystallization kinetics of infiltrated polymers should be close to first order, since in confined environments nucleation is the determining step of the overall crystallization and Avrami indexes (n) of~1 (or lower in some cases) should be obtained [116].

In the present work, for the first time, we study the crystallization behavior of random copolyesters under confinement position using AAO template.

(a)

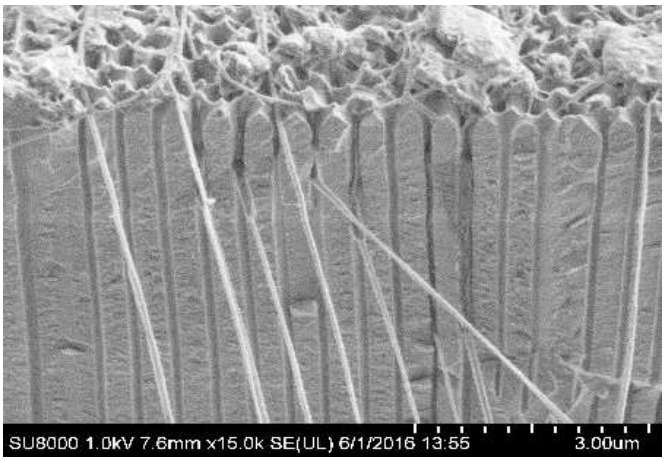


(b)

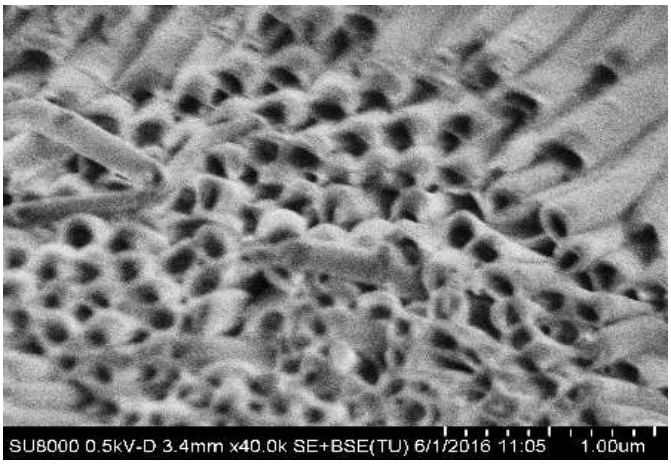


(c)

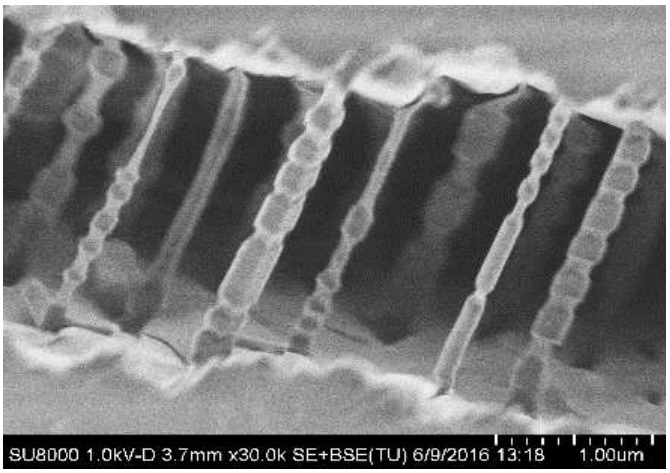


***Figure 2.9.*** *(a) PE nanofiber, (b) PMMA nanotube, and (c) PS-PMMA core-Shell nanostructure within AAO templets.*

## 2.7. REFERENCES

1. Andrady, A. L., *Plastics and the Environment*. John Wiley & Sons: 2003.

2. Mülhaupt, R., Green polymer chemistry and bio-based plastics: dreams and reality. *Macromolecular Chemistry and Physics* **2013,** *214* (2), 159-174.

3. Brodin, M.; Vallejos, M.; Opedal, M. T.; Area, M. C.; Chinga-Carrasco, G., Lignocellulosics as sustainable resources for production of bioplastics–A review. *Journal of Cleaner Production* **2017,** *162*, 646-664.

4. De Clercq, R.; Dusselier, M.; Sels, B., Heterogeneous catalysis for bio-based polyester monomers from cellulosic biomass: advances, challenges and prospects. *Green Chemistry* **2017,** *19* (21), 5012-5040.

5. Hong, M.; Chen, E. Y.-X., Chemically recyclable polymers: a circular economy approach to sustainability. *Green Chemistry* **2017,** *19* (16), 3692-3706.

6. Chen, G.-Q.; Patel, M. K., Plastics derived from biological sources: present and future: a technical and environmental review. *Chemical reviews* **2011,** *112* (4), 2082-2099.

7. Corma, A.; Iborra, S.; Velty, A., Chemical routes for the transformation of biomass into chemicals. *Chemical reviews* **2007,** *107* (6), 2411-2502.

8. Gandini, A.; Lacerda, T. M., From monomers to polymers from renewable resources: Recent advances. *Progress in Polymer Science* **2015,** *48*, 1-39.

9. Gandini, A.; Lacerda, T. M.; Carvalho, A. J.; Trovatti, E., Progress of polymers from renewable resources: furans, vegetable oils, and polysaccharides. *Chemical reviews* **2015,** *116* (3), 1637-1669.

10. Tschan, M. J.-L.; Brulé, E.; Haquette, P.; Thomas, C. M., Synthesis of biodegradable polymers from renewable resources. *Polymer Chemistry* **2012,** *3* (4), 836-851.

11. Storz, H.; Vorlop, K.-D., Bio-based plastics: status, challenges and trends. *Landbauforschung-Ger* **2013,** *63*, 321-332.

12. Shen, L.; Worrell, E.; Patel, M., Present and future development in plastics from biomass. *Biofuels, Bioproducts and Biorefining: Innovation for a sustainable economy* **2010,** *4* (1), 25-40.

13. Michell, R. M.; Blaszczyk-Lezak, I.; Mijangos, C.; Mueller, A. J., Confinement effects on polymer crystallization: From droplets to alumina nanopores. *Polymer* **2013,** *54* (16), 4059-4077.

14. Michell, R. M.; Mueller, A. J., Confined crystallization of polymeric materials. *Progress in Polymer Science* **2016,** *54*, 183-213.

15. Wu, H.; Higaki, Y.; Takahara, A., Molecular self-assembly of one-dimensional polymer nanostructures in nanopores of anodic alumina oxide templates. *Progress in Polymer Science* **2018,** *77*, 95-117.

16. Deopura, B.; Alagirusamy, R.; Joshi, M.; Gupta, B., *Polyesters and polyamides*. Elsevier: 2008.

17. Yamashita, H.; Nakano, Y., *Polyester: properties, preparation and applications*. Nova Science Publishers, Incorporated: 2008.

18. Rosato, D. V.; Rosato, D. V.; v Rosato, M., *Plastic product material and process selection handbook*. Elsevier: 2004.

19. Albertsson, A.-C.; Varma, I. K., Aliphatic polyesters: synthesis, properties and applications. In *Degradable Aliphatic Polyesters*, Springer: 2002; pp 1-40.

20. Rocca, M. C.; Carr, G.; Lambert, A. B.; Macquarrie, D. J.; Clark, J. H., Process for the oxidation of cyclohexanone to ε-caprolactone. Google Patents: 2003.

21. Natta, F. J. v.; Hill, J. W.; Carothers, W. H., Studies of polymerization and ring formation. XXIII. 1 ε-Caprolactone and its polymers. *Journal of the American Chemical Society* **1934,** *56* (2), 455-457.

22. Perrin, D. E.; English, J. P., Handbook of biodegradable polymers. *Domb, AJ* **1997**, 63.

23. Chandra, R., Biodegradable polymers. *Progress in polymer science* **1998,** *23*, 1273-1335.

24. Nair, L. S.; Laurencin, C. T., Biodegradable polymers as biomaterials. *Progress in polymer science* **2007,** *32* (8-9), 762-798.

25. Sisson, A. L.; Ekinci, D.; Lendlein, A., The contemporary role of ε-caprolactone chemistry to create advanced polymer architectures. *Polymer* **2013,** *54* (17), 4333-4350.

26. Chynoweth, K.; Stachurski, Z., Crystallization of poly (ε-caprolactone). *Polymer* **1986,** *27* (12), 1912-1916.

27. Gutiérrez, J. K. P. Multi-crystalline polymer systems: biodegradable triblock terpolymers and nanostructured blends. Morphology, crystallization and properties. Universidad del País Vasco-Euskal Herriko Unibertsitatea, 2017.

28. Gumede, T.; Luyt, A.; Muller, A., Review on PCL, PBS, and PCL/PBS blends containing carbon nanotubes. **2018**.

29. Yarici, T.; Kodal, M.; Ozkoc, G., Non-isothermal crystallization kinetics of Poly (Butylene succinate)(PBS) nanocomposites with different modified carbon nanotubes. *Polymer* **2018,** *146*, 361-377.

30. Di Lorenzo, M. L.; Androsch, R.; Righetti, M. C., Low-temperature crystallization of poly (butylene succinate). *European Polymer Journal* **2017,** *94*, 384-391.

31. Papageorgiou, D. G.; Zhuravlev, E.; Papageorgiou, G. Z.; Bikiaris, D.; Chrissafis, K.; Schick, C., Kinetics of nucleation and crystallization in poly (butylene succinate) nanocomposites. *Polymer* **2014,** *55* (26), 6725-6734.

32. Marcano, D. C.; Kosynkin, D. V.; Berlin, J. M.; Sinitskii, A.; Sun, Z.; Slesarev, A.; Alemany, L. B.; Lu, W.; Tour, J. M., Improved synthesis of graphene oxide. *ACS nano* **2010,** *4* (8), 4806-4814.

33. Odian, G., *Principles of polymerization*. John Wiley & Sons: 2004.

34. Pérez-Camargo, R. A.; Arandia, I.; Safari, M.; Cavallo, D.; Lotti, N.; Soccio, M.; Müller, A. J., Crystallization of isodimorphic aliphatic random copolyesters: Pseudo-eutectic behavior and double-crystalline materials. *Eur. Polym. J.* **2018,** *101*, 233-247.

35. Natta, G.; Corradini, P.; Sianesi, D.; Morero, D., Isomorphism phenomena in macromolecules. *Journal of Polymer Science* **1961,** *51* (156), 527-539.

36. Allegra, G.; Bassi, I., Isomorphism in synthetic macromolecular systems. In *Fortschritte der Hochpolymeren-Forschung*, Springer: 1969; pp 549-574.

37. Yu, Y.; Sang, L.; Wei, Z.; Leng, X.; Li, Y., Unique isodimorphism and isomorphism behaviors of even-odd poly (hexamethylene dicarboxylate) aliphatic copolyesters. *Polymer* **2017,** *115*, 106-117.

38. Latere Dwan'Isa, J.-P.; Lecomte, P.; Dubois, P.; Jérôme, R., Synthesis and characterization of random copolyesters of ε-caprolactone and 2-oxepane-1, 5-dione. *Macromolecules* **2003,** *36* (8), 2609-2615.

39. Ceccorulli, G.; Scandola, M.; Kumar, A.; Kalra, B.; Gross, R. A., Cocrystallization of random copolymers of ω-pentadecalactone and ε-caprolactone synthesized by lipase catalysis. *Biomacromolecules* **2005,** *6* (2), 902-907.

40. Ye, H.-M.; Wang, R.-D.; Liu, J.; Xu, J.; Guo, B.-H., Isomorphism in poly (butylene succinate-co-butylene fumarate) and its application as polymeric nucleating agent for poly (butylene succinate). *macromolecules* **2012,** *45* (14), 5667-5675.

41. Zhang, J.; Zhu, W.; Li, C.; Zhang, D.; Xiao, Y.; Guan, G.; Zheng, L., Effect of the biobased linear long-chain monomer on crystallization and biodegradation behaviors of poly (butylene carbonate)-based copolycarbonates. *RSC Advances* **2015,** *5* (3), 2213-2222.

42. Mandelkern, L., *Crystallization of Polymers: Volume 2, Kinetics and Mechanisms*. Cambridge University Press: 2004.

43. Young, R. J.; Lovell, P. A., *Introduction to polymers*. CRC press: 2011.

44. Arandia, I.; Mugica, A.; Zubitur, M.; Arbe, A.; Liu, G.; Wang, D.; Mincheva, R.; Dubois, P.; Müller, A. J., How Composition Determines the Properties of Isodimorphic Poly(butylene succinate-ran-butylene azelate) Random Biobased Copolymers: From Single to Double Crystalline Random Copolymers. *Macromolecules* **2015,** *48* (1), 43-57.

45. Ciulik, C.; Safari, M.; Martínez de Ilarduya, A.; Morales-Huerta, J. C.; Iturrospe, A.; Arbe, A.; Müller, A. J.; Muñoz-Guerra, S., Poly(butylene succinate-ran-ε-caprolactone) copolyesters: Enzymatic synthesis and crystalline isodimorphic character. *Eur. Polym. J.* **2017**.

46. Safari, M.; Martínez de Ilarduya, A.; Mugica, A.; Zubitur, M.; Muñoz-Guerra, S. n.; Müller, A. J., Tuning the Thermal Properties and Morphology of Isodimorphic Poly [(butylene succinate)-ran-(ε-caprolactone)] Copolyesters by Changing Composition, Molecular Weight, and Thermal History. *Macromolecules* **2018,** *51* (23), 9589-9601.

47. Pérez-Camargo, R. A.; Fernández-d'Arlas, B.; Cavallo, D.; Debuissy, T.; Pollet, E.; Avérous, L.; Müller, A. J., Tailoring the Structure, Morphology, and Crystallization

of Isodimorphic Poly(butylene succinate-ran-butylene adipate) Random Copolymers by Changing Composition and Thermal History. *Macromolecules* **2017,** *50* (2), 597-608.

48. Yu, Y.; Wei, Z.; Zheng, L.; Jin, C.; Leng, X.; Li, Y., Competition and miscibility of isodimorphism and their effects on band spherulites and mechanical properties of poly(butylene succinate-co-cis-butene succinate) unsaturated aliphatic copolyesters. *Polymer* **2018,** *150*, 52-63.

49. Vouyiouka, S.; Karakatsani, E.; Papaspyrides, C., Solid state polymerization. *Progress in Polymer science* **2005,** *30* (1), 10-37.

50. Rogers, M. E.; Long, T. E., *Synthetic methods in step-growth polymers*. John Wiley & Sons: 2003.

51. Pang, K.; Kotek, R.; Tonelli, A., Review of conventional and novel polymerization processes for polyesters. *Progress in polymer science* **2006,** *31* (11), 1009-1037.

52. Brunelle, D. J.; Bradt, J. E.; Serth-Guzzo, J.; Takekoshi, T.; Evans, T. L.; Pearce, E. J.; Wilson, P. R., Semicrystalline polymers via ring-opening polymerization: preparation and polymerization of alkylene phthalate cyclic oligomers. *Macromolecules* **1998,** *31* (15), 4782-4790.

53. Jiang, Y.; Woortman, A. J.; van Ekenstein, G. O. A.; Loos, K., A biocatalytic approach towards sustainable furanic–aliphatic polyesters. *Polymer Chemistry* **2015,** *6* (29), 5198-5211.

54. Kobayashi, S., Green polymer chemistry: new methods of polymer synthesis using renewable starting materials. *Structural Chemistry* **2017,** *28* (2), 461-474.

55. Champagne, E.; Strandman, S.; Zhu, X. X., Recent developments and optimization of lipase-catalyzed lactone formation and ring-opening polymerization. *Macromolecular rapid communications* **2016,** *37* (24), 1986-2004.

56. Morales Huerta, J. C., Polyesters containing cyclic carbohydrate-based units obtained by ring opening polymerization. **2018**.

57. Gedde, U. W., *Polymer physics*. Chapman & Hall: London; New York, 1995.

58. Mandelkern, L., *Crystallization of Polymers*. 2 ed.; Cambridge University Press: Cambridge, 2004; Vol. 2.

59. Schultz, J. M., *Polymer Crystallization: The Development of Crystalline Order in Thermoplastic Polymers.* Oxford: Oxford University Press, 2001.

60. Reiter, G.; Strobl, G. R., *Progress in understanding of polymer crystallization*. Springer: Berlin, 2007.

61. Hiemenz, P. C.; Lodge, T. P., *Polymer Chemistry, Second Edition*. Taylor & Francis: 2007.

62. Lorenzo, A. T.; Müller, A. J., Estimation of the nucleation and crystal growth contributions to the overall crystallization energy barrier. *Journal of Polymer Science Part B: Polymer Physics* **2008,** *46* (14), 1478-1487.

63. Gerngross, O.; Herrmann, L.; Abitz, W., *Z Physik Chem* **1930,** *10B*, 371.

64. Dargazany, R.; Khiêm, V. N.; Poshtan, E. A.; Itskov, M., Constitutive modeling of strain-induced crystallization in filled rubbers. *Physical Review E* **2014,** *89* (2), 022604.

65. Keller, A., A note on single crystals in polymers: Evidence for a folded chain configuration. *Philosophical Magazine* **1957,** *2* (21), 1171-1175.

66. Fischer, E. W., Step and spiral crystal growth of high polymers. *Z. Naturforch* **1957,** *12a*, 753-754.

67. Till, P. H., The growth of single crystals of linear polyethylene. *Journal of Polymer Science* **1957,** *24* (106), 301-306.

68. Kumaki, J.; Kawauchi, T.; Yashima, E., Two-dimensional folded chain crystals of a synthetic polymer in a Langmuir− Blodgett film. *Journal of the American Chemical Society* **2005,** *127* (16), 5788-5789.

69. Mullin, N.; Hobbs, J. K., Direct imaging of polyethylene films at single-chain resolution with torsional tapping atomic force microscopy. *Physical review letters* **2011,** *107* (19), 197801.

70. Chatani, Y.; Okita, Y.; Tadokoro, H.; Yamashita, Y., Structural studies of polyesters. III. Crystal structure of poly-ε-caprolactone. *Polymer Journal* **1970,** *1* (5), 555.

71. Hu, H.; Dorset, D. L., Crystal structure of poly (iε-caprolactone). *Macromolecules* **1990,** *23* (21), 4604-4607.

72. Bassett, D. C., *Principles of polymer morphology*. CUP Archive: 1981.

73. Flory, P. J., *Principles of polymer chemistry*. Ithaca : Cornell University Press, 1953.: 1953.

74. Hoffman, J. D.; Davis, G. T.; Lauritzen, J. I., The Rate of Crystallization of Linear Polymers with Chain Folding. In *Treatise on Solid State Chemistry: Volume 3 Crystalline and Noncrystalline Solids*, Hannay, N. B., Ed. Springer US: Boston, MA, 1976; pp 497-614.

75. Lauritzen Jr, J. I.; Hoffman, J. D., Formation of Polymer Crystals with Folder Chains from Dilute Solution. *The Journal of Chemical Physics* **1959,** *31*, 1959.

76. Hoffman, J. D.; Miller, R. L., Kinetic of crystallization from the melt and chain folding in polyethylene fractions revisited: theory and experiment. *Polymer* **1997,** *38* (13), 3151-3212.

77. Sharples, A., *Introduction to polymer crystallization*. Edward Arnold: 1966.

78. Van Krevelen, D. W.; Te Nijenhuis, K., *Calorimetric Properties*. 2009; p 109-128.

79. Turnbull, D.; Fischer, J. C., Rate of Nucleation in Condensed Systems. *Journal of Chemical Physics* **1949,** *17* (1), 71-73.

80. Müller, A. J.; Michel, R. M.; Lorenzo, A. T., Isothermal Crystallization Kinetics of Polymers," in Polymer Morphology: Principles, Characterization, and Processing, Q. Guo, Ed. Hoboken, NJ: John Wiley & Sons, Inc,. 2016; pp 181-203.

81. Frank, F. C., I. Liquid crystals. On the theory of liquid crystals. *Discussions of the Faraday Society* **1958,** *25* (0), 19-28.

82. Peterlin, A.; Fischer, E. W.; Reinhold, C., Thermodynamic theory of finite thickness of polyethylene crystals. *Journal of Polymer Science* **1962,** *62* (174), S59-S62.

83. D. M. Sadler and G. H. Gilmer, "Selection of lamellar thickness in polymer crystal growth: A rate-theory model," Physical Review B, vol. 38, no. 8, pp. 5684-5693, 09/15/ 1988.

84. E. Ergoz, J. G. Fatou, and L. Mandelkern, "Molecular Weight Dependence of the Crystallization Kinetics of Linear Polyethylene. I. Experimental Results," Macromolecules, doi: 10.1021/ma60026a011 vol. 5, no. 2, pp. 147-157, 1972/03/01 1972.

85. Lorenzo, A. T.; Arnal, M. L.; Albuerne, J.; Müller, A. J., DSC isothermal polymer crystallization kinetics measurements and the use of the Avrami equation to fit the data: Guidelines to avoid common problems. *Polymer Testing* **2007,** *26* (2), 222-231.

86. Muthukumar, M., Shifting Paradigms in Polymer Crystallization. In *Progress in Understanding of Polymer Crystallization*, Reiter, G.; Strobl, G. R., Eds. Springer Berlin Heidelberg: Berlin, Heidelberg, 2007; pp 1-18.

87. Ziabicki, A., *Fundamentals of Fibre Formation: The Sciencs of Fibre Spinning and Drawing*. Wiley, London: 1976.

88. Avrami, M., Kinetics of Phase Change. I, General Theory. *Journal of Chemical Physics* **1939,** *7*, 1103-1112.

89. Avrami, M., Kinetics of Phase Change. II, Transformation-Time Relations of Random Distribution Nuclei. *Journal of Chemical Physics* **1940,** *8*, 212-224.

90. Avrami, M., Granulation, Phase Change, and Microstructure Kinetics of Phase Change. III. *The Journal of Chemical Physics* **1941,** *9*, 177.

91. Wunderlich, B., In *Macromolecular Physics*, Academic Press, New York: 1973; pp xiii-xiv.

92. Hiemenz, P. C., Lodge, T.P., In *Polymer Chemistry*, CRC Press: 2007.

93. Müller, A. J.; Balsamo, V.; Arnal, M. L., Nucleation and Crystallization in Diblock and Triblock Copolymers. In *Block Copolymers II*, Abetz, V., Ed. Springer Berlin Heidelberg: Berlin, Heidelberg, 2005; pp 1-63.

94. Lorenzo, A.; Muller, A.; Lin, M.-C.; Chen, H.-L.; Jeng, U.-S.; Priftis, D.; Pitsikalis, M.; Hadjichristidis, N., Influence of macromolecular architecture on the crystallization of (PCL2)-b-(PS2) 4-miktoarm star block copolymers in comparison to linear PCL-b-PS diblock copolymer analogues. *Macromolecules* **2009,** *42* (21), 8353-8364.

95. Mark, J. E., *Physical Properties of Polymers Handbook*. Springer New York: 2007.

96. Strobl, G., A Multiphase Model Describing Polymer Crystallization and Melting. In *Progress in Understanding of Polymer Crystallization*, Reiter, G.; Strobl, G., Eds. Springer Berlin Heidelberg: 2007; Vol. 714, pp 481-502.

97. Muthukumar, M.; Welch, P., Modeling polymer crystallization from solutions. *Polymer* **2000,** *41* (25), 8833-8837.

98. Muthukumar, M., Commentary on theories of polymer crystallization. *European Physical Journal E* **2000,** *3* (2), 199-202.

99. Lorenzo, A. T.; Müller, A. J., Estimation of the nucleation and crystal growth contributions to the overall crystallization energy barrier. *Journal of Polymer Science, Part B: Polymer Physics* **2008,** *46* (14), 1478-1487.

100. Schultz, J. M., *Polymer Crystallization: The Development of Crystalline Order in Thermoplastic Polymers*. American Chemical Society: 2001.

101. Müller, A. J.; Albuerne, J.; Marquez, L.; Raquez, J. M.; Degée, P.; Dubois, P.; Hobbs, J.; Hamley, I. W., Self-nucleation and crystallization kinetics of double crystalline poly(p-dioxanone)-b-poly(ε-caprolactone) diblock copolymers. *Faraday Discuss.* **2005,** *128*, 231-252.

102. Sabino, M. A.; Albuerne, J.; Müller, A.; Brisson, J.; Prud'homme, R. E., Influence of in vitro hydrolytic degradation on the morphology and crystallization behavior of poly(p-dioxanone). *Biomacromolecules* **2004,** *5* (2), 358-370.

103. Andjelić, S.; Jamiolkowski, D.; McDivitt, J.; Fischer, J.; Zhou, J.; Vetrecin, R., Crystallization study on absorbable poly(p-dioxanone) polymers by differential scanning calorimetry. *J. Appl. Polym. Sci.* **2001,** *79* (4), 742-759.

104. Scott Lambert, W.; Phillips, P. J., Crystallization kinetics of low molecular weight fractions of branched polyethylenes. *Macromolecules* **1994,** *27* (13), 3537-3542.

105. Lorenzo, A. T.; Arnal, M. L.; Müller, A. J.; Boschetti-De-Fierro, A.; Abetz, V., Nucleation and isothermal crystallization of the polyethylene block within diblock copolymers containing polystyrene and poly(ethylene-alt-propylene). *Macromolecules* **2007,** *40* (14), 5023-5037.

106. Lauritzen, J. I.; Hoffman, J. D., Theory of Formation of Polymer Crystals with Folded Chains in Dilute Solution. *Journal of Research of the National Bureau of Standards-A. Physics and Chemistry* **1960,** *64* (1), 73-102.

107. Hoffman, J. D.; Lauritzen, J. I., Crystallization of Bulk Polymers With Chain Folding: Theory of Growth of Lamellar Spherulites. *Journal of Research of the National Bureau of Standards-A. Physics and Chemistry* **1961,** *65* (4), 297-336.

108. Masuda, H.; Fukuda, K., Ordered metal nanohole arrays made by a two-step replication of honeycomb structures of anodic alumina. *science* **1995,** *268* (5216), 1466-1468.

109. Steinhart, M., Supramolecular organization of polymeric materials in nanoporous hard templates. In *Self-Assembled Nanomaterials II*, Springer: 2008; pp 123-187.

110. Martin, J.; Maiz, J.; Sacristan, J.; Mijangos, C., Tailored polymer-based nanorods and nanotubes by" template synthesis": From preparation to applications. *Polymer* **2012,** *53* (6), 1149-1166.

111. Martín, J.; Manzano, C. V.; Caballero-Calero, O.; Martín-González, M., High-aspect-ratio and highly ordered 15-nm porous alumina templates. *ACS applied materials & interfaces* **2012,** *5* (1), 72-79.

112. Martín, J.; Manzano, C. V.; Martín-González, M., In-depth study of self-ordered porous alumina in the 140–400 nm pore diameter range. *Microporous and Mesoporous Materials* **2012,** *151*, 311-316.

113. Nielsch, K.; Choi, J.; Schwirn, K.; Wehrspohn, R. B.; Gösele, U., Self-ordering regimes of porous alumina: the 10 porosity rule. *Nano letters* **2002,** *2* (7), 677-680.

114. Mijangos, C.; Hernandez, R.; Martin, J., A review on the progress of polymer nanostructures with modulated morphologies and properties, using nanoporous AAO templates. *Progress in Polymer Science* **2016,** *54*, 148-182.

115. Martín, J.; Vázquez, M.; Hernández-Vélez, M.; Mijangos, C., Ordered arrays of magnetic polymer-based nanorods by template synthesis. *Journal of nanoscience and nanotechnology* **2009,** *9* (10), 5898-5902.

116. Michell, R. M.; Blaszczyk-Lezak, I.; Mijangos, C.; Müller, A. J., Confined crystallization of polymers within anodic aluminum oxide templates. *Journal of Polymer Science Part B: Polymer Physics* **2014,** *52* (18), 1179-1194.

# *Chapter III:*

# *Experimental Part*

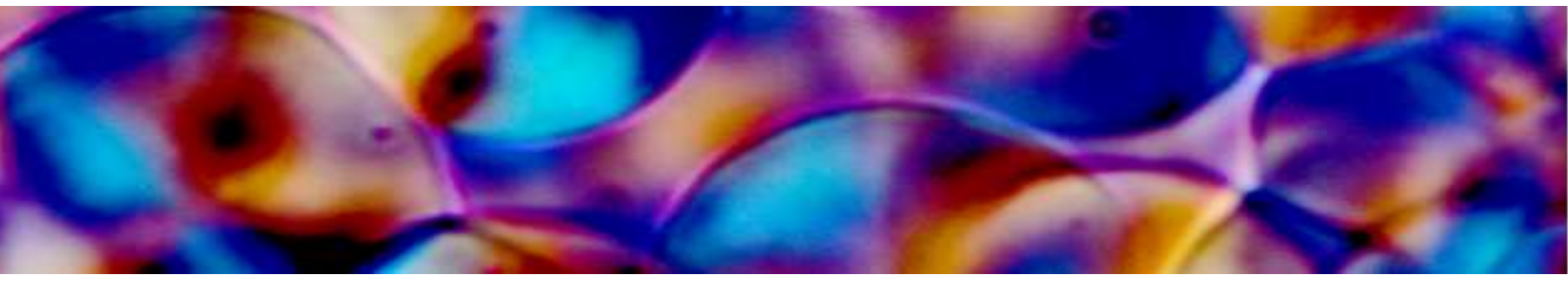

# Table of Contents

In this Chapter, the materials as well as methods used in each topic are explained in detail.

## 3.1. MATERIALS

Dimethyl succinate (DMS), 1,4-butanediol (BD), titanium tetraisopropoxide (TTP) catalyst, and ε-caprolactone (CL) were purchased from Aldrich Co. All materials were used as received. Poly (butylene succinate) with Mw = 15000 g/mol and a glass transition temperature of $T_g$ = -33 °C, was supplied by Aldrich. Poly (butylene adipate) with Mw=12000 g/mol and $T_g$ = -55 °C, was purchased from Aldrich.

## 3.2. SYNTHESIS OF POLYESTERS AND COPOLYESTERS

### 3.2.1. Synthesis of Polybutylene succinate (PBS)

Two main steps exist for the synthesis of PBS: 1. the trans-esterification process (from succinate diesters and 1,4-butanediol) and 2. The polycondensation process. In the first step, an excess of the diol is esterified with the diacid to form PBS oligomers with elimination of water. This step require an appropriate catalyst such as TTP. Then, these oligomers are trans-esterified under vacuum to form a high molar mass polymer. Scheme 3.1 shows the synthesis route and repeating unit of PBS.

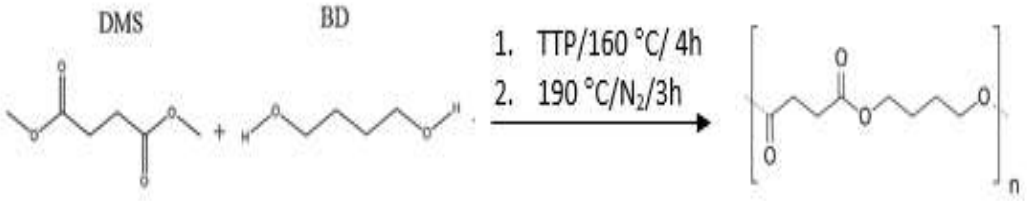


***Scheme 3.1.*** *Synthesis route of Polybutylene succinate (PBS).*

### 3.2.2. Synthesis of polycaprolactone (PCL)

PCL was synthesized by metal catalyzed ring-opening polymerization (ROP) of the cyclic monomer ε -caprolactone. Scheme 3.2 shows the synthesis rout of PCL.

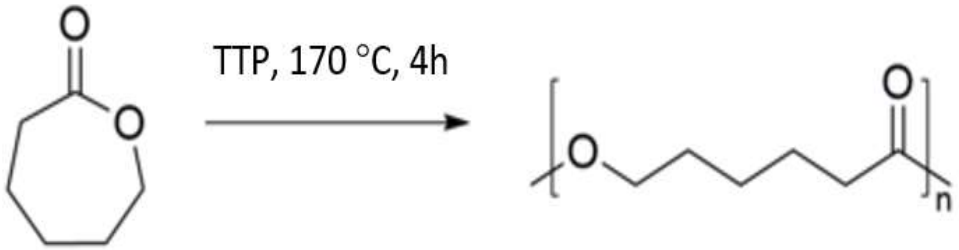


***Scheme 3.2.*** *Synthesis rout of polycaprolactone (PCL).*

### 3.2.3. Enzymatic Synthesis of PBS-*ran*-PCL ($LM_w$-$BS_xCL_y$) copolyesters

Poly(butylene succinate-*ran*-Caprolactone) (PBS-*ran*-PCL) copolymers were synthesized and characterized by Muñoz group in UPB in Barcelona. The cyclic butylene succinate oligomers were synthesized according to the procedure described by Sugihara et al.[1]. In brief, 0.65 mL (0.726 g, 4.97 mmol) of dimethyl succinate and 0.45 mL (0.457 g, 5.07 mmol) of 1,4-butanediol were placed in 250 mL of toluene in a three-necked flask. The mixture was left under magnetic stirring in a thermostatized oil bath until the temperature stabilized at 96.5°C and the medium became homogeneous. Then 1.184 g (100 w% relative to the total monomer concentration) of immobilized lipase CALB were added. The cyclization reaction was left to proceed for 48 h under a low steady stream of nitrogen with 4 Å molecular sieves placed at the top of the flask to absorb the released methanol. The reaction mixture was then dispersed in chloroform and the enzyme was removed by filtration through a fritted

filter. The clean filtrate was evaporated to dryness under reduced pressure to obtain the oligomer mixture of c(BS)n.

The enzymatic ring opening polymerization reaction leading to $LM_w$-$BS_xCL_y$ copolyesters was carried out in the bulk, using c(BS)n/CL mixtures at molar ratios of 90/10, 70/30, 60/40, 50/50, 40/60, 30/70 and 10/90, so that the whole copolyesters composition range was essentially covered. The experimental procedure was as follows: Predetermined relative amounts of the cyclic reactants were placed in a one-necked flask introduced in a thermostatized oil bath at 130 °C, and the mixture was mechanically stirred until complete melting and homogenization. Then immobilized lipase CALB (50% w/w relative to the total reactants mass) was added and the reaction was left to proceed for 24 h under a nitrogen atmosphere. The reaction mass was then dissolved in chloroform and the insolubilized enzyme was removed by filtration through a fritted filter. The filtrate was then evaporated to dryness under reduced pressure to obtain the corresponding copolyester. The same procedure was followed for the synthesis of the parent homopolyesters PBS and PCL using c(BS)n and CL as respective feeds.

The route followed in this work for the preparation of the poly (butylene succinate-*ran*-caprolactone) copolyesters is depicted in Scheme 3.3.

The cyclic oligomers *c*$(BS)_n$ needed for ROP were firstly synthesized by enzymatic cyclization of an approximate equimolar mixture of 1,4-butanediol (BD) and dimethyl succinate (DMS) in toluene, following the method described by Sugihara et al.[1]. The resulting cyclic oligomeric mixture was analyzed by MALDI-Tof MS and NMR (see Figure Apnx.4.1) which demonstrated that its composition is in agreement with previously reported results. Dimer, trimer and tetramers were the main components in the mixture whereas higher size cycles as well as the monomer were present in much smaller amounts.

As it can be seen in Table 3.1, average-weight molecular weights of the LMw-BSxCLy copolyesters were found to range between 4,000 and 14,000 with dispersities

oscillating between 1.9 and 2.6 and without showing apparent correlation with copolymer composition. The molecular weights of the homopolyesters were comparable to those found for the copolyesters with the PCL was obtained with a Mw nearly three times higher than that of PBS. It is known that the molecular weight of the polyesters generated by enzymatic ROP is strongly influenced by polymerization conditions, such as monomers and enzyme concentrations and reaction temperature. Also the presence of minor amounts of water is a critical factor in determining the resulting polyester size, which has to be rigorously avoided if high molecular weights are desired. The enzyme used for catalyzing the reaction is frequently the main source of water which may be easily removed by subjecting CALB to a severe drying just before using.

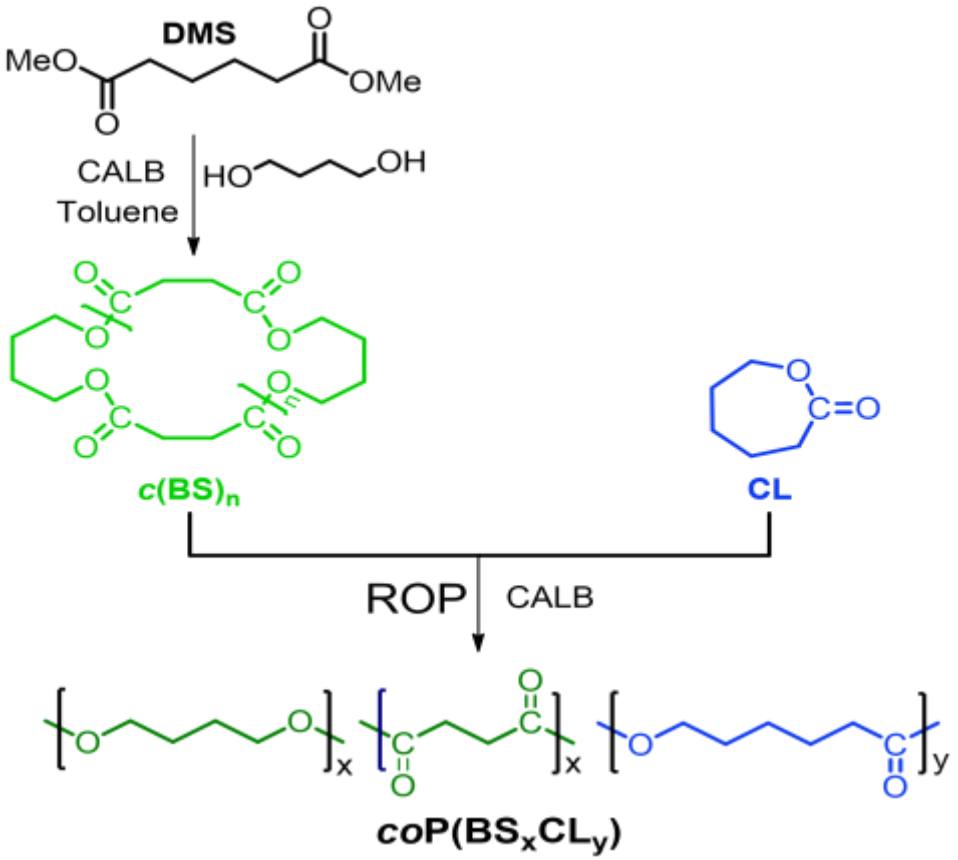


***Scheme 3.3.*** *Route leading to LMw-BSxCLy copolyesters by enzymatically ROP of mixtures of cyclic butylene succinate oligomers and caprolactone.*

***Table 3.1.*** *Synthesis results of the enzymatically assisted ROP copolymerization of cyclic oligo (butylene succinate) oligomers and caprolactone. These polymers are applied in chapter 4.*

| Polyester | Composition[a] (BS/CL mol/mol) | | Molecular weight[b] (mol·g$^{-1}$) | | | Microstructure[c] (S-centered triads content) | | | |
|---|---|---|---|---|---|---|---|---|---|
| | Feed | Polymer | $M_n$ | $M_w$ | $Đ$ | BSB | BSCL/CLSB | CLSCL | $R$ |
| **LMw-PBS** | 100/0 | 100/0 | 4700 | 6100 | 1.3 | - | - | - | - |
| **LMw-BS$_{85}$CL$_{15}$** | 90/10 | 84.6/15.4 | 2100 | 5000 | 2.3 | 84.0 | 16.0 | 0 | 0.96 |
| **LMw-BS$_{64}$CL$_{36}$** | 70/30 | 64.3/35.7 | 2200 | 4100 | 1.9 | 59.6 | 36.0 | 4.4 | 1.03 |
| **LMw-BS$_{54}$CL$_{46}$** | 60/40 | 53.6/46.4 | 2000 | 4300 | 2.2 | 46.5 | 45.1 | 8.4 | 1.02 |
| **LMw-BS$_{48}$CL$_{52}$** | 50/50 | 47.7/52.3 | 6600 | 13500 | 2.1 | 38.1 | 49.0 | 13.0 | 1.06 |
| **LMw-BS$_{45}$CL$_{55}$** | 50/50 | 44.7/55.3 | 3200 | 6100 | 1.9 | 35.9 | 46.2 | 17.9 | 1.07 |
| **LMw-BS$_{36}$CL$_{64}$** | 40/60 | 35.6/64.4 | 2600 | 5300 | 2.0 | 31.2 | 49.7 | 19.1 | 0.93 |
| **LMw-BS$_{26}$CL$_{74}$** | 30/70 | 25.8/74.2 | 2600 | 6300 | 2.4 | 10.4 | 62.1 | 27.6 | 0.99 |
| **LMw-BS$_{9}$CL$_{91}$** | 10/90 | 8.5/91.5 | 4500 | 11800 | 2.6 | 6.6 | 29.7 | 63.7 | 0.93 |
| **LMw-PCL** | 0/100 | 0/100 | 6500 | 16300 | 2.0 | - | - | - | - |

[a]*Composition of the feed and in the resulting polymer as determined by $^1$H NMR.*

[b]*Number and weight average molecular weights and dispersities estimated by GPC against PMMA standards.*

[c]*Copolyester microstructure determined by NMR; R is the randomness degree which should be 1 for a fully statistical distribution.*

### 3.2.2. Organometallic Synthesis of PBS-*ran*-PCL (HMw-$BS_xCL_y$) copolyesters

Concisely, for the $BS_{51}CL_{49}$ a three-necked 50 ml flask was charged with 1.46 g (10 mmol) of dimethyl succinate (DMS), 1.38 g (15 mmol) of 1,4-butanediol (BD), and 1.140g (10 mmol) of ε-caprolactone. DMS /CL mixtures at molar ratios of 90/10, 80/20,70/30, 60/40, 55/45, 50/50, 45/55, 40/60, 30/70, 20/80 and 10/90, were used so the whole range of compositions was essentially covered. The mixture was left under mechanical stirring in a thermostatized silicon oil bath until the temperature stabilized at 160 °C and the medium became homogeneous. Then 0.16 µl (0.0005 mmol) of TTP with the TTP/*ε*-CL molar ratio equal to 0.005 % were added under gentle agitation at 50 rpm. The transesterification/ROP reaction was conducted for 4h and finally the polycondensation was performed under gradually reduced pressure to a final value of 0.1 mm Hg at 190 °C for around 3 h. The high molecular weight values are possibly due to the high vacuum applied during the polycondensation step. The same process was carried out for the synthesis of the corresponding homopolyesters PBS and PCL using DMS and *ε*-CL as respective feeds. Scheme 3.4 shows the route leading to HMw-$BS_xCL_y$ copolyesters using TTP catalyst. Samples are denoted in an abbreviated form, e.g., HMw-$BS_xCL_y$, indicating the molar ratio of each component (determined by $^1$H NMR) as subscripts (x and y) and are specified in Table 3.2. The information about molecular weight determined by GPC and thermal transitions determined by DSC of copolyesters is summarized in Table 3.2.

### 3.2.3. Synthesis of PBS-*ran*-PCL (VHM$_w$-$BS_xCL_y$) copolyesters

To obtain a higher molecular of PBS-*ran*-PCL, the same meyhod written in section 3.2.2 were used, polycondensation was performed under gradually reduced pressure to a final value of 0.1 mm Hg at 230 °C for around 10 h.

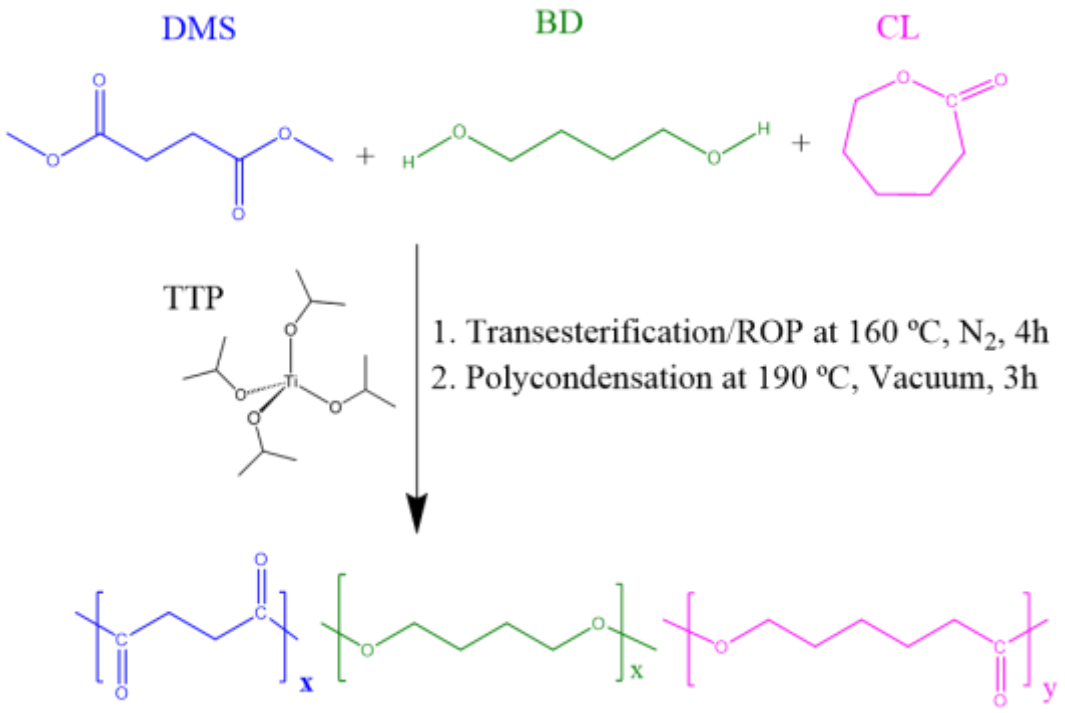


***Scheme 3.4.*** *Synthetic route for the preparation of HMw-BS$_x$CL$_y$.*

***Table 3.2.*** *Synthesis results of the copolymerization of butylene succinate and ε-caprolactone for sampled applied in chapter 5, 6, 7, and 10.*

| Polyester | Composition[a] (BS/CL mol/mol) | | Molecular weight[b] (g/mol) | | | Microstructure[c] (S-centered triads content) | | | |
|---|---|---|---|---|---|---|---|---|---|
| | Feed | Found | $M_n$ | $M_w$ | Đ | CLSC | BSCL/CLSB | BSB | *R* |
| **HMw-PBS** | 100/0 | 100/0 | 7500 | 21470 | 2.9 | - | - | - | - |
| **HMw-BS$_{91}$CL$_{09}$** | 90/10 | 91/09 | 8790 | 21640 | 2.5 | 1 | 21 | 78 | 1.08 |
| **HMw-BS$_{78}$CL$_{22}$** | 80/20 | 78/22 | 6580 | 18000 | 2.7 | 4 | 23 | 73 | 1.03 |
| **HMw-BS$_{66}$CL$_{34}$** | 70/30 | 66/34 | 7830 | 19700 | 2.5 | 9 | 37 | 54 | 1.05 |
| **HMw-BS$_{62}$CL$_{38}$** | 60/40 | 62/38 | 9750 | 27300 | 2.8 | 9 | 38 | 53 | 1.05 |
| **HMw-BS$_{55}$CL$_{45}$** | 55/45 | 55/45 | 8970 | 24700 | 2.7 | 10 | 39 | 51 | 0.98 |
| **HMw-BS$_{51}$CL$_{49}$** | 50/50 | 51/49 | 7400 | 23500 | 3.1 | 17 | 45 | 41 | 1.00 |
| **HMw-BS$_{45}$CL$_{55}$** | 45/55 | 45/55 | 8000 | 17300 | 2.2 | 20 | 43 | 37 | 1.03 |
| **HMw-BS$_{38}$CL$_{62}$** | 40/60 | 38/62 | 11000 | 24300 | 2.2 | 25 | 47 | 28 | 1.05 |
| **HMw-BS$_{34}$CL$_{66}$** | 30/70 | 34/66 | 10000 | 29900 | 2.2 | 27 | 50 | 23 | 1.08 |
| **HMw-BS$_{27}$CL$_{73}$** | 20/80 | 27/73 | 11540 | 28700 | 2.5 | 31 | 48 | 21 | 1.05 |
| **HMw-BS$_{11}$CL$_{89}$** | 10/90 | 11/89 | 6300 | 19500 | 3.1 | 55 | 40 | 5 | 0.98 |
| **HMw-PCL** | 0/100 | 0/100 | 5400 | 17400 | 3.2 | - | - | - | - |

[a] *Composition of the feed and the resulting polymer as determined by $^1$H NMR.*

[b] *Number and weight average molecular weights and dispersities estimated by GPC against PMMA standards.*

[c] *Copolyester microstructure determined by NMR; R is the degree of randomness which should be 1 for a fully statistical distribution of the comonomeric units.*

***Table 3.3.*** *Synthesis results of the copolymerization of butylene succinate and ε-caprolactone chapte 10.*

| Polyester | Composition[a] (BS/CL mol/mol) | | Molecular weight[b] (g/mol ) | | | Microstructure[c] (S-centered triads content) | | | |
|---|---|---|---|---|---|---|---|---|---|
| | Feed | Found | $M_n$ | $M_w$ | Đ | BSB | BSCL/CLSB | CLSCL | R |
| **VHMw-PBS** | 100/0 | 100/0 | 32700 | 70300 | 2.2 | - | - | - | - |
| **VHMw-$BS_{78}CL_{22}$** | 80/20 | 78/22 | 19750 | 51400 | 2.6 | 62 | 26 | 12 | 1.03 |
| **VHMw-$BS_{68}CL_{34}$** | 70/30 | 68/34 | 34000 | 91300 | 2.7 | 55 | 28 | 17 | 1.00 |
| **VHMw-$BS_{60}CL_{40}$** | 60/40 | 60/40 | 18400 | 35500 | 1.9 | 44 | 34 | 22 | 1.10 |
| **VHMw-$BS_{55}CL_{45}$** | 55/45 | 55/45 | 17300 | 39850 | 2.3 | 48 | 18 | 34 | 0.98 |
| **VHMw-$BS_{51}CL_{49}$** | 50/50 | 51/49 | 23200 | 87850 | 3.8 | 44 | 14 | 42 | 1.00 |
| **VHMw-$BS_{46}CL_{4}$** | 45/55 | 46/54 | 26000 | 60700 | 2.3 | 40 | 13 | 47 | 1.02 |
| **VHMw-$BS_{38}CL_{62}$** | 40/60 | 38/62 | 17800 | 39500 | 2.2 | 29 | 16 | 55 | 1.01 |
| **VHMw-$BS_{15}CL_{85}$** | 15/90 | 15/85 | 26350 | 53100 | 2.0 | 8 | 14 | 78 | 1.00 |
| **VHMw-PCL** | 0/100 | 0/100 | 31000 | 60000 | 1.9 | - | - | - | - |

[a] *Composition of the feed and the resulting polymer as determined by $^1H$ NMR.*

[b] *Number and weight average molecular weights and dispersities estimated by GPC against PMMA standards.*

[c] *Copolyester microstructure determined by NMR; R is the degree of randomness which should be 1 for a fully statistical distribution of the comonomeric units.*

## 3.3. EXPERIMENTAL TECHNIQUES

### 3.3.1. Nuclear Magnetic Resonance (NMR)

NMR spectroscopy is one of the most simple and reliable techniques for structural elucidation of polymers. The $^{1}H$ NMR and $^{13}C$ NMR spectra were operated at 300.1 and 75.5 MHz, respectively, on a Bruker AMX-300 NMR instrument. The samples were dissolved in deuterated chloroform, and TMS was used as internal reference. Quantitative $^{13}C$ NMR spectra were recorded applying an inverse gated decoupling pulse sequence to avoid nuclear Overhauser effect (NOE) enhancement of the $^{13}C$ NMR signals and using long delay times. The composition of ε-caprolactone repeating unit present in $BS_xCL_y$ was estimated from methylene proton resonance integrals of $CH_2$ (1) and $CH_2$ (4). Moreover, the sequence distributions of BS and CL repeating units were calculated based on $^{13}C$ NMR signals of the methylene group $CH_2$ (b) in Figure 4.2, 5.1, and 7.1.

### 3.3.2. Gel Permeation Chromatography (GPC)

GPC is an analytical technique that separates molecules in polymers by size and provides the molecular weight distribution of a material. Molecular weight properties were measured by Gel Permeation Chromatograms (GPC) that were acquired at 35 °C with a Waters equipment, a refraction index detector and poly (methyl methacrylate) (PMMA) standards. The samples were chromatographed with 0.05 M sodium trifluoroacetate-hexafluoroisopropanol (NaTFA-HFIP) using a poly(styrene-*co*-divinyl benzene) packed linear column at a flow rate of 0.5 ml/min.

### 3.3.3. Matrix-assisted laser desorption ionization time-of-flight mass spectrometry (MALDI-TOF MS)

Mass spectrometry is an analytical technique in which samples are ionized into charged molecules and ratio of their mass-to-charge (m/z) can be measured. In MALDI-TOF mass spectrometry, the ion source is matrix-assisted laser

desorption/ionization (MALDI), and the mass analyzer is time-of-flight (TOF) analyzer. MALDI-TOF MS was performed using an ABSciex 4800 plus MALDI-TOF/TOF spectrometer equipped with a Nd:YAG laser. Detection was made in the reflection mode and positive ionization was used. About 0.1 mg of sample was dissolved in 50 µL of DCM and 2 µL of this solution were mixed with an equal volume of DCM solution of anthracene (10 mg mL−1), and the mixture left to evaporate to dryness onto the stainless steel plate of the analyser. The residue was then covered with 2 µL of a solution of 2,5-dihydroxibenzoic acid in acetonitrile/$H_2O$ (1/1) containing 0.1 % TFA, and the mixture was left to dry prior to exposition to the laser beam.

### 3.3.4. Differential Scanning Calorimetry (DSC)

Differential scanning calorimetry, or DSC, is a thermoanalytical technique in which the difference in heat capacity ($C_p$) of a sample and a reference is recorded as a function of temperature. This technique is used to observe fusion and crystallization events as well as glass transition temperatures $T_g$. DSC can also be used to study oxidation, as well as other chemical reactions.

DSC is composed by two cells where in one the sample in a suitable pan and in the other the reference pan are placed. Two heating circuits control the temperature average and the difference between the two ovens. The first circuit changes the temperature of the two ovens, both the sample and the reference, at a constant speed as indicated in the program. The second circuit compensates the temperature difference between the two ovens when any exothermic or endothermic process occurs in the sample, maintaining the temperature of the sample and the reference constant. This instrument uses a feedback loop to maintain the sample at a set temperature while measuring the power needed to do this against a reference furnace.

In polymers this technique allows to determine the changes that polymers suffer when the temperature varies, such as the melting temperature ($T_m$), the glass transition temperature ($T_g$), the crystallization temperature ($T_c$) or cold crystallization

temperature ($T_{cc}$), transitions between crystalline phases, the percentage of crystallinity of a material as well as the enthalpies corresponding to the aforementioned thermal transitions. In addition, from the corresponding enthalpies the degree of crystallinity of the samples is calculated following equation;

$$W_c = \frac{\Delta H_m}{\Delta H_{(100\%)}} \qquad \text{Eq.3.1}$$

where $\Delta H_m$ is the value of melting enthalpy and $\Delta H_{(100\%)}$ is the heat of fusion of a 100 % crystalline polymer.

DSC measurements were performed using a PerkinElmer 8500 Pyris 1 calorimeter equipped with a refrigerated cooling system Intracooler 2P, under nitrogen atmosphere flow and calibrated with indium ($T_m$ = 156.61 °C y $\Delta H_m$ = 28.71 J/g). The samples were weighted (~ 5mg) and sealed in aluminum pans.

The experimental conditions used according to the different studies are described in the following sections.

**3.3.4.1. Nonisothermal studies**

For bulk copolyesters, the nonisothermal measurements were performed following next steps:

1) Erasing the previous thermal history by heating the samples to 30 °C above their peak melting temperature for 3 min.
2) Cooling down the molten sample to -60 °C at a controlled temperature (1, 5, 10 or 20 °C/min).
3) Hold the sample at -60 °C for 1 minute.
4 )Heating up from -60 °C to 30 °C above their peak melting temperature at a controlled temperature (1, 5, 10 or 20 °C/min).

From these measurements, the crystallization temperature ($T_c$) or the cold crystallization temperature ($T_{cc}$), the melting temperature ($T_m$) and the corresponding enthalpies of each one have been obtained.

The non-isothermal crystallization behavior of the infiltrated polymers was examined by differential scanning calorimetry (DSC) using a DSC-Q2000, TA calorimeter under a nitrogen atmosphere flow. Indium was used as a standard for calibration. Samples were heated from room temperature to 30 °C above their melting point and held at this temperature for 3 min to erase thermal history. Then, they were cooled to -100 °C at 10 °C/min and subsequently heated above their melting point. Around 15 mg of confined samples inside AAO were sealed in standard aluminum pans and samples were measured with aluminum base.

Previous to DSC measurements, after melt infiltration, and in order to remove the excess polymer on the AAO surfaces, templates were cleaned in four steps, as follows: 1. Removing the excess bulk polymer from the surface using a sharp blade at room temperature, 2. Samples were further cleaned with a soft cloth at a temperature above the melting temperature of the polymer, 3. The samples were polished using fine grade sandpaper, 4. Finally, the surface of the templates was cleaned with chloroform.

#### 3.3.4.1. To determine the glass transition temperature ($T_g$)

Samples were heated from room temperature to 140 °C (for BS-rich samples) or 90 °C (for CL-rich samples) at a rate of 10 °C/min. They were then cooled using the ballistic cooling option of DSC 8500, which cools the sample at an average nominal rate of approximately 160 °C/min) to -90 °C. Finally, the sample was heated to 150 °C (for BS-rich samples) or 90 °C (for CL-rich samples) at a rate of 20 °C/min. The glass transition temperatures $T_g$, were calculated from the DCS scans as the midpoint of the heat capacity change.

#### 3.3.4.2. Isothermal studies

Isothermal measurements were performed using the procedure recommended by Lorenzo et al: [2]

1) Erasure of previous thermal history by heating the samples to 30 °C above their peak melting temperature for 3 min.
2) Quenching the samples to a chosen isothermal crystallization temperature $T_c$ at 60 °C/min.
3) Isothermal crystallization until saturation.
4) Heating from $T_c$ to 30 °C above their peak melting temperature at 20 °C/min.

In this case, all the samples were able to crystallize during cooling; therefore, before starting with the isothermal procedure, the minimum isothermal crystallization temperature was first determined. This was done by heating the sample directly from the chosen $T_c$ temperature, after being quenched from the melt. The lowest temperature which did not show any melting enthalpy during immediate subsequent heating was the minimum isothermal crystallization temperature employed. In most cases, 5 isothermal temperatures were tested with variations of 1 °C between them.

To make the isothermal measurements of samples with two crystallization peaks, at pseudo-eutectic point, the procedure described below was carried out:

First for the PBS in the copolymer:

1) Hold for 3 min at 90 °C to erase the thermal history.
2) Quench from 90 °C to a chosen isothermal crystallization temperature $T_c$ at 60 °C/min cooling rate.
3) Isothermal crystallization until saturation.
4) Heat from $T_c$ to 90 °C at 20 °C/min.

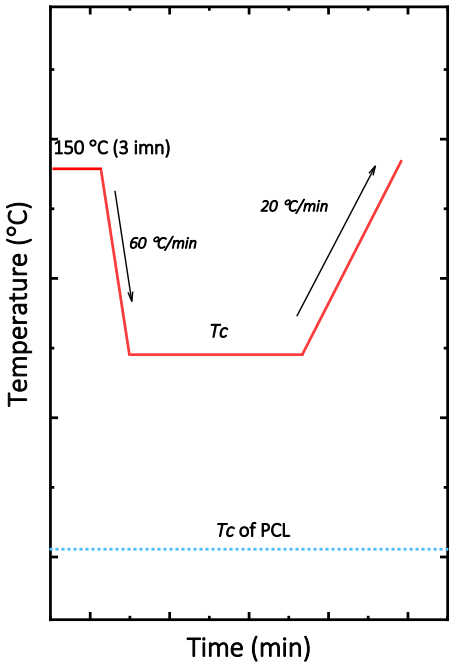


***Figure 3.1.*** *Schematic representation of the thermal protocol employed for isothermal crystallization experiments of PBS phase in the copolymer at pseudo-eutectic point.*

Where the values of $T_c$, correspond to values of crystallization temperatures of the PBS homopolymer present in the copolymer, this means that these measurements were made in a temperature range of 12 to 17 °C. Therefore, the PCL present in the copolyester during these measurements was in the melt state. This protocol is represented in Figure 3.1.

On the other hand, for the isothermal studies of the PCL in the copolymer at eutectic point, the following was done:

*1) Hold for 3 min at $T_{m1}$ (90 °C to erase the thermal history).*

*2) Cool down from 90 °C to -60 °C at 20 °C/min.*

*3) Hold for 3 min at -60 °C.*

*4) Heat up from -60 °C to $T_{m2}$ (25 °C to ensure that all the PCL component in the copolymer is molten and all the PBS component is crystallized)*

*5) Quench from $T_{m2}$ to a $T_{c2}$ at 60 °C/min. $T_{c2}$= from -10 °C to -14 °C (the temperature that PCL can crystallize).*

*6) Isothermal crystallization until saturation.*

*7) Heat from to $T_{c2}$ to $T_{m1}$.*

The procedure described above for the isothermal crystallization of Polyether is shown in Figure 3.2.

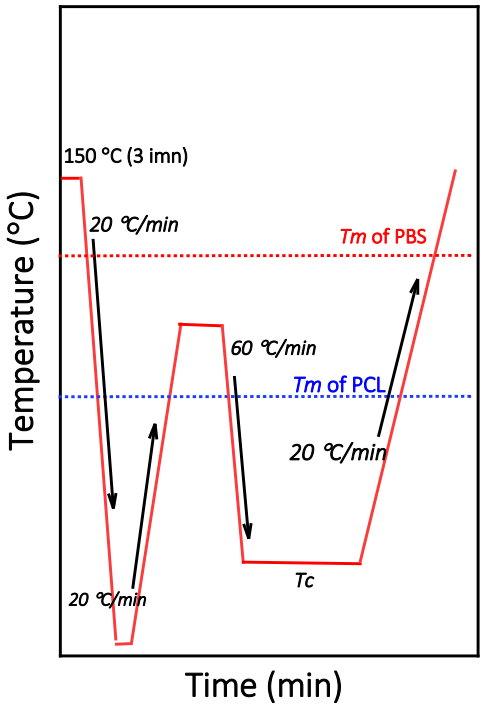


***Figure 3.2.*** *Schematic representation of the thermal protocol employed for isothermal crystallization experiments of PCL phase at pseudo-eutectic point.*

### 3.3.5. Polarized Light Optical Microscopy (PLOM)

The polarized light microscope is an optical microscope equipped with two polarizers located above and below the sample. The polarized light microscope is designed to observe and photograph samples that are visible primarily due to their optically anisotropic character. In order to accomplish this task, the microscope must be equipped with both a polarizer, positioned in the light path somewhere before the specimen, and an analyzer (a second polarizer), placed in the optical pathway between the objective rear aperture and the observation tubes or camera port. When the polarizers are crossed, light goes only in the orthogonal direction. This means that light is not transmitted when there is no sample or when the sample has an isotropic disordered structure, as in the case of amorphous polymers or semicrystalline molten polymers. In the case when polarizers are crossed and a semicrystalline polymer is observed, a birefringent sample, an interference phenomenon occurs allowing the light beam to pass through the microscope. Therefore, the areas of the sample with ordered anisotropic regions appear bright on a smooth and dark background, which corresponds to the fraction of amorphous or molten material.

A polarized light optical microscope, Olympus BX51 equipped with an Olympus SC50 digital camera and in combination with a Linkam TP-91 hot stage was used to observe spherulite development. Films with around 50 μm thickness were prepared by melting the samples in between two glass slides.

For non-isothermal experiments, the samples were first heated to 30 °C above their melting point $T_m$ to erase their thermal history and then they were crystallized from the melt by cooling to 40 °C below their crystallization temperature $T_c$ at 10 °C/min. The experimental conditions used for isothermal studies are described in the following.

#### 3.3.5.1. Spherulitic growth rate (*G*)

Spherulite growth rate experiments were also performed by recording their growth by PLOM (Olympus BX51), incorporating a λ plate in between the polarizers at

45° to facilitate observation and determine the sign of the birefringence. In order to determine the spherulitic growth rate (*G*) as a function of crystallization temperature ($T_c$) The dimensions of the spherulites were periodically registered with an Olympus SC50 digital camera after following procedure described below:

(a) Erasure of thermal history by heating the samples to 30 °C above their peak melting temperature for 3 min.

(b) The sample is cooled from the melt to a selected isothermal crystallization temperature ($T_c$) at 60 °C /min.

(c) At this temperature ($T_c$) the dimensions of the spherulites are periodically registered until they impinged on one another completely filling the microscope observation field.

(d) With DIGIMIZER program, the radius of the spherulites are measured taking into account the scale used in the measurements. Once the radio data is obtained, it is plotted as a function of time obtaining a straight line whose slope corresponds to G at that measured $T_c$.

(e) The processes described from a) to d) are repeated at different crystallization temperatures ($T_c$) in order to know spherulite growth rate at different temperatures.

#### 3.3.5.2. Nucleation density (*ρ)*

The density of nuclei as a function of time was determined counting the number of nuclei as a function of time. To do this, the steps from (a) to (c) described in the 3.3.5.1 section are followed. In this case once $T_c$ is reached, photographs are taken until the saturation when spherulites impinge on one another completely filling the microscope field. As the thickness of the sample is also determined, the nuclei number in a given volume, the density of nuclei ($\rho$) at a selected crystallization temperature ($T_c$) is obtained according to equation 3.2;

$$\rho_{nuclei} = N°Nuclei \cdot V \qquad \text{Eq.3.2.}$$

### 3.3.6. X-ray Diffraction (XRD)

XRD is a primary technique to 1) Identification of semicrystalline polymers and recognition of crystalline phases (polymorphism) of polymers. 2) Determine the degree of crystallinity in polymers. 3) Determine the size of crystallites using variants of the Scherrer equation. 4) Determine the crystalline orientation through the Hermans orientation function.

#### 3.3.6.1. Wide Angle X-ray Scattering (WAXS), Small Angle X-ray Scattering (SAXS)

Wide-angle *X*-ray Scattering (WAXS) and Small Angle *X*-ray Scattering (SAXS) are *X*-ray-diffraction techniques that are often used to determine the crystalline structure of polymers. WAXS specifically refers to the analysis of Bragg peaks scattered to wide angles, which (by Bragg's law) implies that they are caused by sub-nanometer-sized structures. When X-rays are directed in solids they will scatter in predictable patterns based upon the internal structure of the solid. The diffraction pattern generated allows researchers to determine the chemical composition or phase composition of the film, the texture of the film (preferred alignment of crystallites), the crystallite size and presence of film stress. According to this method the sample is scanned in a wide-angle X-ray goniometer, and the scattering intensity is plotted as a function of the 2θ angle. X-ray diffraction is a non destructive method of characterization of solid materials. A crystalline solid consists of regularly spaced atoms (electrons) that can be described by imaginary planes. The distance between these planes is called the d-spacing. The intensity of the d-space pattern is directly proportional to the number of electrons (atoms) that are found in the imaginary planes.

By using Small Angle *X*-ray Scaterring (SAXS) technique, nanoscale density differences in a sample can be quantified. This is achieved by analyzing the elastic scattering behaviour of X-rays when travelling through the material, recording their scattering at small angles (typically 0.1 - 10°, hence the "Small-angle" in its name). Depending on the angular range in which a clear scattering signal can be recorded,

SAXS is capable of delivering structural information of dimensions between 1 and 100 nm, and of repeat distances in partially ordered systems of up to 150 nm.

For $LM_w$-$BS_xCL_y$, Wide angle X-ray scattering measurements were performed with a Bruker D8 Advance diffractometer using parallel beamgeometry and a line focus X-ray tube operating at 40 kV and 40 mA withfiltered Cu-Kαradiation (0.154 nm). Experiments werecarried out under vacuum at both 25 °C and −60 °C with the temperature controlled at ± 0.1 °C by an Anton Paar TTK 450 low-temperature chamber. Measurements were made in the reflection mode with 2θvarying from 4° to 30° at steps of 0.05°.

### 3.3.6.2. Simultaneous Wide-Angle and Small-Angle X-ray Scattering (WAXS/SAXS)

The HMw-$BS_xCL_y$ samples were examined under nonisothermal conditions by simultaneous in situ WAXS/SAXS performed at beamline BL11-NCD at the ALBA Synchrotron radiation facility in Barcelona, Spain. The samples in DSC pans were placed in a Linkam THMS600 stage coupled to a liquid nitrogen cooling system. First, they were heated at 10 °C/min from room temperature to 30 °C above the melting temperature Tm and held for 3 min to erase their thermal history. Second, the samples were cooled to −60 °C at a rate of 10 °C/min and held at this temperature for 5 min. Third, the samples were heated to 30 °C above the melting point at 10 °C/min rate. During the mentioned protocol, SAXS/WAXS spectra were recorded every 10 s.

WAXS and SAXS scans were taken periodically at two scans per degree centigrade. The energy of the X-ray source was 12.4 keV (λ = 1.0 Å). In the WAXS configuration, the sample–detector (WAXS detector, Rayonix LX255-HS with an active area of 230.4 × 76.8 mm (pixel size: 44 μm2)) distance employed was 15.5 mm with a tilt angle of 27.3°. In the case of the SAXS configuration, the sample–detector (SAXS detector, Pilatus 1M (from Dectris)) had an activated image area of 168.7 × 179.4 mm2, a total number of pixels of 981 × 1043, 172 × 172 μm2 pixels size, and a frame rate of 25 frames/s, and the distance employed was 6463 mm. The intensity profile was output as the plot of the scattering intensity vs scattering vector, $q = 4\pi \sin \theta\lambda^{-1}$,

where λ is the X-ray wavelength (λ = 1 Å) and 2θ is the scattering angle. The scattering vector was calibrated using silver behenate (SAXS) and chromium(III) oxide (WAXS).

To study the crystal structure during isothermal crystallization at the pseudo-eutectic point, the $HM_w$-$BS_{45}CL_{55}$ sample at eutectic point were examined conditions by simultaneous WAXS/SAXS performed using described protocol in 3.3.4.2 section.

**3.3.6.3. 2D Wide-Angle X-ray Diffraction (WAXD).**

The 2D wide-angle X-ray diffraction (WAXD) measurements were performed at 25 °C on a Xeuss 2.0 SAXS/WAXS system (Xenocs SA, France). The Cu Kα X-ray source (GeniX3D Cu ULD), generated at 50 kV and 0.6 mA, was utilized to produce X-ray radiation with a wavelength of 1.5418 Å. A semiconductor detector (Pilatus 300K, DECTRIS, Swiss) with a resolution of 487 × 619 pixels (pixel size = 172 × 172 $\mu m^2$ ) was used to collect the scattering signals. The X-rays irradiate the sample along the x-axis with an incident angle of 3° with respect to the AAO surface. The 2D detector was placed perpendicular to the incident beam. The exposure time for each pattern was 20 min for infiltrated samples and 5 min for bulk samples. The one-dimensional intensity profiles were integrated from the 2D WAXS patterns and averaged along the azimuthal angle. Samples were treated before the measurement using a Linkam hot-stage to: 1. erase thermal history at 30 °C above their melting point, 2. Cool down to -60 °C K at 5 °C/min. Then, the samples were stored at room temperature, and the measurements were made at room temperature.

The Scheme 3.5 is a schematic illustration of the experimental setup of the measurement. The normal of the plane for the AAO surface is defined as the z-axis, while two lines in the AAO surface perpendicular to each other are defined as the x and y axes. The selection of the x and y axes is random based on the symmetry [3].

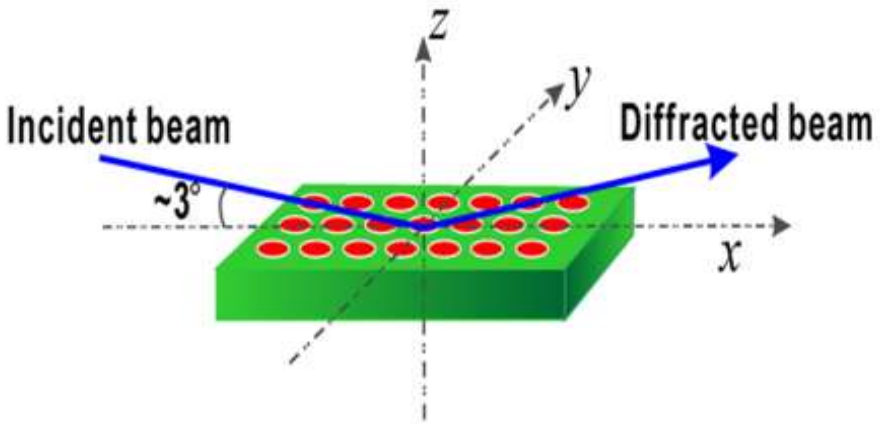


***Scheme 3.5.*** *Schematic illustration of the experimental geometry of the 2D WAXD measurements.*

### 3.3.7. Fabrication of anodic aluminum oxide (AAO) templates

The homemade AAO templates have been fabricated using the well-known two-step electrochemical anodization process of aluminum foils [4], which has been previously described in detail [4-6]. Previously, the aluminum was cleaned by sonication in different solvents that have different polarity (acetone, 2-propanol, water, and ethanol). Subsequently, the foils undergo a 4 min electropolishing process in a solution of perchloric acid and ethanol (1/3) with a constant voltage of 20 V and a temperature below 10 °C. Firstly, AAO templates of 35 nm pore diameter and 30 µm in length were synthesized. For the first electrochemical anodization process, oxalic acid was used as an electrolyte in a concentration of 0.03 M. Anodization time was 19 hours at 0 °C. For the second electrochemical anodization process to length the nanopores, similar conditions were used. Subsequently, a process of widening of the pores in 5% $H_3PO_4$ was carried out until a size of 70 nm pore diameter was reached. See scheme 3.6 for electrochemical anodization process.

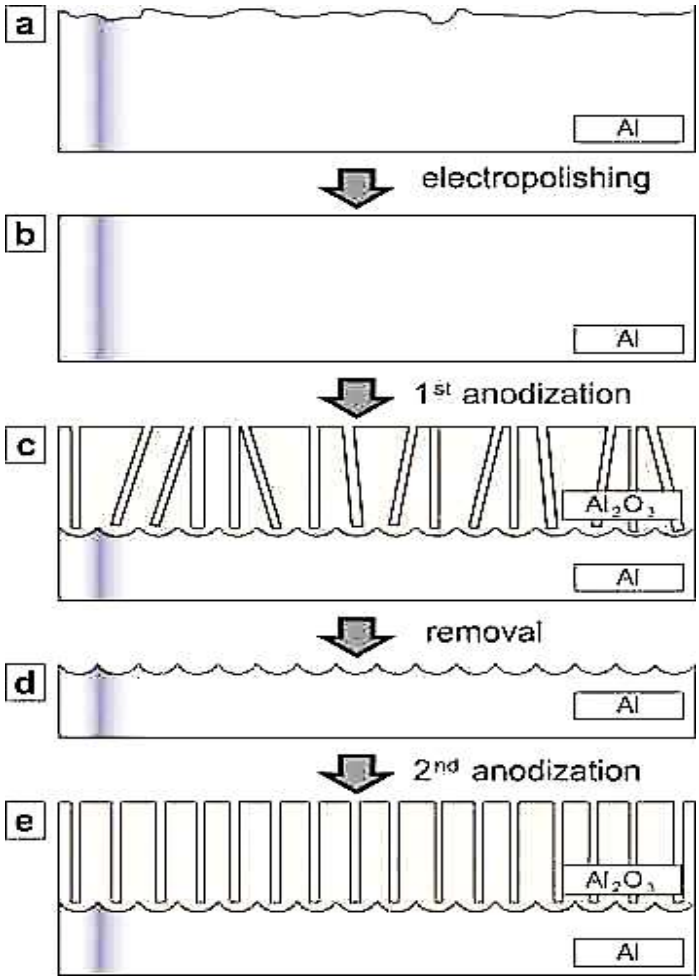


***Scheme 3.6.*** *Schematic diagram of the process for the fabrication of the AAO template. (a) A high purity Al foil is electropolished (b) and then the first anodization is performed (c). The first alumina layer is removed (d) and the second anodization is carried out* [5].

### 3.3.8. Preparation of polyesters and copolyesters nanofibers

The infiltration of poly (butylene succinate), poly (butylene adipate), polycaprolactone, and PBS-*ran*-PCL copolyesters was carried out by the melt precursor film wetting method. Polymer films were employed and placed on the AAO template surface. Then infiltrated by heating them to 40 °C above their melting point for 12 h under nitrogen flow. Later, samples were quenched to room temperature and

carefully cleaned to remove any residual polymer from the template surface. Scheme 3.7 shows the fabrication of nanofibers and their characteristic method.

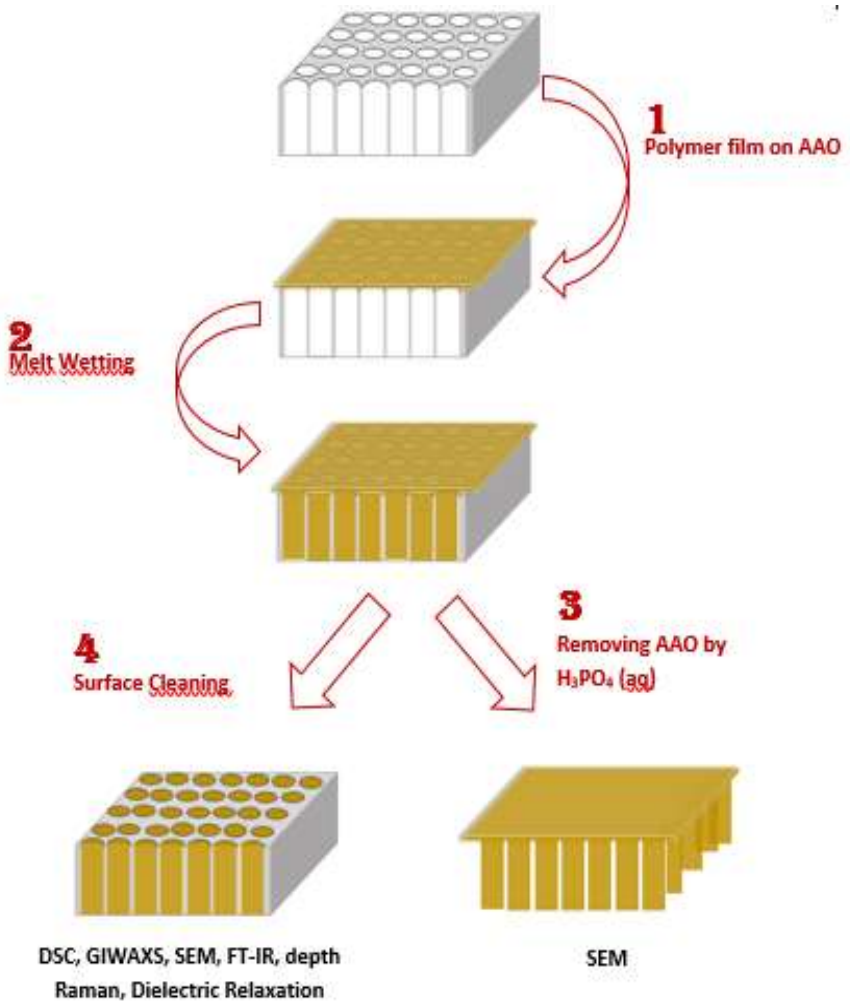


***Scheme 3.7.*** *Schematic of fabrication of polymer nanostructures through polymer melt wetting and its characterization.*

### 3.3.9. Scanning Electron Microscopy (SEM)

SEM is a multifold tool that can be used for advanced characterization of polymers. Philips XL-30 ESEM was used to morphologically characterize the AAO

templates and confined polymer samples. To observe the polymer nanofibers by SEM, alumina substrates were dissolved with NaOH 1 M during 1 h at room temperature (RT). In addition, another method were applied to prepare the samples for SEM; the sample was held in liquid nitrogen for 3-4 min and then bent outward quickly. This technique allow us to see the nanostructures, which were brought out of the broken template.

### 3.3.10. Raman Spectroscopy (RAMAN) and Fourier Transformed Infrared Spectroscopy (FTIR).

FT-IR on and Raman scattering are molecular spectroscopies widely used to obtain information on polymeric systems from their vibrational properties. While infrared radiation arises from a direct resonance interaction between the frequency of the infrared incident radiation and that of a particular vibrational mode, the Raman effect is an inelastic scattering of light occurring upon the irradiation of a molecule with a monochromatic light (usually a laser). One major advantage of Raman scattering is to allow the analysis of thick polymer samples while only very thin films can be examined by infrared transmission spectroscopy, since infrared radiation is readily absorbed by functional groups of the polymers [7].

Raman spectroscopy was applied to study and verify the effectiveness of the infiltration of PBA and PBS. Renishaw InVia Raman Microscope (Renishaw plc, Wottonunder-Edge, UK) was used fitted with a grating spectrometer of 785 nm near-infrared diode laser and a Peltier-cooled charge-coupled device (CCD) detector, attached to a confocal microscope. All spectra were processed using Renishaw WiRE 3.3 software. Data acquisition covered the spectral range 3000−200 $cm^{-1}$ with a spectral resolution of 4 $cm^{-1}$.

To verify if any conformational changes happened during the infiltration processes, polymer nanofibers were examined by Fourier transform infrared spectroscopy (FTIR) employing a PerkinElmer Spectrum One coupled with an attenuated total reflectance (ATR) accessory.

### 3.3.11. Dielectric Relaxation Processes

The dielectric spectroscopy technique is used to study relaxation processes which are caused by the rotational fluctuations of molecular dipoles. This technique is based on the application of an external field which weakly perturb the molecular dipole system of a sample from the equilibrium. Once the field is removed, the dipole system is able to return to the equilibrium supplying information about the spontaneous fluctuations in the system, and therefore through this technique information about the dynamical processes of characteristic parts of a molecules or systems is obtained. Whit this technique the dielectric properties of a medium can be measured as a function of the frequency, by an external oscillating field, and also in the time domain [8].

The complex dielectric permittivity $\varepsilon^*(\omega) = \varepsilon'(\omega) - i\varepsilon''(\omega)$, where $\varepsilon'$ is the real and $\varepsilon''$ is the imaginary part, was obtained as a function of the frequency ω and temperature $T$ [8] by using a Novocontrol high-resolution dielectric analyzer (Alpha-N analyzer). The sample cell was set in a cryostat, and its temperature was controlled via a nitrogen gas jet stream coupled with the Novocontrol Quatro controller. The dielectric measurements were performed at different temperatures in the range of 120 K and 390 K and at frequencies in the range of $10^{-1}$-$10^{6}$ Hz. For PBA and PBS homopolymer samples, measurements were carried out in the usual parallel plate geometry with electrodes of 20 mm in diameter. A separation of 100 mm between both electrodes was maintained by using a cross-shaped Teflon® spacer of a small area. For the samples infiltrated in the AAO templates, the measurements were carried out with a 15 mm electrode placed on top of the template without spacers. Before the dielectric measurements, the sample capacitor (inside the BDS cell) was heated above the melting temperature of each polymer to erase the thermal history.

### 3.3.12. Dynamic Mechanical Thermal Analysis (DMTA)

A Dynamic Mechanical Thermal Analyzer (DMTA), Triton 2000 DMA from Triton Technology, was used in a single cantilever bending deformation mode to carry

out Mechanical Dynamic Thermal Analysis (DMTA). DMA tests using material pockets to analyze powdered materials, as well as the procedure to perform such tests has been reported in the literature [12]. The temperature of the sample or the frequency of the stress are often varied, leading to variations in the complex modulus; this approach can be used to locate the glass transition temperature of the material, as well as to identify transitions corresponding to other molecular motions [9]. In this work, material pockets were used. A material pocket is a stainless-steel envelope that holds the sample. As stainless steel does not have any relaxation or phase transitions over the temperature range of the instrument, this is an ideal sample mounting material. To prepare the samples, the powder material was put inside the metal pocket. Then, the pocket was folded in half, closed to form a sandwich and placed in the DMTA. The samples were heated from -100 °C to 60 °C at a constant heating rate of 4 °C/min and frequency of 1 Hz. These tests allowed detecting the glass transition temperature ($T_g$), given by the maximum peak in loss tangent, tan $\delta$. This method was used to analyze the copolymers of the Chapter 7 (VHMw-$BS_xCL_y$) and the parent homopolymers that formed them.

### 3.3.13. Tensile Testing

Tensile tests are performed for several reasons. Tensile properties frequently are included in material specifications to ensure quality. Tensile properties often are measured during development of new materials and processes, so that different materials and processes can be compared. Finally, tensile properties often are used to predict the behavior of a material under forms of loading other than uniaxial tension. The strength of a material often is the primary concern. A dog-bone specimen is usually a standardized sample cross-section and It has two shoulders and a gage (section) in between. The shoulders are large so they can be readily gripped, whereas the gage section has a smaller cross-section so that the deformation and failure can occur in this area [10-11].

The tensile tests were carried out in an Instron 5569 tensile tester (Instron, Norwood, MA, USA). Sample's thickness was 200 micrometer, which obtained using

the hot-pressing molding method. Young's modulus was determined by means of an extensometer at a crosshead speed of 1 mm/min. Tensile strength ($\sigma_t$) and ductility, measured as the break strain ($\varepsilon_b$) were determined from the load-displacement curves at a crosshead speed of 10 mm/min. A minimum of five tensile specimens were tested for each reported value.

## 3.4. REFERENCES


1. Sugihara, S.; Toshima, K.; Matsumura, S., New Strategy for Enzymatic Synthesis of High-Molecular-Weight Poly (butylene succinate) via Cyclic Oligomers. *Macromolecular rapid communications* **2006,** *27* (3), 203-207.

2. Lorenzo, A.; Arnal, M.; Albuerne, J.; Müller, A., *DSC isothermal polymer crystallization kinetics measurements and the use of the Avrami equation to fit the data: Guidelines to avoid common problems*. 2007; Vol. 26, p 222-231.

3. Guan, Y.; Liu, G.; Gao, P.; Li, L.; Ding, G.; Wang, D., Manipulating crystal orientation of poly (ethylene oxide) by nanopores. *ACS Macro Letters* **2013,** *2* (3), 181-184.

4. Masuda, H.; Fukuda, K., Ordered metal nanohole arrays made by a two-step replication of honeycomb structures of anodic alumina. *science* **1995,** *268* (5216), 1466-1468.

5. Martin, J.; Maiz, J.; Sacristan, J.; Mijangos, C., Tailored polymer-based nanorods and nanotubes by" template synthesis": From preparation to applications. *Polymer* **2012,** *53* (6), 1149-1166.

6. Jessensky, O.; Müller, F.; Gösele, U., Self-organized formation of hexagonal pore structures in anodic alumina. *Journal of the Electrochemical Society* **1998,** *145* (11), 3735-3740.

7. Bokobza, L., Spectroscopic techniques for the characterization of polymer nanocomposites: A review. *Polymers* **2017,** *10* (1), 7.

8. Kremer, F.; Schönhals, A., *Broadband dielectric spectroscopy*. Springer Science & Business Media: 2012.

9. Menard, K., Dynamic Mechanical Analysis: A Practical Introduction, CRC Press. *Boca Raton* **1999**.

10. Czichos, H.; Saito, T.; Smith, L., *Springer handbook of materials measurement methods*. Springer: 2006; Vol. 978.

11. Davis, J. R., *Tensile testing*. ASM international: 2004.

# *Chapter IV:*

# *Enzymatic Synthesis and Crystalline Isodimorphic Character of Poly (butylene Succinate-ran-Caprolactone) Copolyesters*

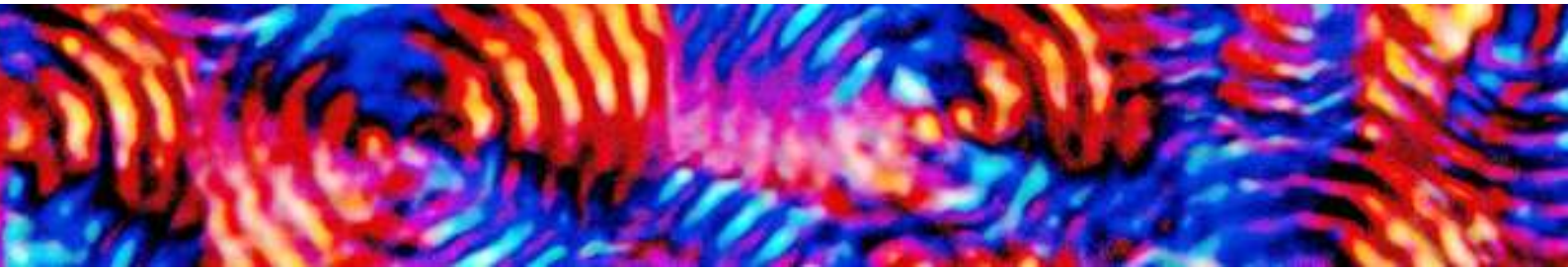

# Table of Contents

## Abstract

In this chapter, the preparation of PBS-*ran*-PCL copolyesters by enzymatic ring opening polymerization is presented. The copolyesters were produced in a wide composition range and free of metallic contaminants, so they may be regarded as potential biomaterials. The copolymers have been characterized by proton and carbon nuclear magnetic resonance ($^{1}$H and $^{13}$C NMR), gel permeation chromatography (GPC), thermogravimetric analysis (TGA), differential scanning calorimetry (DSC), polarized light optical microscopy (PLOM) and wide angle X-ray scattering (WAXS). The PBS-*ran*-PCL copolyesters were able to crystallize in the entire composition range and displayed a pseudo-eutectic region.

Most copolymers away from the pseudo-eutectic region exhibited a single crystalline phase (PBS-rich or PCL-rich crystalline phase), while within the pseudo-eutectic region the copolymers were double crystalline. Observations by PLOM, during isothermal crystallization showed that both nucleation density and spherulitic growth rate of the copolyesters are determined by the component that constitutes the majority phase. WAXS studies demonstrated that the copolymers are isodimorphic, as the PBS-rich crystalline phase contains small inclusions of PCL *co*-units, while the PCL-rich crystalline domains also contain a minor quantity of PBS *co*-units inside.

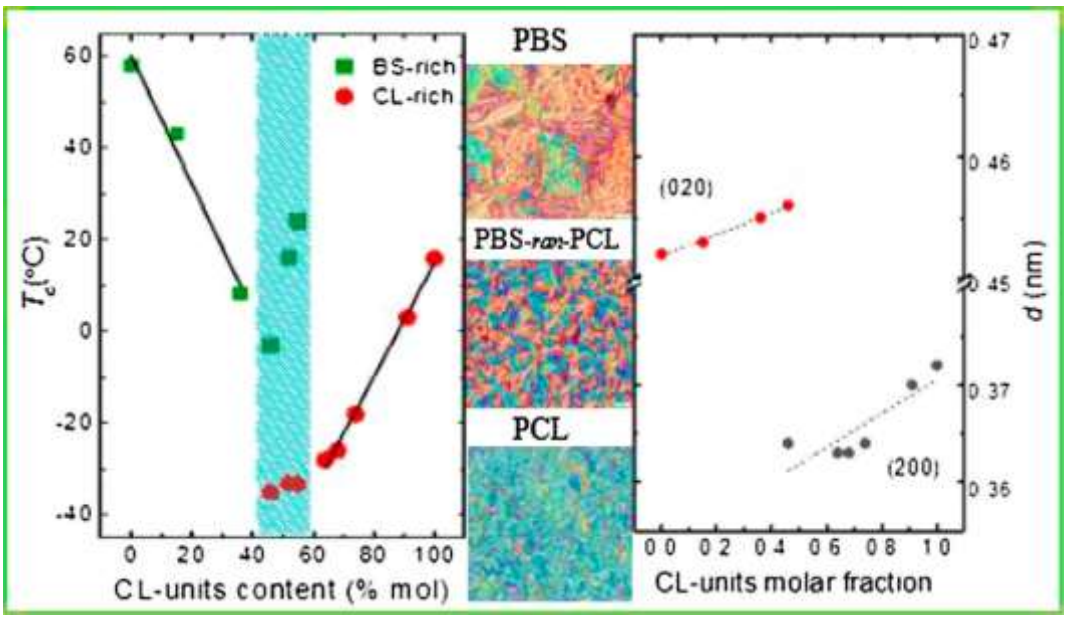
PBS
PBS-ran-PCL
PCL
BS-rich
CL-rich
$T_c$(°C)
CL-units content (% mol)
(020)
(200)
d (nm)
CL-units molar fraction

## 4.1. INTRODUCTION

Aliphatic polyesters have achieved an outstanding position among bio-based polymers intended for biodegradable applications [1]. Many of these polyesters can be easily synthesized from bio-based monomers and display a remarkable sensitivity to biodegradation that can be controlled by adjusting the composition. Nevertheless, it is true that thermal and mechanical properties of aliphatic polyesters are not always in agreement with expectations, and copolymerization has been an approach frequently used to overcome such limitation. Poly(caprolactone) (PCL) is a polyester that exemplifies well this issue (see Scheme 4.1) [2]. PCL is inexpensively produced, shows both high biodegradability and good biocompatibility, and counts with FDA approval. However PCL melts around 60 °C and its glass transition temperature ($T_g$) is near -60 °C. On the other hand, poly(butylene succinate) (PBS) is another aliphatic polyester (see Scheme 4.1) with $T_m$ ~120 °C and $T_g$~ -30 °C that is accessible from bio-based 1,4-butanediol and succinic acid, and that has mechanical properties comparable to those of polypropylene [3]. The combination of PCL and PBS either as blends or as copolyesters, both random and blocks, has been used in several occasions to render new materials with improved behavior [4-7].

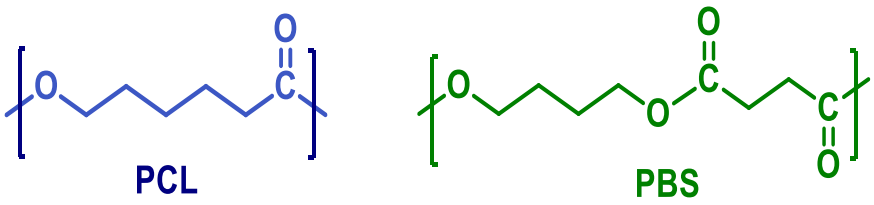


***Scheme 4.1****. Chemical repeating units of PCL and PBS homopolyesters.*

Copolyesters made of butylene succinate and caprolactone have been synthesized so far using compounds of petrochemical origin, however, they could be made employing fully biobased chemicals in the near future. 1,4-butanediol and succinic acid are today readily available by sugar fermentations at industrial scale [8] and caprolactone can be prepared with high selectivity from 1,6-hexanediol produced from lignocelluloses *via* 5-hydroxymetyl furfural [9]. These copolyesters are gaining therefore relevance in the biomaterial field since they are able to combine sustainability with satisfactory bio related properties. Ideal polymers designed to be used as biomaterials should be exempted of metallic compounds. However, all synyheses reported so far to prepare poly(butylene succinate-*ran*-caprolactone) copolyesters have been performed with the concourse of organometallic catalysts. Cao et al. [5] have reported mechanical and thermal characterization of PBS-*ran*-PCL random copolymers synthesized this way.

In this Chapter, we present for the first time the preparation of these copolyesters by enzymatic ring opening polymerization (*e*ROP). Although PBS is prepared at industrial scale by melt Polycondensation [10], the successful synthesis of this homopolyester by *e*ROP has been reported in several occasions by using cyclic (butylene succinate) oligomers *c*$(BS)_n$ which were previously prepared by enzymatic cyclization.[11] On the other hand, PCL is usually synthesized by chemically catalyzed ROP making use of a wide variety of organometallic catalysts but the enzymatic procedure is gaining importance in these last years [12].

The copolymerization of the oligomeric *c*$(BS)_n$ with CL has allowed us the preparation of a series of random copolyesters, abbreviated LMw-$BS_xCL_y$ (with x and y indicating the molar contents in BS and CL units, respectively), exempted of metallic contaminants and with additional merits to be considered as potential candidates for biomaterials. In addition to the organocatalyzed (enzymatically) synthesis, the copolyesters prepared here have been characterized by Differential Scanning Calorimetry (DSC), Polarized Light Optical Microscopy (PLOM) and Wide Angle X-ray Scattering (WAXS). With these techniques we were able to determine

their thermal properties, morphology and structure and we have found that they display isodimorphic properties.

## 4.2. RESULTS

The chemical constitution of the polyesters was determined by NMR. Both the $^{1}H$ and $^{13}C$ NMR of the $PBS_{48}CL_{52}$ copolyester are shown in Figure 4.2 for illustration, whereas the spectra of the whole series are compared in the Appendix (Figure A.4.3). Weight average molecular weights of the $BS_xCL_y$ copolyesters were found to range between 4,000 and 14,000 $g \cdot mol^{-1}$ with dispersities oscillating between 1.9 and 2.6 and showing no apparent correlation with copolymer composition. The homopolyesters were obtained with molecular weights comparable to those found for the copolyesters although the $M_w$ of PCL was nearly three times higher than that of PBS.

It should be noted that other authors [11-12] have reported the preparation of these homopolyesters by the same procedure with much higher molecular weight, *i.e*., about 150,000 for PBS and 80,000 for PCL. It is known that the molecular weight of polyesters generated by enzymatic ROP is strongly influenced by polymerization conditions, such as monomers and enzyme concentrations, and reaction temperature as well. Also, the presence of small amounts of water is a critical factor in determining the resulting polyester size, which has to be rigorously avoided if high molecular weights are desired. In the experimental practice, the CALB used for catalyzing the reaction is frequently the main source of water but it may be readily removed by subjecting the enzyme to a severe drying just before using. In the present work, no special precautions for water removal were taken, since moderate to low polymer molecular weights were quite convenient for the calorimetric study that was intended to be carried out with PBS-*ran*-PCL copolyesters.

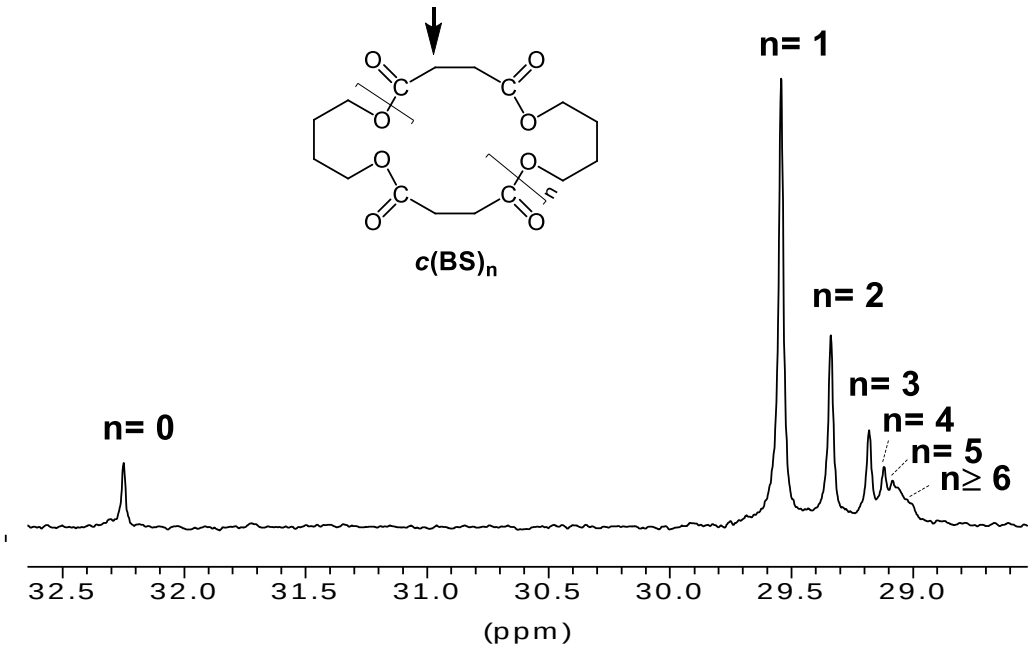


***Figure 4.1.*** *Quantitative $^{13}C$ NMR spectrum of $c(BS)_n$ cyclic oligomers in the region of the succinate methylene carbon (indicated with an arrow).*

### 4.2.2. Composition and microstructure of $BS_xCL_y$ copolyesters

The composition of the PBS-*ran*-PCL copolyesters regarding BS and CL units was determined by comparing the areas of $^1H$ NMR signals specifically arising from each of these two units. As it can be seen in Table 4.1 the copolyester compositions are in general consistent with the BS/CL ratios used for feeding although some noticeable differences are observed between them. Deviations are in general around 10%, with the content of BS in the copolyesters found to be lower than expected from the composition of the feed where a small amount of cyclic BS oligomers were removed by volatilization during polymerization. It can be inferred from these results that CL is more prone to react than the BS oligomeric cycles, which is indeed a reasonable fact, taking into account that larger ring opening driving forces must be operating in the relatively more strained CL cycles.

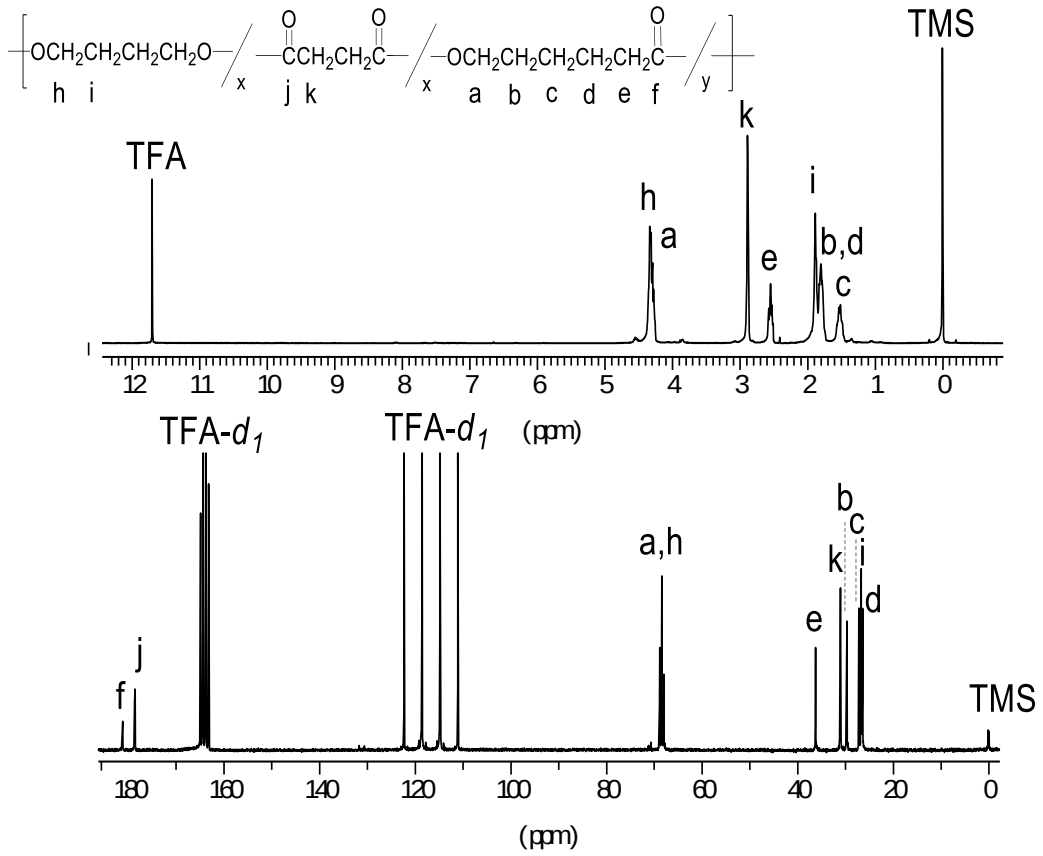


***Figure 4.2***. *$^{1}H$ (top) and $^{13}C$ NMR (bottom) spectra of $BS_{48}CL_{52}$ copolyester as representative of the PBS-ran-PCL copolyesters series recorded in TFA-d. Peaks were assigned according to the expected copolyester constitution depicted in the attached formula.*

The microstructure of the copolyesters was analyzed by $^{13}C$ NMR by taking benefit from the splitting of the methylene signals of the succinate moiety located around 31 ppm. As it is shown in Figure 4.3, these signals are sensitive to sequence effects so that three peaks corresponding to the four succinate-centered triads, B*S*B, B*S*CL/CL*S*B and CL*S*CL, became observed and used for quantification. The relative contents in the four triads for every copolymer composition and the application of the statistical method previously used by us for other copolyesters

of AABB-*co*-AB type [13], led to determine the degree of randomness *R* for the PBS-*ran*-PCL copolyesters.

Triads contents and *R* values are given in Table 3.1 in chapter 3, indicating that the microstructure of these copolyesters is essentially random. Given the oligomeric size of *c*$(BS)_n$ and the monomeric constitution of CL, the statistical distribution of BS and CL units observed in the copolyesters implies the occurrence of randomization reactions during ROP. Transesterification reactions catalyzed by organometallic compounds and leading to randomization are known to be common in polyesterifications carried out at high temperatures, usually above 150 °C. In the present case, although reaction temperature is rather low, transesterification reactions may be feasible due to the probable enhancing effect exerted by the lipase used for polymerization. This fact is supported by the presence of high contents of CL*S*CL triads that are only present in the copolymers if these reactions take place.

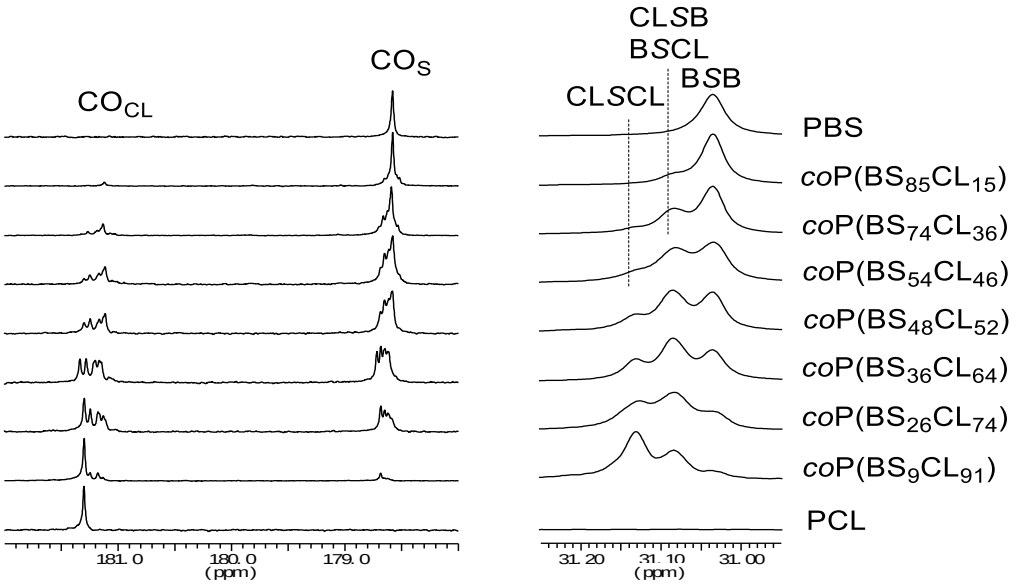


***Figure 4.3.*** *Carbonyls and succinate methylene carbon regions of the [13]C NMR spectra of PBS, PCL and PBS-ran-PCL copolyesters recorded in TFA-d. Peaks generated by splitting of the signals due to sequence effects are assigned to the four succinate-centered triads that are feasible for these copolyesters.*

### 4.2.3. Thermal stability

The thermal stability of $BS_xCL_y$ copolyesters was evaluated by thermogravimetry analysis conducted under an inert atmosphere. The TGA traces recorded for the whole series in the 50-600 °C range are represented together in Figure 4.4, including an inset in which the 300-360 °C region is enlarged in order to illustrate more clearly the differences in the onset decomposition temperatures. Thermal decomposition parameters, for PBS-*ran*-PCL in addition to those recorded for the PBS and PCL homopolyesters used as references are listed in Table 4.2.

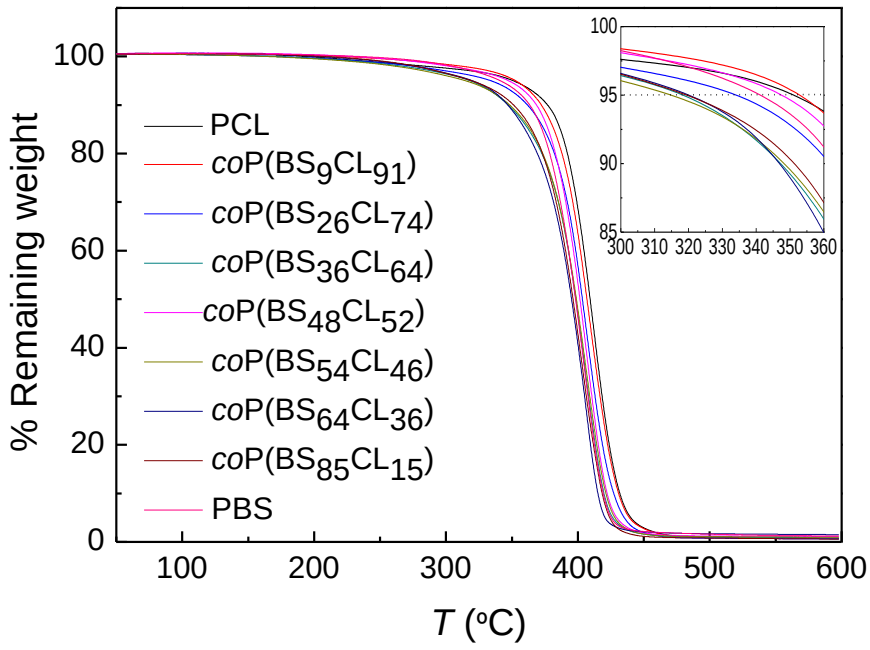


***Figure 4.4.*** *TGA traces of the PBS-ran-PCL series recorded under a nitrogen atmosphere. Inset: Enlarged onset temperature region.*

All the copolyesters start to decompose well above 300 °C, but at lower values than the parent homopolyesters, a behavior which is different to what it was observed for blocky CL related copolyesters, where CL was observed to enhance

the thermal stability of these copolymers [14]. Both the different microstructure and the presence of residual Ti catalyst can be the factors for this different behavior observed. In all cases, decomposition takes place in a single step with a maximum rate at temperatures near 400 °C, a value very close to those of both PBS and PCL. The remaining weight after heating to 600 °C is about 1% with no significant variations in between samples. The useful conclusion that can be drawn from the TGA analysis is that these copolyesters are well resistant to heat so that, as it will be seen below, they display a wide $T_d$-$T_m$ window that will allow carrying out a safety melting-crystallization study, as well as comfortable thermal processing in the eventual case that they were to be subjected to transformation.

*Table 4.2. Thermal parameters obtained by TGA in this work.*

| **Copolyester** | $^{o}T_d$ [a] (°C) | $^{max}T_d$ (°C) | $R_w$ [b] (%) |
|---|---|---|---|
| **LMw-PBS** | 341 | 403 | 1.2 |
| **LMw-$BS_{85}CL_{15}$** | 320 | 399 | 0.6 |
| **LMw-$BS_{64}CL_{36}$** | 320 | 402 | 1.5 |
| **LMw-$BS_{54}CL_{46}$** | 315 | 403 | 1.0 |
| **LMw-$BS_{48}CL_{52}$** | 320 | 404 | 1.1 |
| **LMw-$BS_{36}CL_{64}$** | 318 | 402 | 0.8 |
| **LMw-$BS_{26}CL_{74}$** | 334 | 405 | 0.6 |
| **LMw-$BS_{9}CL_{91}$** | 353 | 406 | 0.7 |
| **LMw-PCL** | 351 | 410 | 0.6 |

[a] *$^{o}T_d$, onset temperature corresponding to 5% of weight lost.*
[b] *Remaining weight at 600 °C.*

### 4.2.4. Glass transition temperatures

All copolymers exhibited a single glass transition temperature, as expected for random copolymers that are characterized by a miscible amorphous phase. The $T_g$ values of the random copolymers are between the $T_g$ values of two parent homopolymers and depend on composition. As it can be seen in Figure 4.5, the composition dependence was found to follow closely, the well-known Gordon-Taylor equation (equation 1) with $k_{GT}$ = 0.23:

$$T_{g,copolymer} = \frac{w_1\, T_{g,1} + k(1-w_1)\, T_{g,2}}{w_1 + k(1-w_1)} \qquad \text{Eq.4.1}$$

where $T_{g,1}$ and $T_{g,2}$ are the glass transition temperatures of homopolymers 1 and 2 ($T_{g,1} < T_{g,2}$), $w_1$ the mass fraction of homopolymer 1 and $k$ is the Gordon-Taylor parameter [15]. These results are consistent with the random character of the copolyesters, as demonstrated above by NMR (see Table 4.1).

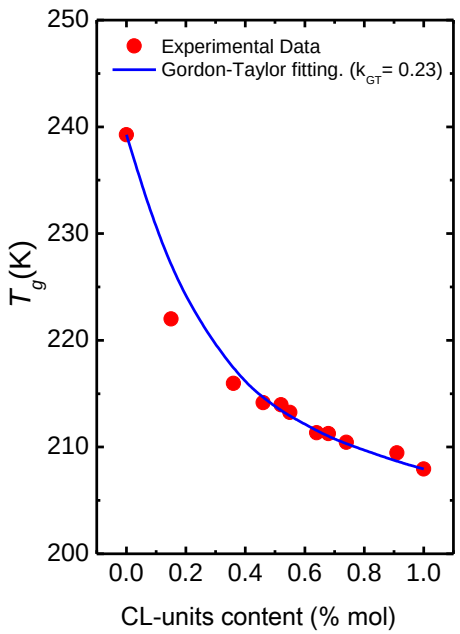


***Figure 4.5.*** *$T_g$ values of LMw-$BS_xCL_y$ copolyesters as a function of the content in CL units and their fitting in the Gordon-Taylor equation.*

### 4.2.5. Melting-crystallization of LMw-$BS_xCL_y$ copolyesters

The non-isothermal crystallization and melting of neat homopolymers and LMw-$BS_xCL_y$ copolymers are illustrated in the DSC scans presented in Figure 4.6. In Table 4.3, extracted data from DSC traces are collected.

Figure 4.6a shows that all copolyesters exhibit a sharp crystallization peak during cooling from the melt, except in the case of three copolymers LMw-$BS_{45}CL_{55}$, LMw-$BS_{48}CL_{52}$, and LMw-$BS_{54}CL_{46}$ that exhibit two broad crystallization peaks, which are not very clear at the scale employed in Figure 4.6a. A close up from these DSC curves is shown in Figure Apnx.4.4 (see Appendix), while the corresponding two peak crystallization temperature values for these three cases are reported in Table 4.3. In Appendix, also you can find DSC curves, which have been done at 10 °C/min rate (figure A.4.5).

The copolymers are capable of crystallization in the entire composition range. This behavior indicates that frequent interruption of the crystallizable sequences of one component by the other (for example in copolymers with compositions close to 50/50) cannot frustrate crystallization, as it happens for instance in ethylene/alfa-olefin copolymers. When the comonomer units are linear and have similar chemical structures, then crystallization can be found in the entire composition range, especially for copolyesters. Figure 4.6b shows the subsequent DSC heating scans, where melting transitions can be also observed for all samples. For copolymers with close to symmetric compositions (i.e., LMw-$BS_{45}CL_{55}$, LMw-$BS_{48}CL_{52}$, and LMw-$BS_{54}CL_{46}$), two characteristic melting points can be observed preceded by cold-crystallization processes.

As can be seen in Table 4.3, $T_c$, $\Delta H_c$, $T_m$, and $\Delta H_m$ strongly depend on copolymer composition. In a previous study about thermal properties of $BS_xCL_y$, $T_m$ and $T_c$ of the copolyesters shifted toward a lower temperature with an increase in the CL/BS molar ratio, however, no double crystallization or melting peaks where reported, as the composition range explored was limited [14]. On the other hand,

PBS/PCL blends have been found to be immiscible with two separated melting peaks observed at temperatures very close to those of the neat LMw-PBS and LMw-PCL components.[14]

These two melting peaks (Figure 4.6b) can be attributed to the previous crystallization (Figure 4.6a) of a PBS-rich phase (higher $T_c$ peak) and the crystallization of the PCL-rich phase (lower $T_c$ peak). As we will show by WAXS below, a small degree of cocrystallization occurs in these phases, as these copolyesters display an isodimorphic character. In isodimorphic copolymers, the comonomer that constitutes the major phase typically crystallizes in the unit cell of the corresponding homopolymer but can include a small amount of comonomer units of the minor second component in the crystal lattice.

PBS and the two copolymers with 85 and 64 mol% BS units exhibit cold crystallization during heating (Figure 4.6b), followed by a double melting peak, which indicates that PBS probably undergoes melting and recrystallization. The PCL homopolymer and also CL-rich phase copolymers (with CL contents between 91 and 40 mol%) display a single or double sharp melting peaks.

Figure 4.7a and 4.7b show plots of peak crystallization and melting temperatures respectively for the LMw-$BS_xCL_y$ copolyesters as a function of composition (CL-units content in mol%), with legends identifying the crystalline phases present according to WAXS experiments (presented below) and corresponding scan rates. In the case of Figure 4.7a, it is noteworthy how composition can shift the melting point of the copolymers by as much as 100 °C, thus providing an easy way to tailor the properties of the copolymers. On the other hand, $T_g$ values only change by about 30 °C and their composition dependence is very different than that exhibited by $T_m$ values. Random copolymers are one of the few families of polymeric materials where a separate control of $T_g$ and $T_m$ can be obtained by regulating composition, while for other polymeric systems, a linear correlation between $T_g$ and $T_m$ generally exists.

Figure 4.7a, shows how the melting point of the copolymers exhibit a pseudo-eutectic region in between 46-55 mol% CL content. To the left of the eutectic region, only PBS like crystals are formed (i.e., with unit cells that are very similar to that of neat PBS), and to the right of it, only PCL like crystals are obtained (according to WAXS). The pseudo-eutectic compositions have been shaded in Figure 4.7. For those three specific compositions, two crystalline phases were detected with distinct crystallization and melting temperatures. These two phases correspond to PBS like and PCL like crystals according to WAXS. Almost, there is no significant difference between obtained $T_m$ at 20 °C/min and 10 °C/min rate.

Figure 4.7b shows how cooling the samples from the melt, their crystallization temperatures also exhibit a pseudo-eutectic like behavior that resembles Figure 4.7a, except that temperatures are displaced to lower values, as supercooling is needed for crystallization. It is interesting to observe that if samples are cooled from the melt to room temperature (20-25 °C), only PBS and the copolymer with 85 mol% BS units can crystallize. All other samples need to be cooled down to much lower temperatures in order to become semi-crystalline. This behavior also provides control over the physical state of the copolymers depending on composition, which could be useful for specific applications. The lower scan rate (10 °C/min) led to a slight increase in $T_c$ values.

Figure 4.7c shows how the enthalpy of crystallization (normalized by the content of the crystallizable phase) depends on copolymer composition. The degrees of crystallinity ($X_c$) of the random copolymers were calculated from these normalized enthalpies of crystallization, and the values are summarized in Table 4.3 and plotted in Figure 4.7d. The values of the enthalpy of crystallization for 100% crystalline samples ($\Delta H_m^\circ$) were taken as 110.3 J/g and 139.5 J/g [15] for PBS and PCL respectively. As shown in both Figures 4.7c and 4.7d, the enthalpy of crystallization and degree of crystallinity derived from it also display a pseudo-eutectic point with composition that matches those exhibited by $T_m$ and $T_c$ versus composition. The reduction in crystallinity of the phases as their composition approaches the

pseudo-eutectic point is a reflection of the increase difficulty in crystallization experienced by the copolymers when there is an abundance or similar amount of both comonomer units. As only a rather small amount of the second comonomer units can be included in the crystal lattice of each phase (as indicated by the WAXS results below), as the amount of the second comonomer increases, the capacity of crystallization decreases as increasingly higher amounts of the second comonomer are excluded from the crystal lattice. As polymers with reduced crystallinity tend to have faster biodegradation, we expect that copolyesters within the pseudo-eutectic region could be potentially biodegraded faster than other compositions. It was predictable that copolyestres at the lower cooling rate (10 °C/min) exhibit higher $\Delta H_c$ and *Xc* values due to copolymers have more chance to be crystalized.

In summary, the calorimetric behavior of the LMw-$BS_xCL_y$ random copolyesters is characteristic of isodimorphic random copolymers [16], a fact that has not been previously recognized in the literature [14]. The results indicate that a certain level of co-monomer inclusion can occur in the entire composition range. Therefore two distinct crystalline phases can be formed: a PBS rich crystalline phase, where the crystals contain a small amount of CL units and a PCL rich crystalline phase, where small amounts of PBS units are included. The small content of the second monomer implies that the unit cells will remain very similar to those corresponding to neat PBS and neat PCL. In the special case of the pseudo-eutectic compositions the materials are double crystalline, with the two types of crystalline phases coexisting with a mixed amorphous phase. Such double crystalline character is reported in this work for the first time in LMw-$BS_xCL_y$ random copolyesters.

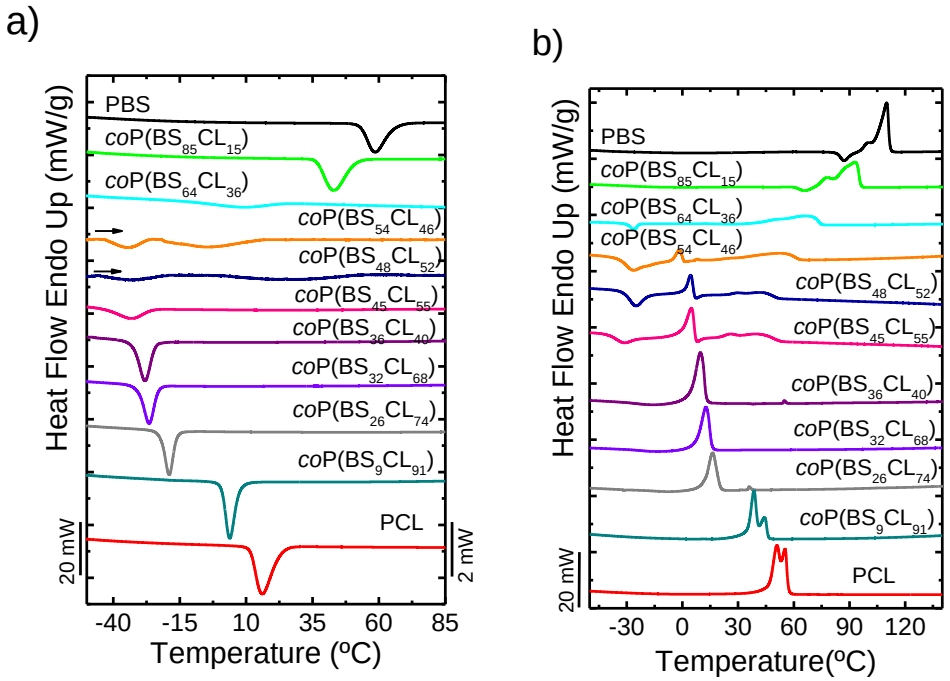


***Figure 4.6.*** *DSC scans of the LMw-$BS_xCL_y$ copolyester series and the parent homopolyesters PBS and PCL. Traces recorded during cooling from the melt (a) and subsequent heating (b) at 20 °C/min rate.*

***Table 4.3. A. Thermal parameters obtained by DSC of polymers in this work at 20 °C/min scan rate.***

| Copolyester | $T_g$ (°C) | BS-rich copolyesters | | | | | | | CL-rich copolyesters | | | | |
|---|---|---|---|---|---|---|---|---|---|---|---|---|---|
| | | Cooling | | | | | Heating | | Cooling | | | | Heating |
| | | $T_{c1}$ (°C) | $\Delta H_{c1}$ (J/g) | $X_{c1}$ (%) | $T_{cc}$ (°C) | $\Delta H_{cc}$ (J/g) | $T_{m1}$ (°C) | $\Delta H_{m1}$ (J/g) | $T_{c2}$ (°C) | $\Delta H_{c2}$ (J/g) | $X_{c2}$ (%) | $T_{m2}$ (°C) | $\Delta H_{m2}$ (J/g) |
| LMw-PBS | -33.9 | 58 | -61 | 55 | 87.1 | -11 | 110 | 64 | - | - | - | - | - |
| LMw-$BS_{85}CL_{15}$ | -54.5 | 43 | -59 | 53 | 25.2 | -7 | 93 | 72 | - | - | - | - | - |
| LMw-$BS_{64}CL_{36}$ | -57.2 | 8.3 | -49 | 44 | 25.8 | -31 | 66.8 | 81 | - | - | - | - | - |
| LMw-$BS_{54}CL_{46}$ | -58.8 | -3 | -4 | 4 | 25.4 | -58 | 52.7 | 68 | 35.0 | -2 | 1 | -1.0 | 20 |
| LMw-$BS_{48}CL_{52}$ | -59.2 | 16 | -6 | 5 | 26.5 | -63 | 40.5 | 56 | 34.0 | -4 | 3 | 4.0 | 29 |
| LMw-$BS_{45}CL_{55}$ | -59.9 | 23 | -6 | 5 | 31.4 | -27 | 39.0 | 58 | 33.1 | -18 | 12 | 4.8 | 53 |
| LMw-$BS_{36}CL_{64}$ | -61.6 | - | - | - | - | - | - | - | 28.3 | -45 | 32 | 9.7 | 78 |
| LMw-$BS_{26}CL_{74}$ | -62.7 | - | - | - | - | - | - | - | 18.0 | -52 | 37 | 16.3 | 77 |
| LMw-$BS_{9}CL_{91}$ | -63.2 | - | - | - | - | - | - | - | 3.2 | -64 | 45 | 38.5 | 74 |
| LMw-PCL | -65.2 | - | - | - | - | - | - | - | 16.1 | -72 | 52 | 55.4 | 75 |

*Table 4.3. B.* ***Thermal parameters obtained by DSC of polymers in this work at 10 °C/min scan rate.***

| Copolyester | $T_g$ (°C) | BS-rich copolyesters | | | | | | | CL-rich copolyesters | | | | |
|---|---|---|---|---|---|---|---|---|---|---|---|---|---|
| | | Cooling | | | | | Heating | | Cooling | | | Heating | |
| | | $T_{c1}$ (°C) | $\Delta H_{c1}$ (J/g) | $X_{c1}$ (%) | $T_{cc}$ (°C) | $\Delta H_{cc}$ (J/g) | $T_{m1}$ (°C) | $\Delta H_{m1}$ (J/g) | $T_{c2}$ (°C) | $\Delta H_{c2}$ (J/g) | $X_{c2}$ (%) | $T_{m2}$ (°C) | $\Delta H_{m2}$ (J/g) |
| LMw-PBS | -33.9 | 61.7 | -71 | 64 | 86.1 | -8 | 109.9 | 78 | - | - | - | - | - |
| LMw-$BS_{85}CL_{15}$ | -54.5 | 47.8 | -66 | 60 | 67.6 | -5 | 94.3 | 70 | - | - | - | - | - |
| LMw-$BS_{64}CL_{36}$ | -57.2 | 18.9 | -51 | 46 | 18.1 | -3 | 67.7 | 35 | - | - | - | - | - |
| LMw-$BS_{54}CL_{46}$ | -58.8 | -0.5 | -17 | 15 | -31.5 | -8 | 54.2 | 12 | -32.0 | -6 | 4 | -4.0 | 9 |
| LMw-$BS_{48}CL_{52}$ | -59.2 | - | - | - | -30.1 | -9 | 45.8 | 18 | -29.2 | -14 | 10 | 4.8 | 15 |
| LMw-$BS_{45}CL_{55}$ | -59.9 | - | - | - | - | - | 43.1 | 21 | -27.5 | -30 | 21 | 5.0 | 20 |
| LMw-$BS_{36}CL_{64}$ | -61.6 | - | - | - | - | - | - | - | -22.4 | -51 | 36 | 7.5 | 49 |
| LMw-$BS_{26}CL_{74}$ | -62.7 | - | - | - | - | - | - | - | -5.2 | -60 | 43 | 22.7 | 61 |
| LMw-$BS_{9}CL_{91}$ | -63.2 | - | - | - | - | - | - | - | 7.0 | -67 | 49 | 40.6 | 70 |
| LMw-PCL | -65.2 | - | - | - | - | - | - | - | 24.1 | -80 | 57 | 53.1 | 78 |

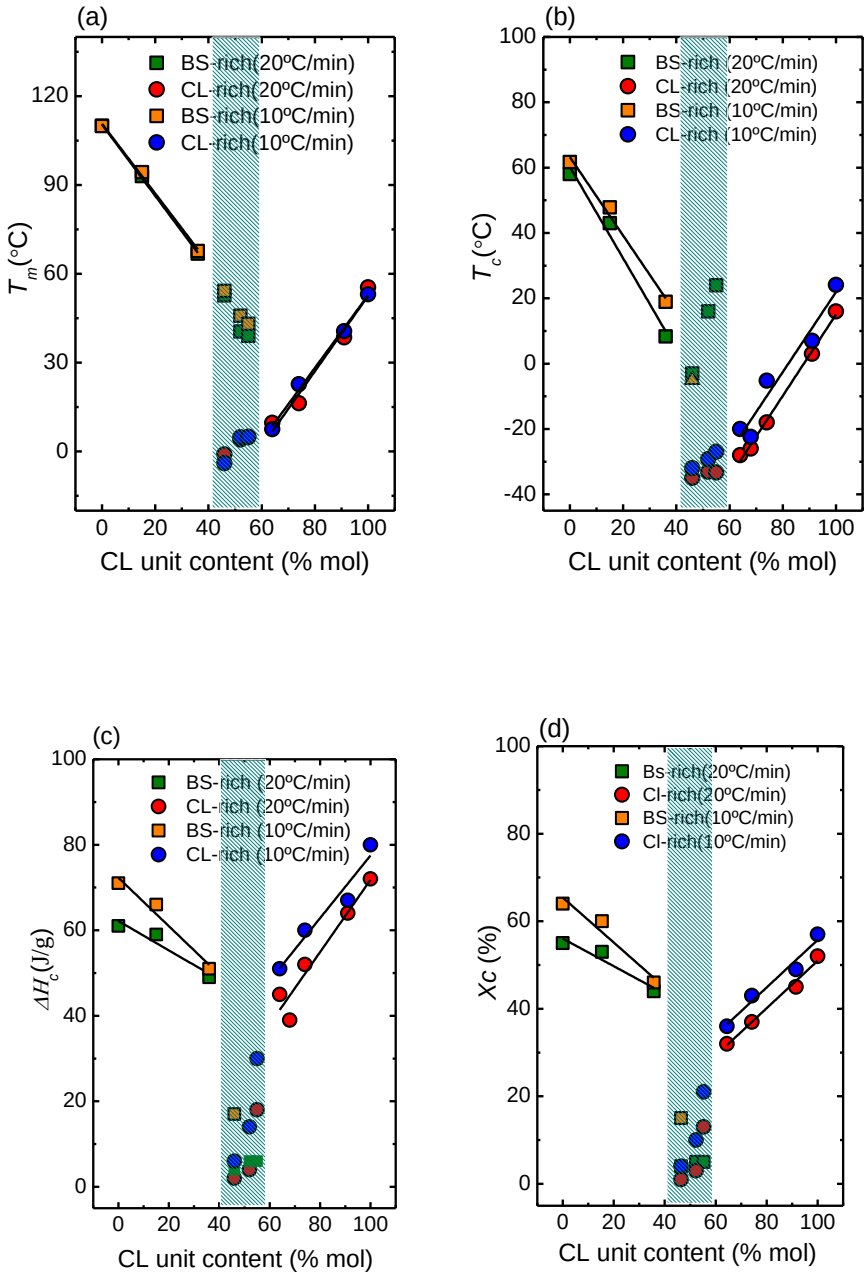


***Figure 4.7.*** *Peak melting temperature (a), peak crystaline temperature (b), enthalpy of crystallization ($\Delta H_c$) (c) and degree of crystallinity (d) for the LMw-$BS_xCL_y$ series as a function of composition in two different scan rate.*

### 4.2.6. Crystalline morphology

We studied the effect of copolymer composition and crystallization temperature on the spherulitic morphologies of LMw-$BS_xCL_y$ copolymers. Figure 4.8a and Figure 4.8b show PLOM micrographs for BS-rich samples and CL-rich samples during isothermal crystallization at the indicated temperatures and times, respectively. In general, the spherulitic morphology of all samples shows the classical Maltese cross patterns. Using a red tint plate, the colors of the first and third quadrant of the spherulites indicate a negative sign (i.e., the tangential refractive index is longer than the radial one).

The isothermal crystallization temperature values were chosen, so that for each group of materials, a constant apparent supercooling was applied (see experimental section). In the case of PBS and PBS-rich copolymers, a supercooling of 40 °C was applied. In the case of PCL and PCL rich copolymers, in view of the intrinsically higher nucleation density of PCL as compared to PBS, a lower supercooling degree had to be employed (i.e., 20 °C), otherwise, the nucleation density was so high, that the spherulitic size was too small in most of the PCL-rich samples.

Figure 4.8 shows that both spherulitic texture and nucleation density are affected by copolymerization. In Figure 4.8a, increasing the amount of PCL in the BS-rich copolymers leads to an increase in nucleation density and a reduction in spherulitic size. In obvious contrast, in Figure 4.8b, increasing the amount of PBS in the copolymer causes a reduction in nucleation density and hence an increase in spherulitic size. Therefore, composition can dramatically influence the superstructure of the copolymers, a factor that could be potentially interesting, as it can influence the mechanical properties of the samples. In a previous study of PBS/PCL blends, the individual spherulitic morphology of each phase remains unaltered, while their size depended on composition, as the blends are reported to be immiscible [17].

Figure 4.8 also shows that the spherulitic growth rate in the homopolymers (at constant supercooling) is much faster (as judged by the time needed for spherulite

impingement, given in the inner legend above each micrograph in Figure 4.8) than in the copolymers. As these copolymers are isodimorphic, only a small amount of the second comonomer is incorporated inside the unit cell of the crystallizing phase. In Figure 4.8, the crystallization temperatures chosen for PBS and PBS rich copolymers are so high, that only PBS spherulites (in the homopolymer) or PBS rich spherulites (in the copolymers) are formed. The majority of the PCL phase is amorphous at such high temperatures (except for those few PCL comonomer units that co-crystallized with PBS segments in the co-crystals formed in the copolymers) and lies in the interlamellar regions of the formed spherulites. A similar situation occurs as far as PCL rich copolymers are concerned. According to Figure 4.8, the incorporation of the comonomer units has important consequences for both the nucleation and the growth of the majority phase spherulites.

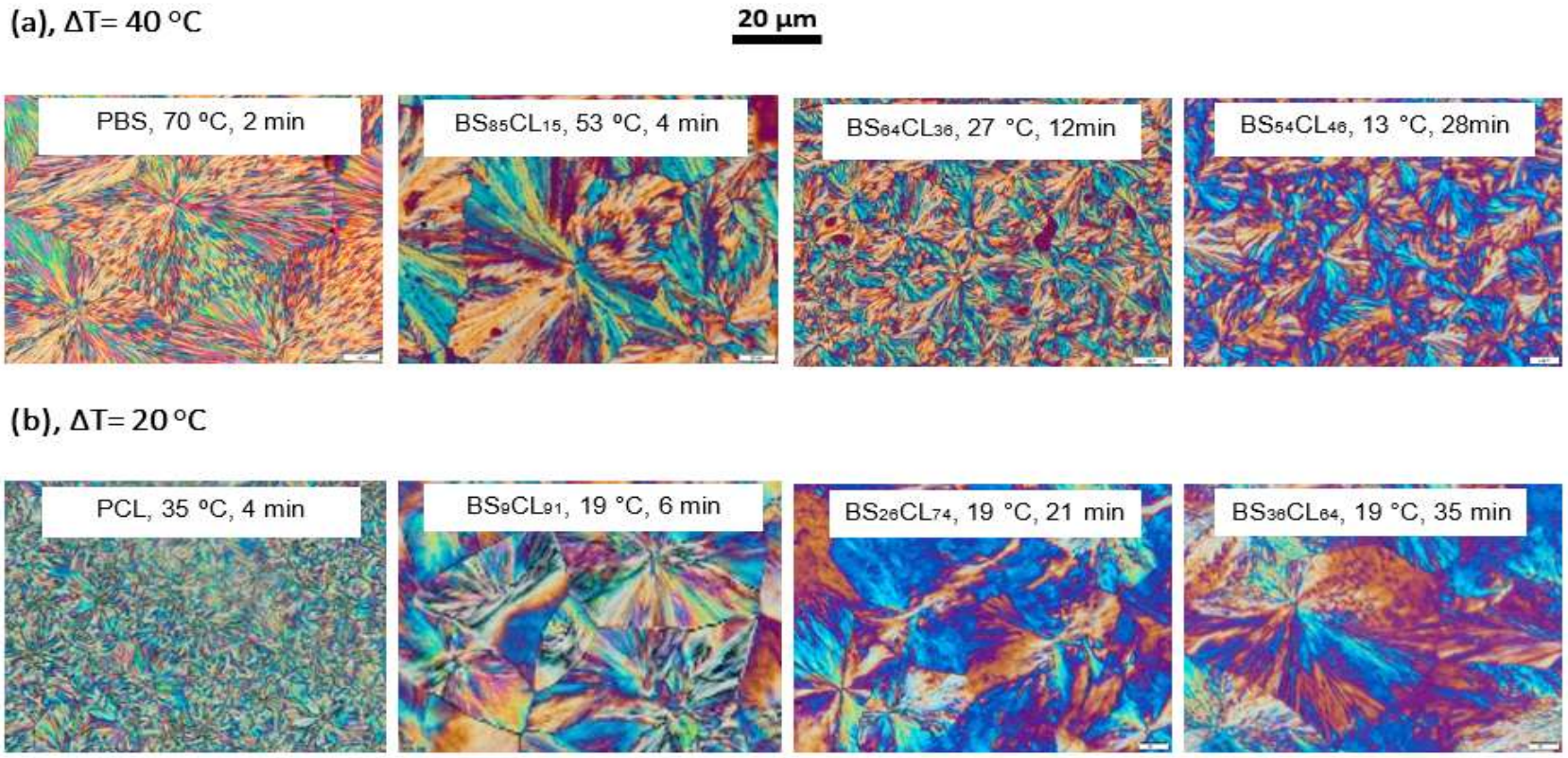


***Figure 4.8.*** *Polarized optical micrographs of LMw-$BS_xCL_y$ copolymers with different compositions, after isothermal crystallization at the indicated temperatures and times.*

### 4.2.7. Wide Angle X-ray scattering (WAXS)

For the WAXS study, the LMw-$BS_xCL_y$ samples were cooled down to -60 °C at a rate of 10 °C/min to promote crystallization, and afterward they were heated up to 25 °C at a rate of 20 °C/min. The WAXS patterns were registered at -60 °C and 25 °C and they are comparatively shown in Figures 4.9a and 4.9b, respectively. All the reflections and the calculated *d* values are collected in a table included in Table Apnx.4.1.

The WAXS diffractogram registered for PBS is consistent with the most common α form of PBS, whose monoclinic unit cell dimensions are: *a* = 5.23 Å, *b* = 9.08−9.12 Å, *c* = 10.79−10.90 Å and and *β*= 123.87°. Three distinct diffraction peaks are observable for PBS at 4.53, 4.05, and 3.92 Å, which are indexed as (020), (021) and (110)[18-19], as shown in Figure 4.9. Neat PCL shows peaks attributed to its orthorhombic unit cell [20]: *a* = 7.48 Å, *b* = 4.98 Å, and *c* = 17.26 Å. The most intense reflections (4.16, 4.04, and 3.74 Å) for PCL can be assigned to (110), (111), and (200) [21-23] planes, respectively. In the WAXS patterns at -60 °C (see Figure 4.9a), samples with more than 60 mol% BS display distinctive PBS reflections and samples with more than 60 mol% CL show PCL reflections. Only the samples in the pseudo-eutectic region (e.g., $BS_{54}CL_{46}$ in this case) display reflections of both combined crystal types, and some PCL reflections are overlapped with PBS reflections.

As it could be expected from DSC results, WAXS patterns depicted in Figure 4.9b indicate that some copolyester samples are amorphous at 25 °C because their $T_m$ values are below such temperature (see Figure 4.7a). The samples with more than 54 mol% of BS only display reflections attributable to the PBS unit cell, whereas $BS_9CL_{91}$ exhibits the characteristic scattering of neat PCL. The WAXS profile measured at 25 °C for $BS_{26}CL_{74}$ shows a couple of weak reflections that are characteristic of PCL revealing that this copolyester contains a small amount of PCL-rich crystalline phase at this temperature.

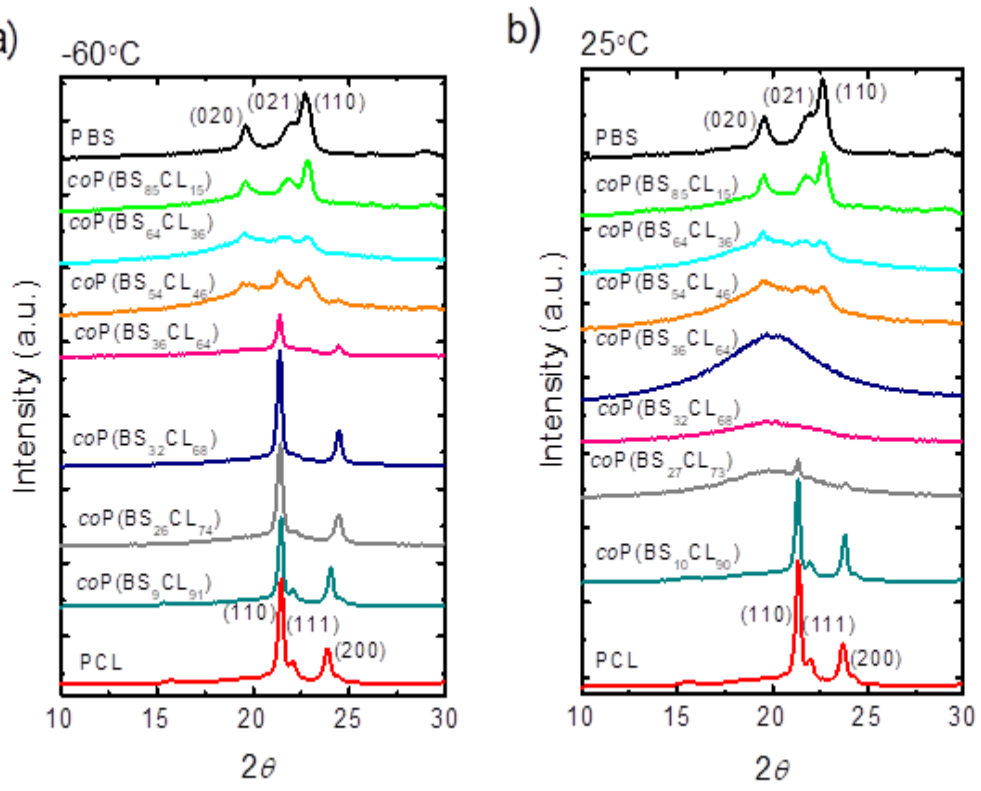


***Figure 4.9**. Powder WAXS diffraction patterns of LMw-$BS_xCL_y$ registered at -60 °C (a) and 25 °C (b). The profiles produced by the homopolyesters PBS and PCL are included for comparison.*

The *d*-spacings observed in the WAXS profiles registered at -60 °C versus CL content are plotted in Figure 4.10. We have chosen -60 °C, as at this temperature all samples were able to crystallize during the previous cooling (at 10 °C/min) from the melt. At -60 °C, *d*-spacings for PBS-rich samples arising from (020) planes, as well as those for PCL-rich copolymers corresponding to (200) planes, display an increasing trend with the content in CL-units. These increases correspond to changes in unit cell sizes that can be attributed to the limited incorporation of comonomer units. The changes in *d* values shown in Figure 4.10 are very small, indicating that the degree of comonomer inclusion in each phase is also limited. The degree of comonomer inclusion is a function of how the two repeating units resemble each

other chemically and in size. In view of the differences in chemical repeat units between PBS and PCL (see Scheme 4.1), it is remarkable that a certain degree of isodimorphism can take place in their random copolymers.

Three pieces of evidences are gathered here that are consistent with some degree of isodimorphism:

(1) The fact that all copolymers are capable of crystallization regardless of their composition.

(2) The trend exhibited by the melting point as a function of composition, which displays a clear pseudo-eutectic behavior.

(3) A small dependence of unit cell parameters with copolymer composition.

## 4.3. CONCLUSIONS

For the first time, potentially biobased and biodegradable LMw-PBS-*ran*-PCL random copolymers have been synthesized employing organocatalysis (enzymatic ring opening polymerization). The random microstructure of the copolymers was demonstrated by NMR. The copolymers are capable of displaying spherulitic superstructures whose nucleation and growth rate depend on copolymer composition, according to polarized optical microscopy observations.

The copolymers were able to crystallize in the entire composition range, their calorimetric properties exhibited a well-defined pseudo-eutectic region, and WAXS measurements demonstrated that small shifts of unit cell parameters occur as a result of minor comonomer inclusion. Therefore, we conclude that the copolymers are isodimorphic. Additionally, the compositions within the pseudo-eutectic region were found to be double crystalline with both PBS-rich and PCL-rich crystalline phases coexisting with a mixed amorphous phase.

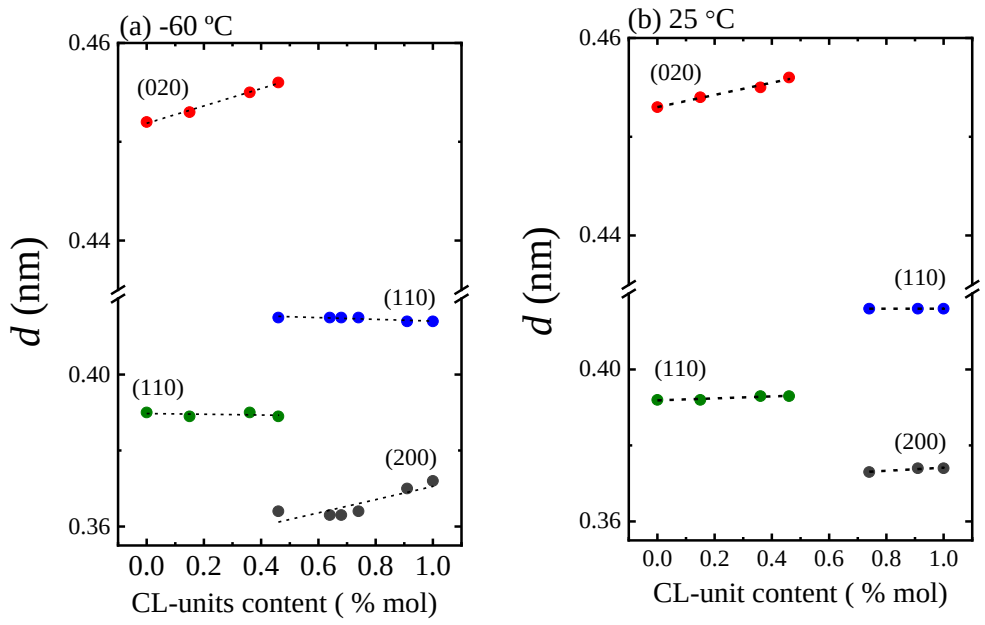


***Figure 4.10**. Plot of the most characteristic Bragg spacings observed by WAXS of LMw-$BS_xCL_y$ registered at -60 °C (a) and 25 °C (b). Indexing has been made on the basis of the monoclinic and rhombic unit cells respectively reported for PBS and PCL.*

## 4.4. REFERENCES

1. Lendlein, A.; Sisson, A., *Handbook of biodegradable polymers: isolation, synthesis, characterization and applications*. John Wiley & Sons: 2011.

2. Woodruff, M. A.; Hutmacher, D. W., The return of a forgotten polymer—Polycaprolactone in the 21st century. *Progress in polymer science* **2010,** *35* (10), 1217-1256.

3. Gigli, M.; Fabbri, M.; Lotti, N.; Gamberini, R.; Rimini, B.; Munari, A., Poly (butylene succinate)-based polyesters for biomedical applications: A review. *European Polymer Journal* **2016,** *75*, 431-460.

4. Qiu, Z.; Komura, M.; Ikehara, T.; Nishi, T., Miscibility and crystallization behavior of biodegradable blends of two aliphatic polyesters. Poly (butylene succinate) and poly (ε-caprolactone). *Polymer* **2003,** *44* (25), 7749-7756.

5. Cao, A.; Okamura, T.; Ishiguro, C.; Nakayama, K.; Inoue, Y.; Masuda, T., Studies on syntheses and physical characterization of biodegradable aliphatic poly (butylene succinate-co-ε-caprolactone) s. *Polymer* **2002,** *43* (3), 671-679.

6. Zheng, L.; Li, C.; Wang, Z.; Wang, J.; Xiao, Y.; Zhang, D.; Guan, G., Novel biodegradable and double crystalline multiblock copolymers comprising of poly (butylene succinate) and poly (ε-caprolactone): synthesis, characterization, and properties. *Industrial & Engineering Chemistry Research* **2012,** *51* (21), 7264-7272.

7. Liu, Q.; Zhou, X.-M., Preparation of Poly (butylene succinate)/poly (ϵ-caprolactone) Blends Compatibilized With Poly (butylene succinate-co-ϵ-caprolactone) Copolymer. *Journal of Macromolecular Science, Part A* **2015,** *52* (8), 625-629.

8. Bechthold, I.; Bretz, K.; Kabasci, S.; Kopitzky, R.; Springer, A., Succinic acid: a new platform chemical for biobased polymers from renewable resources. *Chemical Engineering & Technology: Industrial Chemistry-Plant Equipment-Process Engineering-Biotechnology* **2008,** *31* (5), 647-654.

9. Buntara, T.; Noel, S.; Phua, P. H.; Melián-Cabrera, I.; de Vries, J. G.; Heeres, H. J., Caprolactam from renewable resources: catalytic conversion of 5-hydroxymethylfurfural into caprolactone. *Angewandte Chemie International Edition* **2011,** *50* (31), 7083-7087.

10. Xu, J.; Guo, B. H., Poly (butylene succinate) and its copolymers: research, development and industrialization. *Biotechnology journal* **2010,** *5* (11), 1149-1163.

11. Sugihara, S.; Toshima, K.; Matsumura, S., New Strategy for Enzymatic Synthesis of High-Molecular-Weight Poly (butylene succinate) via Cyclic Oligomers. *Macromolecular rapid communications* **2006,** *27* (3), 203-207.

12. Kondo, A.; Sugihara, S.; Kuwahara, M.; Toshima, K.; Matsumura, S., Lipase-Catalyzed Ring-Opening Polymerization of Molecularly Pure Cyclic Oligomers for Use in Synthesis and Chemical Recycling of Aliphatic Polyesters. *Macromolecular bioscience* **2008,** *8* (6), 533-539.

13. Giammanco, G.; Martínez de Ilarduya, A.; Alla, A.; Muñoz-Guerra, S., Hydrolyzable aromatic copolyesters of p-dioxanone. *Biomacromolecules* **2010,** *11* (9), 2512-2520.

14. Yu, Y.; Sang, L.; Wei, Z.; Leng, X.; Li, Y., Unique isodimorphism and isomorphism behaviors of even-odd poly (hexamethylene dicarboxylate) aliphatic copolyesters. *Polymer* **2017,** *115*, 106-117.

15. Adeniyi, A.; Agboola, O.; Sadiku, E. R.; Durowoju, M.; Olubambi, P.; Reddy, A. B.; Ibrahim, I.; Kupolati, W., Thermoplastic-Thermoset Nanostructured Polymer Blends. In *Design and Applications of Nanostructured Polymer Blends and Nanocomposite Systems*, Elsevier: 2016; pp 15-38.

16. Guan, Y.; Liu, G.; Gao, P.; Li, L.; Ding, G.; Wang, D., Manipulating crystal orientation of poly (ethylene oxide) by nanopores. *ACS Macro Letters* **2013,** *2* (3), 181-184.

17. Can, E.; Bucak, S.; Kınacı, E.; Çalıkoğlu, A. C.; Köse, G. T., Polybutylene Succinate (PBS)–Polycaprolactone (PCL) Blends Compatibilized with Poly (ethylene oxide)-block-poly (propylene oxide)-block-poly (ethylene oxide)(PEO-PPO-PEO) Copolymer for Biomaterial Applications. *Polymer-Plastics Technology and Engineering* **2014,** *53* (11), 1178-1193.

18. Ichikawa, Y.; Suzuki, J.; Washiyama, J.; Moteki, Y.; Noguchi, K.; Okuyama, K., Strain-induced crystal modification in poly (tetramethylene succinate). *Polymer* **1994,** *35* (15), 3338-3339.

19. Wang, X.; Zhou, J.; Li, L., Multiple melting behavior of poly (butylene succinate). *European polymer journal* **2007,** *43* (8), 3163-3170.

20. Gan, Z.; Abe, H.; Kurokawa, H.; Doi, Y., Solid-state microstructures, thermal properties, and crystallization of biodegradable poly (butylene succinate)(PBS) and its copolyesters. *Biomacromolecules* **2001,** *2* (2), 605-613.

21. Hu, H.; Dorset, D. L., Crystal structure of poly (iε-caprolactone). *Macromolecules* **1990,** *23* (21), 4604-4607.

22. Kołbuk, D.; Sajkiewicz, P.; Maniura-Weber, K.; Fortunato, G., Structure and morphology of electrospun polycaprolactone/gelatine nanofibres. *European Polymer Journal* **2013,** *49* (8), 2052-2061.

23. Bittiger, H.; Marchessault, R.; Niegisch, W., Crystal structure of poly-ε-caprolactone. *Acta Crystallographica Section B: Structural Crystallography and Crystal Chemistry* **1970,** *26* (12), 1923-1927.

# *Chapter V:*

# *Tuning the Thermal Properties and Morphology of PBS-ran-PCL Copolyesters by Changing Composition, Molecular Weight, and Thermal History*

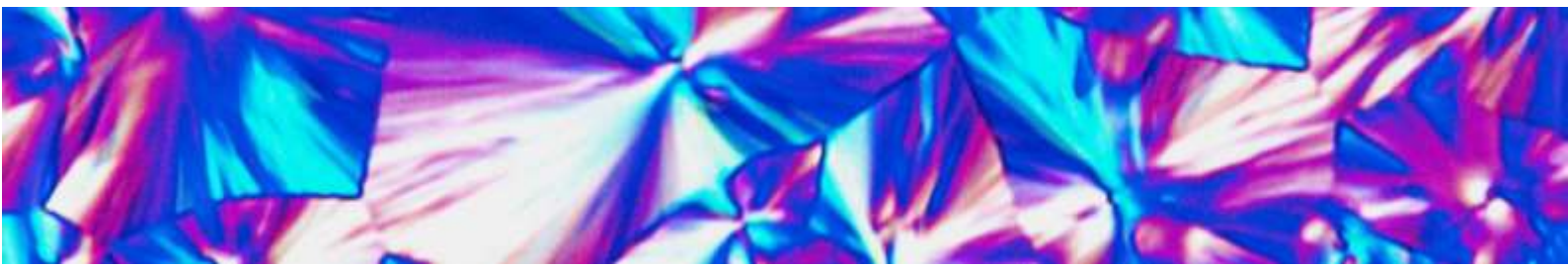

# Table of Contents

## Abstract

High molecular weight poly((butylene succinate)-*ran*-*ε*-caprolactone) copolyesters (HMw-PBS-*ran*-PCL) were synthesized in a wide composition range and compared with significantly lower molecular weight samples synthesized previously. DSC and WAXS showed that these copolyesters are isodimorphic (i.e., each crystalline phase contains a small amount of the second comonomer) as they able to crystallize in the entire composition range, display a pseudo-eutectic point, and their unit cell dimensions are a function of composition. Copolymers close or away from the pseudo-eutectic point exhibited a single crystalline phase, i.e., PBS-rich or PCL-rich crystalline phase. At the pseudo-eutectic point, both phases are able to crystallize in double crystalline banded spherulites, as demonstrated by Polarized Light Optical Microscopy (PLOM) studies.

An increase in molecular weight of the copolyester does not influence $T_m$ and $T_c$ significantly, as their values are determined by the randomness of the comonomer distribution that controls the long period values. However, crystallinity values are higher for lower $M_w$ copolymers because of their faster crystallization rate. Copolymers with higher $M_w$ exhibited higher $T_g$ values as expected for random copolymers that are characterized by a single phase in the amorphous regions. Therefore, changing composition and molecular weight, a remarkable separate control over $T_g$ and $T_m$ values can be achieved in these copolyesters. SAXS results revealed that the lamellar thickness $l_c$ decreases with composition at each side of the eutectic point, as comonomer exclusion limits the length of crystallizable sequences.

At the pseudo-eutectic copolyester composition, the cooling rate determines if one or two crystalline phases can develop: only PCL-rich crystalline phase, only PBS-crystalline phase or both crystalline phases. This behavior was studied in detail by DSC, *in situ* WAXS/SAXS and PLOM. Our studies demonstrate that these biodegradable copolymers are versatile materials, whose properties can

be tuned by composition, molecular weight and thermal history to better target specific applications.

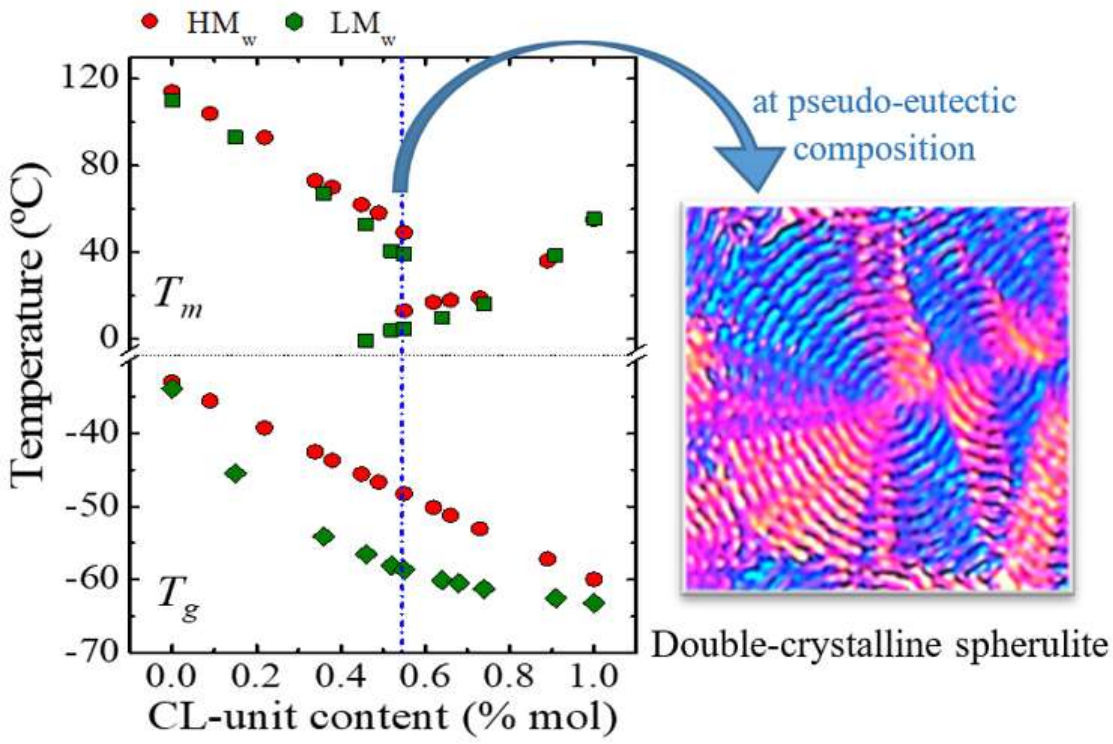

## 5.1. INTRODUCTION

Crystallizable random copolymers display a wide variety of properties depending on the chemical structure of the two comonomeric units and their composition. Considering two potentially crystallizable components, three different cases are possible, which have been recently reviewed [1].

The first case is that of total comonomer inclusion inside the crystal unit cell, or co-crystallization in the entire composition range. A plot of melting temperature versus composition yields a straight line that follows a simple rule of mixtures. These copolymers are denoted as isomorphic [2-3]. In the case of copolyesters, very few cases of isomorphism have been reported [4-7], and they occur when the chemical structure of both comonomers are very similar.

The second case occurs when the chemical structure of the two constituent comonomers differ more than in the previous case. A competition between exclusion and inclusion (inside the crystal lattice) of the minor comonomer component with respect to the major comonomer component is established during crystallization. But in these copolymers, there is always a small amount of inclusion of the second comonomer within the crystal unit cell of the majority comonomer.

As a result, the copolymers crystallize in the entire composition range and are classified as isodimorphic. This means that two crystalline phases are formed with crystal structures that resemble those of the parent homopolymers. When the melting temperature is plotted as a function of composition, a pseudo-eutectic point is observed. To each side of the eutectic, only one crystalline phase is formed, that is rich in the major component with limited inclusion of the second comonomer. We have recently found that at the eutectic point, two crystalline phases can co-exist depending on the thermal history, with crystalline unit cells resembling those of the parent homopolymers.[1] Several isodimorphic random copolyesters have been recently studied [8-18].

The third and final case is that of total exclusion of the minor comonomeric units and it is the most frequently reported case, when the chemical structures of the comonomers are very different from one another. For random copolyesters, this behavior has been reported by Soccio et al. in poly(propylene isophthalate-*ran*-propylene succinate)[19] and poly(propylene isophthalate-*ran*-propylene adipate) [20].

Aliphatic biodegradable polyesters, such as poly (butylene succinate) (PBS) and poly (ε-caprolactone) (PCL) have received much attention since they are potentially biodegradable and may contribute to reduce environmental pollution caused by plastic waste.[21-22] The combination of PCL and PBS as random or block copolyesters, has been used to design new materials with improved behavior and performance.[23-24] The mechanical and functional properties of semicrystalline polymers depend on structural and morphological features that are controlled by their molecular weight and crystallization conditions during processing [25-26]. To enhance product performance of random copolyesters for specific applications, it is essential to know in detail how the molecular weight and composition influence their main properties.

Recently, we synthesized poly[(butylene succinate)-ran-*ε*-caprolactone]cs (PBS-*ran*-PCL) by enzymatic ring opening polymerization. The copolyesters obtained had low molecular weights (in most cases the weight average molecular weight was lower than 6000 g/mol), but they displayed a remarkable isodimorphic behavior. [27] In this work, higher molecular weight poly (butylene succinate-*ran*-caprolactone)s (PBS-*ran*-PCL) copolyesters were prepared in a wide composition range by changing the synthetic strategy to a direct transesterification/ROP and polycondensation route. A detailed comparison between the results obtained with the presently synthesized high molecular weight copolyesters (denoted $HM_w$ $BS_xCL_y$, where x and y are the molar % of BS and CL units respectively) and our previous series of copolyesters with lower molecular weight (denoted $LM_w$ $BS_xCL_y$) [27] is presented.

Cao *et al.* [28] also prepared PBS-*ran*-PCL copolymers with a similar synthetic approach. However, to the best of our knowledge, this is the first time that the non-isothermal crystallization and thermal transitions of these copolymers have been studied as a function of molecular weight. In the current investigation, non-isothermal crystallization of $HM_w$ $BS_xCL_y$ and their parent homopolymers are studied by means of polarized light optical microscopy (PLOM), differential scanning calorimetry (DSC), *in situ* simultaneous synchrotron wide angle X-ray scattering (WAXS) and small angle X-ray scattering (SAXS). We investigate the role of molecular weight and composition on the thermal properties, structure and crystallization of these random copolyesters. Additionally, we have found remarkable results at the pseudo-eutectic composition by varying the cooling rate from the melt, so that the formation of one or two crystalline phases can be controlled.

## 5.2. RESULTS

### 5.2.1. Nuclear Magnetic Resonance (NMR) and GPC

Table 3.2 in chapter 3 shows molecular weight and microstructural data for the synthesized copolyesters in the presence of TTP catalyst. The microstructure of the prepared copolyesters is essentially random as judged by the triads contents and R values given in Table 3.2. NMR results confirm the chemical structure of copolyesters. $^{1}H$ and $^{13}C$ NMR spectra, of the $BS_{51}CL_{49}$ copolyester are shown in Figure 5.1 and the spectra of the entire series are compared in Figure 5.2.

The weight average molecular weights ($M_w$) of the $HM_w$-$BS_xCL_y$ copolyesters are in the range 17000- 30000 g/mol with dispersities ($Đ$) between 2.2 and 3.2. Overall, the $M_w$ of $HM_w$-$BS_xCL_y$ copolyesters are approximately four times higher than most of the similar copolyesters previously synthesized by enzymatic (CALB) ROP copolymerization ($LM_w$-$BS_xCL_y$) in our previous work [27].

The composition of $\varepsilon$-caprolactone repeating unit present in $BS_xCL_y$ was estimated from methylene proton resonance integrals of $CH_2$ (1) and $CH_2$ (4).

Moreover, the sequence distributions of BS and CL repeating units were calculated based on $^{13}C$ NMR signals of the methylene group $CH_2$ (b) in Figure 5.1.

### 5.2.2. Thermal behavior

Differential Scanning Calorimetry (DSC) experiments were performed using a Perkin Elmer 8500 calorimeter equipped with a refrigerated cooling system Intracooler 2P, under a nitrogen atmosphere flow of 20 ml/min and calibrated with high purity indium and tin standards. Samples crystallization experiments were hermetically sealed in standard aluminum pans and tested according to the following protocol: Samples were heated from room temperature to 30 °C above their melting temperature ($T_m$) and held at this temperature for 3 min to erase thermal history. They were then cooled to -60°C and reheated again to 30 °C above their $T_m$. Measurements were done at two different scan rates, 20 °C/min and 10 °C/min, with the purpose of evaluating the scan rate effect on melting and crystallization behavior. The melting temperature $T_m$ was determined from the second scan as the temperature of the main peak in the DSC curves.

The thermal behavior of the samples was explored by non-isothermal DSC experiments. The samples were first heated to a temperature high enough to erase their thermal history, and then they were cooled at 10 °C/min. After this controlled cooling, their melting behavior was recorded in the DSC second heating scans shown in Figure 5.3a. The previous cooling runs as well as the calorimetric data derived from all the DSC non-isothermal runs can be found in the Appendix (see Figure Apnx 5.1 and Tables Apnx 5.1 and 5.2).

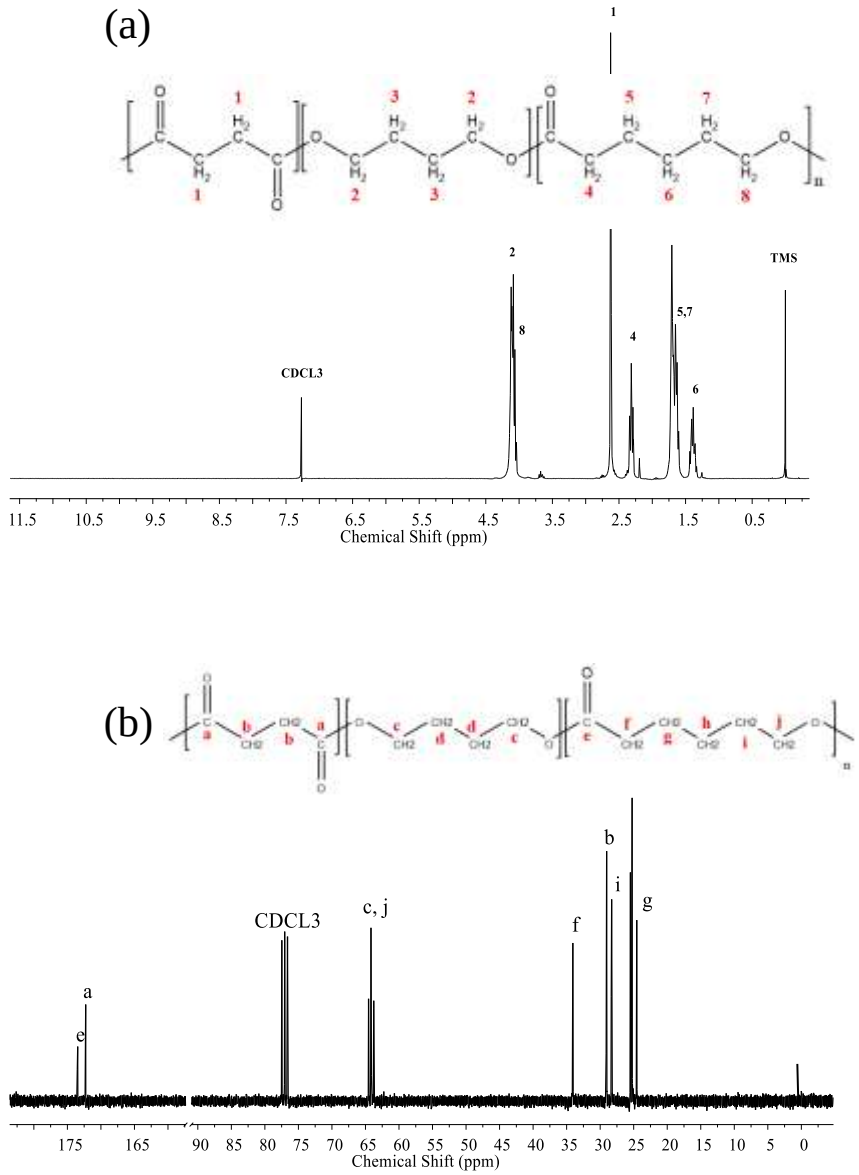


***Figure 5.1***. *$^{1}H$ (a) and $^{13}C$ (b) NMR spectra of $BS_{51}CL_{49}$ as representative of the $BS_xCL_y$ copolyesters series recorded in $CDCl_3$. Peaks were assigned according to the expected copolyester constitution depicted in the attached formula.*

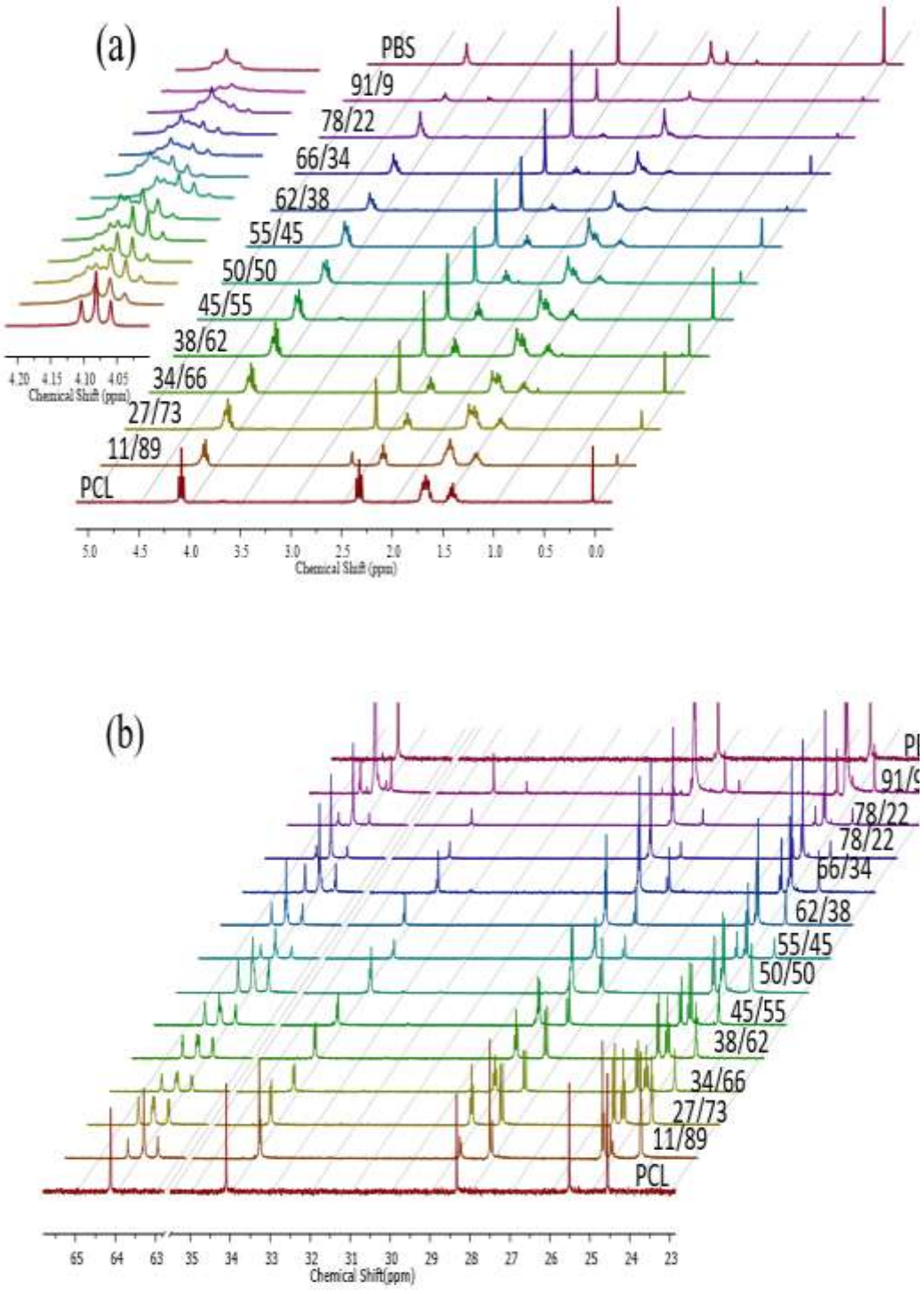


***Figure 5.2****. Comparison $^{1}H$ (a) and $^{13}C$ (b) NMR spectra of all copolyesters series.*

Figure 5.3a shows that these random copolymers are able to crystallize in the entire composition range, even for compositions close to equimolarity. As demonstrated by NMR, the copolymers are random (see Table 1, values of R=1 indicate complete randomness). Only isomorphic or isodimorphic random copolymers can crystallize in the entire composition range. However, Figure 5.3b illustrates that the melting point follows a pseudo-eutectic trend with composition indicating that the $HM_w$ PBS-*ran*-PCL copolymers are isodimorphic.[1, 3] In the $HM_w$ $BS_{45}CL_{55}$ sample, there are two melting temperatures and two crystallization temperatures indicating the presence of two crystalline phases at the eutectic point, i.e., a PCL-rich and a PBS-rich crystalline phases.

Figure 5.3b also illustrates the tremendous versatility of these random copolyesters. Thanks to their isodimorphic character, their melting point can be tailored by changing composition with a variation of 100 °C.

In isodimorphic copolymers, the comonomer that constitutes the major phase typically crystallizes with the unit cell of its corresponding homopolymer, but including a small number of comonomer units of the minor second component within the crystal lattice. There is always a competition between comonomer exclusion and comonomer inclusion in isodimorphic copolymers. Their behavior is typically dominated by a higher amount of comonomer exclusion but comonomer inclusion is indispensable for crystallization in the entire composition range.

According to WAXS results (see Figure 5.3c), to the left side of the pseudo-eutectic point, only PBS-like crystals are formed and to the right side of this point, only PCL-like crystals are found. The indexation of the WAXS patterns can be found in the Appendix along with WAXS data taken at different temperatures (see Table Apnx 5.3 and Table Apnx 5.3 and table apnx 5.4). In HMw-$BS_xCL_y$ copolymers, for the composition that corresponds to the eutectic point ($BS_{45}CL_{55}$), two crystalline phases (PBS-rich crystalline phase and PCL-rich crystalline phase) were found that correspond to those observed by DSC (See Figure A.5.1 and Table A.5.1).

The *d*-spacings observed in the WAXS profiles registered at -60 °C versus CL unit content are plotted in Figure 5.3d. At -60 °C, *d*-spacings for PBS-rich crystalline phases arising from (020) and (110) planes, as well as those for PCL-rich crystalline phases corresponding to (110) planes, display an increasing trend with comonomer content. These increases correspond to changes in unit cell sizes that reflect a certain degree of comonomer inclusion that takes place within the crystal unit cells of the corresponding crystal phases of these random copolymers. The *d*-spacings observed in the WAXS profiles registered versus CL-unit content at -60 °C and 25 °C are compared in Figure Apendix 5.3.

The results presented in Figure 5.3 are fully consistent with the isodimorphic character of the HMw-PBS-*ran*-PCL copolymers. These results are qualitatively similar to those obtained previously by us with LMw-PCL-*ran*-PBS copolymers.[27] The specific differences observed between low and high $M_w$ copolymers are discussed in the next section.

## 5.2.2. PLOM

We studied the effect of copolymer composition on the spherulitic texture of HMw-PCL-*ran*-PBS copolyesters. Figure 5.4 shows PLOM micrographs during non-isothermal crystallization, after spherulites had impinged on each other for HMw copolymers. The incorporation of comonomer units has a strong impact on nucleation of the majority phase spherulites. Increasing the amount of comonomer unit content leads to the formation of a higher concentration of spherulites with smaller sizes, indicating an increase in nucleation density. These results are very similar to those obtained previously with LMw- $\mathrm{BS_xCL_y}$. [27] In both cases, adding comonomer enhances nucleation density during non-isothermal crystallization, thereby decreasing spherulitic size.

HMw-$BS_{45}CL_{55}$ is a random copolymer whose composition corresponds to the pseudo-eutectic point. This is the only copolymer from those HMw random copolyesters prepared in this work that exhibited a double crystalline morphology.

We have previously found that only those copolymers at the pseudo-eutectic point or pseudo-eutectic region are able to exhibit double crystallization. [1, 16, 27, 29]

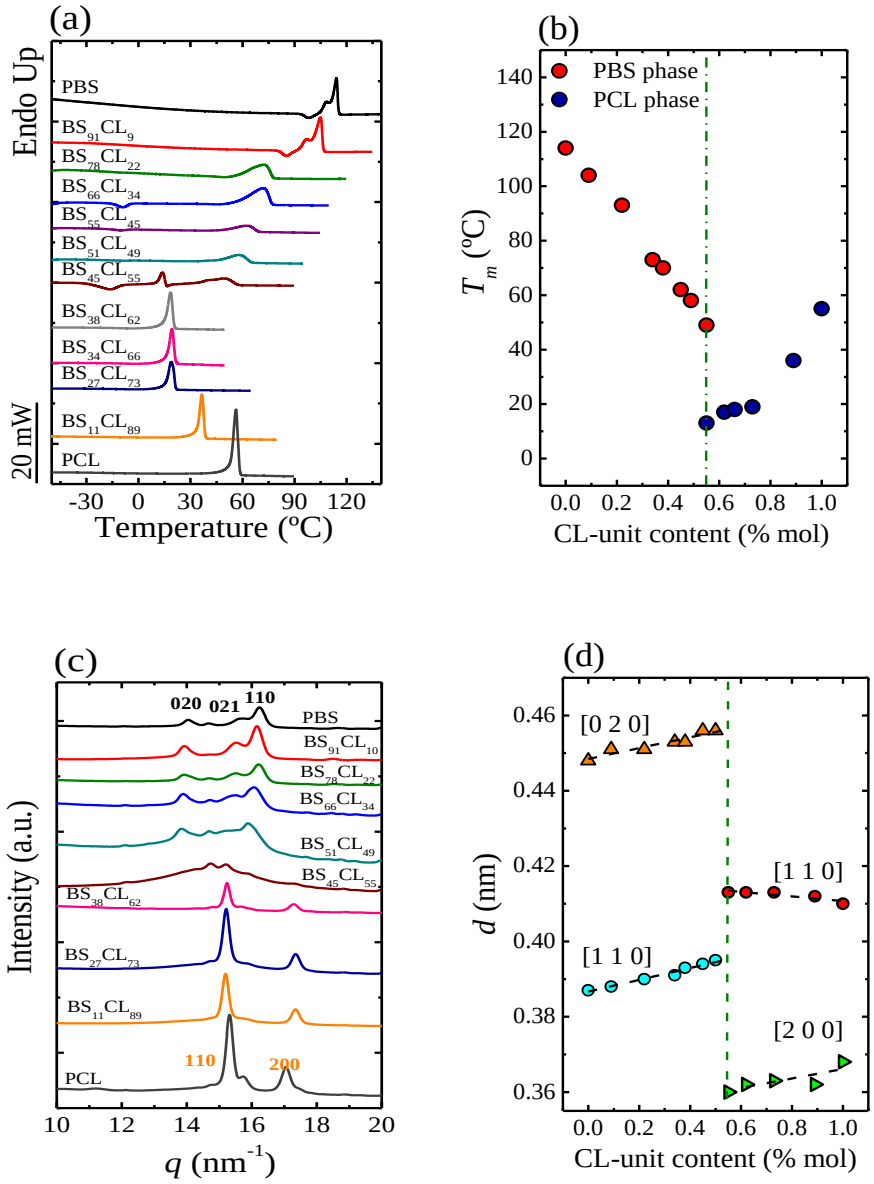


***Figure 5.3.*** *(a) DSC second heating runs at 10 °C/min for the indicated samples. (b) Peak melting temperature as a function of composition, the dashed vertical line indicates the pseudo-eutectic composition. (c) WAXS diffraction patterns taken at -60 °C after cooling from the melt at 10 °C/min. (d) d-spacings obtained from the WAXS results presented in (c) as a function of composition.*

Figure 5.5a shows PBS-rich spherulites after the $HM_w$-$BS_{45}CL_{55}$ sample was cooled from the melt and held at 20 °C for 2h. At this temperature, the PCL-rich crystals are in the melt (see Figure 5.5a and 5.5b), and negative ring banded PBS-rich spherulites fill the microscope field. Therefore, upon cooling from a single phase melt, the PBS-rich phase is the first to crystallize forming spherulitic templates. These impinging spherulites contain lamellar crystals of the PBS-rich phase with amorphous interlamellar regions of copolymer chains. A schematic diagram representing these spherulites is also included in Figure 5.3a, only the crystalline PBS-rich lamellae growing radially are represented.

Figure 5.5b shows the result of quenching the sample shown in Figure 5.3a from 20 °C down to -25 °C, a temperature at which the PCL-rich phase can crystallize within the intraspherulitic region of the PBS-rich phase (i.e., within the interlamellar regions of the spherulite). The crystallization of the PCL component can be observed in Figure 5.2b, as the birefringence increases in the sample and the spherulitic structures look brighter (compare the close up spherulite shown in Figure 5.5a, before PCL crystallization with that in Figure 5.4b, after PCL-rich crystals are formed).

The PBS-rich phase crystals templates the crystalline superstructural morphology (blue lamellae in schematic model of Figure 5.5a), and the PCL-rich crystals can only form upon cooling from the melt (see red inner lamellae in Figure 5.5b) inside the pre-formed templates. Hence, in Figure 5.5b we have examples of double crystalline spherulites. Similar double crystalline superstructures have been observed in PBS-*ran*-PBAz copolyester at the pseudo-eutectic composition [29] and in weakly segregated or melt mixed block copolymers [30-31].

Figure 5.5c shows the morphology after the sample was reheated up to 20 °C to melt the PCL-rich phase crystals. The field remains full with PBS-rich phase spherulites as expected since the molten PCL-rich phase is within the intraspherulitic regions of the PBS phase.

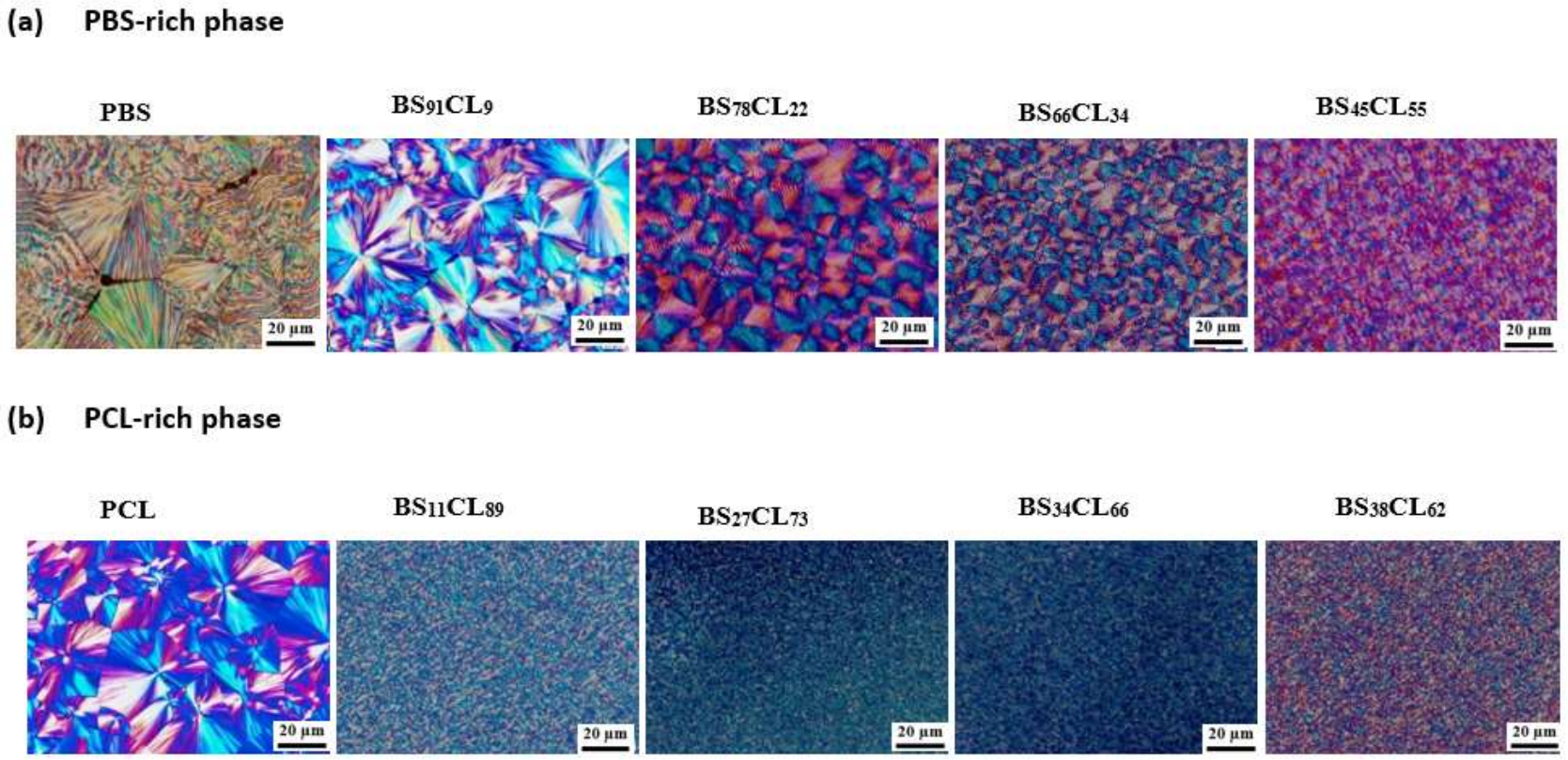


***Figure 5.4****. Polarized optical micrographs of* $HM_w$ $BS_xCL_y$ *during non-isothermal crystallization from the melt at 10 °C/min for PBS-rich phase (a) and PCL-rich phase (b). Pictures were taken when spherulites were fully impinged.*

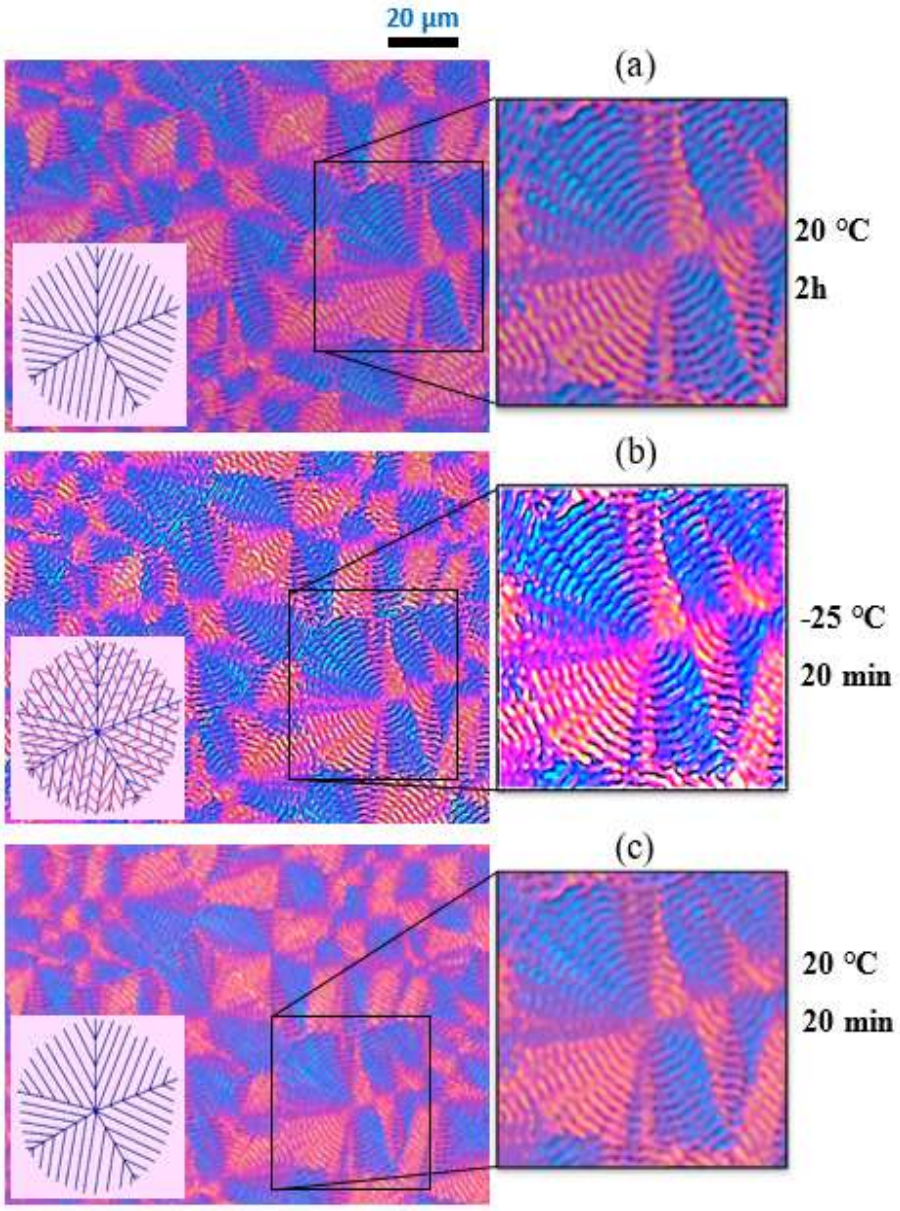


***Figure 5.5.*** *PLOM micrographs for HMw-$BS_{45}CL_{55}$ copolymer with schematic models: (a) the sample was cooled from the melt and held at 20 °C for 2h, (b) micrograph taken after the sample was quenched rapidly from 20 °C to -25 °C and held 20 min at -25 °C, and (c) sample was reheated to 20 °C. In the schematic models (bottom left hand side), the blue lines indicate PBS-rich lamellae while the red lines correspond to PCL-rich lamellae and the pink background indicates the amorphous regions of homogeneous mixtures of copolymer chains.*

### 5.2.3. Influence of molecular weight on crystallization and melting

In this work, only one of the prepared compositions fell within the eutectic point (i.e., HMw-$BS_{45}CL_{55}$), as signaled by the presence of two crystalline phases.[1] When the composition was changed to $BS_{38}CL_{62}$ (i.e., 7 molar % more CL units in the copolymer with respect to the eutectic composition), then only the PCL-rich crystalline phase was formed. On the other hand, when it was changed to $BS_{51}CL_{49}$ (i.e., 6 molar % less CL units than the eutectic composition) just the PBS-rich crystalline phase was formed, see Figure 5.3.

In the LMw-$BS_xCL_y$ case, three copolymers were inside the eutectic region ($BS_{45}CL_{55}$, $BS_{48}CL_{52}$, and $BS_{54}CL_{46}$) as for these copolyesters two characteristic crystallization and melting peaks were observed [27]. These three copolyesters span a CL composition range of 11 molar %. Therefore, lower molecular weights apparently cause a widening of the pseudo-eutectic region in these isodimorphic systems. However, more compositions would have to be prepared to confirm this trend.

A comparison between the non-isothermal crystallization and melting of both sets of samples can be observed in Figure 5.6. As it is well known, in homopolymers, $T_m$ values increase with chain length until they saturate at high molecular weights. Figure 5.6 clearly shows that in these random copolyesters, both $T_c$ and $T_m$ are not affected by the changes in molecular weight. This result can be explained as in random copolymers, the comonomeric content and its distribution can dominate the crystallizable sequence selection during crystallization [12, 32]. As both types of copolymers are nearly perfectly random, the size of the average crystallizable sequence is clearly much lower than the lowest $M_w$ copolymer chain length.

Figures 5.6c and 5.6d show how the enthalpy of crystallization and melting (normalized by the content of the crystallizable phase) depend on copolymer composition. Figure 5.6e plots the degree of crystallinity (obtained from the DSC

heating scans) as a function of composition. Two important observations can be made from these plots.

Firstly, the degree of crystallinity displays a pseudo-eutectic point when plotted as a function of composition. This is a consequence of the influence of comonomer exclusion during crystallization. As the amount of comonomer increases for a particular crystalline phase (either PBS-rich or PCL-rich crystalline phases), comonomer exclusion (which predominates over comonomer inclusion) interferes with crystallization, as the length of crystallizable sequences (which can include a limited number of the second comonomer units) decreases. As a consequence, the degree of crystallinity decreases when the minority comonomer content increases for any given crystalline phase.

Secondly, Figures 5.6c-5.6e show that the lower molecular weight samples can develop a higher degree of crystallinity than the higher molecular weight copolymers. This is due to their higher non-isothermal crystallization rate, which stems from the faster diffusion of smaller molecules.

The crystallinity of copolyesters has been determined by dividing the observed heat of fusion $\Delta H_m$ by the theoretical value for 100% crystalline polymer. The theoretical $\Delta H_m^0$ values for PBS and PCL are 110.3 and 139.5 J/g [33-34], respectively. The data for the copolymers plotted in Figure 5.6e show that the crystallinity levels are sensitive to molecular weight, as well as, to the copolymer composition.

### 5.2.4. Influence of molecular weight on $T_g$

Random copolymers form a single phase in the melt and in the amorphous state. They exhibit a single $T_g$ that depends on composition. Figure 5.7 shows how the $T_g$, in both copolymer groups (low and high molecular weight), is a strong function of composition and molecular weight. For both homopolymers and random copolymers, $T_g$ values increase with molecular weight until they saturate at a limiting molecular weight value. This trend is explained by the higher fraction of chain ends present in lower $M_w$ polymers that can increase the free volume. As the $M_w$ increases the effect of chain ends is diluted and it becomes negligible for very long chains [35].

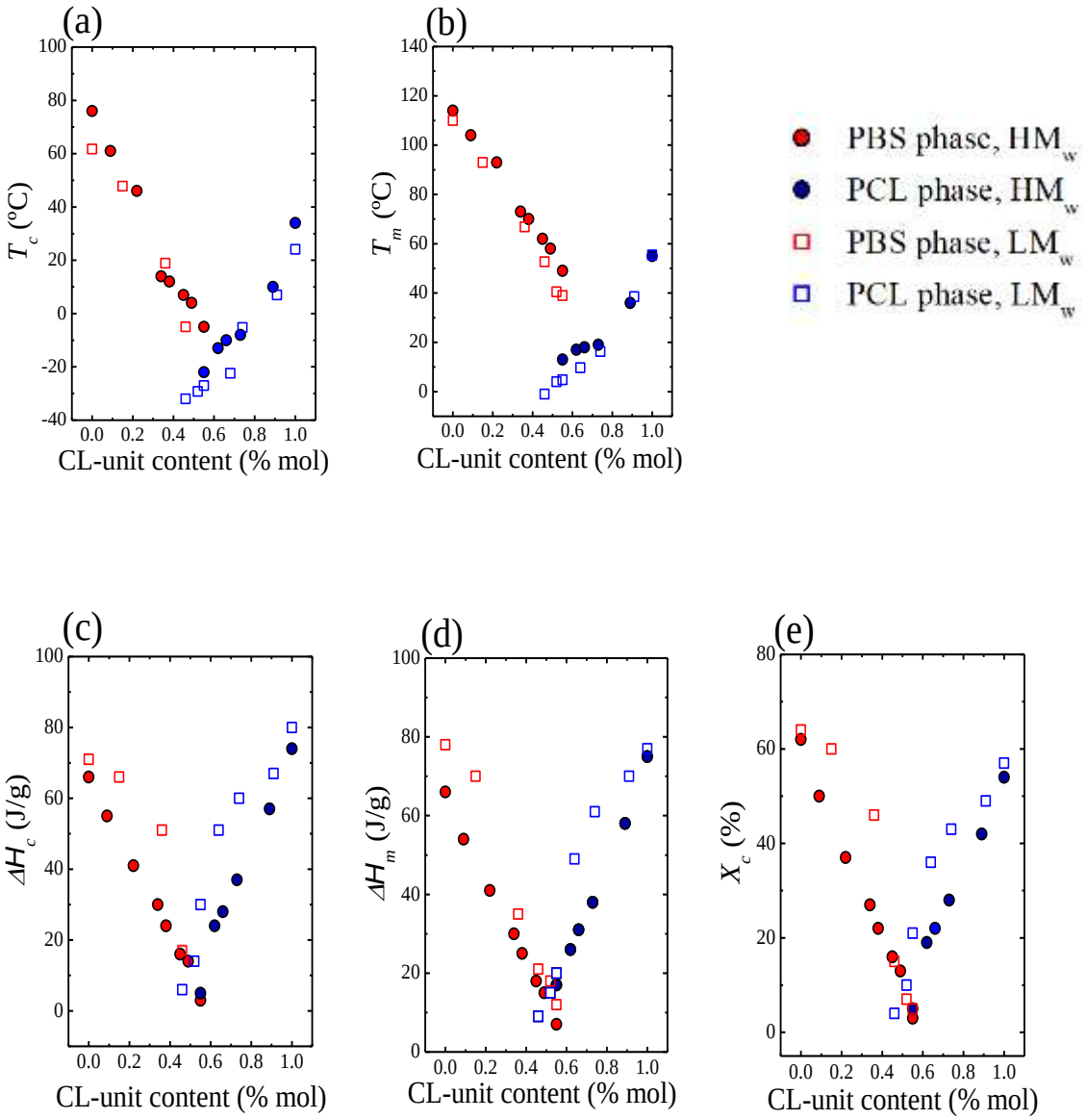


***Figure 5.6.*** *Composition dependence of (a) peak crystallization temperature $T_c$ (b), peak melting temperature $T_m$, (c) crystallization enthalpy $\Delta H_c$, (d) melting enthalpy $\Delta H_m$, and (e) crystallization degree $X_c$ of the indicated samples.*

In random copolyesters, $T_g$ is usually a monotonic function of composition that can be predicted by semi-empirical equations. In this work, the Gordon-Taylor equation (i.e., Equation 5.1), was found to adequately describe the experimental data for both types of samples ($LM_w$ and $HM_w$):

$$T_{g,copo} = \frac{w_1\, T_{g,1} + k(1-w_1)\, T_{g,2}}{w_1 + k(1-w_1)} \qquad \text{Eq.5.1}$$

where $T_{g,1}$ and $T_{g,2}$ are the glass transition temperature of the homopolyesters, $w_1$ the respective mass fraction of one of the components and $k$ the Gordon-Taylor parameter.

PBS and PCL homopolymers were used for comparison purposes only. In the case of PCL, the values of $M_w$ do not differ much (16.3 and 17.4 kg/mol) but their dispersities are quite different (2 and 3.2 for the low and high $M_w$ samples respectively). This may explain the differences in $T_g$ observed in Figure 5.7, as the PCL sample with a lower dispersity probably contains a higher density of chain ends.

In the case of PBS homopolymer, even though the differences in $M_w$ between the samples are larger than in the case of PCLs, the observed difference in $T_g$ is very small. We do not have an explanation for this result. It should be considered that as the crystallinity increases (the homopolymers have crystallinity degrees around 50%), determination of $T_g$ values by DSC become increasingly difficult, as the size of the change decreases, especially if a rigid amorphous phase develops in the material. Further studies would be needed that are outside the scope of the present investigation.

As shown in Figure 4, the Gordon-Taylor equation fits well the experimental data with $k$ = 0.62 for $HM_w$ samples and $k$ =0.23 for $LM_w$ samples. The term $k$ in Equation 5.1 is a parameter whose value depends on the change in thermal expansion coefficient ($\alpha$) of the components as they change from the glassy

(amorphous) to the liquid (rubbery) form, during the glass transition. Accordingly, $k = (V_2/V_1)(\Delta\alpha_2/\Delta\alpha_1)$[36], where $V$ represents the specific volume at the corresponding $T_g$. By the Simha-Boyer law [37] ($\Delta\alpha.T_g$ = constant) we obtain $k \approx (V_2T_{g1}/V_1T_{g2})$ [38]. As copolyesters with higher molecular weight show a higher $k$ value and $T_g$ of homopolymers are approximately similar in both $HM_w$ and $LM_w$, therefore the $V_{PCL}/V_{PBS}$ value for $HM_w$ should be higher than in $LM_w$ copolyesters. In other words, the rate of specific volume changes in PCL has been greater than PBS.

If a comparison is made between Figure 5.3b and Figure 5.6, a very interesting characteristic of isodimorphic random copolymers can be appreciated. These copolymers allow a separate control of $T_m$ and $T_g$, both as a function of composition and molecular weight. While in homopolymers both $T_m$ and $T_g$ follow similar empirical correlations as molecular weight increases, in isodimorphic copolymers $T_g$ is a function of $M_w$ while $T_m$ is independent of $M_w$, as long as the average length of the crystallizable sequences is smaller than the molecular weights of the random copolymers under consideration.

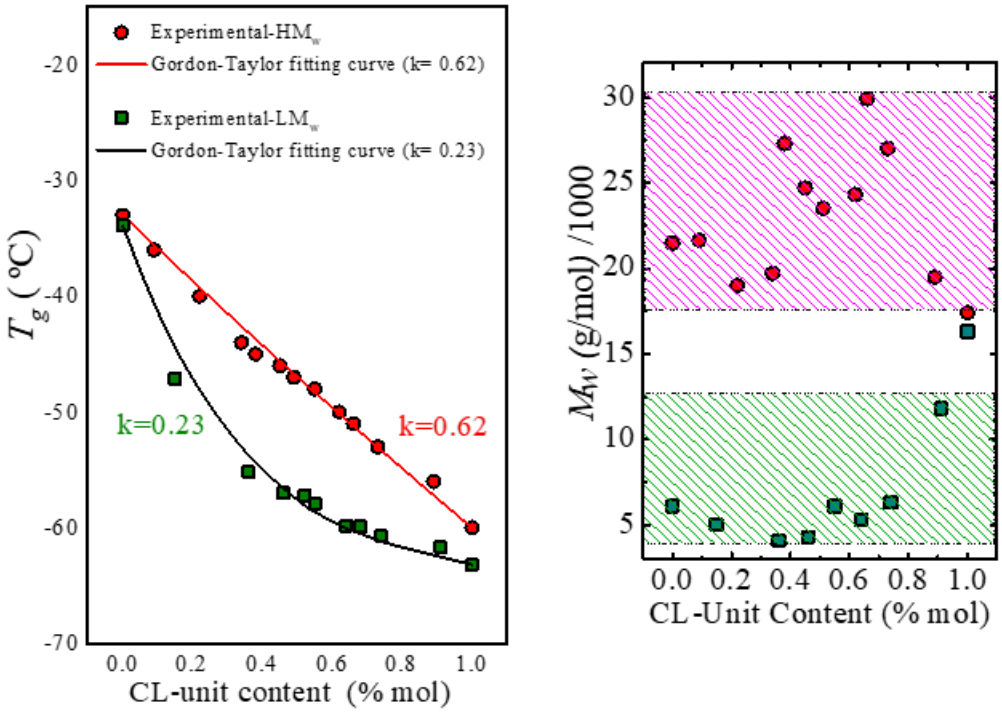


***Figure 5.7.*** *Glass transition temperature as a function of composition for the indicated samples. The inset plots show the $M_w$ values of the samples.*

### 5.2.5. Influence of composition on lamellar thickness

Figures 5.8a-5.8d show SAXS diffractograms for all $HM_w$ and $LM_w$ PBS-*ran*-PCL copolymers and parent homopolymers measured at -60 °C, after the samples were cooled from the melt at 10 °C/min. In all cases, a single scattering peak can be observed. This reflection arises from the X-ray scattering produced by lamellar stacks within the spherulitic structures in the sample. From the position of this peak, the long period (*L*) can be calculated.

In two samples ($LM_w$ $BS_{45}CL_{55}$ and $HM_wBS_{45}CL_{55}$), no SAXS signal was detected, as these samples crystallize a very small amount (approximately 10% or less) during cooling at 10 °C/min and there was probably not enough lamellar

stacking or the long period was so large (as the sample is 90% amorphous) that it fell at angles that are too low for detection.

Figure 5.6e shows a plot of the long period determined at -60 °C as a function of composition for $HM_w$ and $LM_w$ copolyesters. For both $HM_w$ and $LM_w$ BS-*ran*-CL, there is an increase in long period in the PBS rich phase, as the amount of CL units increase in the copolymer. For $LM_w$ copolyester in the PCL rich phase, by increasing BS unit in copolyesters the long period increase. On the right hand side of the pseudo-eutectic point for HMw copolyesters, the long period first increases when the long period of the PBS homopolymer is compared with that of the $BS_{91}CL_{09}$ copolymer. As the amount of BS units in the copolymer increases, the long period decreases. Similar changes in the long period of the PBS-rich phase have been reported by Arandia et al. in isodimorphic poly(butylene succinate)-*ran*-poly(butylene azelate) random copolymers. [29]

The average lamellar thickness, $l_c$, of LMw and HMw PS-*ran*-PCL samples at -60 °C were calculated by the approximation: $l_c = L.X_c$ (where $X_c$ is the crystallinity degree) and plotted as a function of CL-content in Figure 5.7f. The $l_c$ values for PBS-rich and PCL-rich copolymers decrease with increases of comonomer unit content and in contrast, the intervening amorphous layer thickness, $l_a$, values ($l_a = L-l_c$) increase with comonomer content. In fact, for these copolymers, the $l_a$ and $l_c$ values exhibit a pseudo-eutectic-like behavior as a function of composition. This behavior is closely correlated with the changes in crystallinity of the samples shown in Figure 5.3e. The results can be explained if we consider that as comonomer content increases in each phase (i.e., PCL rich crystalline phase or PBS rich crystalline phase) exclusion of the second comonomer predominates. Comonomer exclusion limits the average length of the crystallizable sequences and therefore lamellar thickness ($l_c$) decreases. Comonomer exclusion also limits the amount of crystals that can be formed and the degree of crystallinity also decrease with CL units content while $l_a$ increases.

Moreover, Figure 5.8 (e) shows that the molecular weight does not affect the long period values. These results support our assumption that in random

copolymer, the random sequence of linear crystallizable chains controls the long period values and therefore $T_m$ values do not change by increasing the molecular weight of the random copolyester.

### 5.2.6. Influence of the cooling rate on non-isothermal crystallization for compositions close and at the pseudo-eutectic point

In order to better understand the sequential and coincident crystallization processes at and near the pseudo-eutectic point, rate-dependent experiments were performed. Figure 5.8a, 5.8b, and 5.8c show cooling scans from the melt at different cooling rates corresponding to the following HMw copolymers: $\mathrm{BS_{51}CL_{49}}$, $\mathrm{BS_{45}CL_{55}}$ and $\mathrm{BS_{38}CL_{62}}$, respectively. These compositions are located left of the pseudo-eutectic point, at the pseudo-eutectic point, and right of the pseudo-eutectic point. Subsequent heating scans performed at the constant rate of 20 °C/min are shown in Figures 5.8d, 5.8e, 5.8f. Figure 5.9a, 5.9b, 5.9c,5.9d and 5.9e show cooling scans from the melt at different cooling rates corresponding to the copolymer left of the pseudo-eutectic region( $\mathrm{BS_{64}CL_{36}}$), copolymers at the pseudo-eutectic region($\mathrm{BS_{54}CL_{46}}$, $\mathrm{BS_{48}CL_{52}}$, $\mathrm{BS_{45}CL_{55}}$) and copolymer right of the pseudo-eutectic region( $\mathrm{BS_{36}CL_{64}}$). Subsequent heating scans performed at the constant rate of 20 °C/min are shown in Figures 5.9f to 5.9j.

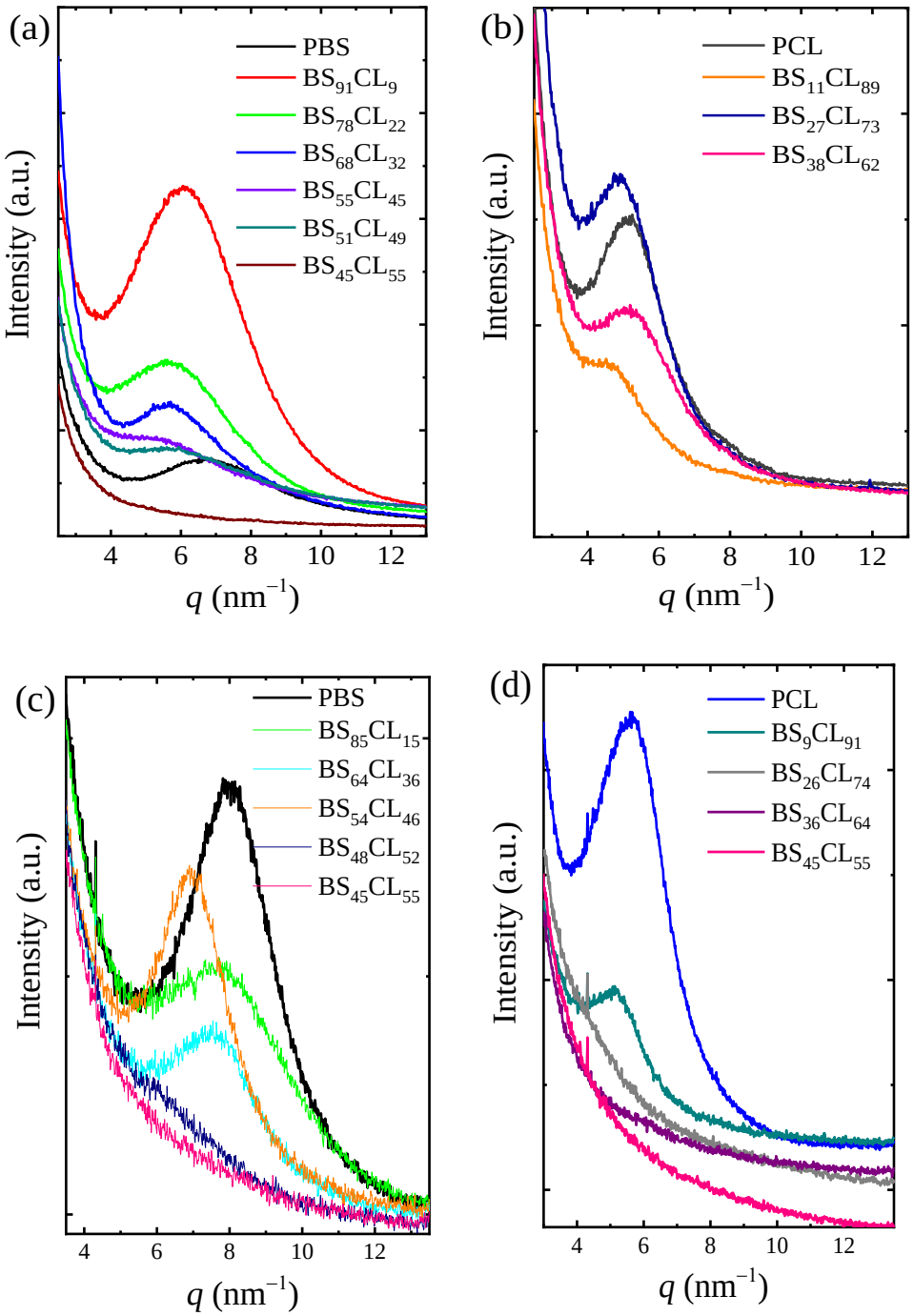
(a)
PBS
BS91CL9
BS78CL22
BS68CL32
BS55CL45
BS51CL49
BS45CL55
Intensity (a.u.)
q (nm−1)
(b)
PCL
BS11CL89
BS27CL73
BS38CL62
Intensity (a.u.)
q (nm−1)
(c)
PBS
BS85CL15
BS64CL36
BS54CL46
BS48CL52
BS45CL55
Intensity (a.u.)
q (nm−1)
(d)
PCL
BS9CL91
BS26CL74
BS36CL64
BS45CL55
Intensity (a.u.)
q (nm−1)

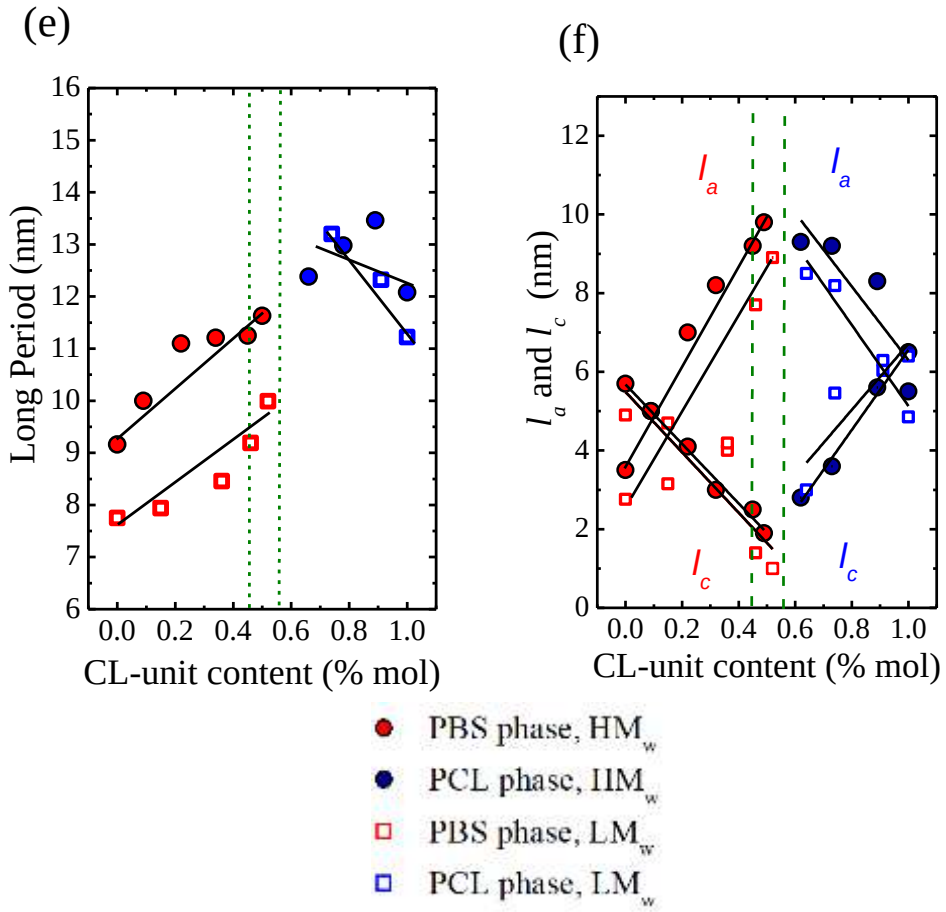


***Figure 5.8****. SAXS diffractograms for HM$_w$-PBS-rich phases (a), HMw-PCL-rich phases (b), LMw-PBS-rich phases (c), and LMw-PCL-rich phases (d) at -60 °C. Long period values as a function of composition for HMw and LMw BS-ran-CL (e). Average lamellar thickness ($l_c$) and amorphous layer thickness ($l_a$) for HMw and LMw BS-ran-CL (f).*

At the pseudo-eutectic point of HMw copolyesters, Figure 5.8b shows that when the $BS_{45}CL_{55}$ copolymer is cooled at a very slow rate (at 0.5 and 1 °C/min), only the PBS-rich phase can crystallize, as indicated by the subsequent DSC scan (see Figure 5.8e), where a single melting peak (with some bimodal character) at temperatures higher than the melting point of the PCL-rich phase can be observed. When the PBS-rich phase has enough time to crystallize during cooling, it inhibits the crystallization of the PCL-rich phase at lower temperatures. This could be due

to confinement effects, as the PBS-rich phase crystallizes from the melt into well-develop spherulitic superstructures (of small size according to PLOM observations, see Figure 5.4) formed by radially growing PBS-rich lamellae. Upon further cooling, the PCL-rich lamellae would have to crystallize in the interlamellar regions of these PBS-rich spherulitic templates. The similar results were obtained for poly(butylene succinate)-*ran*-(butylene adipate) [16] and poly(butylene succinate)-*ran*- azelate) copolymers at pseudo-eutectic point. [39]

Figure 5.9b, 5.9c, 5.9d show that at the pseudo-eutectic region of $LM_w$ copolyesters when the cooling rate is slow or intermediate (1, 5 and 10 °C) both PBS and PCL-rich phases are able to crystallize, as indicated by the subsequent DSC scans (figure 5.9g, 5.9h and 5.9i).

The DSC cooling scans for $HM_w$ in Figure 5.8b performed at 5 °C/min shows a bimodal crystallization exotherm. When the subsequent heating DSC scan is examined in Figure 5.8e, the sample that was cooled at 5 °C/min shows a clear but small melting peak at around 10 °C, that corresponds to the melting of the PCL-rich phase. Notice the absence of cold crystallization before the PCL-rich crystals melt. At higher temperatures, a cold crystallization exotherm (which could be incomplete as a result of an overlap with the PCL-rich crystalline phase melting endotherm) of the PBS-rich phase can be observed, followed by the melting of the PBS-rich phase crystals. The DSC evidence clearly indicates that at 5 °C/min, both PBS and PCL-rich phases are able to crystallize, but judging by their normalized melting enthalpies, the PBS-rich phase can crystallize much more (for PBS-rich phase $\Delta H_m$=24 J/g and PCL-rich phase $\Delta H_m$=5 J/g). A similar bimodal crystallization behavior occurred during cooling for compositions at the pseudo-eutectic region for $LM_w$ copolyesters in Figure 5.9b, 5.9c, 5.9d that were performed at 1 °C/min and 5 °C/min cooling rate.

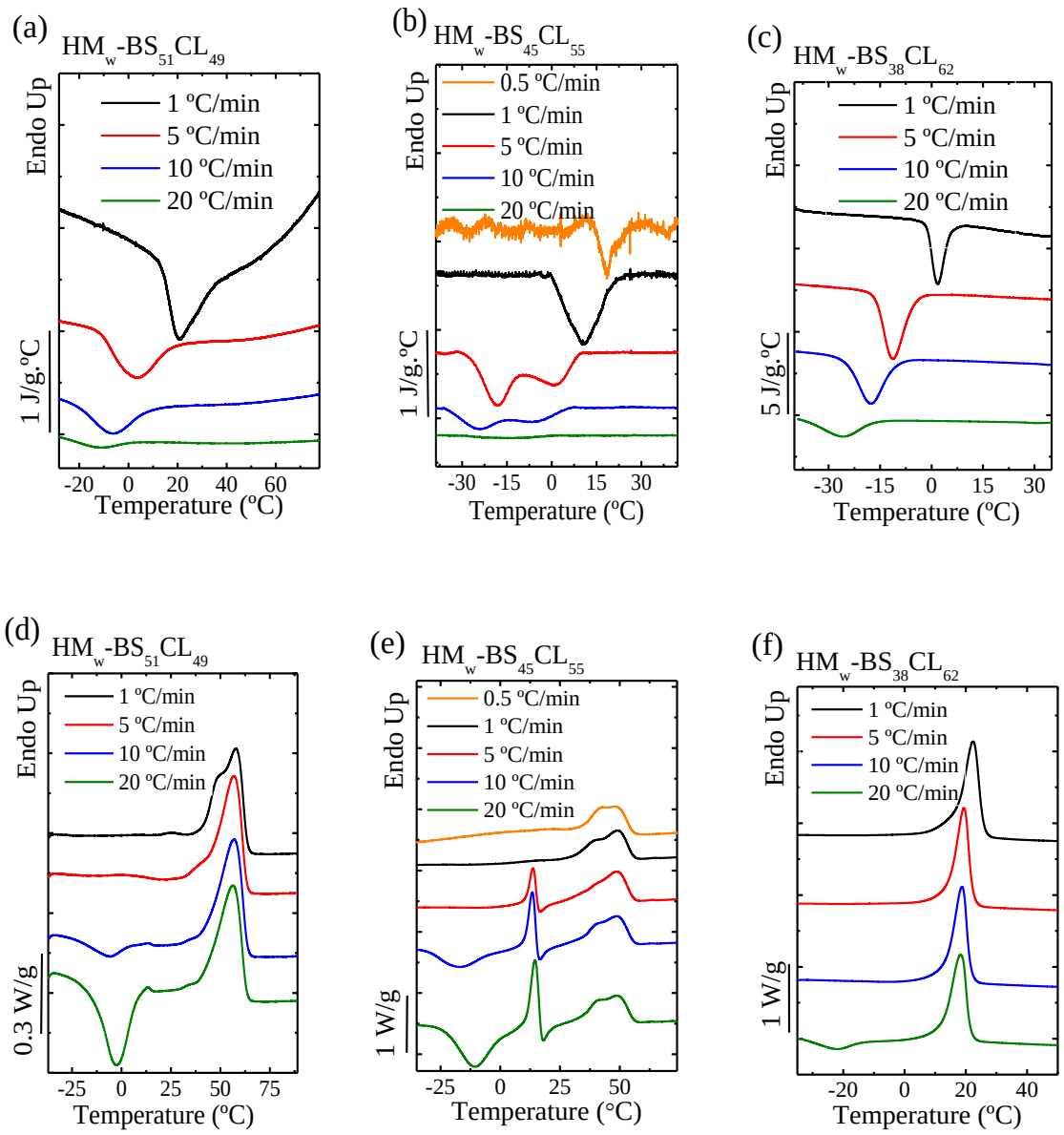


***Figure 5.8.*** *For HM$_w$ copolyesters, $BS_{51}CL_{49}$ (a), $BS_{45}CL_{55}$(b), and $BS_{38}CL_{62}$(c) cooling scans to -60 °C at different cooling rates and (d), (e), (f) are subsequent heating scans performed at 20 °C/min for each copolyester.*

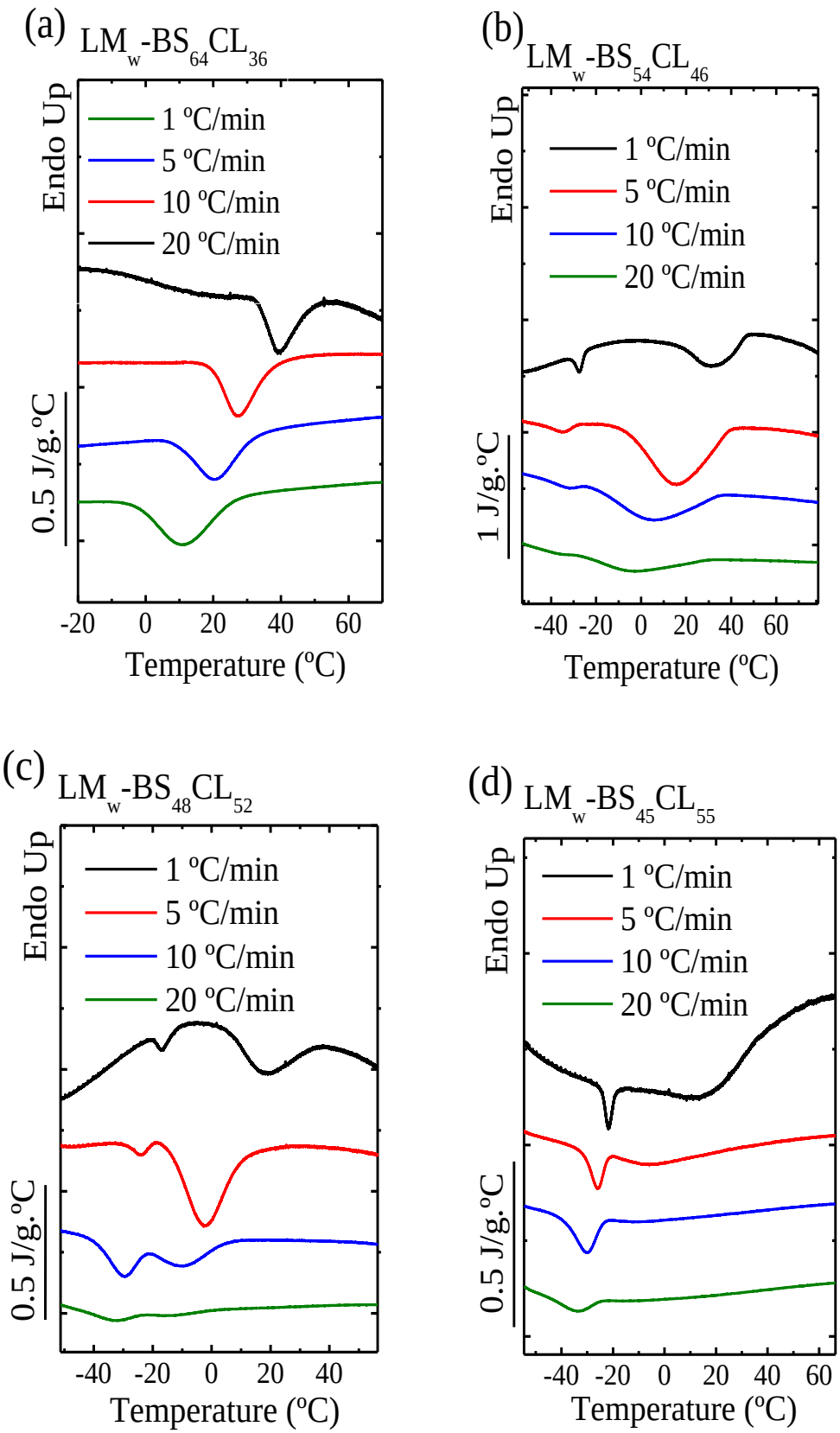
(a) LM$_w$-BS$_{64}$CL$_{36}$
Endo Up
1 °C/min
5 °C/min
10 °C/min
20 °C/min
0.5 J/g.°C
-20 0 20 40 60
Temperature (°C)
(b) LM$_w$-BS$_{54}$CL$_{46}$
Endo Up
1 °C/min
5 °C/min
10 °C/min
20 °C/min
1 J/g.°C
-40 -20 0 20 40 60
Temperature (°C)
(c) LM$_w$-BS$_{48}$CL$_{52}$
Endo Up
1 °C/min
5 °C/min
10 °C/min
20 °C/min
0.5 J/g.°C
-40 -20 0 20 40
Temperature (°C)
(d) LM$_w$-BS$_{45}$CL$_{55}$
Endo Up
1 °C/min
5 °C/min
10 °C/min
20 °C/min
0.5 J/g.°C
-40 -20 0 20 40 60
Temperature (°C)

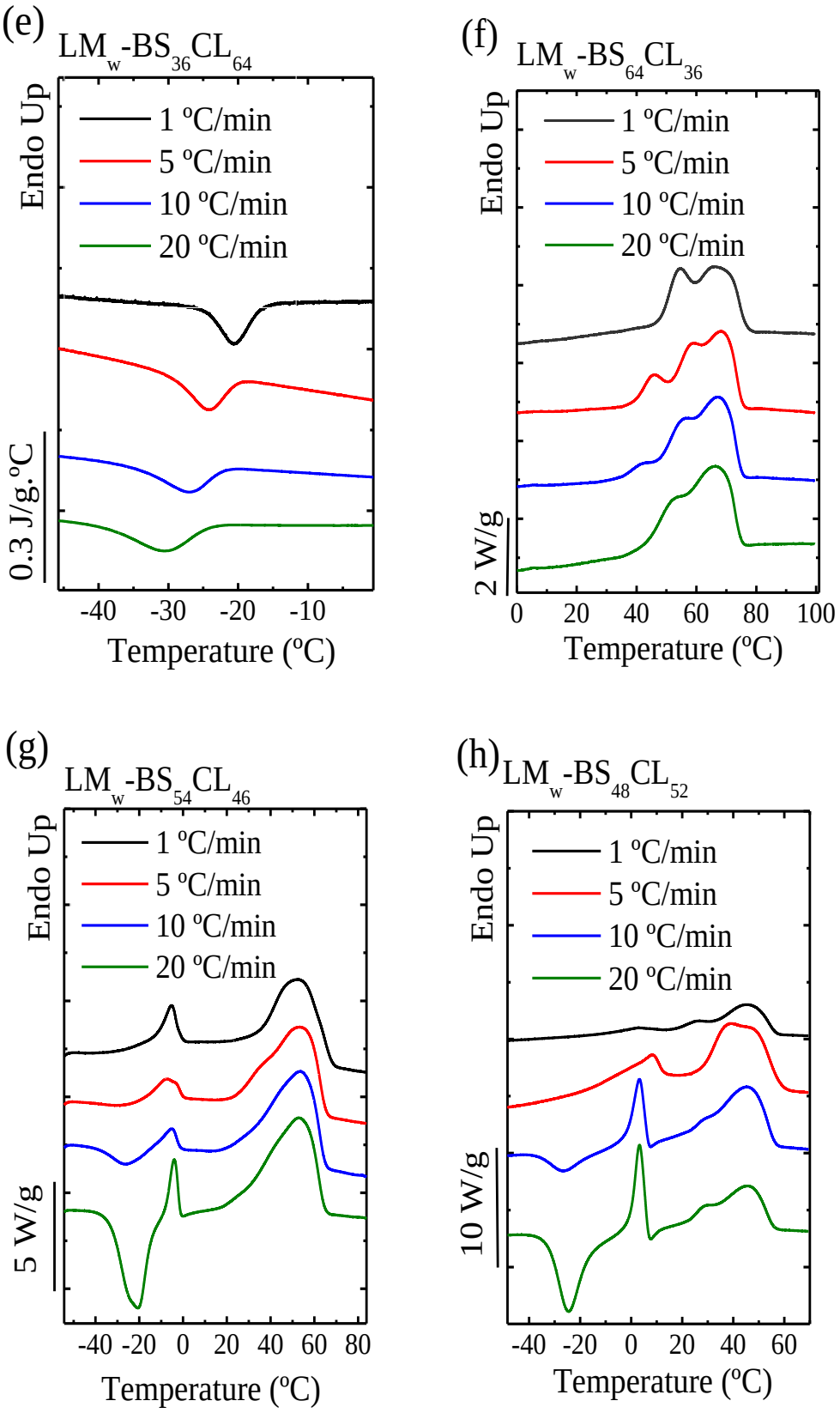
(e)
LM$_w$-BS$_{36}$CL$_{64}$
Endo Up
1 °C/min
5 °C/min
10 °C/min
20 °C/min
0.3 J/g.°C
-40 -30 -20 -10
Temperature (°C)
(f)
LM$_w$-BS$_{64}$CL$_{36}$
Endo Up
1 °C/min
5 °C/min
10 °C/min
20 °C/min
2 W/g
0 20 40 60 80 100
Temperature (°C)
(g)
LM$_w$-BS$_{54}$CL$_{46}$
Endo Up
1 °C/min
5 °C/min
10 °C/min
20 °C/min
5 W/g
-40 -20 0 20 40 60 80
Temperature (°C)
(h)
LM$_w$-BS$_{48}$CL$_{52}$
Endo Up
1 °C/min
5 °C/min
10 °C/min
20 °C/min
10 W/g
-40 -20 0 20 40 60
Temperature (°C)

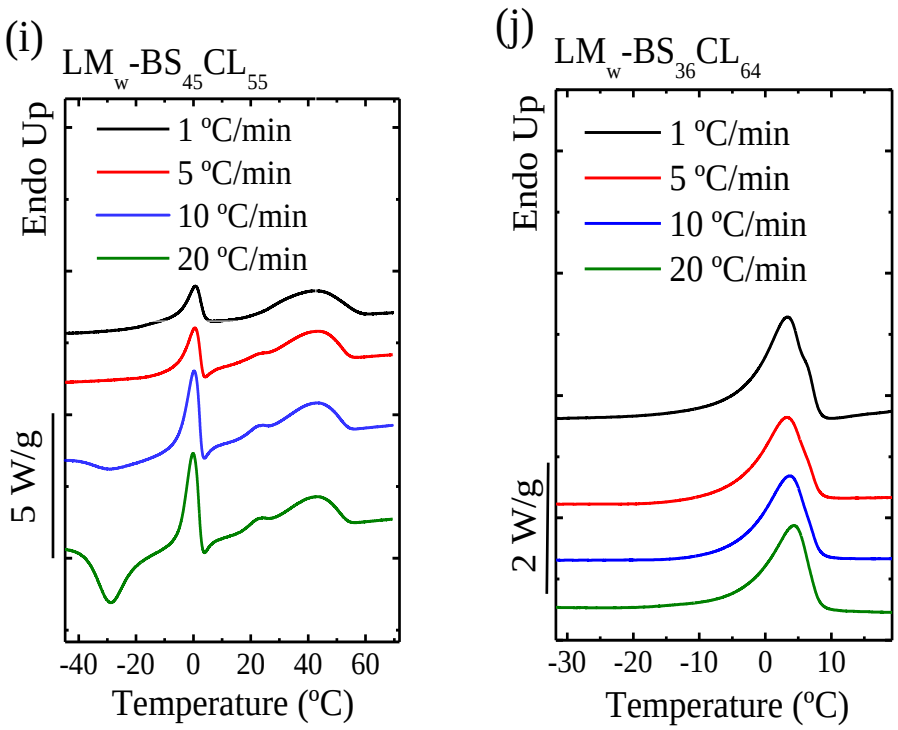


***Figure 5.9.*** *For $LM_w$ copolyesters, $BS_{64}CL_{36}$ (a), $BS_{54}CL_{46}$(b), $BS_{48}CL_{52}$(c), $BS_{45}CL_{55}$ (d), and $BS_{36}CL_{64}$(e) cooling scans to -60 °C at different cooling rates and (f), (g), (h),(i), (j) are subsequent heating scans performed at 20 °C/min for each copolyester.*

Figure 5.10a shows PLOM micrographs taken during cooling from the melt at 5 °/min for the $BS_{45}CL_{55}$ copolymer sample, whose composition corresponds to the pseudo-eutectic point. At 0 °C, a series of well-defined negative spherulites (with sizes close to 10 µm) with clear Maltese crosses can be seen, that must correspond to the PBS-rich phase (as this is the first component to crystallize as corroborated by WAXS results presented below), surrounded by a melt of copolyester chains. Upon further cooling, at around -10 °C, the PCL-rich phase starts to crystallize and additional small birefringent structures (circa 2 µm) were observed (together with small changes in the birefringence of the pre-existing

spherulites, indicating that some PCL crystallization must have occurred inside the PBS-rich spherulitic templates, in analogy to Figure 5.5). Finally, at -30 °C, two populations of spherulites coexist (although they are difficult to appreciate in Figure 5.10a, because of the scale of the micrograph), some are bigger (12 μm aprox) and are the double crystalline spherulites formed during cooling from the melt filled with both PBS-rich and PCL-rich lamellae. The second type are much smaller spherulites formed at temperatures of -10 °C and lower, which must also correspond to double crystalline spherulites, although they may contain a higher population of PCL lamellae because they were formed at lower temperatures.

As the cooling rate increases to 10 °C/min, the subsequent heating scans (performed always at 20 °C/min) in Figure 5.8e show cold crystallization exotherms below the melting transition of the PCL-rich phase melting.

Figure 5.10b shows three PBS-rich phase spherulites (white circles were drawn to guide the eye) at higher temperature (-5 °C) and at -15 °C smaller birefringent structures appear that must correspond to PCL-rich phase spherulites. As WAXS experiments will demonstrate below, only PCL-rich crystals are detected at this cooling rate. At an even higher cooling rate of 20 °C/min, for both $HM_w$ and $LM_w$ copolyesters, the PBS-rich phase cannot crystallize at all during cooling, and only PCL-rich crystals are formed (see Figure 5.8b, 5.9b, 5.9c, 5.9d and Figure 5.10c). The birefringent structures formed at 20 °C/min, Figure 5.8c, corresponding to PCL-rich crystals are very small, with sizes barely discernible by PLOM.

In thses interesting eutectic copolyester samples ($HM_w$ $BS_{45}CL_{55}$ and $LM_w$ $BS_{54}CL_{46}$, $BS_{48}CL_{52}$, $BS_{45}CL_{55}$), the control of the cooling rate is crucial, as the crystallinity and type of crystals formed depend on this parameter.

Similar experiments were performed for two other copolymer samples, $HM_w$ $BS_{51}CL_{49}$ and LMw $BS_{64}CL_{36}$ whose compositions fall to the left of the pseudo-eutectic region and $HM_w$ $BS_{38}CL_{62}$ and $BS_{36}CL_{64}$, whose compositions fall to the right of the pseudo-eutectic region. In both cases, only one phase was able to crystallize

(i.e., the PBS-rich phase in $HM_w$ $BS_{51}CL_{49}$ and the PCL-rich phase in HMw $BS_{38}CL_{62}$) and the increase in cooling rate just caused a shift of the crystallization exotherm to lower temperatures as expected (together with a reduction in crystallization enthalpy), see Figures 5.8a, 5.8c, 5.9a and 5.9e. The subsequent heating scans are shown in Figures 5.8d, 5.8f, 5.9f and 5.9j (performed at a constant heating rate of 20 °C/min). The expected melting of the corresponding crystallizable phase (only one phase) can be observed, as well as cold crystallization in samples rapidly cooled.

In summary, the crystallization of the PBS-rich and PCL-rich crystal phases have a strong dependence on cooling rate at the pseudo-eutectic point. If the cooling rate is low enough (lower than 5 °C/min), as the PBS-rich phase forms first during cooling from the melt, it produces spherulitic templates that had time to fully develop during slow cooling. The PCL-rich phase would have to crystallize within the PBS-rich interlamellar space and this does not happen, possibly because of confinement effects.

When the cooling rate is intermediate (5 °C/min), the PBS-rich phase can still form spherulitic templates (as indicated in Figure 5.8a), but they may not be as well structured as those formed at lower cooling rates, and the PCL-rich phase is able to develop some crystallinity. At a cooling rate of 10 °C/min, only a few spherulites of the PBS-rich phase can form (marked by white circles in Figure 5.10b), and the PCL-phase crystallizes at lower temperatures and constitutes the majority of the crystal phase of the material.

At cooling rates of 20 °C/min and faster, the PBS-rich phase cannot crystallize during cooling, giving the PCL-rich phase the possibility to develop some crystallinity during cooling (see Figure 5.10c). Upon subsequent heating, the PCL-rich phase can undergo cold-crystallization and enhances its crystallinity content. At even higher temperatures, the PBS-rich phase cold-crystallizes while the PCL-rich crystals melt.

**5 °C/min**

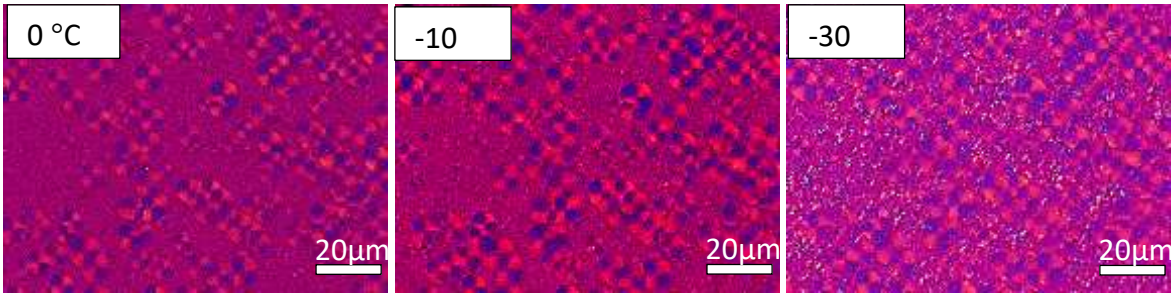


**10 °C/min**

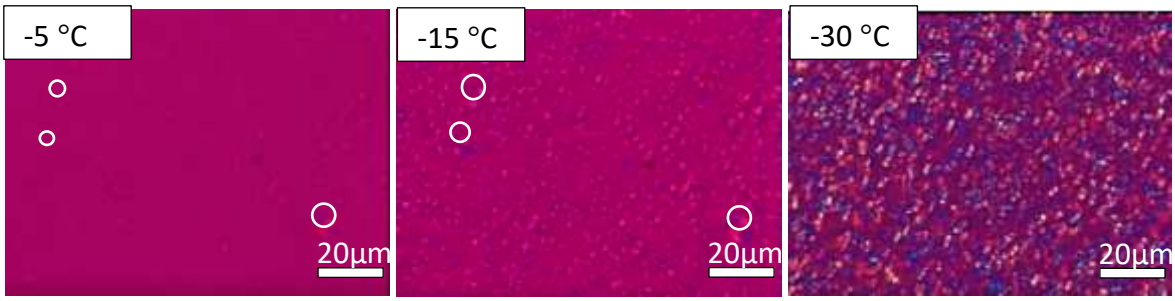


**20 °C/min**

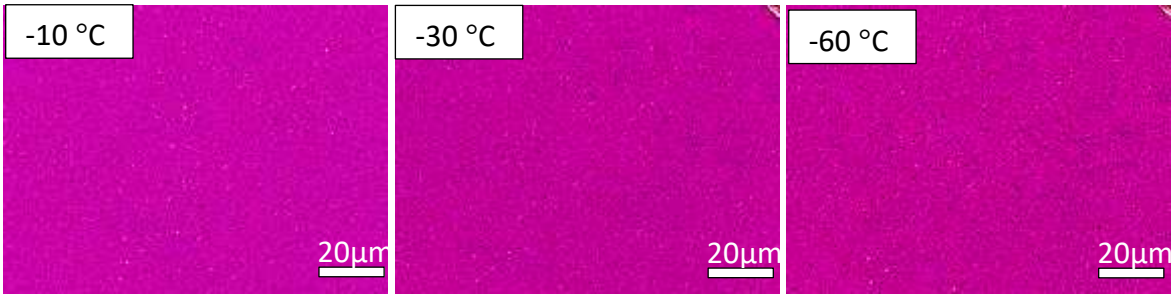


***Figure 5.10.*** *PLOM micrographs taken during cooling from the melt at different cooling rates for the HM$_w$ $BS_{45}CL_{55}$ copolyester sample (whose composition corresponds to the pseudo-eutectic point): (a) 5 °C/min, (b) 10 °C/min, and (c) 20 °C/min. The white scale bar is equal to 20 µm. The white circles in Figure 5.10b were drawn to highlight the presence of the few PBS-rich spherulites that were formed.*

We performed *in situ* synchrotron SAXS/WAXS experiments for the 3 selected $HM_w$ samples shown in Figure 5.8. These experiments were performed only at 10 °C/min during both cooling and subsequent heating from the melt. The results obtained during heating at 10 °C/min (i.e., second heating, as the samples were first molten and then controlled cooled from the melt at 10 °C/min) are presented in Figure 5.11, where selected diffractograms were chosen for a series of temperatures.

In the case of the two copolymer samples at each side of the pseudo-eutectic point, WAXS demonstrates that only one type of crystals is present, i.e., PBS like crystals for the $BS_{51}CL_{49}$ sample and PCL like crystals for the $BS_{38}CL_{62}$. These results are consistent with the previously discussed DSC data (Figure 5.8d and 5.8f, see the curves at 10 °C/min). SAXS curves for these same copolymers also exhibit the expected behavior, as the SAXS maximum shifts to lower q values (higher long periods) as temperature is increased (see Figure 5.12), until the sample completely melts and a single phase isotropic melt is obtained.

The most interesting results are those obtained for the copolymer composition at the pseudo-eutectic point, i.e., the $HM_w$ $BS_{45}CL_{55}$ copolyester sample. Figure 5.10b should be read from bottom to top, as the sample was being heated, and it should be compared with Figure 5.8e (i.e., specifically with the DSC heating trace performed at 10 °C/min).

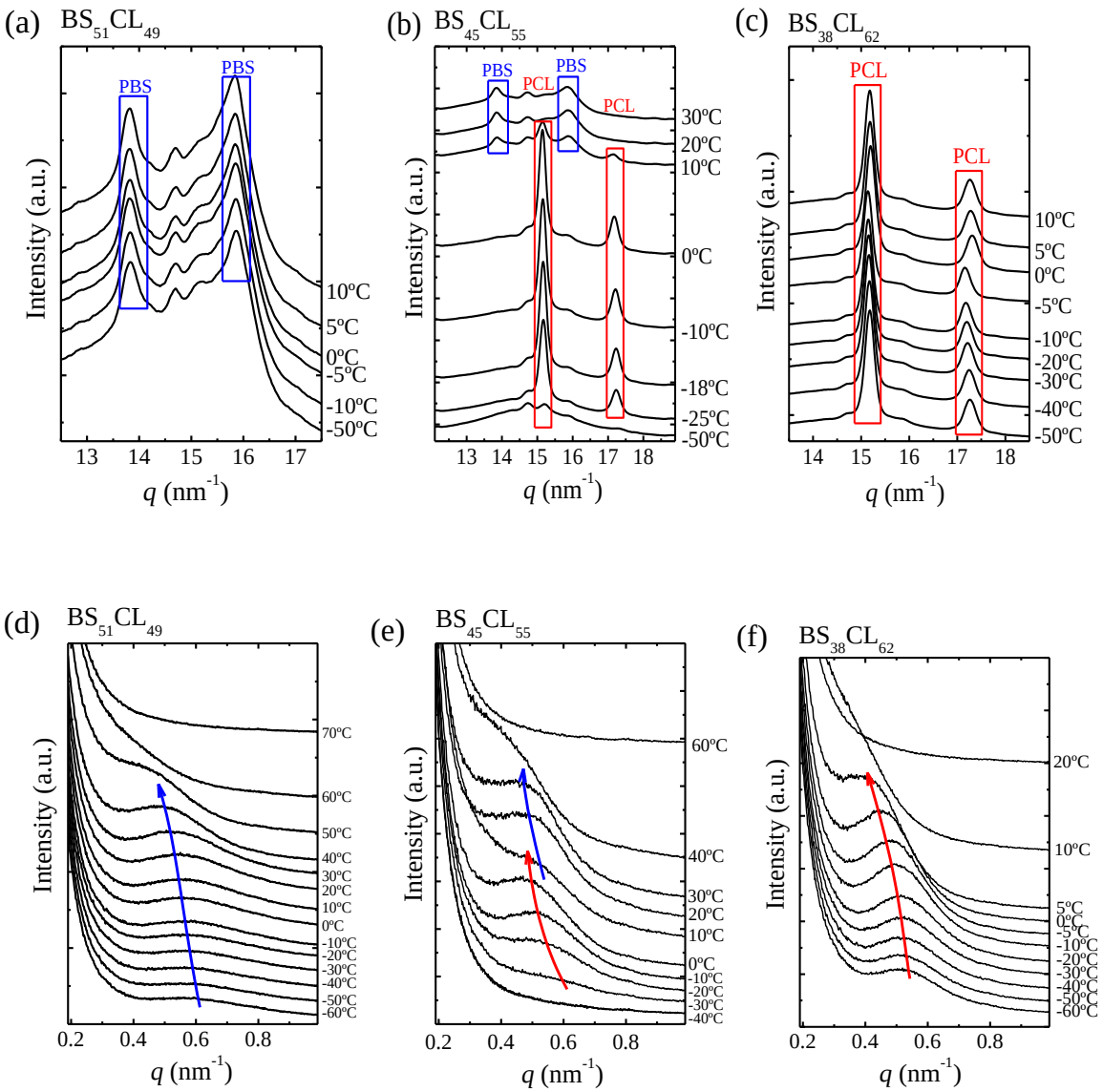


***Figure 5.11.*** *(a), (b), and (c) are WAXS patterns and (d), (e), and (f) are SAXS patterns during heating at 10 °C/min (after cooling from the melt at 10 °C/min) for the indicated copolyesters.*

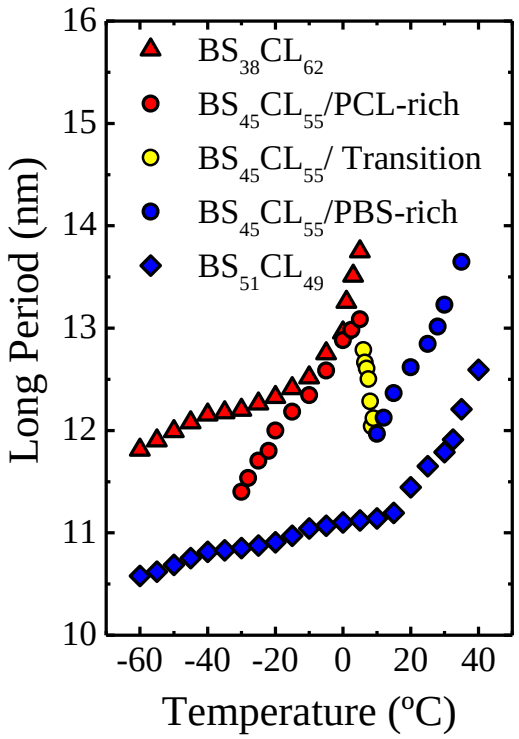


***Figure 5.12.*** *Long period values obtained from the SAXS maxima as a function of temperature during cooling for copolyester compositions close and at the pseudo-eutectic point.*

Firstly, it is interesting to note that according to WAXS data, the PCL-rich phase is the only one whose crystallization can be detected during cooling at 10 °C/min (see WAXS patterns taken during cooling at 10 °C/min in Figure 5.9a), since the low temperature WAXS traces only show reflections that correspond to PCL (see the selected temperatures of -50, -25, -18, -10 and °C in Figure 5.11 ). The DSC cooling curve, on the other hand, in Figure 5.8b shows a bimodal exotherm, that we interpret as arising from the crystallization of the PBS-rich component first (at

higher temperatures) and then of the PCL component, at lower temperatures. However, the WAXS data shows that if such crystallization from the PBS phase occurs, it cannot be detected by WAXS. This is probably due to the lateral size of the crystals, which are too small for WAXS detection. However, PLOM results shown in Figure 5.10b, also evidenced the presence of a very small population of spherulites at -5 °C, suggesting that a small amount of PBS-rich crystals are indeed formed during cooling from the melt, in accordance with the DSC data presented in Figure 5.6b.

The DSC heating scan in Figure 5.8e does show the melting of both phases during heating, but there is a strong cold crystallization exotherm located in the range -10 to 0 °C, where WAXS evidences the crystallization of the PCL-rich crystalline phase (Figure 5.11b). In fact, at temperatures of -50 °C, the WAXS trace in Figure 5.8b indicates a very low degree of crystallinity for the PCL-rich phase (as judged by the area under the crystalline reflections). Such degree of crystallinity increases upon heating in a consistent way as the PCL-rich phase undergoes cold crystallization.

The PBS-rich phase only starts to crystallize during heating at 10 °C, a temperature at which, according to DSC data (Figure 5.8e), PCL is in the process of melting. WAXS also shows a strong decrease in the PCL (110) reflection at 10 °C (Figure 5.9b). Therefore, a comparison between DSC and WAXS indicates that there is an overlap between the melting of the PCL-rich phase and the cold crystallization of the PBS-rich phase.

Figure 5.11e shows the SAXS patterns as a function of temperature during heating of the $BS_{45}CL_{55}$ sample at 10 °C/min. Even though a single SAXS peak can be observed for all temperatures, the trend in peak position and widths of the curves changes with temperature. The biggest change occurs above 0 °C, when the PCL-rich crystals start to melt and new PBS-rich crystals form by a cold-crystallization process.

Figure 5.12 plots the long periods obtained from the SAXS maxima as a function of temperature for the three samples examined. The increase of long periods with temperature is a common trend observed in semi-crystalline materials, as lamellar crystals tend to reorganize by thickening during heating (at temperatures below their melting points). At temperatures where partial melting occurs, the long period increases, typically more rapidly, as the average distance between lamellae increases as the fraction of molten polymer increases.

The sample whose composition is at the pseudo-eutectic point shows in Figure 5.11 a clear transition region, where the long period briefly decreases with temperature, exactly at the temperature region where PCL-rich crystals melt and PBS-rich crystals form. At temperatures below the transition, the long period is dominated by the PCL-rich lamellar crystals and above the transition by the PBS-rich lamellar crystals, as the comparison with the other two copolyester samples clearly suggests. The results are consistent with WAXS, DSC and PLOM results.

## 5.3. CONCLUSIONS

The HMw synthesized copolymers are also isodimorphic, as our previously prepared analogous LMw copolyesters. Nevertheless, the effect of molecular weight is very interesting. We found that $T_c$ and $T_m$ values are insensitive to large molecular weight variations as these first order thermal transitions are determined by the randomness of the comonomer sequence distribution and hence their selection during crystallization. In fact, the long period value drives $T_m$ and $T_c$ values in random copolymers. However, both the crystallinity degree and the $T_g$ of the copolymers did vary significantly with increases in molecular weight, as their values depend on the entire chain length and chain mobility. Therefore, changing the molecular weight of the copolymer affords separate control over $T_g$ and $T_m$ depending on composition.

The copolymers display spherulitic superstructures whose nucleation depends on copolymer composition. At the pseudo-eutectic point, HMw-$BS_{45}CL_{55}$

copolyester was the only double crystalline copolymer, whose PBS-rich phase forms space filling spherulites at higher temperatures that template the superstructural morphology of the copolymer. These PBS-rich phase spherulites contain radial lamellar stacks. After cooling down to lower temperatures, the PCL-rich phase crystallizes in the intraspherulitic amorphous regions with newly formed lamellae.

Comonomer exclusion limits the average length of the crystallizable sequences and therefore $l_c$ decreases. Comonomer exclusion also limits the amount of crystals that can be formed and the degree of crystallinity also decrease with comonomer content while $l_a$ increases.

In the specific cases of the HMw-$BS_{45}CL_{55}$, $LM_w$-$BS_{54}CL_{46,}$ LMw-$BS_{48}CL_{52}$ and LMw-$BS_{45}CL_{55}$ copolyesters (whose compositions correspond to the pseudo-eutectic point or region), our results indicate that the cooling rate can determine which phase can crystallize and also if a single phase or two phases are formed. Very low cooling rates (below 5 °C/min) lead to the formation of only PBS-rich crystals in HMw, although for LMw both PBS-rich and PCL-rich phases can crystallize at these low cooling rate. Intermediate cooling rates allow the formation of double crystalline spherulites composed by PBS-rich and PCL-rich lamellae in both HMw and LMw copolyesters. Finally, for both HMw and LMw copolyesters when heating rates are as high as 20 °C/min, only PCL-rich crystals can form. In this way, the morphology and thermal transitions of this copolyester at the pseudo-eutectic composition can be tailored for specific applications.

## 5.4. REFERENCES

1. Pérez-Camargo, R. A.; Arandia, I.; Safari, M.; Cavallo, D.; Lotti, N.; Soccio, M.; Müller, A. J., Crystallization of isodimorphic aliphatic random copolyesters: Pseudo-eutectic behavior and double-crystalline materials. *European Polymer Journal* **2018,** *101*, 233-247.

2. Natta, G.; Corradini, P.; Sianesi, D.; Morero, D., Isomorphism phenomena in macromolecules. *Journal of Polymer Science* **1961,** *51* (156), 527-539.

3. Allegra, G.; Bassi, I., Isomorphism in synthetic macromolecular systems. In *Fortschritte der Hochpolymeren-Forschung*, Springer: 1969; pp 549-574.

4. Yu, Y.; Sang, L.; Wei, Z.; Leng, X.; Li, Y., Unique isodimorphism and isomorphism behaviors of even-odd poly (hexamethylene dicarboxylate) aliphatic copolyesters. *Polymer* **2017,** *115*, 106-117.

5. Latere Dwan'Isa, J.-P.; Lecomte, P.; Dubois, P.; Jérôme, R., Synthesis and characterization of random copolyesters of ε-caprolactone and 2-oxepane-1, 5-dione. *Macromolecules* **2003,** *36* (8), 2609-2615.

6. Ye, H.-M.; Wang, R.-D.; Liu, J.; Xu, J.; Guo, B.-H., Isomorphism in poly (butylene succinate-co-butylene fumarate) and its application as polymeric nucleating agent for poly (butylene succinate). *macromolecules* **2012,** *45* (14), 5667-5675.

7. Ceccorulli, G.; Scandola, M.; Kumar, A.; Kalra, B.; Gross, R. A., Cocrystallization of random copolymers of ω-pentadecalactone and ε-caprolactone synthesized by lipase catalysis. *Biomacromolecules* **2005,** *6* (2), 902-907.

8. Yu, Y.; Wei, Z.; Liu, Y.; Hua, Z.; Leng, X.; Li, Y., Effect of chain length of comonomeric diols on competition and miscibility of isodimorphism: A comparative study of poly (butylene glutarate-co-butylene azelate) and poly (octylene glutarate-co-octylene azelate). *European Polymer Journal* **2018,** *105*, 274-285.

9. Siracusa, V.; Gazzano, M.; Finelli, L.; Lotti, N.; Munari, A., Cocrystallization phenomena in novel poly (diethylene terephthalate-co-thiodiethylene terephthalate) copolyesters. *Journal of Polymer Science Part B: Polymer Physics* **2006,** *44* (11), 1562-1571.

10. Morales-Huerta, J. C.; Martinez de Ilarduya, A.; Muñoz-Guerra, S. n., Sustainable aromatic copolyesters via ring opening polymerization: poly (butylene 2, 5-furandicarboxylate-co-terephthalate) s. *ACS Sustainable Chemistry & Engineering* **2016,** *4* (9), 4965-4973.

11. Li, X.; Hong, Z.; Sun, J.; Geng, Y.; Huang, Y.; An, H.; Ma, Z.; Zhao, B.; Shao, C.; Fang, Y., Identifying the phase behavior of biodegradable poly (hexamethylene succinate-co-hexamethylene adipate) copolymers with FTIR. *The Journal of Physical Chemistry B* **2009,** *113* (9), 2695-2704.

12. Hong, M.; Tang, X.; Newell, B. S.; Chen, E. Y.-X., "Nonstrained" γ-Butyrolactone-Based Copolyesters: Copolymerization Characteristics and Composition-Dependent (Thermal, Eutectic, Cocrystallization, and Degradation) Properties. *Macromolecules* **2017,** *50* (21), 8469-8479.

13. Yu, Y.; Wei, Z.; Zhou, C.; Zheng, L.; Leng, X.; Li, Y., Miscibility and competition of cocrystallization behavior of poly (hexamethylene dicarboxylate) s aliphatic copolyesters: effect of chain length of aliphatic diacids. *European Polymer Journal* **2017,** *92*, 71-85.

14. Liang, Z.; Pan, P.; Zhu, B.; Dong, T.; Hua, L.; Inoue, Y., Crystalline phase of isomorphic poly (hexamethylene sebacate-co-hexamethylene adipate) copolyester: Effects of comonomer composition and crystallization temperature. *Macromolecules* **2010,** *43* (6), 2925-2932.

15. Papageorgiou, G. Z.; Bikiaris, D. N., Synthesis and Properties of Novel Biodegradable/Biocompatible Poly [propylene-co-(ethylene succinate)] Random Copolyesters. *Macromolecular Chemistry and Physics* **2009,** *210* (17), 1408-1421.

16. Pérez-Camargo, R. A.; Fernández-d'Arlas, B.; Cavallo, D.; Debuissy, T.; Pollet, E.; Avérous, L.; Müller, A. J., Tailoring the structure, morphology, and crystallization of isodimorphic poly (butylene succinate-ran-butylene adipate) random copolymers by changing composition and thermal history. *Macromolecules* **2017,** *50* (2), 597-608.

17. Debuissy, T.; Sangwan, P.; Pollet, E.; Avérous, L., Study on the structure-properties relationship of biodegradable and biobased aliphatic copolyesters based on 1, 3-propanediol, 1, 4-butanediol, succinic and adipic acids. *Polymer* **2017,** *122*, 105-116.

18. Wang, K.; Jia, Y.-G.; Zhu, X., Two-Way Reversible Shape Memory Polymers Made of Cross-Linked Cocrystallizable Random Copolymers with Tunable Actuation Temperatures. *Macromolecules* **2017,** *50* (21), 8570-8579.

19. Soccio, M.; Finelli, L.; Lotti, N.; Gazzano, M.; Munari, A., Poly (propylene isophthalate), poly (propylene succinate), and their random copolymers: synthesis and thermal properties. *Journal of Polymer Science Part B: Polymer Physics* **2007,** *45* (3), 310-321.

20. Soccio, M.; Finelli, L.; Lotti, N.; Gazzano, M.; Munari, A., Novel random poly (propylene isophthalate/adipate) copolyesters: Synthesis and characterization. *European polymer journal* **2006,** *42* (11), 2949-2958.

21. Lendlein, A.; Sisson, A., *Handbook of biodegradable polymers: isolation, synthesis, characterization and applications*. John Wiley & Sons: 2011.

22. Bechthold, I.; Bretz, K.; Kabasci, S.; Kopitzky, R.; Springer, A., Succinic acid: a new platform chemical for biobased polymers from renewable resources. *Chemical engineering & technology* **2008,** *31* (5), 647-654.

23. Zheng, L.; Li, C.; Wang, Z.; Wang, J.; Xiao, Y.; Zhang, D.; Guan, G., Novel biodegradable and double crystalline multiblock copolymers comprising of poly (butylene succinate) and poly (ε-caprolactone): synthesis, characterization, and properties. *Industrial & Engineering Chemistry Research* **2012,** *51* (21), 7264-7272.

24. Qiu, Z.; Komura, M.; Ikehara, T.; Nishi, T., Miscibility and crystallization behavior of biodegradable blends of two aliphatic polyesters. Poly (butylene succinate) and poly (ε-caprolactone). *Polymer* **2003,** *44* (25), 7749-7756.

25. Alamo, R. G.; Viers, B. D.; Mandelkern, L., Phase structure of random ethylene copolymers: a study of counit content and molecular weight as independent variables. *Macromolecules* **1993,** *26* (21), 5740-5747.

26. Di Lorenzo, M.; Silvestre, C., Non-isothermal crystallization of polymers. *Progress in Polymer Science* **1999,** *24* (6), 917-950.

27. Ciulik, C.; Safari, M.; Martínez de Ilarduya, A.; Morales-Huerta, J. C.; Iturrospe, A.; Arbe, A.; Müller, A. J.; Muñoz-Guerra, S., Poly (butylene succinate-ran-ε-caprolactone) copolyesters: Enzymatic synthesis and crystalline isodimorphic character. *European Polymer Journal* **2017,** *95*, 795-808.

28. Cao, A.; Okamura, T.; Ishiguro, C.; Nakayama, K.; Inoue, Y.; Masuda, T., Studies on syntheses and physical characterization of biodegradable aliphatic poly (butylene succinate-co-ε-caprolactone) s. *Polymer* **2002,** *43* (3), 671-679.

29. Arandia, I.; Mugica, A.; Zubitur, M.; Arbe, A.; Liu, G.; Wang, D.; Mincheva, R.; Dubois, P.; Müller, A. J., How composition determines the properties of isodimorphic poly (butylene succinate-ran-butylene azelate) random biobased copolymers: from single to double crystalline random copolymers. *Macromolecules* **2014,** *48* (1), 43-57.

30. Castillo, R.; Müller, A., Crystallization and morphology of biodegradable or biostable single and double crystalline block copolymers. *Progress in Polymer Science* **2009,** *34* (6), 516-560.

31. Palacios, J. K.; Mugica, A.; Zubitur, M.; Müller, A. J., Crystallization and Morphology of Block Copolymers and Terpolymers With More Than One Crystallizable Block. In *Crystallization in Multiphase Polymer Systems*, Elsevier: **2018**; pp 123-180.

32. Mandelkern, L., *Crystallization of polymers*. 2nd edition ed.; Cambridge University Press: Cambridge 2002; Vol. 1, Equilibrium Concepts.

33. Van Krevelen, D. W.; Te Nijenhuis, K., *Properties of polymers: their correlation with chemical structure; their numerical estimation and prediction from additive group contributions*. Elsevier: Amsterdam, 2009.

34. Pitt, C. G.; Chasalow, F.; Hibionada, Y.; Klimas, D.; Schindler, A., Aliphatic polyesters. I. The degradation of poly (ϵ-caprolactone) in vivo. *Journal of Applied Polymer Science* **1981,** *26* (11), 3779-3787.

35. Hiemenz, P. C.; Lodge, T. P., *Polymer chemistry*. CRC press: Boca Raton, 2007.

36. Schneider, H.; Rieger, J.; Penzel, E., The glass transition temperature of random copolymers: 2. Extension of the Gordon-Taylor equation for asymmetric Tg vs composition curves. *Polymer* **1997,** *38* (6), 1323-1337.

37. Simha, R.; Boyer, R., On a general relation involving the glass temperature and coefficients of expansion of polymers. *The Journal of Chemical Physics* **1962,** *37* (5), 1003-1007.

38. Pinal, R., Entropy of mixing and the glass transition of amorphous mixtures. *Entropy* **2008,** *10* (3), 207-223.

39. Díaz, A.; Franco, L.; Puiggalí, J., Study on the crystallization of poly (butylene azelate-co-butylene succinate) copolymers. *Thermochimica Acta* **2014,** *575*, 45-54.

# *Chapter VI*

# *Isothermal Crystallization of HMw PBS-ran-PCL*

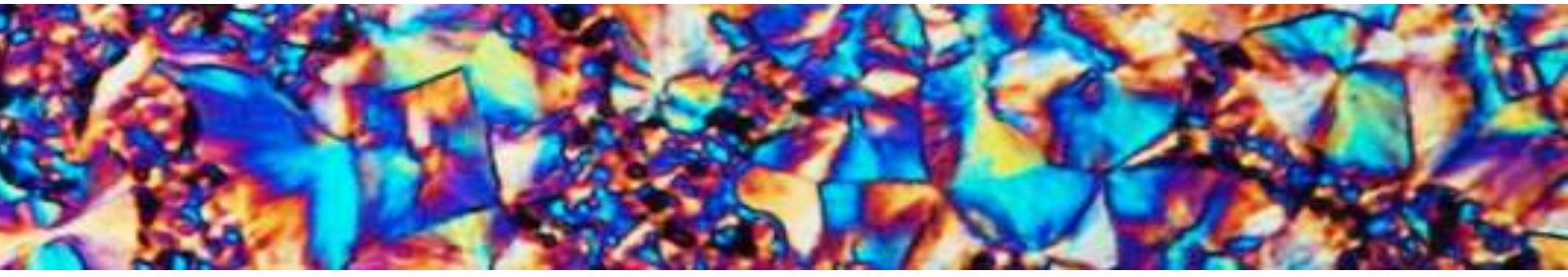

# Table of Contents

## Abstract

In this work, we study for the first time, the isothermal crystallization behavior of isodimorphic random poly(butylene succinate)-*ran*-poly(*ε*-caprolactone) copolyesters, PBS-*ran*-PCL, previously synthesized by us. We perform nucleation and spherulitic growth kinetics by Polarized Light Optical Microscopy (PLOM) and overall isothermal crystallization kinetics by Differential Scanning Calorimetry (DSC). Selected samples were also studied by real-time Wide Angle X-ray Diffraction (WAXS). Under isothermal conditions, only the PBS-rich phase or the PCL-rich phase could crystallize as long as the composition was away from the pseudo-eutectic point. In comparison with the parent homopolymers, as comonomer content increased, both PBS-rich and PCL-rich phases nucleated much faster but their spherulitic growth rates were much slower. Therefore, the overall crystallization kinetics was a strong function of composition and supercooling. The only copolymer with the eutectic composition exhibited a remarkable behavior. By tuning the crystallization temperature, this copolyester could form either a single crystalline phase or both phases with remarkably different thermal properties.

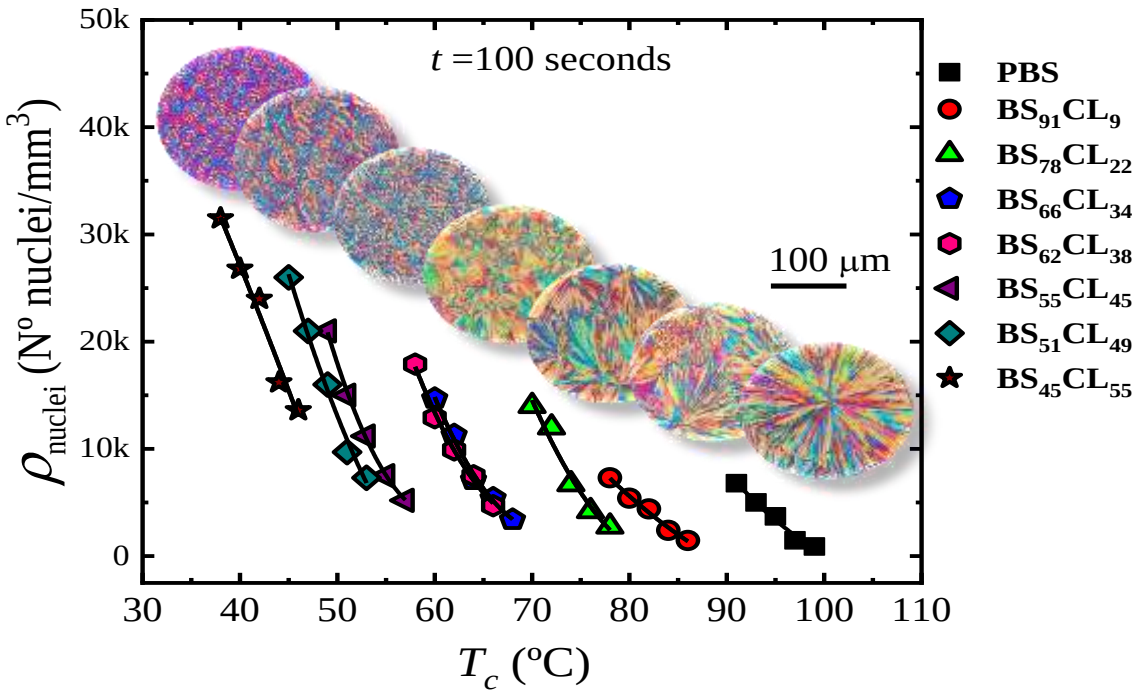
50k
40k
30k
20k
10k
0
30
40
50
60
70
80
90
100
110
$\rho_{nuclei}$ (N° nuclei/mm$^3$)
$T_c$ (ºC)
$t$ =100 seconds
100 μm
PBS
$BS_{91}CL_9$
$BS_{78}CL_{22}$
$BS_{66}CL_{34}$
$BS_{62}CL_{38}$
$BS_{55}CL_{45}$
$BS_{51}CL_{49}$
$BS_{45}CL_{55}$

## 6.1. INTRODUCTION

Biocompatible and biodegradable polymers are being developed for a wide range of applications due to their potential to solve the environmental concerns caused by traditional non-degradable plastics [1-4]. Among the biodegradable polymers that have been most intensively studied are aliphatic polyesters such as Poly (glycolide) (PGA), Poly(L-lactide) (PLLA), Poly(ethylene succinate) (PES), Poly (butylene succinate) (PBS), and Poly(*ε*-caprolactone) (PCL) [5-6]. Although aliphatic polyesters have been used for many years in industrial, biomedical, agricultural, and pharmaceutical applications, there is still room for many improvements [7-8]. The synthesis of random copolyesters, using biobased comonomers, can overcome some of the drawbacks of biodegradable polyesters, such as slow biodegradation rate (due to high crystallinity degrees) and undesirable mechanical properties [9-11].

The properties of crystallizable random copolymers constituted by two semicrystalline parent components have been recently reviewed [12]. Depending on their ability to share crystal lattices, three different cases have been reported: [12-14] (a) Total comonomer exclusion occurs when the chemical repeat units are very different and the crystal lattice of each one of the components cannot tolerate the presence of the other; (b) Total comonomer inclusion or isomorphic behavior can only be obtained in cases where the components can co-crystallize in the entire composition range (as their chemical structures are very similar), forming a single crystal structure [15-16], and (c) An intermediate and complex case, where a balance between comonomer inclusion and exclusion occurs, leading to isodimorphic copolymers.

In isodimorphic random copolymers, at least one of the two crystalline phases includes some repeat units of the minor component in its crystal lattice. When the melting point is plotted as a function of composition a pseudo-eutectic behavior is commonly observed, where, on each side of the pseudo-eutectic point, only the crystalline phase of the major component is formed, which may contain a limited amount of the minor comonomer chains included in the crystal lattice [12].

In our previous works [10, 17], we have synthesized and studied the morphology and crystallinity of poly (butylene succinate-*ran*-caprolactone) (PBS-*ran*-PCL) copolyesters. *In situ* wide angle X-ray scattering (WAXS) indicated that changes were produced in the crystalline unit cell dimensions of the dominant crystalline phase. In addition, differential scanning calorimetry (DSC) measurements showed that all copolymers could crystallize, regardless of composition, and their thermal transitions temperatures (i.e., $T_c$ and $T_m$) went through a pseudo-eutectic point when plotted as a function of composition. Therefore, all these evidences demonstrated an isodimorphic behavior. At the pseudo-eutectic composition, both PBS-rich and PCL-rich phases can crystallize. [17-18]

In the current work, we perform a detailed isothermal crystallization study of PBS-*ran*-PCL copolymers to determine the nucleation and crystallization kinetics of the copolyesters and study the influence of composition on the crystallization kinetics. This information is very important as it allows tailoring the properties of random copolymers as well as their applications. The analysis of the isothermal crystallization kinetics of PBS-*ran*-PCL was performed using differential scanning calorimetry (DSC), polarized light optical microscopy (PLOM) and *in situ* wide angle X-ray scattering (WAXS).

## 6.2. RESULTS AND DISCUSSIONS

### 6.2.1. Overview of the previous results

We have studied previously (chapter 3-5) [17] the non-isothermal crystallization behavior of the same PBS-*ran*-PCL random copolymers employed in this Chapter. The results demonstrated that these copolymers exhibit an isodimorphic behaviour.

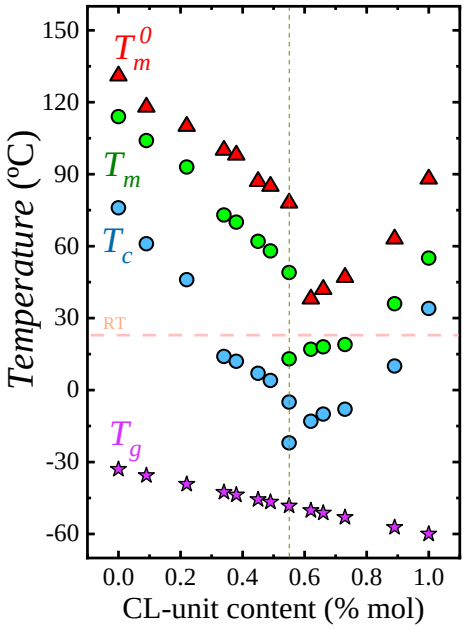


***Figure 6.1.*** *Phase diagram based on data published in ref. 17 on the non-isothermal crystallization of the PBS-ran-PCL copolymers under study. Additionally, equilibrium melting temperatures obtained in the present work by Hoffman-Weeks analysis of isothermally obtained data, are also included. The dashed vertical line indicates the pseudo-eutectic point. The dashed horizontal line indicates an arbitrary room temperature value.*

Figure 6.1 presents a phase diagram for the PBS-*ran*-PCL system. These random copolymers exhibit a single-phase melt and a single glass transition temperature, as expected for random copolymers. Upon cooling from the melt the materials are capable of crystallizing in the entire composition range, in spite of being random, as demonstrated by NMR studies.[17] The copolymers display a pseudo-eutectic point at the composition $BS_{45}CL_{55}$. This $BS_{45}CL_{55}$ copolymer is the only one in the series that can form two crystalline phases upon cooling from the melt, i.e., a PBS-rich phase and a PCL-rich phase (as evidence earlier by WAXS and DSC[17]), hence the two melting point values reported in Figure 6.1 for this

composition. To each side of the pseudo-eutectic point, a single crystalline phase is formed, either a PBS-rich phase (i.e., left hand side of the eutectic) or a PCL-rich phase (i.e., right hand side of the eutectic), with crystalline unit cells resembling those of PBS and PCL respectively.

In the present work, we have performed isothermal crystallization studies and calculated the equilibrium melting temperatures ($T_m^0$) of homopolymers and copolymers by employing the Hoffman-Weeks extrapolation. Examples of Hoffman-Weeks plots can be found in the Appendix, while Figure 6.1 reports the variation of the equilibrium melting temperatures obtained with composition. The $T_m^0$ values show a similar trend with composition as the apparent melting peak temperatures determined by DSC during non-isothermal experiments, and they also display a pseudo-eutectic point. These $T_m^0$ values will be employed in through this chapter, as they are needed to fit the Lauritzen and Hoffman nucleation and crystallization theory to analyze the experimental data.

### 6.2.2. Nucleation kinetics studied by PLOM

Counting the number of spherulites in PLOM experiments is the usual way of obtaining nucleation data by assuming that each spherulite grows from one heterogeneous nucleus. In this work, we have studied the nucleation kinetics by determining the nucleation density as a function of time by PLOM, from which nucleation rates can be calculated.

Figure 6.2 shows four examples of plots of the nucleation density $\rho_{nuclei}$ (nuclei/mm$^3$) as a function of time for neat PBS, neat PCL and two copolymers. The rest of the data can be found in the Supplementary Information (Figure A.6.1). The nucleation density increases almost linearly with time at short times, then it tends to saturate. The number of heterogeneous nuclei that are activated at longer times increase as nucleation temperature decreases, a typical behavior of polymer nucleation.[19] As expected, the nucleation density at any given time increases as $T_c$ decreases, because the thermodynamic driving force for primary nucleation increases with supercooling.[20]

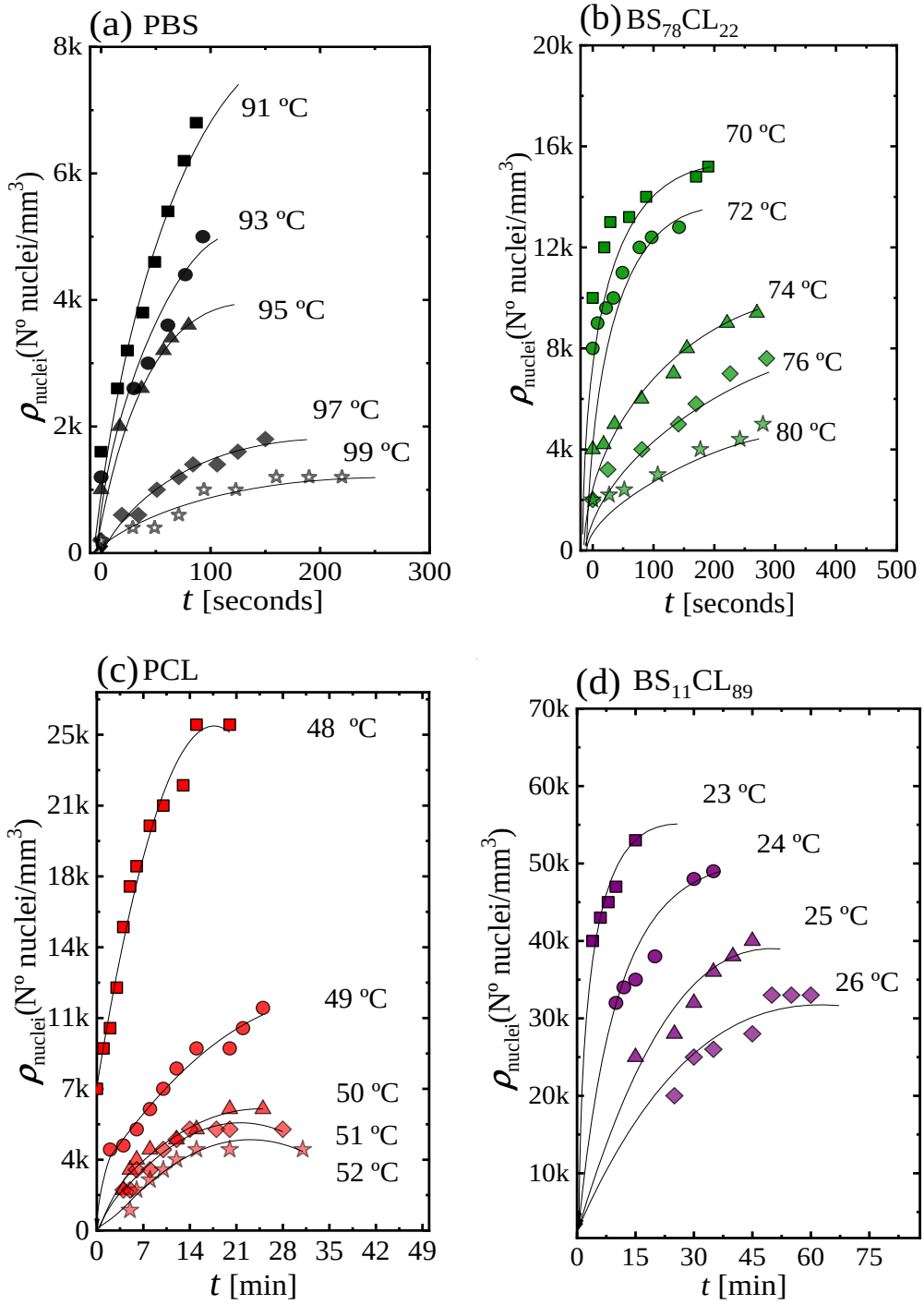


***Figure 6.2.*** *Nucleation kinetics data obtained by PLOM. Nuclei density as a function of time at different crystallization temperatures for the indicated samples.*

Figure 6.3 shows plots of nucleation density versus temperature taken at a constant nucleation time of 100 s for neat PBS and PBS-rich copolymers (Figure 6.3a) and 10 min in the case of PCL and $BS_{11}CL_{89}$ copolymer (Figure 6.3b).

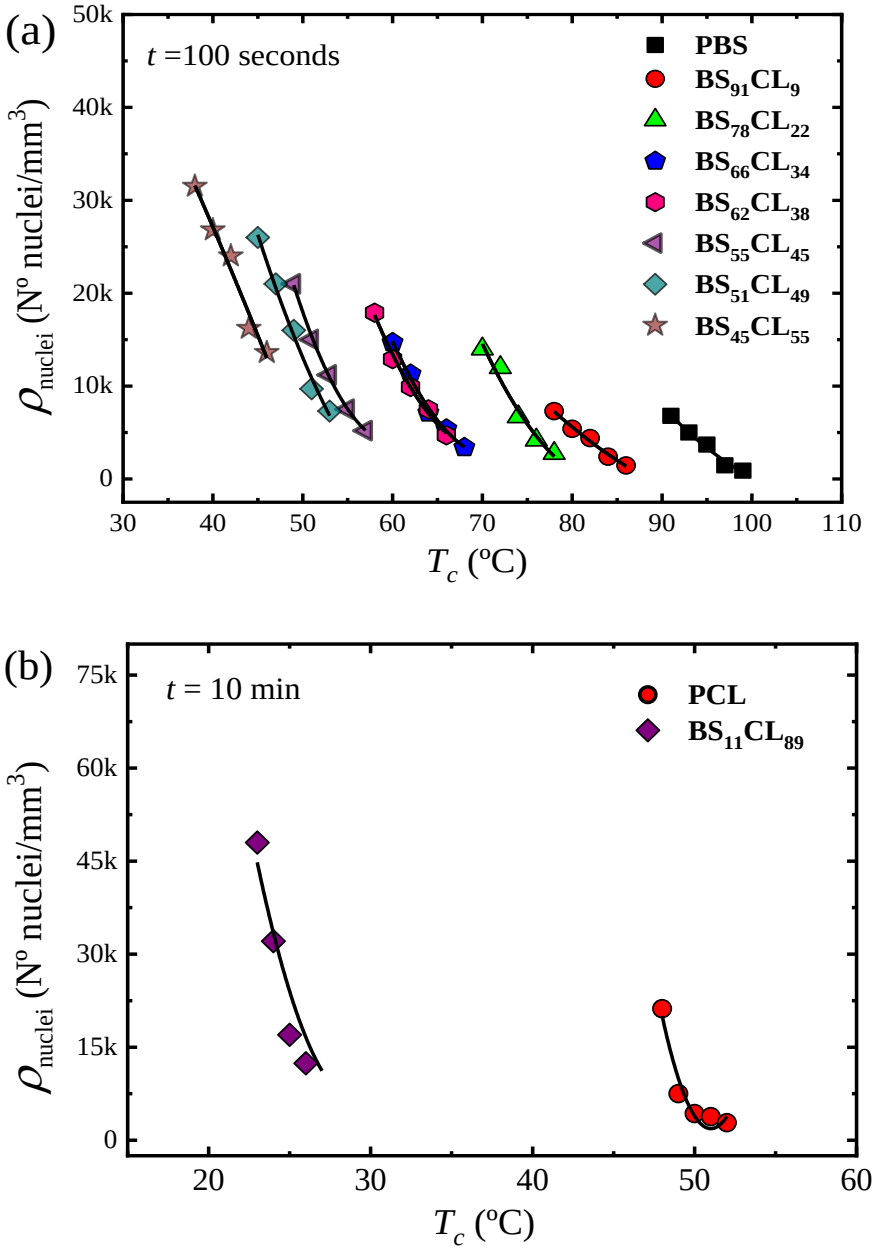


***Figure 6.3.*** *(a) Nuclei density during isothermal crystallization as a function of $T_c$ at a constant time of 100 seconds for PBS-rich compositions and (b) at 10 min for PCL-rich compositions.*

PBS exhibits the lowest nucleation density of all samples, therefore, the largest spherulites (see Figure 6.5 below). As the amount of CL comonomer increases in the PBS-rich copolymers (Figure 6.3a), the nucleation density increases, as well as the supercooling needed for nucleation. In the case of PBS-rich copolymers, Figure 6.3a (and Figure A.6.1 in the Appendix) shows that nucleation data for 7 different copolymers, with compositions ranging from 91 to 45% PBS.

The dependence of nucleation density on supercooling, can be observed in Figure A.6.2. The data presented in Figure 6.3a can be reduced to a supercooling range in between 32 and 40 °C, i.e., only 8 °C. This means that a large part of the horizontal shift in the curves of Figure 3a (spanning nearly 60 °C in crystallization temperature) is due to changes in supercooling. These changes are caused by the variations in equilibrium melting temperatures with composition (see Figure 6.1).

PCL has a higher nucleation density than PBS when compared at equal $T_c$ values or at equal supercoolings (see Figure 6.2). When a small amount of BS comonomer is incorporated, as in random copolymer $BS_{11}CL_{89}$, the nucleation density increases significantly (Figure 6.3b). Due to the very high nucleation density of the other PCL-rich composition copolymers (with higher amounts of PBS), it was impossible to determine their nucleation kinetics. Examples of the micro-spherulitic morphologies obtained for such PCL-rich copolymers can be observed in Figure 6.5 below.

It is interesting to note than in both sides of the pseudo-eutectic point (i.e., the PBS-rich side represented in Figure 6.3a and the PCL-rich side represented in Figure 6.3b), the copolymers exhibit higher nucleation density than their corresponding homopolymers. This behavior could be somewhat analogous to what has been observed in long chain branched polylactides (PLLAs) [21] or long-chain branched polypropylenes (PPs) with respect to linear analogues.[22] The interruption of crystallizable linear sequences with defects has been reported to increase nucleation density although the reasons are not clear.

In the present case, the linear crystallizable sequence of PBS, for instance, is being changed by the introduction of randomly placed PCL repeat units. Even though the random copolyesters can form a single phase in the melt, there may be at the segmental level, some preference for PBS-PBS local chain segmental contacts in comparison to less favorable PBS-PCL contacts. We speculate that this may drive the enhancement of nucleation, but more in depth studies would be needed to ascertain the exact reason for this behavior.

The Fisher-Turnbull nucleation theory [23] can be used to quantify the activation free energy of primary nucleation. This theory gives the steady-state rate of primary nucleation per unit volume and time, $I$ = d$N$/d$t$, for a heterogeneous nucleation process on a preexisting flat surface (or heterogeneous nucleus) as:

$$\log I = logI_0 - \frac{\Delta F^*}{2.3kT} - \frac{16\sigma\sigma_e(\Delta\sigma)T_m^{\circ 2}}{2.3kT(\Delta T)^2(\Delta H_V)^2} \qquad \text{Eq.6.1}$$

where $I_0$ is related to diffusion of polymeric segments from the melt to the nucleation site, $\Delta F^*$ is a parameter proportional to the primary nucleation free energy, and $\sigma$ and $\sigma_e$ are the lateral and fold surface free energies, respectively. $\Delta T$ is the supercooling defined as $\Delta T = T_m^0 - T_c$ and $T_m^0$ is the equilibrium melting point. $\Delta\sigma$ is the interfacial free energy difference, given by:

$$\Delta\sigma = \sigma + \sigma_{s/c} - \sigma_{s/m} \qquad \text{Eq.6.2}$$

in which $\sigma_{s/c}$ is the crystal-substrate interfacial energy and $\sigma_{s/m}$ is the melt-substrate interfacial energy. Therefore, $\Delta\sigma$ can be considered proportional to the surface tension properties of the substrate, polymer crystal and polymer melt. The interfacial free energy difference is a convenient way to express the nucleating ability of the substrate towards the polymer melt.

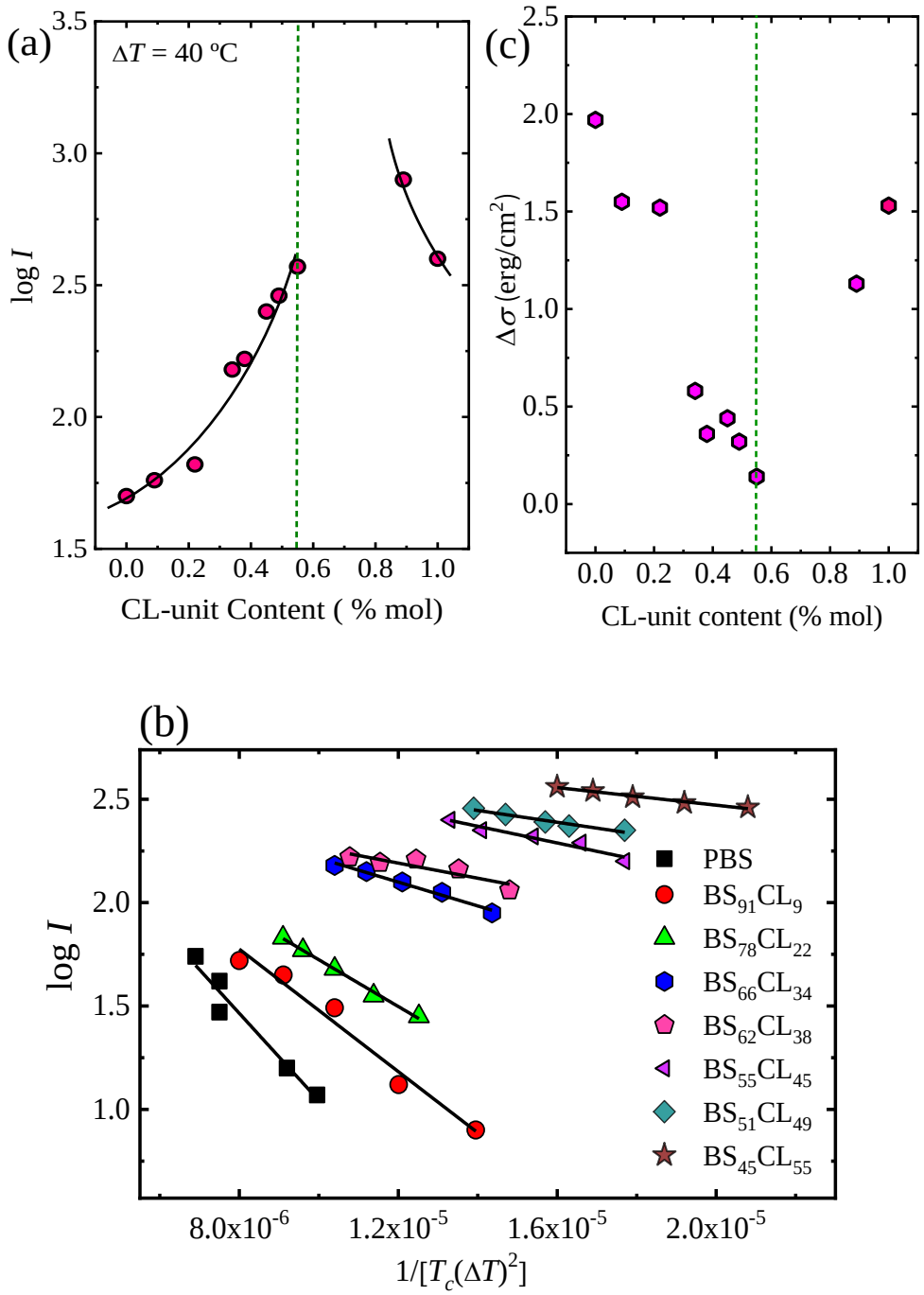


***Figure 6.4.*** *Nucleation rate (I) data: (a) Log I as a function of copolymer composition, expressed as mol % of CL units, taken at a constant supercooling of ΔT= 40 ºC. The segmented vertical line is drawn to indicate the pseudo-eutectic composition. (b) Plot of log I versus $1/T_c(\Delta T)^2$ for PBS-rich compositions. The black lines represent fittings to the Turnbull–Fisher equation (Equation 1). (c) Interfacial free energy difference (Δσ) as a*

*function of composition. The segmented vertical line is drawn to indicate the pseudo-eutectic composition.*

In this work, the values of $T_m^0$ (listed in Table A.6.1 and plotted in Figure 6.1) were obtained by isothermal crystallization DSC experiments followed by Hoffman-Weeks extrapolations (see Figure A.6.3). $\Delta H_v$ is the volumetric melting enthalpy (J/m$^3$) and it was estimated by $\Delta H_V = \Delta H_m^0 \times \rho$, so that $\rho$ = 1.26 g/cm$^3$ and $\Delta H_m^0$ =213 J/g for neat PBS [24] and $\rho$ = 1.14 g/cm$^3$ and $\Delta H_m^0 = 139.5$ J/g for neat PCL.[25]

In this chapter, we applied $\Delta H_m^0 = 213$ J/g for neat PBS that recently was practically measured by our group[24], which determined employing a combined DSC and X-ray diffraction method using isothermal crystallization data. This practical value is higher than $\Delta H_m^0$ = 110 J/g estimated empirically by the group contribution method [26], and fairly close to the = 210 J/g reported by Papageorgiu et al. [27]

The values of the nucleation rate *I* were obtained from the initial slope (i.e., at short measurement times, where linear trends are obtained) of the plots shown in Figure 6.2 and in Figure A.6.1. Figure 6.4a shows log *I* as a function of CL-unit molar fraction for a constant supercooling of $\Delta T$= 40 °C. The nucleation rate strongly depends on copolymer composition. Adding a comonomer randomly along the chain to either PBS or PCL largely increases the nucleation rate. In the PBS-rich composition side (to the left of the pseudo-eutectic point signaled by a vertical line in Figure 6.4a) the nucleation rate increases up to 7.5 times with respect to neat PBS, as the amount of PCL units in the random copolymer increases. Neat PCL nucleates faster than neat PBS. In the PCL-rich composition side, only one copolymer was measured (whose nucleation rate increased two-fold with respect to neat PCL), as increasing PBS content towards the pseudo-eutectic point increased nucleation rate so much that measurements were no longer possible.

Figure 6.4b shows the Turnbull–Fisher plots for PBS and PBS-rich compositions based on Equation 1. Turnbull–Fisher plots for PCL and $BS_{11}CL_{89}$

copolymer are presented in the supplementary information (Figure A.6.4). The nucleation data can be successfully fitted with the linearized version of Equation 6.1. From the slope, a value of the interfacial free energy difference ($\Delta\sigma$) can be obtained.

Small values of $\Delta\sigma$ are indicative of good nucleation efficiency since a lower amount of interfacial energy is required to form the crystal–substrate interface. Table 6.1 reports a value of $\Delta\sigma$ for PBS equal to 1.97 erg/cm$^2$. As seen in Figure 4c (and Table 6.1), this interfacial free energy difference progressively decreases in the copolymers as the amount of CL comonomer increases, indicating that the primary nucleation process is facilitated by copolymerization with PCL until the pseudo-eutectic point is reached. On the right-hand side of the pseudo-eutetic point in Figure 6.4c, PCL has a $\Delta\sigma$ value of 1.53 erg/cm$^2$, which is, as expected, smaller than that of PBS, as PCL has a larger nucleation density at equivalent supercoolings than PBS. The copolymer $B_{11}CL_{89}$ shows an even smaller value of $\Delta\sigma$, as the incorporation of PBS in the copolymer increases its nucleation capacity.

**Table 6.1.** Primary nucleation and growth isothermal kinetics data parameters according to equations 1 and 3 derived from experimental results obtained by PLOM.

| Copolyester | Nucleation, Eq.6.1 | | Growth, Eq.6.3 | | | | |
|---|---|---|---|---|---|---|---|
| | $\Delta\sigma$ (erg/cm$^2$) | [a] $R^2$ | $K_g^G$ (K$^2$) | $\sigma$ (erg/cm$^2$) | $\sigma_e$ (erg/cm$^2$) | $q$ (erg) | [b] $R^2$ |
| **PBS** | 1.97 | 0.938 | 8.66E+04 | 12.36 | 79.52 | 3.37E-13 | 0.983 |
| $\mathbf{BS_{91}CL_9}$ | 1.55 | 0.963 | 5.80E+04 | 12.36 | 55.01 | 2.33E-13 | 0.994 |
| $\mathbf{BS_{78}CL_{22}}$ | 1.52 | 0.993 | 5.12E+04 | 12.36 | 49.55 | 2.10E-13 | 0.973 |
| $\mathbf{BS_{66}CL_{34}}$ | 0.58 | 0.977 | 8.94E+04 | 12.36 | 88.90 | 3.78E-13 | 0.982 |
| $\mathbf{BS_{62}CL_{38}}$ | 0.36 | 0.913 | 8.92E+04 | 12.36 | 89.42 | 3.87E-13 | 0.982 |
| $\mathbf{BS_{55}CL_{45}}$ | 0.44 | 0.920 | 14.4E+04 | 12.36 | 148.8 | 6.30E-13 | 0.999 |
| $\mathbf{BS_{51}CL_{49}}$ | 0.32 | 0.944 | 14.5E+04 | 12.36 | 148.9 | 6.32E-13 | 0.999 |
| $\mathbf{BS_{45}CL_{55}}$ | 0.14 | 0.973 | 15.7E+04 | 12.36 | 165.5 | 7.02E-13 | 0.974 |
| $\mathbf{BS_{11}CL_{89}}$ | 1.13 | 0.867 | 14.7E+04 | 6.83 | 169.58 | 6.32E-13 | 0.999 |
| **PCL** | 1.53 | 0.999 | 10.4E+04 | 6.83 | 111.97 | 4.17E-13 | 0.996 |

[a] $R^2$ is the correlation coefficient for the fitting to the nucleation kinetic Turnbull-Fisher model (Eq.1), log $I$ vs. $1/T(\Delta T)^2$.

[b] $R^2$ is the correlation coefficient for the Lauritzen–Hoffman (Eq.3) linear plots, $lnG + U^*/R(T_c - T_0)$ vs. $1/f.Tc.\Delta T$.

### 6.2.3. Kinetics of superstructural growth (secondary nucleation) by PLOM

PBS, PCL and all the random copolymers prepared in this work exhibited spherulitic superstructural morphologies. Examples of the spherulites obtained at a constant supercooling value of 40 °C can be observed in Figure 6.5. Both PBS and PCL exhibited well-developed spherulites without banding. PBS-rich copolymers that contain more than 34% PCL exhibit clear banding. This is consistent with previous works indicating that the addition of diluents (for PBS-rich compositions, crystallization occurs while PCL chains are in the liquid state) to several polyesters induces banding. [28, 29]

Isothermal crystallization experiments were performed to follow the growth of spherulites as a function of time using PLOM. The growth rate was calculated from the slope of spherulite radius versus time plots, which were always observed to be highly linear.[30,31]

The experimental growth rates are plotted as a function of the isothermal crystallization temperatures employed in Figure 6a with a linear scale and in Figure 6b with a log scale, so that differences in *G* values for PBS-rich samples with PCL contents larger than 22% are observed. The incorporation of PCL repeat units in the random copolymers have a dramatic influence on the growth rate of the PBS-rich phase spherulites, as *G* decreases up to 3.5 orders of magnitude (Figure 6.6b). The decrease in *G* values with comonomer incorporation for the PBS rich copolymers is due to two reasons.

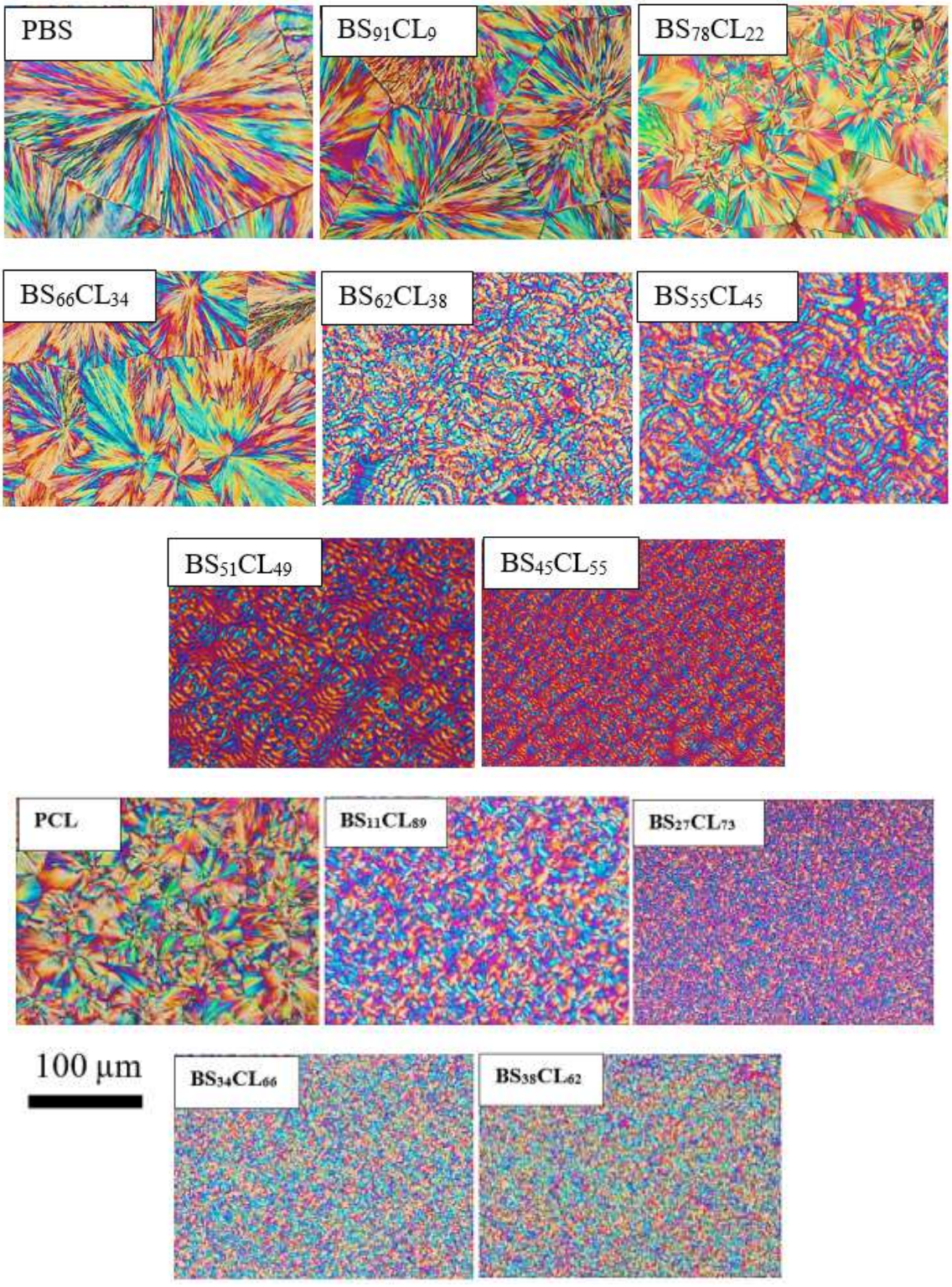


***Figure 6.5.*** *PLOM micrographs after isothermal crystallization at ΔT= 40 °C for all composition under this study.*

Firstly, as in any isodimorphic copolymer, there is a competition between inclusion and exclusion of repeat units within the PBS crystal lattice, where exclusion typically predominates. Secondly, incorporation of PCL repeat units in the copolymer chains reduces $T_g$ values (as shown in Figure 6.1), thereby causing a plasticization effect on the PBS-rich phase. In the case of the PCL-rich compositions, the spherulitic growth rate was determined for only one copolymer (i.e., $BS_{11}CL_{89}$), as in the other cases, as pointed out above, the nucleation rate and nucleation density were so high, that it was impossible to measure the extremely fast growth of very small spherulites. For this copolymer, the growth rate decreased in relative terms (see Figure 6.6c) by a factor of approximately 2.5 at a supercooling of 40 °C.

The data presented in Figures 6.6a are plotted as a function of supercooling in the Supplementary Information (Figure A.6.5). The PBS-rich growth rate data is shifted horizontally and but there is no overlap in the y axis values. If we were dealing with a simple solvent effect, the growth rate curves at different compositions should completely overlap in a master curve when plotted as a function of supercooling. The lack of superposition is due to the fact that PCL repeat units are randomly incorporated and covalently bonded with the PBS repeat units. The interruption of crystallizable PBS repeat units (by the majority of PCL repeat units that are excluded from the crystals) difficults the secondary nucleation process.

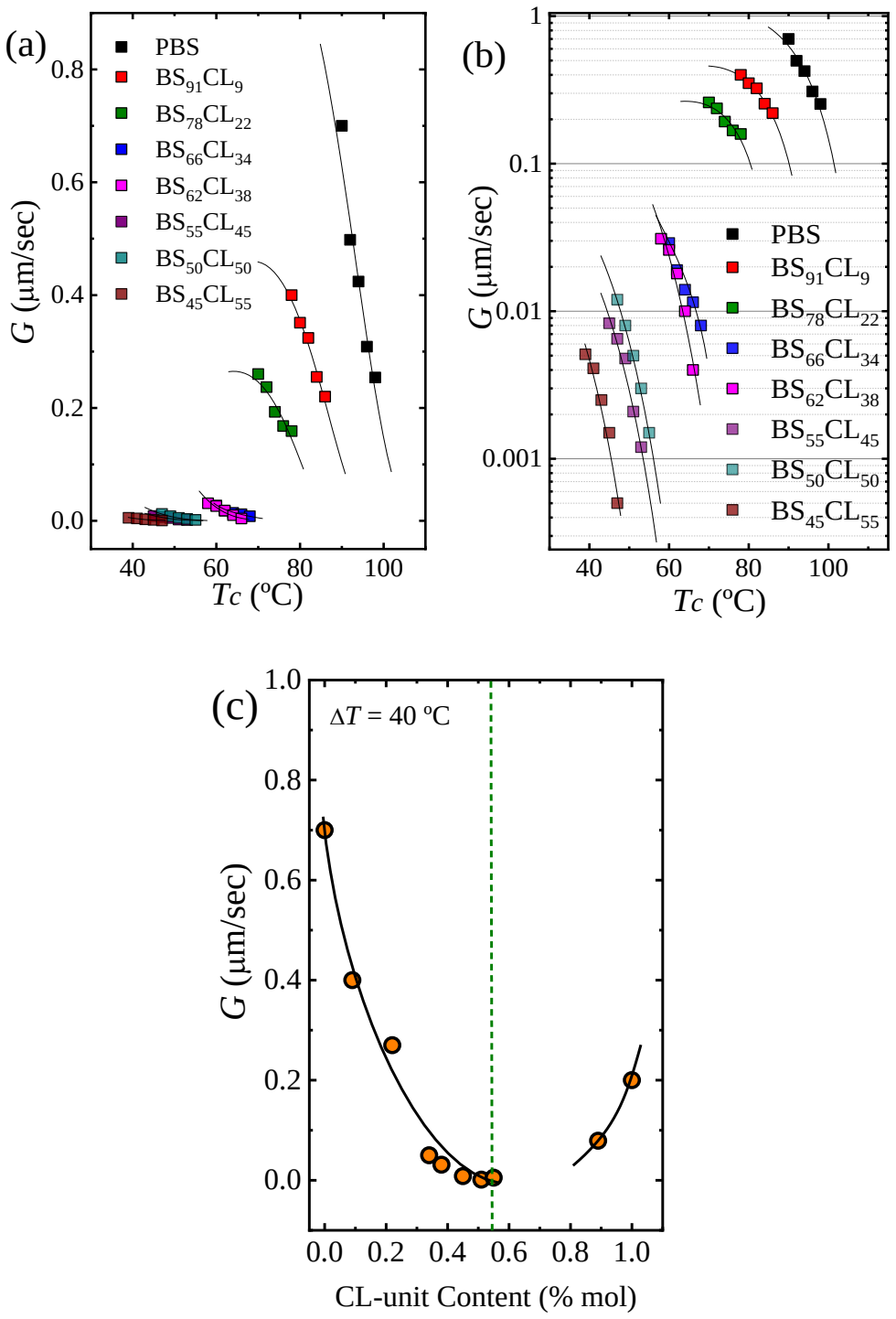


***Figure 6.6.*** *Spherulitic growth rates determined by PLOM. (a) Growth rate, G, as a function of $T_c$. (b) Same data as in (a) but G is plotted on a logarithmic scale. The black solid line are fits to the experimental data performed with the Lauritzen and Hoffman theory (L-H). (c) G versus CL-unit content at ΔT= 40 °C. The black line is polynomial fit.*

Figure 6.6c shows how the growth rate depends on composition at a constant supercooling of 40 ºC. The trend is the opposite as that obtained for primary nucleation (compare Figure 6.6c with Figure 6.4a). In order to quantify the restrictions imposed by the comonomer on the crystallization of the major component, we employ the Lauritzen and Hoffman theory, as it allows the calculation of energetic terms related to the secondary nucleation process (i.e., growth process).

The Lauritzen and Hoffman (LH) nucleation and growth theory was used to fit the spherulitic growth rate data as a function of isothermal crystallization temperature [32], according to the following equation:

$$G = G_0 \exp\left[\frac{-U^*}{R(T_c - T_0)}\right]\left[\frac{-K_g^G}{fT(T_m^0 - T_c)}\right] \qquad \text{Eq.6.3}$$

where $G_0$ is the growth rate constant that includes all the terms that are temperature-insensitive, $U^*$ is the transport activation energy which characterizes molecular diffusion across the interfacial boundary between melt and crystals (in this work, we employ a constant value of 1500 cal/mol). $T_c$ is the crystallization temperature and $T_0$ is a hypothetical temperature at which all chain movements freeze (taken as $T_g$-30 °C); $T_m^0$ is the equilibrium melting temperature and $f$ is a temperature correction factor given by the following expression: $f = 2T_c/(T_c + T_m^0)$.

The equilibrium melting temperatures $T_m^0$ were estimated by the Hoffman–Weeks linear extrapolation (Figure SI-3 and Table SI-1). The parameter $K_g^G$ is proportional to the energy barrier for secondary nucleation or spherulitic growth and is given by:

$$K_g^G = \frac{j b_0 \sigma \sigma_e T_m^0}{k \Delta h_f} \qquad \text{Eq.6.4}$$

where $j$ is assumed to be equal to 2 for crystallization in the so called Regime II, a regime where both secondary nucleation at the growth front and the rate of spread along the growing crystal face are comparable[26]. The other terms in the

equation are: the width of the chain $b_o$, the lateral surface free energy $\sigma$, the fold surface free energy $\sigma_e$, the Boltzman constant $k$, and the equilibrium latent heat of fusion, $\Delta H_m^0$.

Plotting $\ln G + \frac{-U}{R(Tc-T0)}$ versus $1/T_c(\Delta T)f$ (i.e., the Lauritzen and Hoffman plots) gives a straight line and its slope and intercept are equal to $K_g^G$ and $G_0$ respectively. Examples of LH plots can be found in the Supplementary Information, Figures SI-6. Having the value of $K_g^G$, the magnitude of $\sigma\sigma_e$ can be calculated from equation 5. In order to calculate separately the values of $\sigma$ and $\sigma_e$, the following expression can be used [33]:

$$\sigma = 0.1\ \Delta\ h_f \sqrt{a_0 b_0} \qquad \text{Eq.6.5}$$

where $a_0b_0$ is the cross sectional area of the chain. To obtain the parameters of the LH theory, the following values were used for neat PBS and BS-rich compositions: $a_0$ = 5.25Å and $b_0$ = 4.04 Å [34-35], and for neat PCL and CL-rich compositions : $a_0$= 4.52 Å and $b_0$= 4.12 Å [36].

Finally, $q$, the work done by the macromolecule to form a fold is given by [33]:

$$q = 2a_0b_0\sigma_e \qquad \text{Eq.6.6}$$

The solid lines in Figure 6a and 6b correspond to fittings to Equation 6.3. Table 6.1 shows that $K_g^G$ values (which are proportional to the energy barrier for spherulitic growth) for the PBS-rich crystal phase tend to increase as PCL repeat units are incorporated in the random copolymers until a maximum value is reached at the pseudo-eutectic point. Similar trends are observed for the fold surface free energy and for the work done to form folds.

A plot of fold surface free energy versus composition can be found in the Supplementary Information (Figure A.6.7). These results quantitatively measure how comonomer incorporation difficults the spherulitic growth of the PBS-rich phase. A similar interpretation can be done to the mirror values presented in Table 6.1 for PCL and the $BS_{11}CL_{89}$ copolymer with respect to the PCL phase.

The results presented in the two sections above can be summarized by comparing Figure 6.4 with Figure 6.6. The incorporation of comonomers at each

side of the eutectic causes an increase in the nucleation density and nucleation rate but at the same time a decrease in spherulitic growth rate. These two processes, primary nucleation and growth are combined when a semi-crystalline polymer is crystallized from the melt. Their simultaneous effect can be ascertained by determining overall crystallization kinetics by DSC.

### 6.2.4. Overall crystallization kinetics studied by DSC

The overall isothermal crystallization kinetics considers both nucleation and growth, and can be conveniently determined by isothermal DSC experiments. Figure 7a and Figure 7b show the experimental overall crystallization rate expressed as the inverse of the crystallization half time ($\tau_{50\%}$). By DSC, we were able to determine the overall isothermal crystallization kinetics for both homopolymers and all copolymers (5 copolymers where only the PBS-rich phase crystallized and 4 copolymers where only the PCL-rich phase can crystallize).

For the special composition at the eutectic point (i.e., $BS_{45}CL_{55}$) that shows two crystalline phases, PBS-rich phase and PCL-rich phase, we have performed isothermal crystallization using different protocols. For the PBS-rich phase crystallization, isothermal DSC experiments are performed at temperatures where the PCL-rich phase is in the melt and cannot crystallize, while in the PCL-rich phase, a special protocol has been adopted to previously crystallize the PBS-rich phase to saturation (see experimental part).

Figure 6.7a and Figure 6.7b show the strong dependence of the overall crystallization rate and the temperature range where measurements were possible on copolymer composition. In the case of the PBS and all PBS-rich compositions, the overall crystallization proceeds from a single phase melt. Upon increasing PCL content, the amount of the crystallizable PBS-rich phase decreases and there will be more molten PCL component causing a plasticization (“solvent effect”). In addition, the effect of PCL exclusion in the PBS-rich crystal lattice may cause some further reduction in crystallization rate. Figure 6.7a shows that the temperature

needed for crystallization decreases as PCL content in the copolymer increases, while the overall crystallization rate measured at the minimum $T_c$ value possible tends to decrease.

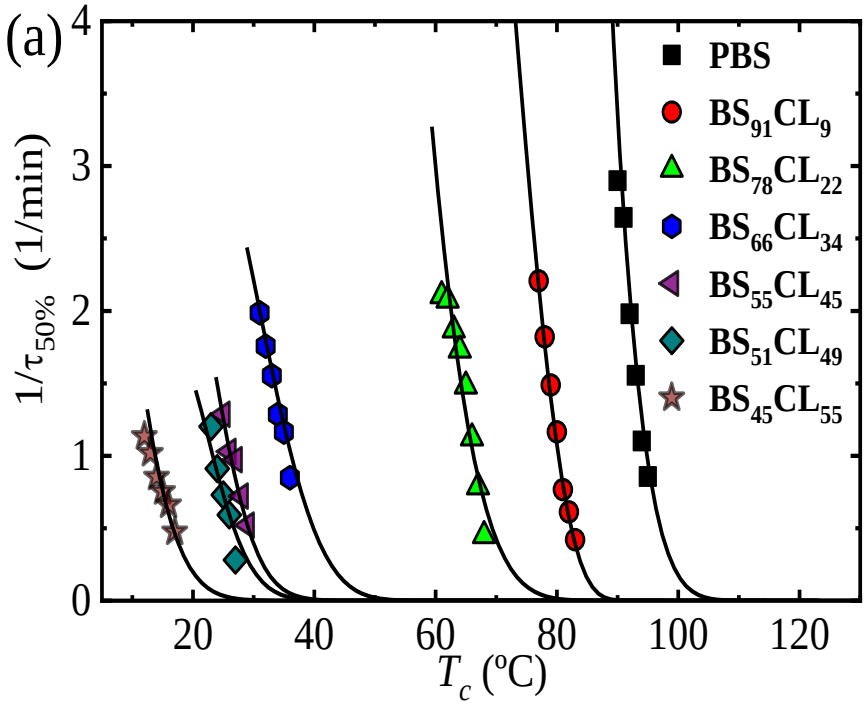


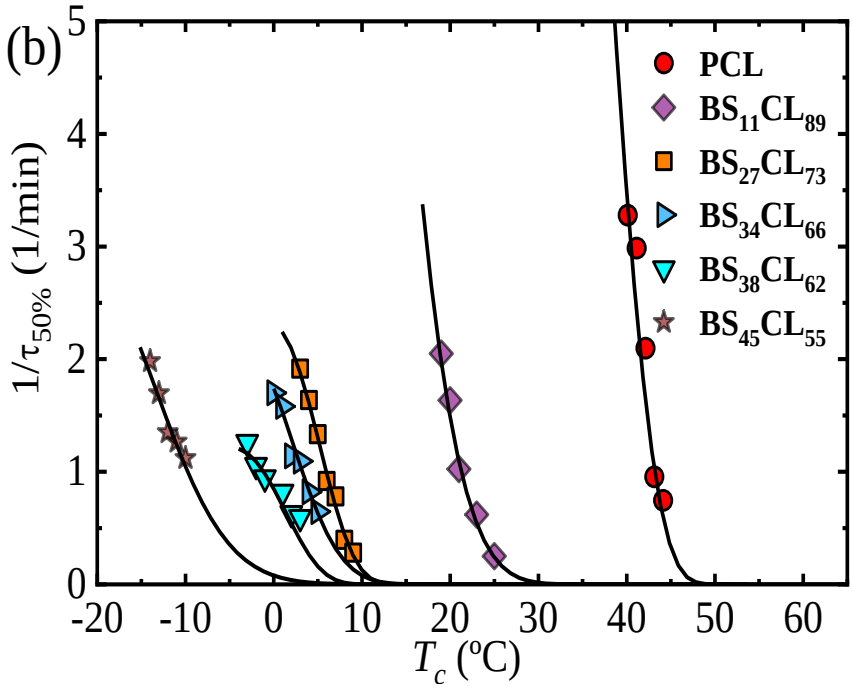

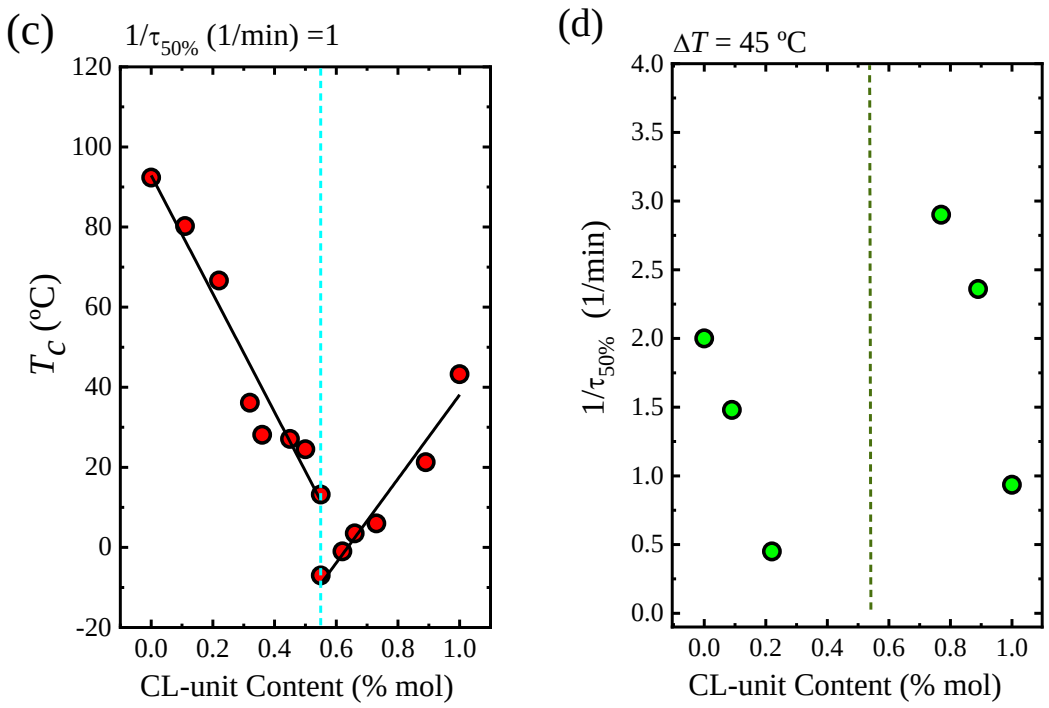


***Figure 6.7.*** *Overall crystallization versus isothermal crystallization temperature for neat PBS and PBS-rich compositions (a) and for neat PCL and PCL-rich compositions (b) versus $T_c$. Continuous lines correspond to the fitting of the Lauritzen-Hoffman theory with the parameters in Table 3. Changes of $T_c$ versus CL-unit content in a constant rate ($1/\tau_{50\%}$ = 1 1/min) (c). Changes of inverse of half-crystallization time, $1/\tau_{50\%}$ versus CL-unit content in a constant supercooling degree, ΔT= 45 °C (d).*

Figure 6.7c plots the crystallization temperature needed to obtain the same overall crystallization rate of 1 $min^{-1}$. These $T_C$ values monotonically decrease with PCL content until the pseudo-eutectic region is reached. On the PCL-rich side, Figure 7b and 7c show similar results, as the crystallization temperatures needed to crystallize the PCL phase decrease as PBS repeat units are added to the copolymer.

To check if the supercooling is playing a major role upon changing composition, we plot the data contained in Figure 6.6a and Figure 6.6b as a function of $\Delta T$ in Figure 8a and Figure 6.8b respectively. Surprisingly, the trends are quite different depending on the phase under consideration, or the composition range.

Figure 8a shows that the curves of PBS-rich overall growth rate data that originally spanned a $T_c$ range of approximately 90 °C (in Figure 6.7a) are now within 30 °C in supercooling, attesting for the thermodynamic compensation of the solvent effect, as the PCL-rich phase is in the melt. In fact, the curves of PBS and $BS_{91}CL_9$ completely overlap, while that of $BS_{78}CL_{22}$ is relatively close to that of neat PBS. However, beyond 22% Cl incorporation in the copolymer, the samples require much larger supercooling to crystallize. It is clear that the dominant factor to the left of the eutectic point is the growth rate, as the results presented in Figures 6.6a and 6.7a imply an overall crystallization rate reduction with PCL, both in terms of crystallization temperature or supercooling. In spite of the increase in nucleation density and nucleation rate (see Figures 6.3 and 6.4) with PCL incorporation in the copolymer, it is the very large decrease in growth rate (of up to 3 orders of magnitude, see Figure 6.7b) that dominates, leading to a decrease in overall crystallization rate (Figures 6.7a and 6.8a).

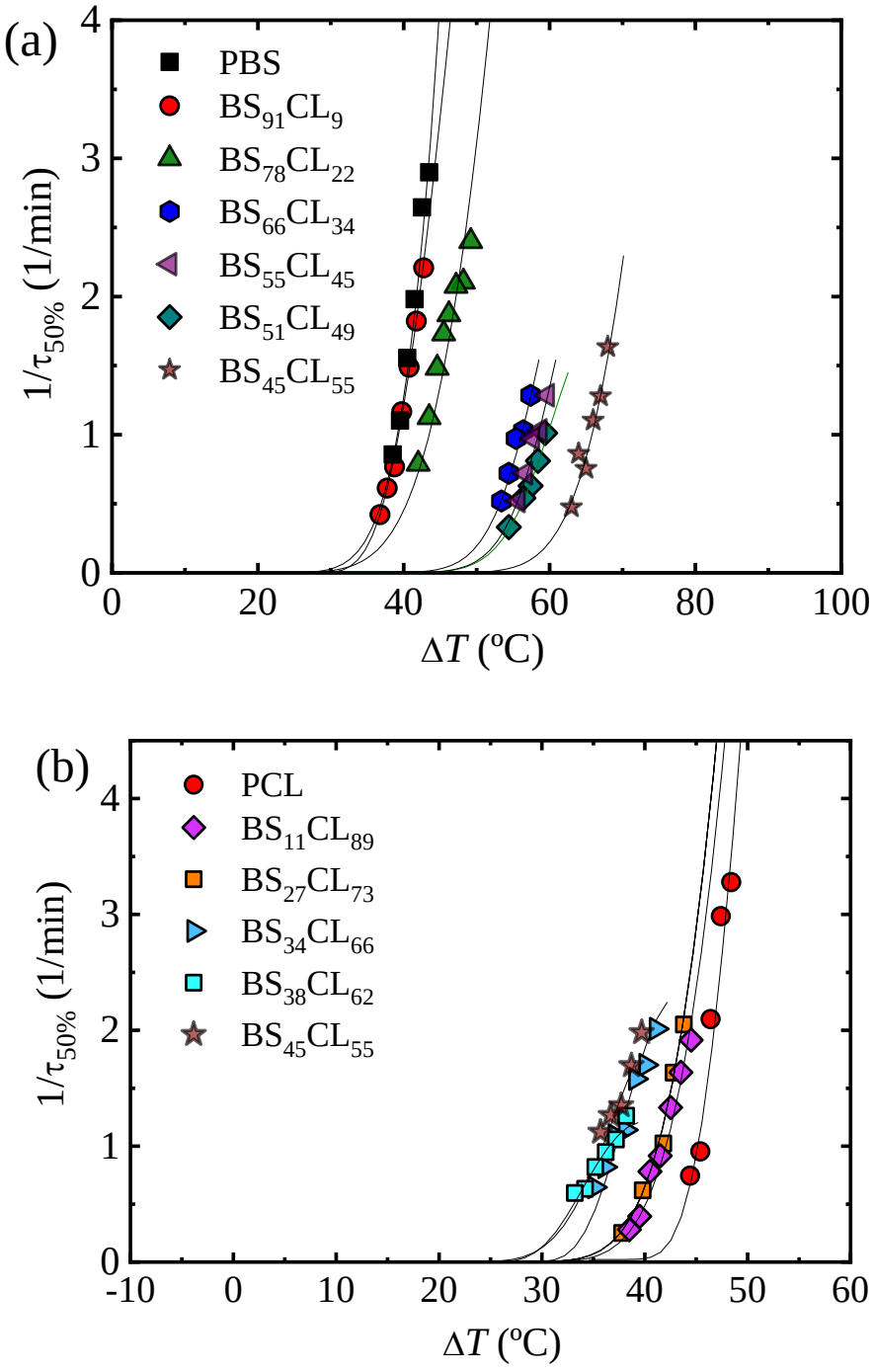


***Figure 6.8.*** *Overall crystallization versus isothermal crystallization temperature for neat PBS and PBS-rich compositions (a) and for neat PCL and PCL-rich compositions (b) versus supercooling temperature.*

Figure 6.7d represents the overall crystallization rate as a function of composition for a constant supercooling of 45 °C. In the PBS-rich side of the pseudo-eutectic region (left hand side of Figure 6.7a), only 3 data points are plotted, as they are the only ones that could be measured at such constant supercooling value (check Figure 6.8a). The trend clearly shows a significant decrease in overall crystallization rate as CL unit content increases, as expected from Figures 6.7a and 8a and the discussion above. Even though the value of supercooling is not exactly the same (with only 5 °C difference), a comparison with Figures 6.4a and 6.6c clearly indicates that the PBS-rich phase overall crystallization is dominated by growth rate.

Figure 6.8b shows remarkable results for the PCL-rich phase overall crystallization. The $1/\tau_{50\%}$ curves versus temperature span a temperature range of 65 °C (Figure 6.6b). When they are plot as a function of supercooling, they only span 15 °C. However, they do not overlap, as would be expected for a simple solvent effect. In fact, the supercooling needed for crystallization of the PCL-rich phase remarkably decreases as PBS repeat units are included in the copolymer. The results indicate an acceleration of the overall crystallization rate (at constant supercooling) that can only be explained by the increase in both nucleation density and nucleation rate. We were only able to measure the increase in nucleation density and nucleation rate in Figure 6.3 and 6.4 for neat PCL and $BS_{11}CL_{89}$, as further incorporation of BS units increased the nucleation density so much that measurements by polarized optical microscopy of nucleation rate became impossible. Hence, we are convinced that primary nucleation enhancement upon PBS repeat unit incorporation in the copolymers is the reason behind the acceleration of the overall crystallization kinetics, when this is considered in terms of supercooling. In the right-hand side of the pseudo-eutectic point in Figure 6.7d, the increase in overall crystallization rate at a constant supercooling of 45 °C can be appreciated.

The Lauritzen and Hoffman theory can also be applied to fit the overall crystallization data presented above. Equation 6.3 has to be modified to employ, as a characteristic rate, the inverse of the half-crystallization time determined by DSC, as follows [37]:

$$1/\tau_{50\%} = 1/\tau_{50\%} \exp\left[\frac{U}{R(T_c - T_0)}\right]\left[\frac{-K_g^{\tau}}{fT(T_m^0 - T_c)}\right] \qquad \text{Eq.6.7}$$

where all the terms have been defined above, except for $K_g^{\tau}$, which now represents a parameter proportional to the energy barrier for both primary nucleation and spherulitic growth. The superscript □ is used to indicate its origin (coming from DSC data, and hence from fitting $1/\tau_{50\%}$ versus crystallization temperature). In this way, it is different from $K_g^G$, defined in Equation 2, derived from growth rate data and therefore proportional just to the free energy barrier for secondary nucleation or growth. The solid lines in Figures 7a, 7b, 8a and 8b represent the fits to the Lauritzen and Hoffman theory. Table 3 on the other hand reports all the relevant parameters.

Wu et al. [38] and Papageorgiou et al.[39] reported the $K_g^{\tau}$ value of neat PBS equal to 1.157x10$^5$ and 2.64x10$^5$ K$^2$, respectively, that those are close to our obtained value 2.04x10$^5$ K$^2$. Besides, the $K_g^G$ value of neat PBS reported [39] equal to 1.88x10$^5$ that is slightly higher than the obtained value in this work, 0.87x10$^5$ K$^2$. For neat PCL sample, $K_g^G$ =7x10$^4$ and $K_g^{\tau}$ =10x10$^4$ K$^2$ values are reported [40], that are higher than the obtained values in this work. In addition, they reported [40] $q_g^G$ =3x10$^{-13}$ and $q_{g\tau}$□ = 4.2x10$^{-13}$ values for neat PCL that are lower in compare to the obtained values in this work.

Figure 6.9 plots both $K_g$ values, obtained by PLOM ( $K_g^G$) and DSC ( $K_g^{\tau}$) as a function of CL-unit molar content. As expected, all $K_g^{\tau}$ values are larger than $K_g^G$ values, as DSC measurements take into account both nucleation and growth while PLOM measurements considered only growth (see more details in ref. [37])

In the case of $K_g^G$ values, the trends observed are expected in view of the results obtained in Figure 6.6. The energy barrier for crystal growth increased with CL-unit molar content, since growth rate decreased as comonomer incorporation increased. On the other hand, when we analyze the results obtained for $K_g^\tau$ in Figure 6.9, we noticed that there is a clear asymmetry depending on which side of the pseudo-eutectic region the material is. On the PBS-rich side (left hand side of Figure 6.9), $K_g^\tau$ values rapidly increased upon Cl units addition. This is expected from the results presented in Figure 7d, where a large decrease in overall crystallization rate for the PBS-rich side of the composition range can be observed.

In the case of the PCL-rich composition range, we would have expected a decrease in $K_g^\tau$ values with PCL content increases according to Figure 6.7d. Instead, we observe in Figure 6.9 that the energy barrier for both nucleation and growth does not significantly change with composition (see right hand side of Figure 6.9). We have to remember that for the PCL-rich copolymers the situation is particularly complicated as the nucleation density and rate increase with CL-unit content but the growth rate decreases. Hence, even though according to Figure 6.7d the overall crystallization rate at constant supercooling seems to be dominated by primary nucleation, the values of $K_g^\tau$ are obtained from the slope of the Lauritzen and Hoffman plots that take into account the full range of supercoolings where the measurements were taken. Therefore, it seems that when the overall energy barrier is considered, there is a balance between nucleation and growth which keeps the $K_g^\tau$ values constant with composition.

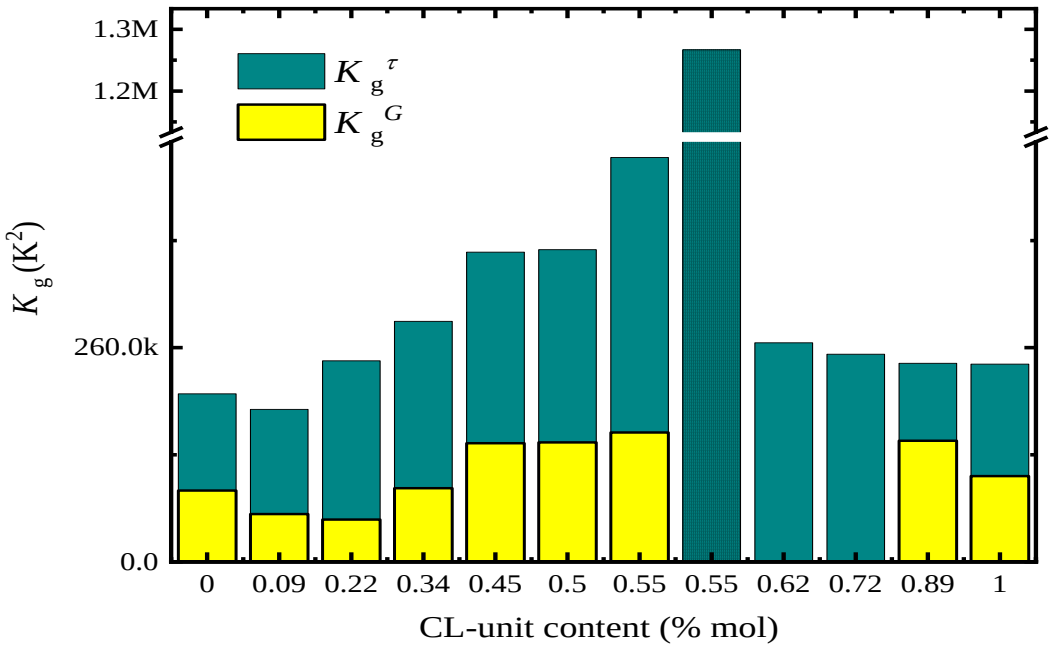


***Figure 6.9.*** *$K_g$ versus CL-unit molar fraction that obtained for PLOM experiments ($K_g^G$) and DSC experiments ($K_g^{\tau}$).*

***Table 6.2.*** *Parameters obtained from fitting the DSC data presented in Figure 7 (a-b) to the Lauritzen–Hoffman model (Equation 6.7).*

| Copolyester | $K_g^t$ (K²) | $R^2$ | $\sigma$ (erg/cm²) | $\sigma_e$ (erg/cTm²) | $q$ (erg) |
|---|---|---|---|---|---|
| **PBS** | 2.04E+05 | 0.9697 | 12.36 | 186.88 | 7.93E-13 |
| $\mathbf{BS_{91}CL_9}$ | 1.85E+05 | 0.9938 | 12.36 | 173.80 | 3.37E-13 |
| $\mathbf{BS_{78}CL_{22}}$ | 2.44E+05 | 0.9514 | 12.36 | 236.34 | 10.0E-13 |
| $\mathbf{BS_{66}CL_{34}}$ | 2.92E+05 | 0.9958 | 12.36 | 290.42 | 12.3E-13 |
| $\mathbf{BS_{55}CL_{45}}$ | 3.76E+05 | 0.9775 | 12.36 | 387.34 | 16.4E-13 |
| $\mathbf{BS_{51}CL_{49}}$ | 3.79E+05 | 0.9973 | 12.36 | 388.50 | 16.8E-13 |
| $\mathbf{BS_{45}CL_{55}}(BS-rich)$ | 4.91E+05 | 0.9502 | 12.36 | 518.73 | 22.0E-13 |
| $\mathbf{BS_{45}CL_{55}}(CL-rich)$ | 12.5E+05 | 0.9880 | 6.83 | 1376.9 | 51.3E-13 |
| $\mathbf{BS_{38}CL_{62}}$ | 2.66E+05 | 0.9917 | 6.83 | 328.01 | 12.6E-13 |
| $\mathbf{BS_{27}CL_{73}}$ | 2.52E+05 | 0.9845 | 6.83 | 305.91 | 11.4E-13 |
| $\mathbf{BS_{11}CL_{89}}$ | 2.41E+05 | 0.9945 | 6.83 | 278.43 | 10.4E-13 |
| **PCL** | 2.40E+05 | 0.9082 | 6.83 | 260.61 | 9.71E-13 |

*$R^2$ is the correlation coefficient for the Lauritzen–Hoffman (Eq.7) linear plots $\ln(1/\tau_{50\%}) + U^*/R(Tc - T\alpha)$ vs. $1/f{\cdot}Tc{\cdot}\Delta T$.*

### 6.2.5. Fitting of DSC Isothermal Data to the Avrami Model

To analyze the isothermal crystallization kinetics, data from DSC (heat flow as a functional time) was fitted to the classical Avrami equation[33, 41-42] (Equation 3) to define the primary crystallization process using the Origin plug-in developed by Lorenzo et al.[43]

$$1 - \phi_c(t - t_0) = \exp(-K(t - t_0)^n) \qquad \text{Eq.6.8}$$

where $\phi$ is the relative crystalline volume fraction of the polymer as a function of time. $t$ is the crystallization time and $t_0$ is the induction time.

The fits to the Avrami equation were performed using the Origin plug-in developed by Lorenzo et al., and in Figure A.6.9 an example of a representative fit of Avrami model for the $BS_{78}CL_{22}$ copolymer crystallization at 65 °C is plotted. Even though Avrami fit estimations were made for all the compositions and at different crystallization temperatures, the result of the $BS_{78}CL_{22}$ copolymer was taken as an example of a good fit between the Avrami model and the experimental data predicted by DSC isothermal scans. In Figure A.6.9c it can be observed how the Avrami equation could perfectly describe the overall crystallization kinetics of the chosen copolymer in the primary crystallization range, i.e., in a conversion range of 3−20%, with a correlation coefficient of 1.000. The fit of the Avrami equation was very good until 100% conversion (see Figure A.6.9a and Figure A.6.9b) and only experienced significant deviations from the experimental data beyond 100% conversion.

The parameters *K* and *n* are dependent on the nucleation type and the crystal growth geometry, *K* can be considered an overall transformation rate constant, and *n* is the Avrami index, which depends on the mechanism of transformation. This fitting allows the determination of the constants *n* and *K* from a plot of *log (-ln( (1-ϕ))* vs *log(t*), and the half-crystallization time $\tau_{50\%}$ (time that is needed from the sample to achieve half of the possible degree of crystallinity at a

given temperature) as well. For all copolyesters, quite good linearity is achieved with the correlation coefficient $R^2 \geq 0.9999$. Overall crystallization kinetic parameters for PBS-*ran*-PCL copolyesters based on the Avrami model are inserted in Appendix, Table A.6.2.

It is known that the value of Avrami index *n* strongly depends on both the mechanism of nucleation ($n_n$) and the morphology of crystal growth ($n_d$). Taking into account the experimental errors, *n* for all copolymers and homopolymers was around ~2.5 that indicates growth dimensionality occurs between 3D spherulites (superstructural three-dimensional aggregates of radial lamellae, *n* = 3), and 2D axialites (two-dimensional lamellar aggregates, *n*=2) [43].

### 6.2.6. Double Crystallization at the pseudo-eutectic point

For the copolymer whose composition is within the pseudo-eutectic point, i.e., $BS_{45}CL_{55}$, we have performed isothermal crystallization in a wide range of crystallization temperatures $T_c$, to find the temperature region where only one of the phases, PBS or PCL, is able to crystallize. Figure 10 shows the heating DSC scan recorded at 10 ºC/min for $BS_{45}CL_{55}$ sample after it was isothermally crystallized at the indicated $T_c$ values.

At least five different endotherms can be found upon close examination of Figure 10 and we have indicated with dashed lines how these endotherms approximately shift depending on the $T_c$ values employed before heating the samples. The first melting peak $T_{m1}$ is present in all melting curves and its location is almost at 7 °C higher than the crystallization temperature. This peak has been traditionally regarded as the melting of thin crystals formed during the secondary crystallization process.[44] The second peak, labeled $T_{m2}$, appeared at $T_c$ values lower than -6 ºC and corresponds to the melting of PCL-rich crystals. The third peak or $T_{m3}$ labeled peak in Figure 10 highly depends on the isothermal crystallization temperature and corresponds to the melting of the PBS-rich crystals, which were formed during the isothermal crystallization.

In addition, a melting peak ($T_{m5}$) at around 50 °C and another one just below it ($T_{m4}$) were observed. The melting peak labeled $T_{m5}$ corresponds to the melting of PBS crystals that have reorganized during the heating scan, and have a melting point which is almost constant at around 50 °C, regardless of the crystallization temperature. [45-46] The $T_{m2}$ and $T_{m3}$ peaks increase almost linearly with increasing $T_c$. As shown in Figure 6.10, $T_{m3}$ disappeared in the DSC heating curves where the crystallization temperature is less than -9 °C.

The morphologies obtained after isothermal crystallization at 3 selected temperatures can be observed in Figure 10 b-d. As it will be shown below, WAXS experiments have confirmed that at very low $T_c$ values including -12 °C, only PCL-rich crystals can be formed. Figure 10b shows small spherulites that were formed at $T_C$ = -4 °C with spherulites size around 10 µm. At $T_C$= -8 °C, where both PCL and PBS crystals can form, there are two crystals size, one with 4 µm radii (PBS crystals) and another with around 1.5 µm size(PCL crystals), see Figure 8c. Figure 8d shows only PCL crystals with small spherulites size (less than 1 µm) at $T_C$ =-12 °C.

We performed in situ synchrotron SAXS/WAXS experiments for the sample at the pseudo-eutectic point in order to clarify the temperature range of crystallization of the PBS-rich and the PCL-rich phases and corroborate the assignment of the thermal transitions in Figure 10. These experiments were performed during isothermal crystallization (for 20 min) at three different $T_c$ values chosen from three different crystallization regions in Figure 6.10.

Figure 11 a-c shows selected real time WAXS diffractograms for $BS_{45}CL_{55}$ (i.e., the sample at the pseudo-eutectic point) measured during isothermal crystallization at -12, -9, and -6 °C. If the sample shows characteristic reflections at $q$=13.9 and 16.1 1/nm, they correspond to the PBS (020) and (110) crystallographic planes. If the sample exhibits reflections at $q$=15.3 and 17.4 1/nm, they are attributed to the PCL (110) and (200) planes [10].

Changes in the crystallization temperature strongly affect the diffraction pattern at the pseudo-eutectic point. As can be seen in Figure 11, at -12 °C only the PCL-rich phase is able to crystalize (Figure 6.11a) while at -6 °C (Figure 11c) only the

PBS-rich phase crystallizes. On the other hand, at the intermediate $T_c$ value of -9 °C, both PBS-rich and PCL-rich phases can crystallize. If the DSC curves of Figure 10 are considered again, the WAXS assignments are consistent with the heating runs after crystallization for all samples crystallized at -9 °C and higher. In the case of low crystallization temperatures, i.e., below -9 °C, it should be noted that WAXS indicate that only the PCL-rich phase can crystallize.

The DSC heating runs shown in Figure 6.10 also show melting transitions corresponding to the melting of PBS-rich phase. These PBS-rich phase crystals must be formed by cold-crystallization during the heating scan for the samples crystallized at -10 °C, -12 °C and -14 °C in Figure 10. In fact, upon close examination of Figure 10, the end of a cold crystallization process can be observed just after the melting peak of the PCL-rich phase crystals.

Taking into account the WAXS and DSC results presented in Figures 6.10 and 6.11, the DSC curves in Figure 6.10 were plotted with a color code to indicate which phases can crystallize during isothermal crystallization depending on the $T_c$ values employed. If the $T_c$ values are -10 °C or lower, only the PCL-rich phase can crystallize, and the curves were arbitrarily plot in red in Figure 6.10. If the $T_c$ values are between -9 °C and -7 °C (including these two temperatures), both the PCL-rich and the PBS-rich phases can crystallize (green curves in Figure 6.10). Finally, if the $T_c$ temperatures are -6 °C and above, only the PBS-rich phase can crystallize.

The pseudo-eutectic sample, $BS_{45}CL_{55}$, exhibits a very interesting phase behavior, as depending on the crystallization conditions, one or both phases can be formed. We have studied previously the non-isothermal crystallization of the same copolymers employed here.[17] It is interesting to note that under non-isothermal conditions, the cooling rate employed determines which phase can crystallize and also if one or two phases are formed. In this work, on the other hand, we show that one or two phases can be formed depending on the isothermal crystallization temperature chosen. Therefore, the properties of this isodimorphic copolyester with pseudo-eutectic composition can be tailored by varying both non-isothermal

or isothermal crystallization conditions, a remarkable and novel behavior as far as the authors are aware.

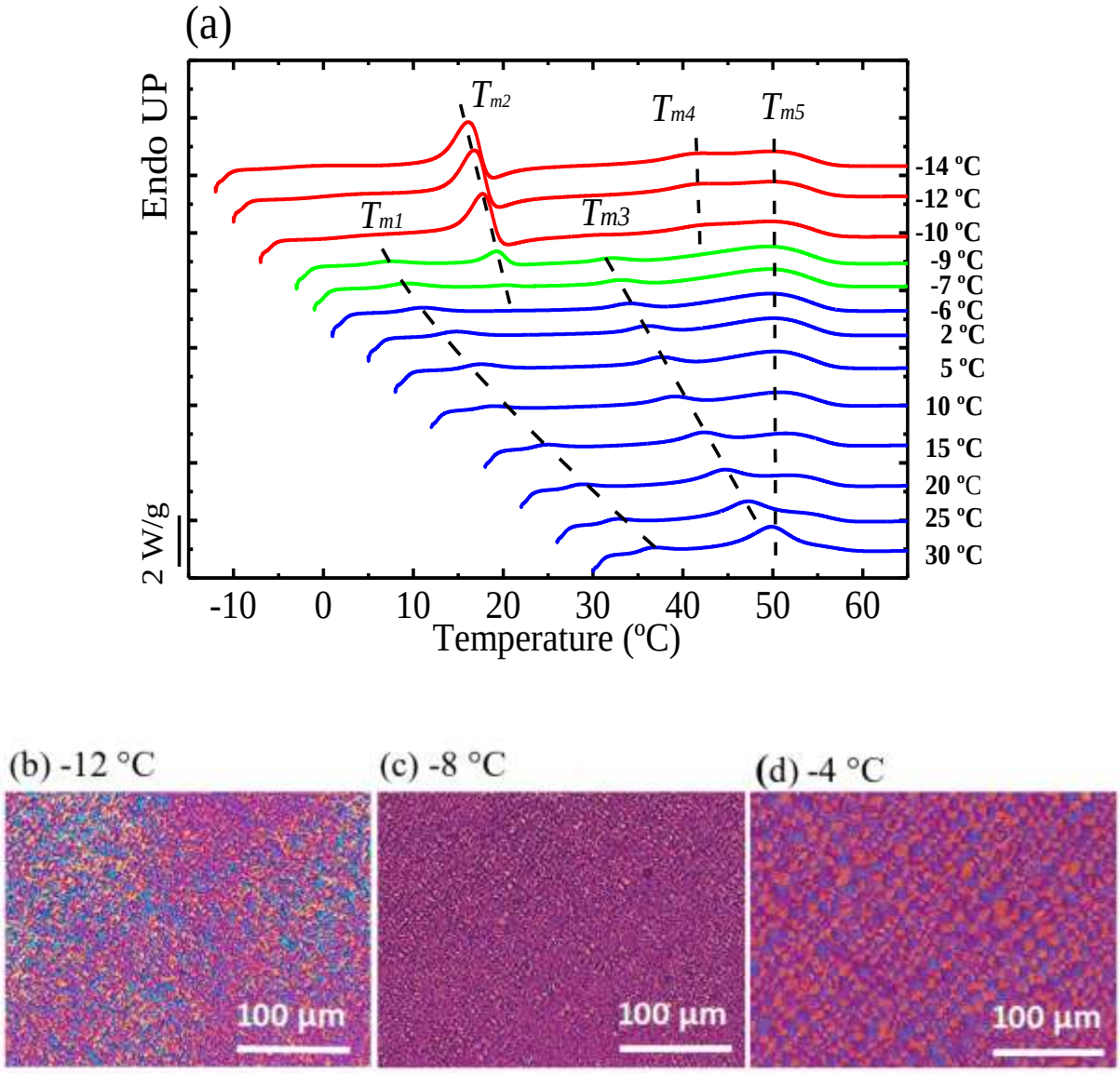


***Figure 6.10.*** *DSC heating runs (at 10 °C/min) after isothermal crystallization at different temperatures. See text for the explanation of the color code employed.*

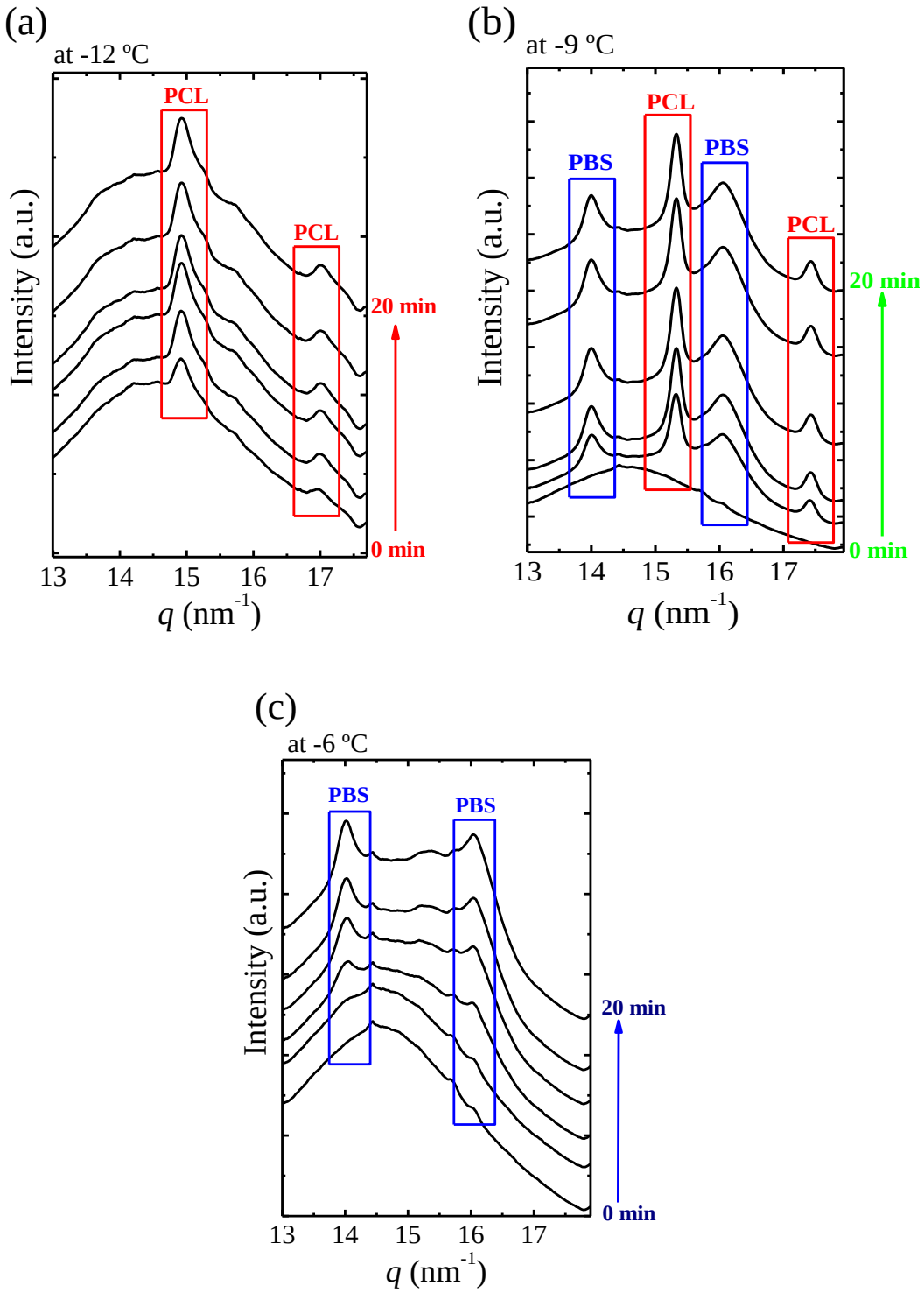


***Figure 6.11.*** *WAXS diffraction patterns of $BS_{45}CL_{55}$ registered during isothermal crystallization at -12 °C (a), -9 °C (b) and -6 °C (c).*

### 6.2.7. Thermodynamics of copolymer

#### 6.2.7.1. Equilibrium melting temperature $T_m^0$

Equilibrium melting temperature $T_m^0$ is an important parameter that is intrinsically the melting temperature of lamellar crystals with an infinite thickness, which is essential to determine in order to analyze crystal growth kinetics. This quantity is one of the most important thermodynamic properties of crystallizable chain polymers, as it is the reference temperature from which the driving force for crystallization is defined.[32, 47-48] In order to estimate equilibrium melting point of $\mathrm{BS_xCL_y}$, analyses of the isothermal crystallization by DSC trace of all compositions at different crystallization temperatures $T_{c,iso}$ were performed.

The Hoffman-Weeks model [49] includes the extrapolation of a linear regression of experimentally observed melting temperatures $T_m$ for various crystallization temperatures $T_{c,iso}$ to the equilibrium line $T_m$=$T_c$ and the intercept gives $T_m^0$.[32, 47-48] This method has been commonly applied and accepted to approximate $T_m^0$ , particularly for the polyester systems.

The Hoffman-Weeks plot of $T_m$ versus $T_{c,iso}$ corresponding to BS-rich phase copolyesters presented in Figure A.6.3. Equilibrium melting temperatures $T_m^0$ determined by the linear Hoffman-Weeks extrapolation. They exhibit melting points which increase with $T_{c,iso}$. As it can be seen in Figure 6.1, $T_m^0$ decreases with increasing the copolymer content in both BS-rich and CL-rich phases. These differences in $T_m^0$ values should be attributed to the differences in the thermodynamic properties of crystallizable chain (i.e. crystal packing and rigidity of chain) in the compositions.

The equilibrium melting points $T_m^0$ values are collected in Table A.6.1. $T_m^0$ measured for pure PBS (131 °C) is in the range reported previously by the Hoffman-Weeks method (125-135 °C) [27, 50-53] and a little lower than reported values in the literature determined by the Gibbs-Thomson equation (137 °C).[27] In the case of

PCL, we found $T_m^0$ equal to 78.4 °C that is a higher than reported value by Hoffman-Weeks method in the literature (74 °C).[54]

#### 6.2.7.2. Study of co-units cocrystallization with theoretical exclusion-inclusion models

An indirect way to derive information on the partitioning of co-units between the crystalline and amorphous phase is to compare the experimental estimations of the equilibrium melting points with theoretical models, which account for the effect of exclusion-inclusion of the comonomer in the crystal on this thermodynamic value.

In order to follow the effect of composition on competition of co-crystallization of these copolyesters, Flory, Baur, Sanchez-Eby and Wendling-Suter theories have been employed to describe the experimental variation of equilibrium melting temperatures of these random copolyesters.

As can be seen, the Flory and Sanchez-Eby[55] models (inclusion models) did not fit the experimental values since they lead to an overestimation of the equilibrium melting points. Regarding Baur (exclusion model) [56], its prediction seems to be more realistic for both PCL rich and PBS rich compositions. It could be due to the fact that the second comonomer is neither complete exclusion nor uniform inclusion within the main crystal.

The Wendling and Suter theory [57-58] proposed a combination of the comonomer exclusion-inclusion and it has been examined successfully on the crystallization behavior in many copolymeric systems. [11, 59-60]

To account for isodimorphic behavior and crystallization of copolymers with a content of co-unit, assuming that the free energy penalty paid to accommodate a defect in the crystal decreases with the incorporation of comonomer. As such, the equilibrium melting point of the copolymer is then given by Equation 6.9:

$$\frac{1}{T_m^0} - \frac{1}{T_{m(XB)}} = \frac{R}{\Delta H_m^0} \ln\left(1 - x_B + x_B e^{\frac{-\varepsilon}{RT}}\right) - 2(x_B - x_B e^{\frac{-\varepsilon}{RT}})(1 - x_B + x_B e^{\frac{-\varepsilon}{RT}})$$

Eq.6.9

The case of complete exclusion and of uniform inclusion can be obtained as particular solutions to this equation. When $X_{CB} = X_B$ and $X_{CB} = 0$ ($\varepsilon \rightarrow \infty$), Equation 5 leads to the uniform inclusion model and the exclusion model (the Baur's model), respectively. In the calculations, the equilibrium melting enthalpy was taken to be 18.9 kJ/mol for PBS-rich side and 15.9 kJ/mol for PCL-rich side compositions.

Figure 6.12 shows that among the models tried in this work the Wendling-Suter equation provides the most satisfactory fit to the experimental data in the range of low comonomer content. The model regardless of the comonomer composition gives a constant $\varepsilon/RT$ value. [61] For PBS-rich composition, best fit was found for $\varepsilon/RT$ = 0.85 which results in a value 2.86 kJ/mol for the average defect free energy $\varepsilon$ in case of incorporation of CL unit into the PBS crystal, in the limiting case of $X_{CL} = 0$.

In the opposite side, incorporation of BS unit in PCL crystals needs a value $\varepsilon/RT$= 2.0 was required for the best fitting, led to 5.84 kJ/mol for the average defect free energy, $\varepsilon$. The $\varepsilon$ in PCL-rich phase is higher than in the case of incorporation of CL units in the PBS crystal. The higher the value, the more difficult is the commoner inclusion in the lattice.

According to the Wendling–Suter theory, the concentration of comonomeric B units in the crystal formed by A units can be expressed as:

$$X_{CB}^{eq} = \frac{X_B\, e^{-\varepsilon/RT}}{1 - X_B + X_B e^{-\varepsilon/RT}} \qquad \text{Eq.6.10}$$

By introducing in Equation 6, the defect free energy and the $T_m$ of the copolymers, the concentration of comonomeric units in the cocrystal ($X_{CB}$) can be estimated. To evaluate if all the comonomeric units enter into the crystal lattice of BS-*ran*-CL, $X_{CB}$ can be plotted against $X_B$ (see Figure 6.13).

The comonomer concentration in the crystal lattice increases with increasing the comonomer content. However, for both cases, the comonomer concentration in each crystal lattice is lower than the comonomer concentration based on the uniform inclusion model ($X_{CB} = X_B$), indicating a certain amount of comonomer units inclusion into the BS-*ran*-CL crystal lattice and the remaining fraction being exclusion in the amorphous phase. Moreover, for PBC-rich compositions, a large amount of CL comonomer inclusions was predicted. In physical viewpoint, for imperfect crystal lattice, it is easier to create the excess volume necessary for a comonomer unit.

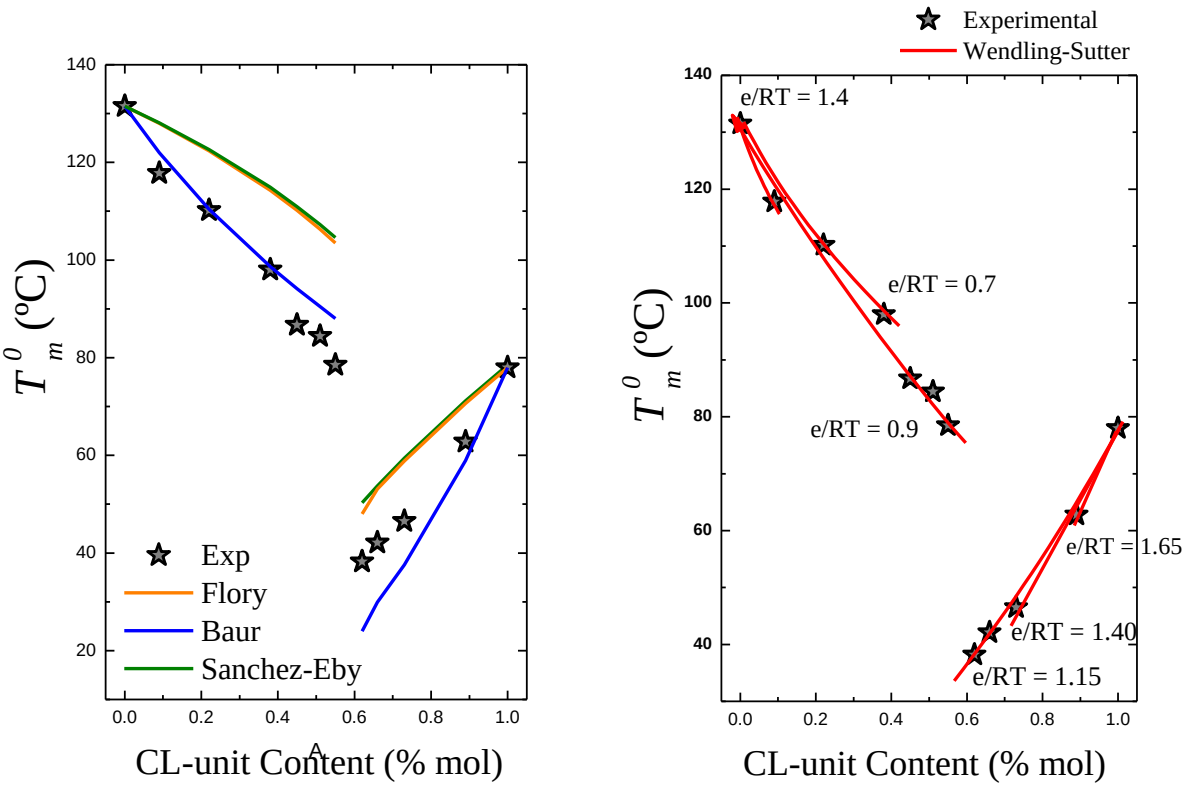


***Figure 6.12.*** *Comparison of the experimental equilibrium melting temperatures with the theoretical melting temperatures predicted by the Shanchez-Eby, Flory, Baur (c), and (d) Wendling-Suter theories.*

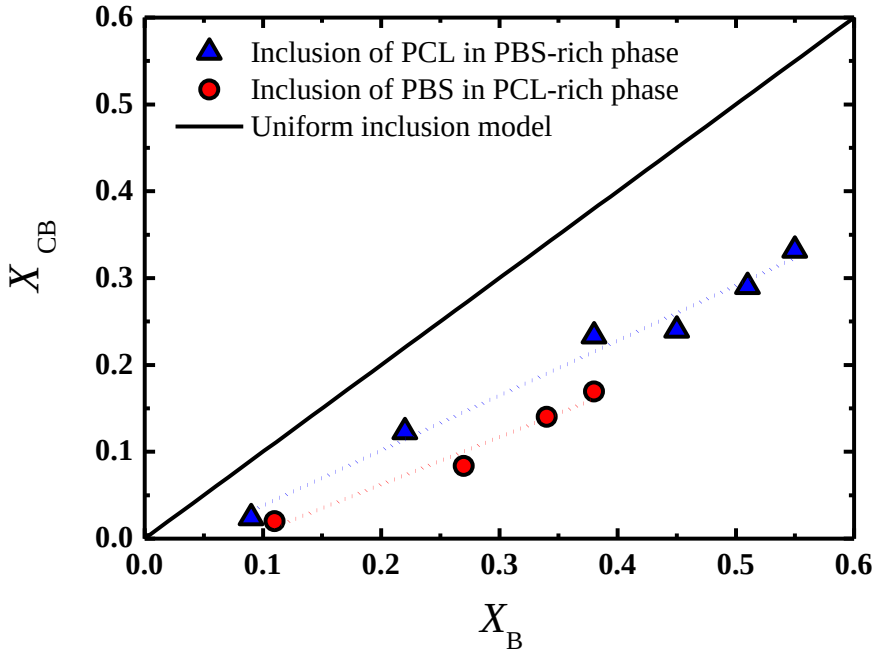


***Figure 6.13.*** *Concentration of copolymer unit ($X_{CB}$) incorporated in BS-ran-CL crystals, as a function of copolymer content in copolyester ($X_B$). The solid line is derived from uniform inclusion model.*

## 6.3. CONCLUSION

The complex isothermal nucleation, growth and overall crystallization of isodimorphic PBS-*ran*-PCL copolyesters have been studied for the first time. The equilibrium melting temperatures show a very clear pseudo-eutectic point at a composition of $BS_{45}CL_{55}$. To the left of the pseudo-eutectic point (in a plot of $T_m^0$ versus CL-unit molar content) only the PBS-rich phase is able to crystallize, at the pseudo-eutectic point both PBS-rich and PCL-rich phases can crystallize and to the right of the pseudo-eutectic point only PCL-rich crystals are formed. With respect to the parent homopolymers, any comonomer incorporation on either side of the pseudo-eutectic point causes as increase in nucleation density and nucleation rate, as well as a decrease in spherulitic growth rate.

As a result, the overall crystallization rate determined by DSC was a strong function of composition and supercooling. For PBS-rich copolymers, the PBS-rich phase overall crystallization rate-determining-step was the spherulitic growth rate. On the other hand, for PCL-rich copolymers, the nucleation rate (which was always larger for mirror compositions) gained more importance in the control of the overall crystallization rate.

The crystallization of the isodimorphic copolyester with pseudo-eutectic composition can be tailored by varying the isothermal crystallization temperature, depending on which, either one or both phases are able to crystallize. Such remarkable property control allows the possibility of having a single copolyester with only PCL crystals, only PBS crystals or both types of crystals, thus exhibiting very different thermal properties.

Applying Wendling-Suter equation, we have calculated the average defect free energy $\varepsilon$ that indicating an easier inclusion of PCL-units inside the PBS crystals lattice than PBS-units inside the PCL crystals. Equilibrium melting temperatures determined from isothermal crystallization data using Hoffman-weeks model and the values are around 20-30 °C above the melting points.

## 6.4. REFERENCES


1. Lendlein, A.; Sisson, A., *Handbook of biodegradable polymers: isolation, synthesis, characterization and applications*. John Wiley & Sons: 2011.

2. Tanaka, M.; Sato, K.; Kitakami, E.; Kobayashi, S.; Hoshiba, T.; Fukushima, K., Design of biocompatible and biodegradable polymers based on intermediate water concept. *Polymer Journal* **2015,** *47* (2), 114.

3. Sisti, L.; Totaro, G.; Marchese, P., PBS makes its entrance into the family of biobased plastics. *Biodegradable and Biobased Polymers for Environmental and Biomedical Applications* **2016**, 225-285.

4. Pan, P.; Inoue, Y., Polymorphism and isomorphism in biodegradable polyesters. *Progress in Polymer Science* **2009,** *34* (7), 605-640.

5. Ikada, Y.; Tsuji, H., Biodegradable polyesters for medical and ecological applications. *Macromolecular rapid communications* **2000,** *21* (3), 117-132.

6. Williams, C. K., Synthesis of functionalized biodegradable polyesters. *Chemical Society Reviews* **2007,** *36* (10), 1573-1580.

7. Fakirov, S., *Biodegradable polyesters*. John Wiley & Sons: 2015.

8. Manavitehrani, I.; Fathi, A.; Badr, H.; Daly, S.; Negahi Shirazi, A.; Dehghani, F., Biomedical applications of biodegradable polyesters. *Polymers* **2016,** *8* (1), 20.

9. Arandia, I.; Mugica, A.; Zubitur, M.; Mincheva, R.; Dubois, P.; Müller, A. J.; Alegría, A., The complex amorphous phase in poly (butylene succinate-ran-butylene azelate) isodimorphic copolyesters. *Macromolecules* **2017,** *50* (4), 1569-1578.

10. Ciulik, C.; Safari, M.; Martínez de Ilarduya, A.; Morales-Huerta, J. C.; Iturrospe, A.; Arbe, A.; Müller, A. J.; Muñoz-Guerra, S., Poly (butylene succinate-ran-ε-caprolactone) copolyesters: Enzymatic synthesis and crystalline isodimorphic character. *European Polymer Journal* **2017,** *95*, 795-808.

11. Yu, Y.; Wei, Z.; Liu, Y.; Hua, Z.; Leng, X.; Li, Y., Effect of chain length of comonomeric diols on competition and miscibility of isodimorphism: A comparative study of poly (butylene glutarate-co-butylene azelate) and poly (octylene glutarate-co-octylene azelate). *European Polymer Journal* **2018,** *105*, 274-285.

12. Pérez-Camargo, R. A.; Arandia, I.; Safari, M.; Cavallo, D.; Lotti, N.; Soccio, M.; Müller, A. J., Crystallization of isodimorphic aliphatic random copolyesters: Pseudo-

eutectic behavior and double-crystalline materials. *European Polymer Journal* **2018,** *101*, 233-247.

13. Mandelkern, L., *Crystallization of Polymers: Volume 1: Equilibrium Concepts*. 2 ed.; Cambridge University Press: Cambridge, 2002; Vol. 1.

14. Allegra, G.; Bassi, I. W., Isomorphism in synthetic macromolecular systems. In *Fortschritte der Hochpolymeren-Forschung*, Springer Berlin Heidelberg: Berlin, Heidelberg, 1969; pp 549-574.

15. Ye, H.-M.; Wang, R.-D.; Liu, J.; Xu, J.; Guo, B.-H., Isomorphism in poly (butylene succinate-co-butylene fumarate) and its application as polymeric nucleating agent for poly (butylene succinate). *macromolecules* **2012,** *45* (14), 5667-5675.

16. Yu, Y.; Sang, L.; Wei, Z.; Leng, X.; Li, Y., Unique isodimorphism and isomorphism behaviors of even-odd poly (hexamethylene dicarboxylate) aliphatic copolyesters. *Polymer* **2017,** *115*, 106-117.

17. Safari, M.; Martínez de Ilarduya, A.; Mugica, A.; Zubitur, M.; Muñoz-Guerra, S. n.; Müller, A. J., Tuning the Thermal Properties and Morphology of Isodimorphic Poly [(butylene succinate)-ran-(ε-caprolactone)] Copolyesters by Changing Composition, Molecular Weight, and Thermal History. *Macromolecules* **2018,** *51* (23), 9589-9601.

18. Ciulik, C.; Safari, M.; de Ilarduya, A. M.; Morales-Huerta, J. C.; Iturrospe, A.; Arbe, A.; Müller, A. J.; Muñoz-Guerra, S., Poly (butylene succinate-ran-ε-caprolactone) copolyesters: Enzymatic synthesis and crystalline isodimorphic character. *European Polymer Journal* **2017,** *95*, 795-808.

19. Sharples, A., Introduction to polymer crystallization. 1966. *London: Edward Arnold Ltd*.

20. Mandelkern, L., *Crystallization of Polymers: Volume 2, Kinetics and Mechanisms*. Cambridge University Press: 2004.

21. Brüster, B.; Montesinos, A.; Reumaux, P.; Pérez-Camargo, R. A.; Mugica, A.; Zubitur, M.; Müller, A. J.; Dubois, P.; Addiego, F., Crystallization kinetics of polylactide: Reactive plasticization and reprocessing effects. *Polymer Degradation and Stability* **2018,** *148*, 56-66.

22. Tian, J.; Yu, W.; Zhou, C., Crystallization kinetics of linear and long-chain branched polypropylene. *Journal of Macromolecular Science, Part B* **2006,** *45* (5), 969-985.

23. Wunderlich, B., Crystal nucleation, growth, annealing, Macromolecular physics, vol. 2. Academic Press, New York: 1976.

24. Arandia, I.; Zaldua, N.; Maiz, J.; Pérez-Camargo, R. A.; Mugica, A.; Zubitur, M.; Mincheva, R.; Dubois, P.; Müller, A. J., Tailoring the isothermal crystallization kinetics of isodimorphic poly (butylene succinate-ran-butylene azelate) random copolymers by changing composition. *Polymer* **2019**, 121863.

25. Pitt, C.; Chasalow, F.; Hibionada, Y.; Klimas, D.; Schindler, A., Aliphatic polyesters. I. The degradation of poly (ϵ-caprolactone) in vivo. *Journal of Applied Polymer Science* **1981,** *26* (11), 3779-3787.

26. Van Krevelen, D. W.; Te Nijenhuis, K., *Chapter 5, Calorimetric Properties, Properties of Polymers (fourth ed.)*. Elsevier: Amsterdam, 2009.

27. Papageorgiou, G. Z.; Bikiaris, D. N., Crystallization and melting behavior of three biodegradable poly (alkylene succinates). A comparative study. *Polymer* **2005,** *46* (26), 12081-12092.

28. Crist, B.; Schultz, J. M., Polymer spherulites: A critical review. *Progress in Polymer Science* **2016,** *56*, 1-63.

29. Woo, E. M.; Lugito, G., Origins of periodic bands in polymer spherulites. *European Polymer Journal* **2015,** *71*, 27-60.

30. Müller, A. J.; Michell, R. M.; Lorenzo, A. T., Isothermal Crystallization Kinetics of Polymers. *Polymer Morphology: Principles, Characterization, and Processing* **2016**, 181-203.

31. Magill, J., Review spherulites: A personal perspective. *Journal of Materials Science* **2001,** *36* (13), 3143-3164.

32. Hoffman, J. D.; Davis, G. T.; Lauritzen, J. I., The rate of crystallization of linear polymers with chain folding. In *Treatise on solid state chemistry*, Springer: 1976; pp 497-614.

33. Mark, J. E., *Physical properties of polymers handbook*. Springer: 2007; Vol. 1076.

34. Ichikawa, Y.; Kondo, H.; Igarashi, Y.; Noguchi, K.; Okuyama, K.; Washiyama, J., Crystal structures of α and β forms of poly (tetramethylene succinate). *Polymer* **2000,** *41* (12), 4719-4727.

35. Ren, M.; Song, J.; Song, C.; Zhang, H.; Sun, X.; Chen, Q.; Zhang, H.; Mo, Z., Crystallization kinetics and morphology of poly (butylene succinate-co-adipate). *Journal of Polymer Science Part B: Polymer Physics* **2005,** *43* (22), 3231-3241.

36. Phillips, P. J.; Rensch, G. J.; Taylor, K. D., Crystallization studies of poly (ε-caprolactone). I. Morphology and kinetics. *Journal of Polymer Science Part B: Polymer Physics* **1987,** *25* (8), 1725-1740.

37. Lorenzo, A.; Müller, A., Estimation of the nucleation and crystal growth contributions to the overall crystallization energy barrier. *Journal of Polymer Science Part B: Polymer Physics* **2008,** *46* (14), 1478-1487.

38. Chen, Y.-A.; Tsai, G.-S.; Chen, E.-C.; Wu, T.-M., Crystallization behaviors and microstructures of poly (butylene succinate-co-adipate)/modified layered double hydroxide nanocomposites. *Journal of materials science* **2016,** *51* (8), 4021-4030.

39. Papageorgiou, G. Z.; Achilias, D. S.; Bikiaris, D. N., Crystallization kinetics of biodegradable poly (butylene succinate) under isothermal and non-isothermal conditions. *Macromolecular Chemistry and Physics* **2007,** *208* (12), 1250-1264.

40. Müller, A. J.; Albuerne, J.; Marquez, L.; Raquez, J.-M.; Degee, P.; Dubois, P.; Hobbs, J.; Hamley, I. W., Self-nucleation and crystallization kinetics of double crystalline poly (p-dioxanone)-b-poly (e-caprolactone) diblock copolymers. *Faraday Discussions* **2005,** (128), 231-252.

41. Avrami, M., Kinetics of phase change. I General theory. *The Journal of chemical physics* **1939,** *7* (12), 1103-1112.

42. Avrami, M., Kinetics of phase change. II transformation-time relations for random distribution of nuclei. *The Journal of chemical physics* **1940,** *8* (2), 212-224.

43. Lorenzo, A. T.; Arnal, M. L.; Albuerne, J.; Müller, A. J., DSC isothermal polymer crystallization kinetics measurements and the use of the Avrami equation to fit the data: guidelines to avoid common problems. *Polymer testing* **2007,** *26* (2), 222-231.

44. Papageorgiou, G. Z.; Papageorgiou, D. G.; Chrissafis, K.; Bikiaris, D.; Will, J.; Hoppe, A.; Roether, J. A.; Boccaccini, A. R., Crystallization and melting behavior of poly (butylene succinate) nanocomposites containing silica-nanotubes and strontium hydroxyapatite nanorods. *Industrial & Engineering Chemistry Research* **2013,** *53* (2), 678-692.

45. Wang, Y.; Chen, S.; Zhang, S.; Ma, L.; Shi, G.; Yang, L., Crystallization and melting behavior of poly (butylene succinate)/silicon nitride composites: the influence of filler's phase structure. *Thermochimica acta* **2016,** *627*, 68-76.

46. Yasuniwa, M.; Satou, T., Multiple melting behavior of poly (butylene succinate). I. Thermal analysis of melt-crystallized samples. *Journal of Polymer Science Part B: Polymer Physics* **2002,** *40* (21), 2411-2420.

47. Marand, H.; Xu, J.; Srinivas, S., Determination of the equilibrium melting temperature of polymer crystals: linear and nonlinear Hoffman− Weeks extrapolations. *Macromolecules* **1998,** *31* (23), 8219-8229.

48. Hoffman, J. D.; Miller, R. L., Kinetic of crystallization from the melt and chain folding in polyethylene fractions revisited: theory and experiment. *Polymer* **1997,** *38* (13), 3151-3212.

49. Hoffman, J. D.; Weeks, J. J., Melting process and the equilibrium melting temperature of polychlorotrifluoroethylene. *J Res Natl Bur Stand A* **1962,** *66* (1), 13-28.

50. Ye, H.-M.; Tang, Y.-R.; Xu, J.; Guo, B.-H., Role of Poly (butylene fumarate) on Crystallization Behavior of Poly (butylene succinate). *Industrial & Engineering Chemistry Research* **2013,** *52* (31), 10682-10689.

51. Gan, Z.; Abe, H.; Kurokawa, H.; Doi, Y., Solid-state microstructures, thermal properties, and crystallization of biodegradable poly (butylene succinate)(PBS) and its copolyesters. *Biomacromolecules* **2001,** *2* (2), 605-613.

52. Zheng, Y.; Tian, G.; Xue, J.; Zhou, J.; Huo, H.; Li, L., Effects of isomorphic poly (butylene succinate-co-butylene fumarate) on the nucleation of poly (butylene succinate) and the formation of poly (butylene succinate) ring-banded spherulites. *CrystEngComm* **2018**.

53. Yoo, E.; Im, S., Melting behavior of poly (butylene succinate) during heating scan by DSC. *Journal of Polymer Science Part B: Polymer Physics* **1999,** *37* (13), 1357-1366.

54. Goulet, L.; Prud'Homme, R. E., Crystallization kinetics and melting of caprolactone random copolymers. *Journal of Polymer Science Part B: Polymer Physics* **1990,** *28* (12), 2329-2352.

55. Sanchez, I.; Eby, R., Thermodynamics and crystallization of random copolymers. *Macromolecules* **1975,** *8* (5), 638-641.

56. Baur, V. H., Einfluß der sequenzlängenverteilung auf das schmelz-ende von copolymeren. *Macromolecular Chemistry and Physics* **1966,** *98* (1), 297-301.

57. Wendling, J.; Gusev, A.; Suter, U.; Braam, A.; Leemans, L.; Meier, R. J.; Aerts, J.; Heuvel, J. v.; Hottenhuis, M., Crystal Morphology and Thermodynamics of Poly (ethylene-4, 4 '-biphenyl dicarboxylate) and Related Copolymers with Ethylene-2, 6-naphthalene Dicarboxylate. *Macromolecules* **1999,** *32* (23), 7866-7878.

58. Wendling, J.; Suter, U., A new model describing the cocrystallization behavior of random copolymers. *Macromolecules* **1998,** *31* (8), 2516-2520.

59. Papageorgiou, G. Z.; Bikiaris, D. N., Synthesis, cocrystallization, and enzymatic degradation of novel poly (butylene-co-propylene succinate) copolymers. *Biomacromolecules* **2007,** *8* (8), 2437-2449.

60. Yu, Y.; Wei, Z.; Zheng, L.; Jin, C.; Leng, X.; Li, Y., Competition and miscibility of isodimorphism and their effects on band spherulites and mechanical properties of poly (butylene succinate-co-cis-butene succinate) unsaturated aliphatic copolyesters. *Polymer* **2018,** *150*, 52-63.

61. Wendling, J.; Gusev, A. A.; Suter, U. W., Predicting the cocrystallization behavior of random copolymers via free energy calculations. *Macromolecules* **1998,** *31* (8), 2509-2515.

# *Chapter VII:*

# *Mechanical Properties of*

# *VHMw PBS-ran-PCL*

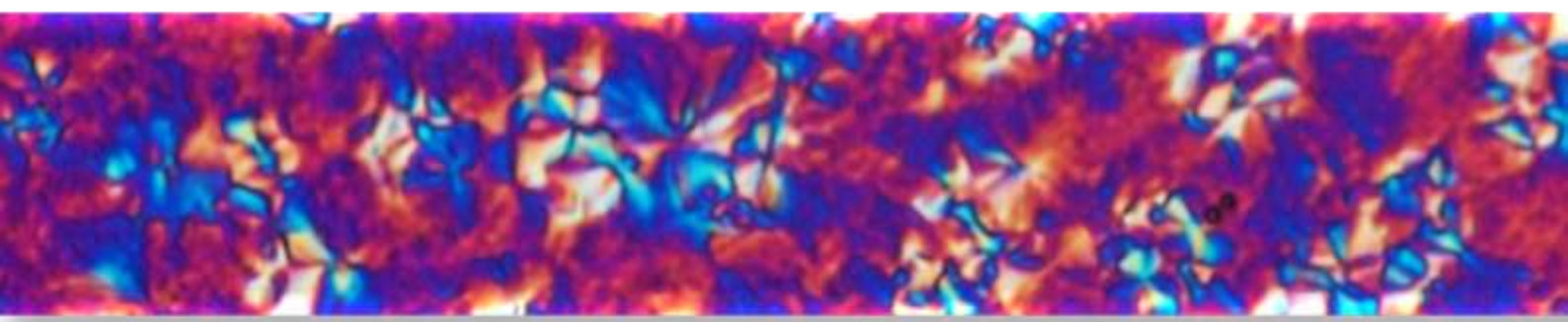

# Table of Contents

## Abstract

The present work deals with the ROP-esterification polycondensation copolymerization of butylene succinate (BS) and *ε*-caprolactone (*ε*-CL) and the effect of the comonomer incorporation on the mechanical/thermal properties of this isodimorphic random polyester. The very high molecular weight synthesized copolyesters were analyzed by differential scanning calorimetry (DSC), tensile test and dynamic mechanical thermal analysis (DMTA). The aim of this research was to gain more information about the mechanical properties of the isodimorphic random copolyesters. The strain, stress at break and elongation at break values as measured in tensile tests, as well as the thermal properties results from DSC, showed that the copolyesters follows a pseudo-eutectic behavior. DMTA results showed that the storage modulus of all compositions remains constant below the glass transition temperature, but decreases above this parameter when adding comonomer. In addition, both storage and loss modulus indicated that this copolyester shows a pseudo-eutectic behavior.

## 7.1. INTRODUCTION

Synthetic aliphatic polyesters are promising materials for the production of high performance and environment-friendly biocompatible and biodegradable plastics [1-2]. Polybutylene succinate (PBS) is a well-known aliphatic polyester that has various potential applications in biomedicine, cosmetics, food-contact products, textiles, packaging, etc. [3-4]. PBS displays similar crystallization behavior and similar mechanical properties to those of polyolefins, such as polyethylene, and its mechanical and thermal properties depend on the crystal structure and the degree of crystallinity [5]. However, its application is rather limited, partly due to its high melting point $T_m$ (approximately 115 °C) and high degree of crystallinity $X_c$ (~ 55 %) that leads to a slow biodegradation rate and poor physical properties. Polyethylene caprolactone (PCL) received the most attention due to its elasticity, biocompatibility and good ductility caused by its low glass transition temperature ($T_g$ around -60 °C). However, PCL has relatively low mechanical strength, which restricts some practical applications [6-8].

The idea of combining PCL-PBS in blends, random or block copolyesters, has been used to design new materials with improved behavior and performance [9-17]. Random copolymerization is a simple synthetic strategy of combining the properties of two distinct homopolymers. It provides random covalent bonds between different comonomers, therefore ensuring total melt miscibility, unlike typical immiscible polymer blends. Their thermal and mechanical properties can be tailored by changing the composition of the copolymer [18-19].

Recently, we synthesized poly (butylene succinate)-*ran*-*ε*-caprolactone (PBS-*ran*-PCL) by two different methods: enzyme-catalyzed ROP-polycondensation and direct melt-polycondensation polymerization and the resulting copolyesters had low and high molecular weights, respectively. The weight average molecular weight was 6000 g/mol for the low molecular weight materials and 20000 g/mol for the high molecular weight copolymers (denoted $LM_w$-$BS_xCL_y$ [20] and $HM_w$-$BS_xCL_y$

[21], respectively). Both displayed a remarkable isodimorphic behavior. When the melting point of isodimorphic random copolymers is plotted as a function of composition, a pseudo-eutectic behavior is commonly observed and only the crystalline phase of the major component, which may contain a limited amount of the minor comonomer chains included in the crystal lattice, is formed on each side of the pseudo-eutectic point.

Here, very high molecular weight poly (butylene succinate-*ran*-caprolactone) (PBS-*ran*-PCL) copolyesters were synthesized in a wide range of compositions by changing the polycondensation conditions. A comparison between the DSC results of the presently synthesized very high molecular weight copolyesters (denoted $VHM_w$-$BS_xCL_y$, where x and y are the molar percentage of BS and CL units respectively) and our previous series of lower molecular weight copolyesters ($LM_w$-$BS_xCL_y$ and $HM_w$-$BS_xCL_y$) is presented.

The main aim of this study was to investigate the mechanical properties of CoP($BS_xCL_y$) as an isodimorphic random copolyester by using DMTA and tensile tests to find the effect of comonomer incorporation on the mechanical properties of random copolyesters.

## 7.2. RESULTS

### 7.2.1. Nuclear Magnetic Resonance (NMR) and GPC

Table 3.3 in chapter 3 shows molecular weight and microstructural data for the copolyesters synthesized in the presence of TTP catalyst. The copolyesters obtained show an essentially random microstructure as judged by the triads content and R values given in Table 3.3. NMR results confirmed the chemical structure of copolyesters. $^{1}H$ and $^{13}C$ NMR spectra of the $BS_{51}CL_{49}$ copolyester are shown in Figure 7.1 and the spectra of the entire series are compared in Figure 7.2.

The weight average molecular weights ($M_w$) of the $VHM_w$-$BS_xCL_y$ copolyesters were in the range 40000- 90000 g/mol with dispersities ($Đ$) between

1.9 and 2.7. Overall, the $M_w$ of the $HM_w$-$BS_xCL_y$ copolyesters were approximately three times higher than those of most of the similar previously synthesized copolyesters ($HM_w$-$BS_xCL_y$)[21], as can be seen in Chapter 5. GPC curves are presented in Figure A.7.1.

Just like in the case of the two previous lower molecular weight series ($LM_w$ and $HM_w$), the composition of the *ε*-caprolactone repeating unit present in $BS_xCL_y$ was estimated from the methylene proton resonance integrals of $CH_2$ (1) and $CH_2$ (4). Moreover, the sequence distributions of the BS and CL repeating units were calculated based on $^{13}C$ NMR signals of the methylene group $CH_2$ (b) in Figure 7.1 [22].

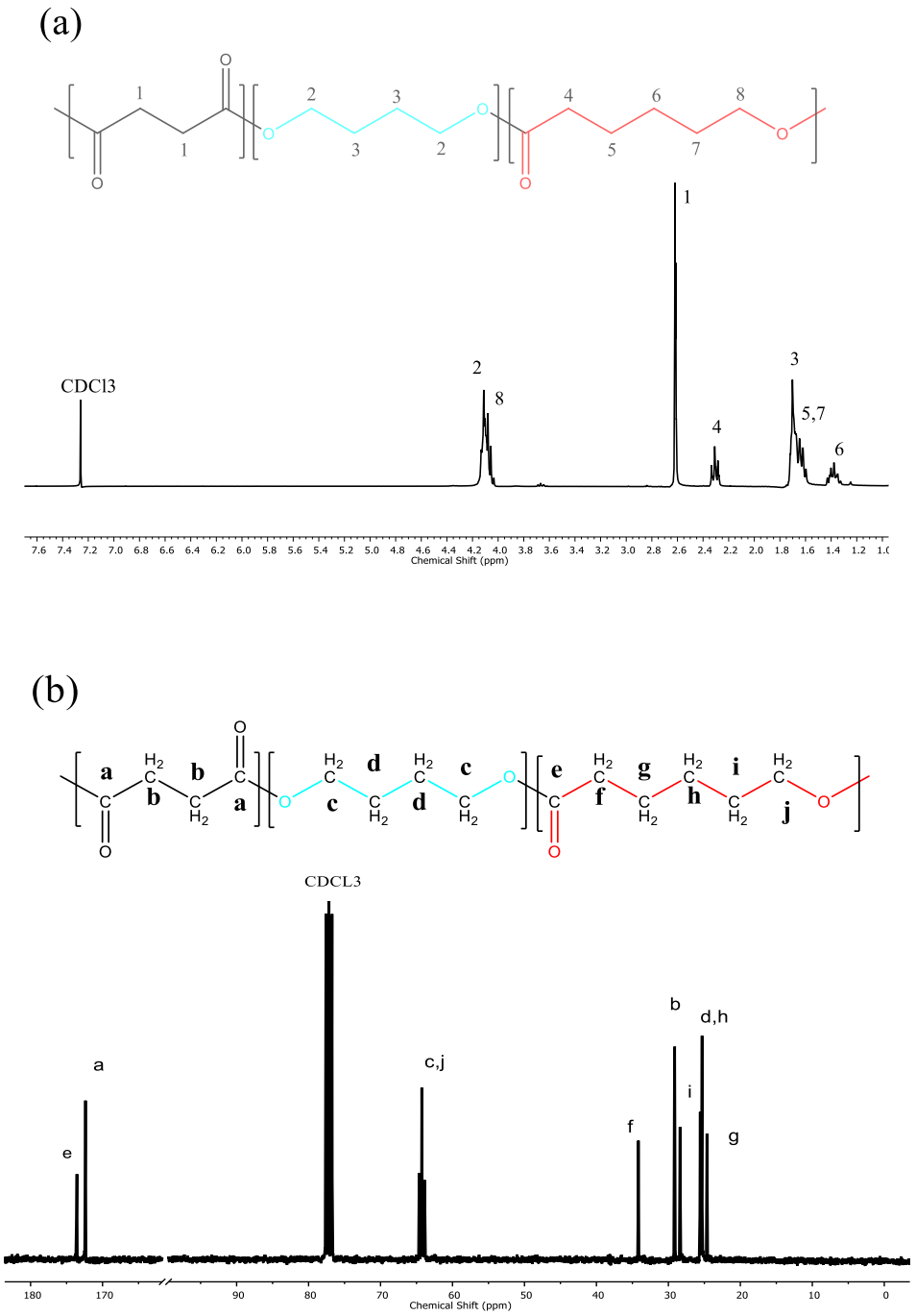


***Figure 7.1.*** *$^{1}H$ (a) and $^{13}C$ (b) NMR spectra of $VHMw - BS_{51}CL_{49}$ (recorded in $CDCl_3$) as a representative sample of the VHMw-$BS_xCL_y$ copolyesters series. Peaks were assigned according to the expected copolyester constitution depicted in the attached formula.*

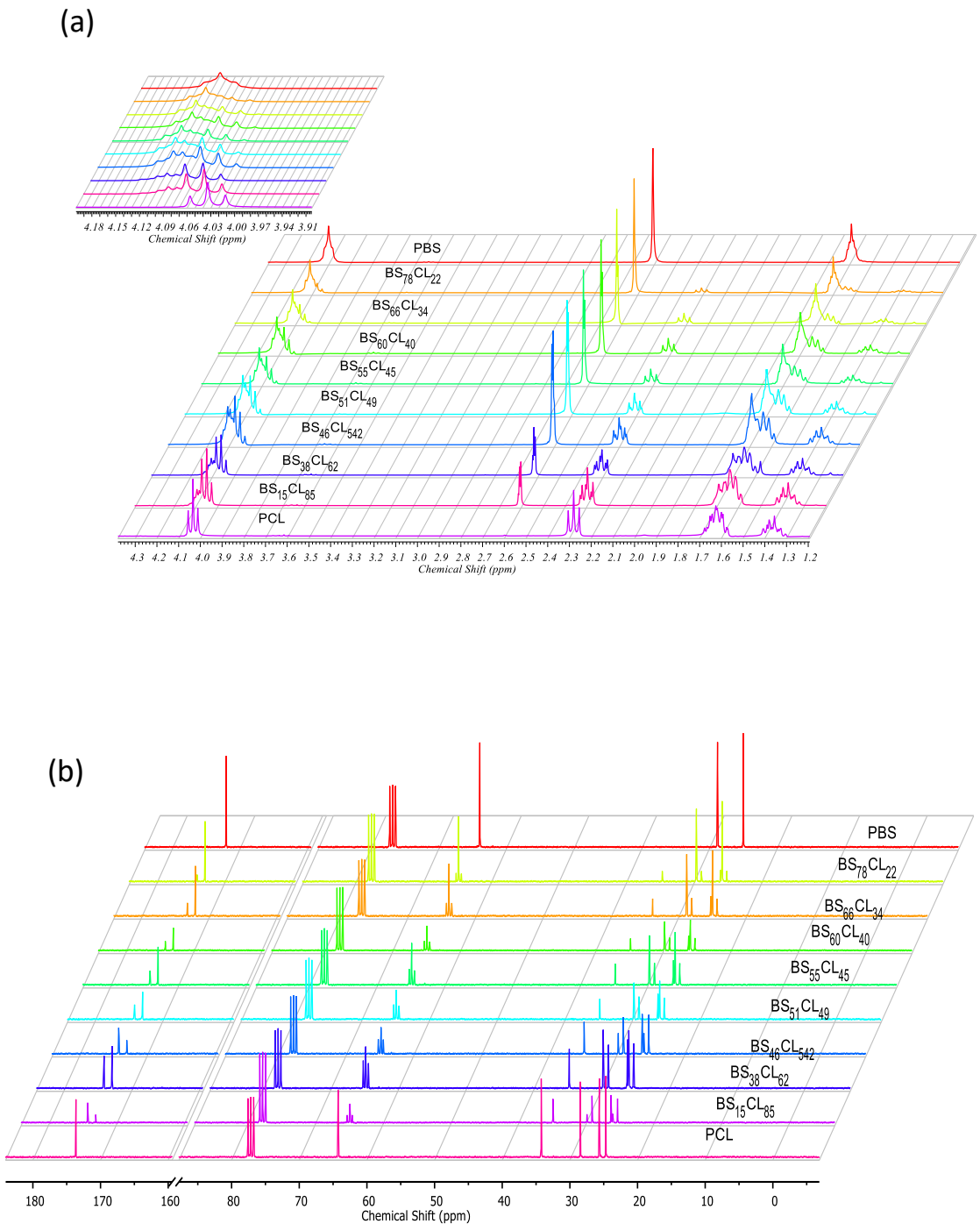


***Figure 7.2.*** *$^{1}H$ (a) and $^{13}C$ (b) NMR spectra comparison of all VHMw-$BS_xCL_y$ copolyesters series.*

### 7.2.2. Melting-crystallization of VHMw-coP(BSxCLy) copolyesters

The thermal properties of the obtained copolymers were studied by nonisothermal DSC experiments. The standard nonisothermal behavior of neat PBS and PCL homopolymers, as well as PBS-*ran*-PCL copolymers at a cooling and heating rate 10 °C/min are shown in Figure 7.3. Table 7.1 shows extracted data from DSC traces. For each sample, a single crystallization peak and a single melting peak could be observed in nonisothermal crystallization and subsequent melting, respectively. A close up of these DSC curves is shown in Figure A.7.2 (see Appendix Chapter).

As can be seen in Figure 7.3.a, all copolyester samples were able to crystallize, and their crystallization temperatures were found to be a strong function of composition. When the parental comonomer units have very similar chemical structures, the crystallization can occur over the entire composition range [23-24].

PBS-rich phase copolymers exhibited a cold crystallization peak during the heating run (see Figure 7.3b), followed by a melting peak, which indicated that PBS probably underwent melting and recrystallization. The PCL homopolymer and PCL-rich phase copolymers displayed a single sharp melting peak.

Figures 7.4a-d shows plots of peak crystallization and melting temperatures, as well as the corresponding enthalpies, for the VHMw-coP(BSxCLy) copolyesters as a function of their composition. The values obtained from the nonisothermal DSC experiments of VHMw-BSxCLy were compared with the values obtained for the lower molecular weight PBS-*ran*-PCL copolyesters (studied in Chapters 4-6). Figures 7.4a and 7.4c imply that the crystallization and melting temperature of the copolymers can be controlled by the composition.

Figure 7.4d shows how the enthalpy of melting depends on the copolymer composition. The degrees of crystallinity ($X_c$) of the random copolymers were calculated from the normalized melting enthalpies (which were normalized by the

content of the crystallizable phase of crystallization) and the values were summarized in Table 7.1 and plotted in Figure 7.4e. The values of the enthalpy of crystallization for 100% crystalline samples ($\Delta H_m^0$) used were 110.3 1/J·g and 139.5 1/J·g for PBS and PCL, respectively.

As shown in both Figures 7.4d and 7.4e, the enthalpy of melting and the degree of crystallinity derived from it also displayed a pseudo-eutectic point. The reduction in crystallinity of the phases as their composition approached the pseudo-eutectic point is caused by the influence of comonomer exclusion during crystallization. As the amount of comonomer increases for both crystalline phases, comonomer exclusion interferes with crystallization by decreasing in the length of crystallizable sequences that are included in a limited number of the second comonomer units. Consequently, as the amount of the second comonomer increases, the ability to crystallize decreases because increasingly higher amounts of the second comonomer are excluded from the crystal lattice.

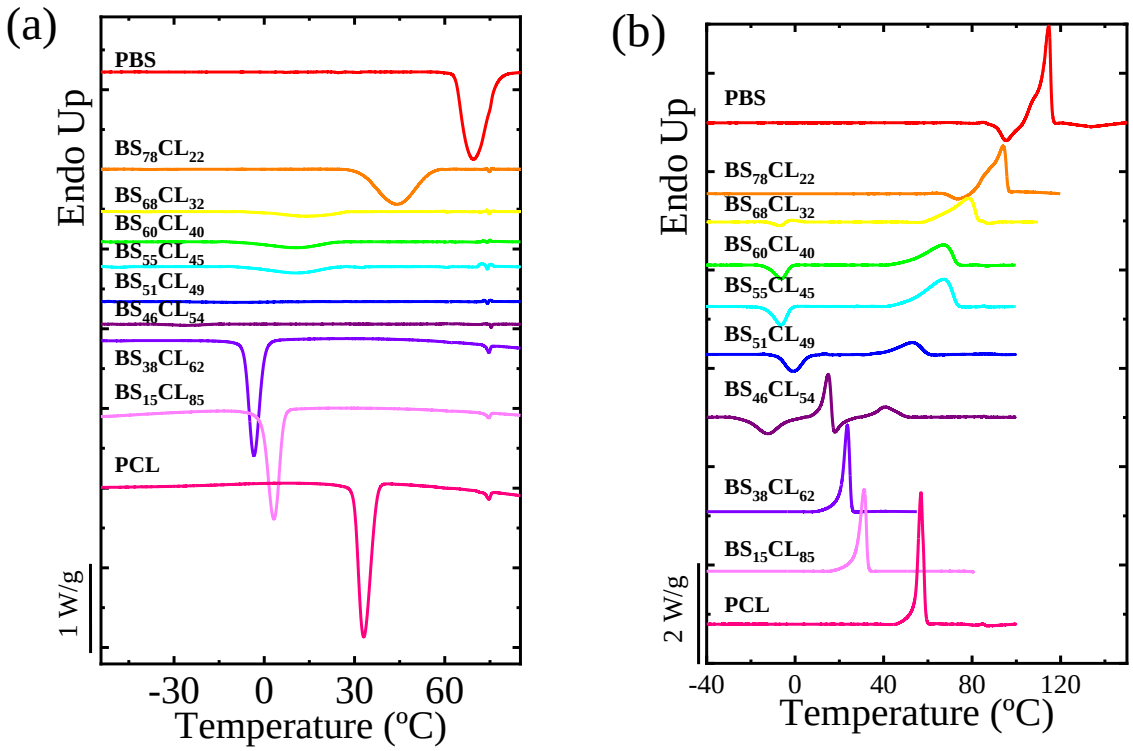


***Figure 7.3.*** *(a) DSC second heating and (b) cooling runs at 10 °C/min for the indicated samples.*

In Addition, Figure 7.4e shows the dependence of the degree of crystallinity on the molecular weight. The highest molecular weight copolyester series showed the lowest crystallinity degree. As we discussed in Chapter 5, the lower molecular weight samples can develop a higher degree of crystallinity than the higher molecular weight copolymers due to the faster diffusion of smaller molecules. Therefore, the highest molecular weight copolyesters, VHMw PBS-*ran*-PCL, presented the lowest crystallinity degree, around 10-20 % lower than the HMw copolyester $X_c$ values.

***Table 7.1.*** *Thermal characterization data of VHMw PBS-ran-PCL copolymer obtained from DSC.*

| Copolymer | $T_m$ (°C) | $\Delta H_m$ (J/g) | $T_c$ (°C) | $\Delta H_c$ (J/g) | $X_c$ (%) |
|---|---|---|---|---|---|
| **VHMw-PBS** | 114.6 | 66 | 69.2 | 59 | 54 |
| **VHMw-$BS_{78}CL_{22}$** | 94.1 | 46 | 43.0 | 41 | 30 |
| **VHMw-$BS_{68}CL_{32}$** | 78.3 | 40 | 13.8 | 8 | 5 |
| **VHMw-$BS_{60}CL_{40}$** | 69.2 | 38 | 10.8 | 8 | 4.5 |
| **UHMw-$BS_{55}CL_{45}$** | 67.0 | 35 | 10.1 | 8 | 4 |
| **VHMw-$BS_{51}CL_{49}$** | 53.8 | 30 | -9.5 | 1.8 | 1 |
| **VHMw-$BS_{46}CL_{54}$** | 40 & 15 | 17 &24 | -25.0 | 0.9 | 0.5 |
| **VHMw-$BS_{38}CL_{62}$** | 23.6 | 32 | -3.8 | 35 | 15 |
| **VHMw-$BS_{15}CL_{85}$** | 31.2 | 42 | 3.2 | 39 | 23 |
| **VHMw-PCL** | 56.8 | 55 | 33 | 55 | 38 |

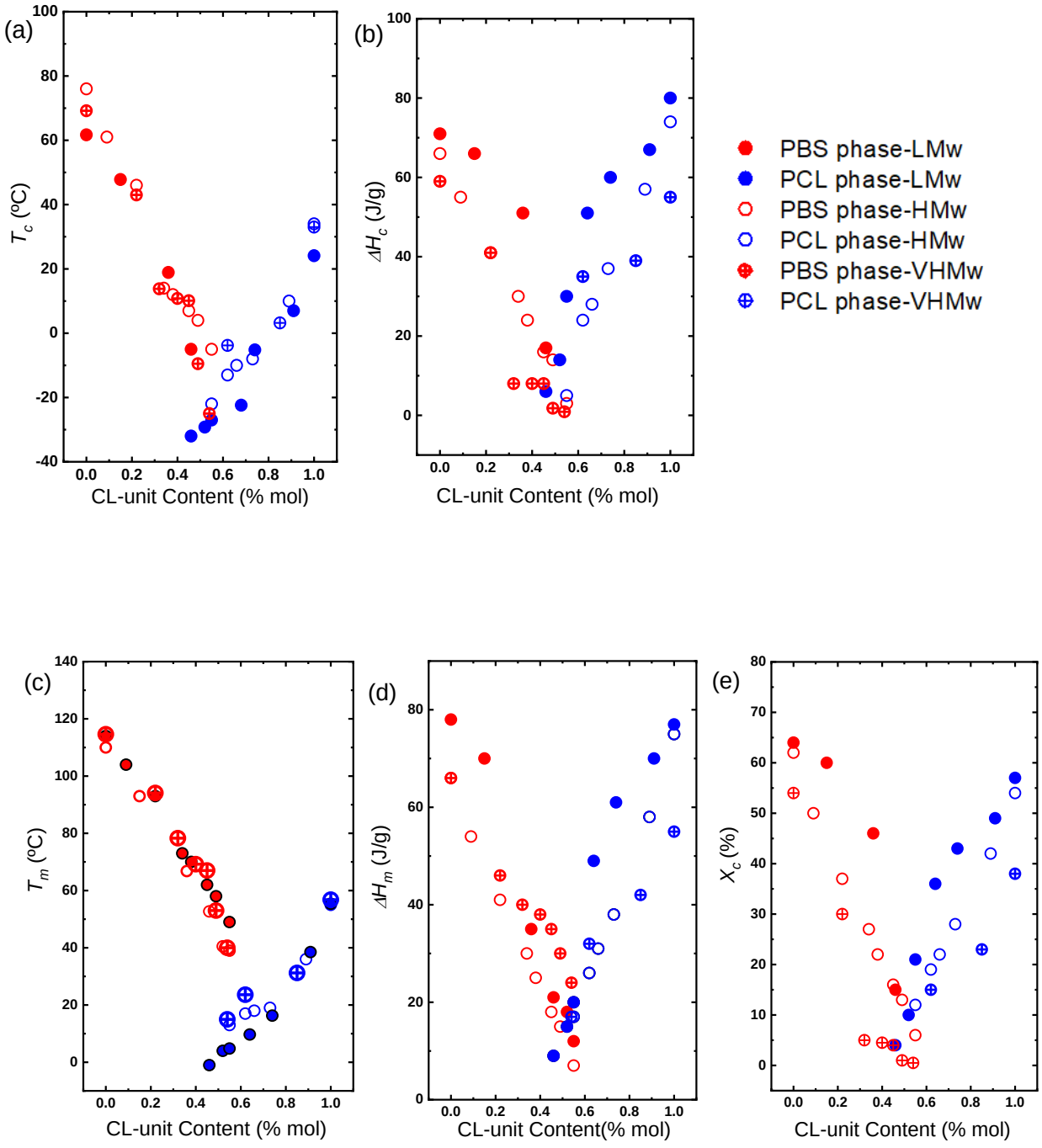


***Figure 7.4.*** *Composition dependence of (a) peak crystallization temperature $T_c$ (b), peak melting temperature $T_m$, (c) crystallization enthalpy $\Delta H_c$, (d) melting enthalpy $\Delta H_m$, and (e) crystallization degree $X_c$ of the indicated samples.*

### 3.2.3. Tensile Tests

The stress–strain curves of the described copolyesters and their parental homopolymer are compared in Figures 7.5a-b for PBS-rich and PCL-rich phase copolyesters, respectively. The mechanical data obtained from the tensile tests (elastic modulus *E*, stress at break $\sigma_b$ and elongation at break $\varepsilon_b$) are listed in Table A.7.1.

The PBS homopolymer appeared to be the most rigid polymer among the synthesized polymers, showing the highest elastic modulus and stress at break, and a relatively low elongation at break (see Figures 7.6a-c). The introduction of the CL comonomer caused a decrease in both *E* and $\sigma$ as compared to the PBS homopolymer. This result is probably related to the gradual reduction of the crystallinity degree $X_c$ in the copolymers with respect to the homopolymer (see Table 7.1 for the $X_c$ values). This trend is proportional to a rise in ductility. The presence of comonomer CL- units also leads to a two-fold increase of $\varepsilon_b$, from neat PBS to the $BS_{46}CL_{54}$ composition. In fact, a PBS homopolymer with a uniform sequence can exhibit a stronger inter-chain attraction due to its regular structure and the incorporation of flexible CL-units reduces the molecular chain regularity and enhances the chain mobility.

On the other hand, for PCL-rich phase compositions (Figure 7.6b), the incorporation of the BS comonomer enhanced the ductility of the composition. In addition, the 15 % PBS composition showed rubbery elongation at break with a high elongation and relatively low elastic modulus. Cao et al.[25] studied the tensile behavior of these copolymers and found that the maximum elongation at break occurred for the 18 % PBS composition, which is fairly close to the results obtained in this work.

As can be clearly seen in Figures 7.6a, 7.6b and 7.6c, the elastic modulus *E*, the stress at break $\sigma_b$ and the elongation at break $\varepsilon_b$ values showed a pseudo-eutectic trend when plotted as a function of the CL-unit composition. Jin et al. [26]

reported a similar pseudo-eutectic behavior in those values for isodimorphic poly (ethylene brassylate-*ran*-δ-valerolactone) copolyesters.

It is worth noting that the crystallinity degree is not the only parameter determining the mechanical properties of the random copolymers. The majority phase, demonstrated by WAXS, also controls the mechanical behavior. For instance, if we consider $BS_{68}CL_{32}$ ($X_c$ = 5 %) and $BS_{15}CL_{85}$ ($X_c$ = 23 %), the copolymer containing BS-rich sequences presented higher $E$ and $\sigma_b$ with a lower $\varepsilon_b$. This trend can be described as the effect of the dominant phase in random copolyesters. Therefore, the mechanical behavior of isodimorphic random copolyesters can be predicted by regarding both crystal unit cell and amorphous phase of copolyesters.

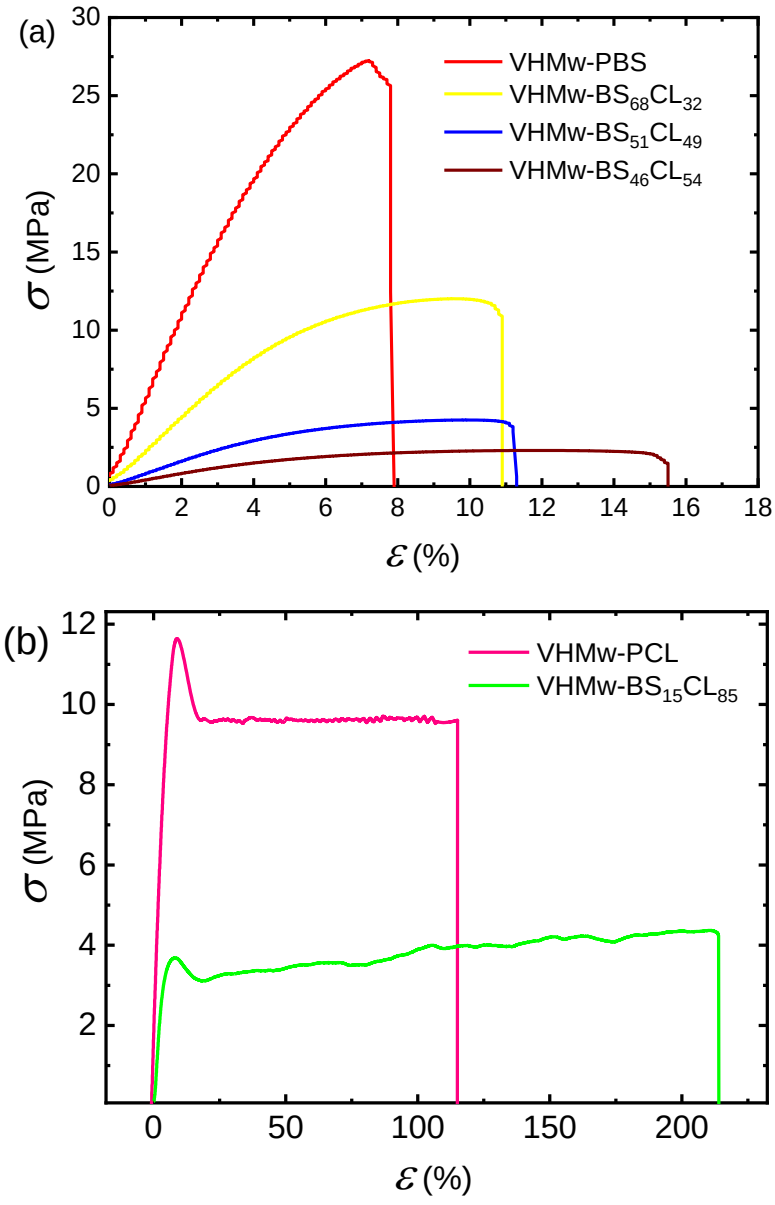


***Figure 7.5.*** *Representative stress-strain curves of (a) BS-rich VHMw-BS$_x$CL$_y$ and (b) CL-rich VHMw-BS$_x$CL$_y$ random copolyesters.*

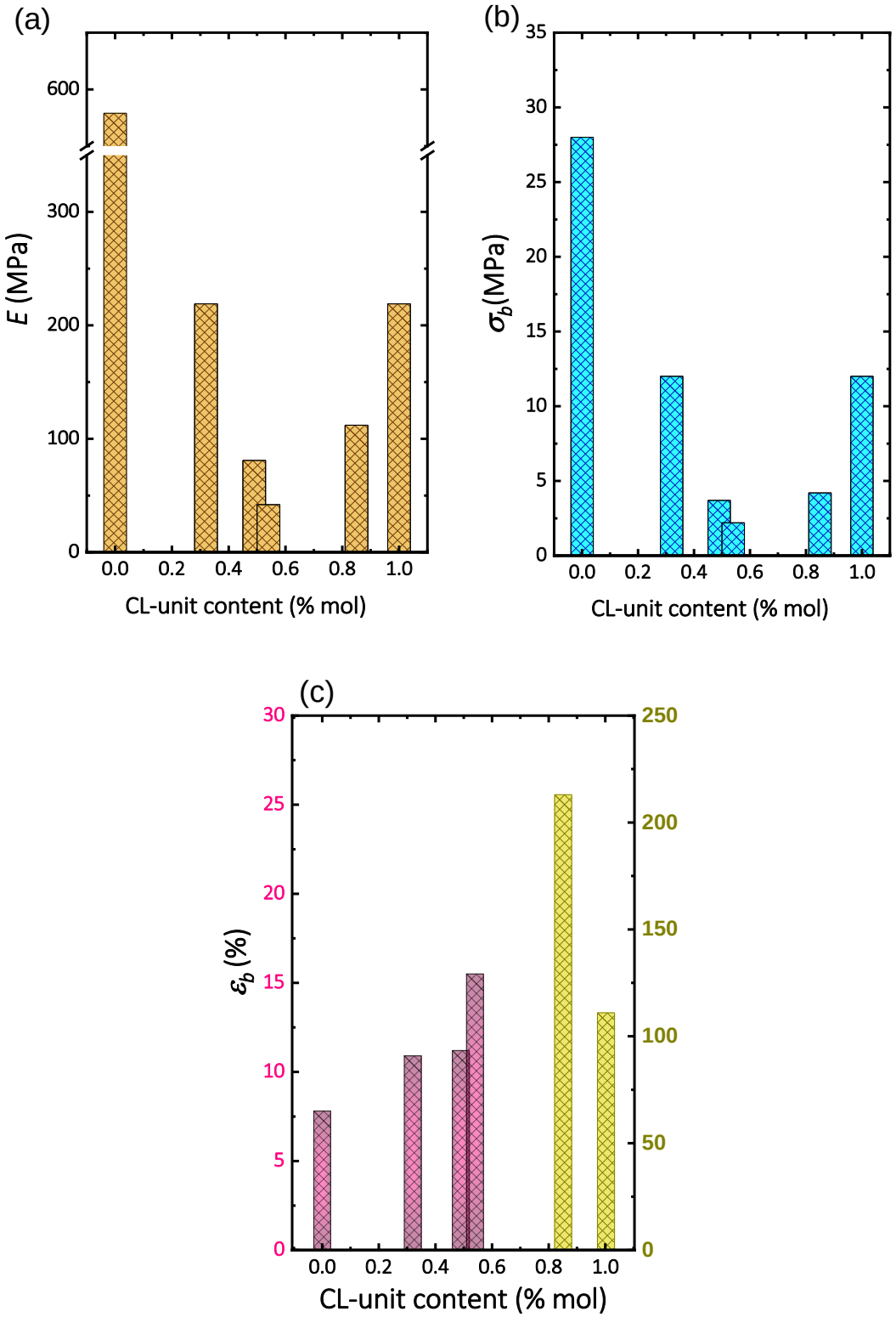


***Figure 7.6.*** *Mechanical properties of VHMw-$BS_xCL_y$ random copolyesters with data derived from stress-strain curves.*

### 7.2.4. DMTA results

Figure 7.7 shows the loss factor (*tan δ*) of hot-pressed samples as a function of temperature. Figure A.7.3 shows the storage modulus. The glass transition temperatures ($T_g$) of copolyesters calculated from the *tan δ* peak temperature are summarized in Table 7.3. The neat PBS sample showed the highest $T_g$ (-10 °C); then, the $T_g$ value shifted to lower temperatures as the amount of CL comonomer was increased (See Table 7.3). $T_g$ values were measured from the *tan δ* changes because the peak *tan δ* corresponds to the transition midpoint and the peak *E″* corresponds to the onset transition region temperature [20].

The $T_g$ values of the random copolymers were between the $T_g$ values of the two parental homopolymers and depended on composition [28]. The Fox equation is usually used to estimate the $T_g$ of miscible blends and random copolymers in a bulk state [29] depending on their composition:

$$\frac{1}{T_g} = \frac{w_1}{T_{g1}} + \frac{1-w_1}{T_{g2}} \qquad \text{Eq.7.1}$$

where $T_{g1}$ and $T_{g2}$ are the glass transition temperatures of homopolymers 1 and 2 (considering $T_{g1} < T_{g2}$) and $w_1$ the mass fraction of homopolymer 1. Thus, $T_g$ is the glass transition temperature of the copolymer and depends on its composition. As can be seen in Figure 7.8a, the composition dependence was found to follow the Fox equation (Equation 7.1). The solid line is the $T_g$ calculated by Eq. 7.1 and the scattered data is the experimental $T_g$.

The $T_g$ values obtained from DMTA (in this chapter, Figure 7.8) and DSC (chapter 5, Figure 5.7) were different for the same samples, $T_{g,DSC} < T_{g,E''}$. The difference was around 20 °C. DMTA applies a heating rate and, at the same time, a mechanical deformation at a particular frequency; therefore, this increases the rate at which $T_g$ is being measured.

The intensity of the *tan δ* peak can be used for the quantitative analysis of the amorphous phase of the polymer [30]. When getting closer to the pseudo-eutectic composition, the intensity of the tan *δ* increased, implying the expansion of the amorphous phase. For PBS-PCL copolymers, the *tan δ* peak became narrower than in the case of the neat PBS and PCL, which may suggest an increase in the chain mobility of the copolymer.

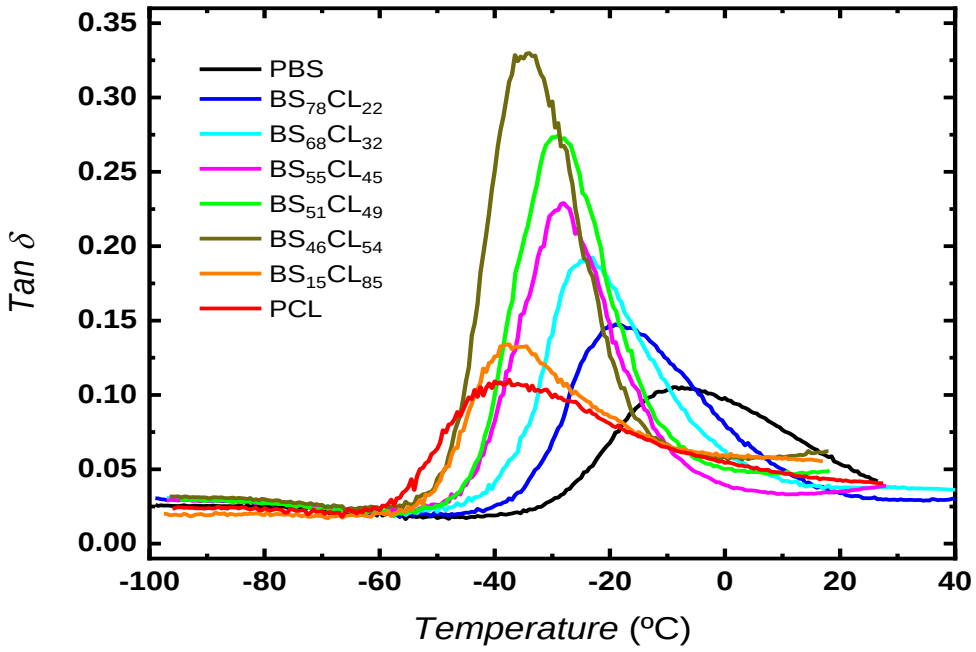


***Figure 7.7.*** *Loss tangent (Tan δ) of the copolyesters as a function of temperature at a constant heating rate of 4 °C/min and a frequency of 1 Hz.*

Figure 7.9a shows that the storage modulus in all copolymers and their corresponding homopolymers decreased very sharply between -40 to -20 °C and this depended on the composition. The loss modulus of all samples is plotted in Figure A.7.3. These changes in the storage modulus were accompanied by a peak in the loss modulus and *tan δ*. Figure 7.9b shows the variations of the storage modulus *E*' at two specific temperatures: -80 and 10 °C. The storage modulus at -80 °C, which is below the glass transition temperature of all composition, almost remained constant within an error of about ±10 %. The storage modulus below the glass transition region, where the amorphous chains are in a rigid state, cannot be affected by changing the crystallinity of the polymer.

***Table 7.3. $T_g$ values for VHMw PBS-ran-PCL copolyesters extracted from the tan δ peak.***

| Composition | $T_g$ (°C) |
|---|---|
| **PBS** | -10.0±0.7 |
| **$BS_{78}CL_{22}$** | -18.1±0.4 |
| **$BS_{68}CL_{32}$** | -23.3±0.5 |
| **$BS_{55}CL_{45}$** | -28.5±0.3 |
| **$BS_{51}CL_{49}$** | -30.0±1.4 |
| **$BS_{45}CL_{55}$** | -33.8±0.9 |
| **$BS_{15}CL_{85}$** | -36.8±0.5 |
| **PCL** | -37.5±0.1 |

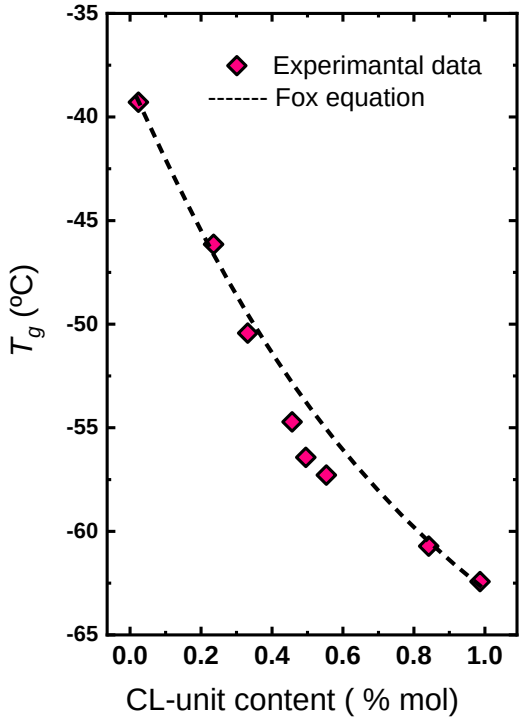


***Figure 7.8.*** *$T_g$ values of VHMw-$BS_xCL_y$ copolyesters as a function of the CL unit content and how they fit to the Fox equation.*

On the other hand, Figure 7.9b shows that the storage modulus *E'* at 10 °C decreased with increasing comonomer unit content. The modulus above $T_g$ was a function of the degree of crystallinity; amorphous chains are mobile and the degree of crystallinity plays a dominant effect on the modulus of the copolymer. This result is consistent with the results of *tan δ* and DSC, which show that crystallinity decreased with the increase of comonomer content in this random copolyester.

The storage modulus values versus CL-unit content in Figure 7.9b presented a similar pseudo-eutectic behavior that indicated a significant correlation between isodimorphism and mechanical properties.

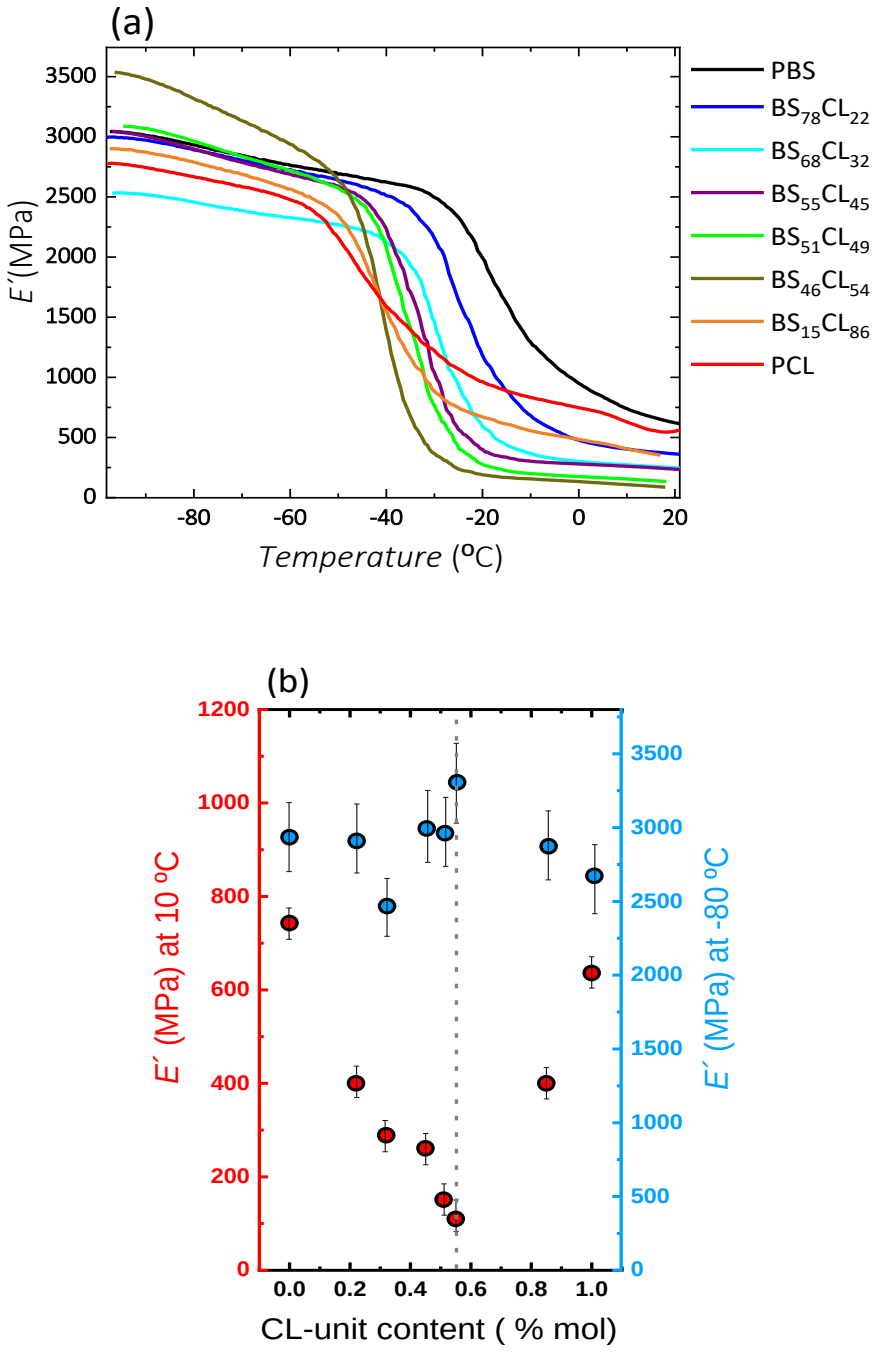


***Figure 7.9.*** *(a) Storage modulus of the copolyesters as a function of temperature at 1 Hz. (b) Changes in the storage modulus at -80 °C and at 10 °C versus CL-unit content. The segmented vertical line is drawn to indicate the pseudo-eutectic composition.*

## 7.3. CONCLUSION

Biodegradable PBS-*ran*-PCL copolyesters with very high molar weight have been successfully synthesized by ring opening-polycondensation copolymerization and characterized by $^{1}H$ NMR. The molecular weights were higher than 40000 g/mol for all synthesized polyesters. These random copolyesters were able to crystallize in the entire composition range and their calorimetric properties exhibited a pseudo-eutectic point like those previously synthesized with a much lower molecular weight.

The incorporation of comonomers at each side of the pseudo-eutectic point caused an increase in the elongation at break, and, among the samples, the $BS_{15}CL_{85}$ composition displayed the maximum elongation at break. In this copolymer, the loss modulus and *tan δ* curves exhibited a single $T_g$ peak that shifted from neat PBS to neat PCL by increasing the CL comonomer content. The composition dependence of the elastic modulus and stress showed a similar pseudo-eutectic behavior at the same eutectic point of isodimorphism, which indicated a significant correlation between the composition in isodimorphic copolymers and their mechanical properties. Storage modulus behaved differently below and above the glass transition temperature. Adding a comonomer randomly along the chain to either PBS or PCL did not affect the storage modulus at temperatures below the glass transition; however, due to the fact that the degree of crystallinity is predominant factor affecting mechanical properties at temperatures above the glass transition, the storage modulus decreased when getting closer to the pseudo-eutectic point.

## 7.4. REFERENCES

1. Babu, R. P.; O'connor, K.; Seeram, R., Current progress on bio-based polymers and their future trends. *Progress in Biomaterials* **2013,** *2* (1), 8.

2. Reddy, M. M.; Vivekanandhan, S.; Misra, M.; Bhatia, S. K.; Mohanty, A. K., Biobased plastics and bionanocomposites: Current status and future opportunities. *Progress in polymer Science* **2013,** *38* (10-11), 1653-1689.

3. Xu, J.; Guo, B.-H., Microbial succinic acid, its polymer poly (butylene succinate), and applications. In *Plastics from Bacteria*, Springer: Heidelberg, Berlin, 2010; pp 347-388.

4. Gigli, M.; Fabbri, M.; Lotti, N.; Gamberini, R.; Rimini, B.; Munari, A., Poly (butylene succinate)-based polyesters for biomedical applications: A review. *European Polymer Journal* **2016,** *75*, 431-460.

5. Jacquel, N.; Freyermouth, F.; Fenouillot, F.; Rousseau, A.; Pascault, J. P.; Fuertes, P.; Saint-Loup, R., Synthesis and properties of poly (butylene succinate): Efficiency of different transesterification catalysts. *Journal of Polymer Science Part A: Polymer Chemistry* **2011,** *49* (24), 5301-5312.

6. Kamal, T.; Shin, T. J.; Park, S.-Y., Uniaxial tensile deformation of poly (ε-caprolactone) studied with SAXS and WAXS techniques using synchrotron radiation. *Macromolecules* **2012,** *45* (21), 8752-8759.

7. Mohamed, R. M.; Yusoh, K. In *A review on the recent research of polycaprolactone (PCL)*, Advanced Materials Research, Trans Tech Publ: 2016; pp 249-255.

8. Labet, M.; Thielemans, W., Synthesis of polycaprolactone: a review. *Chemical Society Reviews* **2009,** *38* (12), 3484-3504.

9. Zheng, L.; Li, C.; Wang, Z.; Wang, J.; Xiao, Y.; Zhang, D.; Guan, G., Novel biodegradable and double crystalline multiblock copolymers comprising of poly (butylene succinate) and poly (ε-caprolactone): synthesis, characterization, and properties. *Industrial & Engineering Chemistry Research* **2012,** *51* (21), 7264-7272.

10. Qiu, Z.; Komura, M.; Ikehara, T.; Nishi, T., Miscibility and crystallization behavior of biodegradable blends of two aliphatic polyesters. Poly (butylene succinate) and poly (ε-caprolactone). *Polymer* **2003,** *44* (25), 7749-7756.

11. Bhatia, A.; Gupta, R.; Bhattacharya, S.; Choi, H., Compatibility of biodegradable poly (lactic acid)(PLA) and poly (butylene succinate)(PBS) blends for packaging application. *Korea-Australia Rheology Journal* **2007,** *19* (3), 125-131.

12. Gumede, T.; Luyt, A.; Muller, A., Review on PCL, PBS, and PCL/PBS blends containing carbon nanotubes. **2018**.

13. Gumede, T. P.; Luyt, A. S.; Tercjak, A.; Müller, A. J., Isothermal Crystallization Kinetics and Morphology of Double Crystalline PCL/PBS Blends Mixed with a Polycarbonate/MWCNTs Masterbatch. *Polymers* **2019,** *11* (4), 682.

14. Huang, J.; Cui, C.; Yan, G.; Huang, J.; Zhang, M., A study on degradation of composite material PBS/PCL. *Polymers and Polymer Composites* **2016,** *24* (2), 143-148.

15. Huang, M.; Dong, X.; Wang, L.; Zheng, L.; Liu, G.; Gao, X.; Li, C.; Müller, A. J.; Wang, D., Reversible Lamellar Periodic Structures Induced by Sequential Crystallization/Melting in PBS-co-PCL Multiblock Copolymer. *Macromolecules* **2018,** *51* (3), 1100-1109.

16. Can, E.; Bucak, S.; Kınacı, E.; Çalıkoğlu, A. C.; Köse, G. T., Polybutylene Succinate (PBS)–Polycaprolactone (PCL) Blends Compatibilized with Poly (ethylene oxide)-block-poly (propylene oxide)-block-poly (ethylene oxide)(PEO-PPO-PEO) Copolymer for Biomaterial Applications. *Polymer-Plastics Technology and Engineering* **2014,** *53* (11), 1178-1193.

17. Van Rie, J.; Declercq, H.; Van Hoorick, J.; Dierick, M.; Van Hoorebeke, L.; Cornelissen, R.; Thienpont, H.; Dubruel, P.; Van Vlierberghe, S., Cryogel-PCL combination scaffolds for bone tissue repair. *Journal of Materials Science: Materials in Medicine* **2015,** *26* (3), 123.

18. Odian, G., *Principles of Polymerization*. John Wiley & Sons: Hoboken, New Jersey, 2004.

19. Fakirov, S., Condensation polymers: Their chemical peculiarities offer great opportunities. *Progress in Polymer Science* **2019,** *89*, 1-18.

20. Ciulik, C.; Safari, M.; de Ilarduya, A. M.; Morales-Huerta, J. C.; Iturrospe, A.; Arbe, A.; Müller, A. J.; Muñoz-Guerra, S., Poly (butylene succinate-ran-ε-caprolactone) copolyesters: Enzymatic synthesis and crystalline isodimorphic character. *European Polymer Journal* **2017,** *95*, 795-808.

21. Safari, M.; Martínez de Ilarduya, A.; Mugica, A.; Zubitur, M.; Muñoz-Guerra, S. n.; Müller, A. J., Tuning the Thermal Properties and Morphology of Isodimorphic Poly [(butylene succinate)-ran-(ε-caprolactone)] Copolyesters by Changing Composition, Molecular Weight, and Thermal History. *Macromolecules* **2018,** *51* (23), 9589-9601.

22. Giammanco, G.; Martínez de Ilarduya, A.; Alla, A.; Muñoz-Guerra, S., Hydrolyzable aromatic copolyesters of p-dioxanone. *Biomacromolecules* **2010,** *11* (9), 2512-2520.

23. Van Krevelen, D. W.; Te Nijenhuis, K., *Properties of polymers: their correlation with chemical structure; their numerical estimation and prediction from additive group contributions*. Elsevier: 2009.

24. Mandelkern, L., The crystalline state. *Physical properties of polymers* **2004,** *3*, 209-315.

25. Cao, A.; Okamura, T.; Ishiguro, C.; Nakayama, K.; Inoue, Y.; Masuda, T., Studies on syntheses and physical characterization of biodegradable aliphatic poly (butylene succinate-co-ε-caprolactone) s. *Polymer* **2002,** *43* (3), 671-679.

26. Jin, C.; Wei, Z.; Yu, Y.; Sui, M.; Leng, X.; Li, Y., Copolymerization of ethylene brassylate with δ-valerolactone towards isodimorphic random copolyesters with continuously tunable mechanical properties. *European Polymer Journal* **2018,** *102*, 90-100.

27. Turi, E., Thermal Characterization of Polymeric Materials. Academic Press. *New York* **1997**.

28. Hiemenz, P. C.; Lodge, T. P., *Polymer chemistry*. CRC press: 2007.

29. Fox, T. G., Influence of Diluent and of Copolymer Composition on the Glass Temperature of a Poly-mer System. *Bull. Am. Phys. Soc.* **1956,** *1*, 123.

30. Tsagaropoulos, G.; Eisenberg, A., Dynamic mechanical study of the factors affecting the two glass transition behavior of filled polymers. Similarities and differences with random ionomers. *Macromolecules* **1995,** *28* (18), 6067-6077.

# *Chapter VIII:*

# *The Nucleation, Crystallization and Dielectric Relaxation of PBS and PBA Infiltrated within AAO Templates*

# Table of Contents

## ABSTRACT

This work describes the successful melt infiltration of poly(butylene succinate) (PBS) and poly(butylene adipate) (PBA) within 70 nm diameter anodic aluminum oxide (AAO) templates. The infiltrated samples were characterized by SEM, Raman, and FTIR spectroscopy. The crystallization behavior and crystalline structure of both polymers, bulk and confined, were analyzed by differential scanning calorimetry (DSC) and grazing incidence wide angle x-ray scattering (GIWAXS).

DSC revealed that a change in the nucleation process occurred from heterogeneous nucleation for bulk samples, to homogeneous nucleation for infiltrated PBA, and to surface-induced nucleation for infiltrated PBS. GIWAXS results indicate that PBS nanofibers crystallize in the α-phase, as well as their bulk samples. However, PBA nanofibers crystallize just in the β-phase, whereas PBA bulk samples crystallize in a mixture of α- and β-phases. The crystal orientation within the pores was determined, and differences between PBS and PBA were also found.

Finally, broadband dielectric spectroscopy (BDS) was applied to study the segmental dynamics for bulk and infiltrated samples. The glass temperature was found to significantly decrease in the PBS case upon infiltration while that of PBA remained unchanged. These differences were correlated with the higher affinity of PBS to the AAO walls as compared to PBA, in accordance with their nucleation behavior (surface-induced versus homogeneous nucleation respectively).

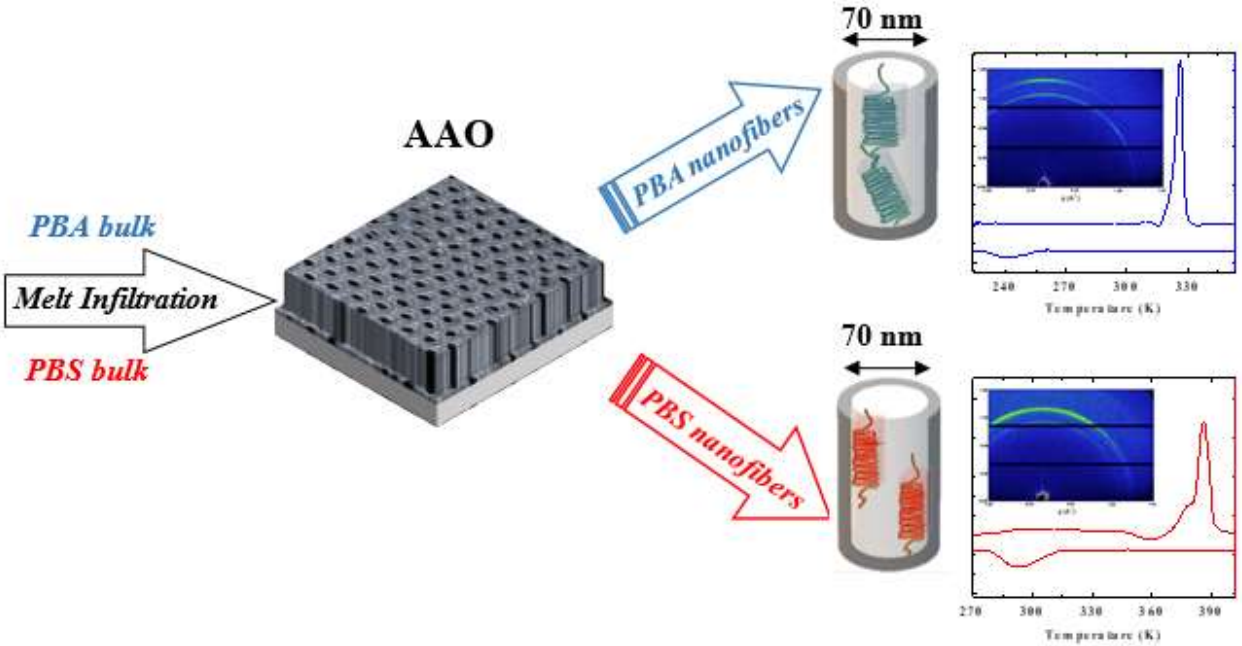
70 nm
AAO
PBA nanofibers
PBA bulk
Melt Infiltration
PBS bulk
70 nm
PBS nanofibers
240
270
300
330
Temperature (K)
270
300
330
360
390
Temperature (K)

## 8.1. INTRODUCTION

Poly(butylene succinate) (PBS) and poly(butylene adipate) (PBA) are biodegradable commercial synthetic polyesters. These polymers have similar properties to linear low-density polyethylene and can be processed in conventional equipment commonly used for polyolefins [1]. This is the reason, why the applications of these biopolyesters have found a place in the market. Nevertheless, although from a macroscopic point of view, polymer properties of both polyesters have already been studied, their properties at the nanoscale level have been scarcely reported, even when it is known that confining a polymeric material into nanosized cavities introduces a new variable to those determining the properties of the material. In fact, the nucleation and crystallization of semi-crystalline polymers are dramatically affected by confinement [2-5] and also segmental, and molecular dynamics are hindered or restricted in many polymers, by confinement [6-8]. Moreover, when confining polymers in nanocavities, polymer-wall, and polymer-substrate interactions can give rise to adsorption and/or to the formation of different chain conformations that will affect both structural and dynamic properties. So, it seems crucial to determine how polymer properties, crystallization and polymer dynamics of PBS and PBA can be affected by confinement, in particular, in cylindrical Anodic Aluminum Oxide (AAO) templates, one of the most studied spatial confinement systems.

Tailored anodic aluminum oxide templates fabricated by a two anodization procedure [9-13], contain arrays of aligned cylindrical nanopores with narrow pore diameter distributions. Nanocavities of AAO templates provide versatility with respect to the diameter and length of the pores that are not interconnected. As reported in the literature, self-ordered nanoporous anodic aluminum oxide templates have been largely employed in the preparation of polymer nanofibers and nanotubes with diameters ranging from 20 to 400 nm and lengths from 700 nm to higher than 100 microns. Thus, AAO nanocavities have been infiltrated by many polymers and polymer-based composites of different chemical nature and

their polymer properties/structure relationship studied as a function of the degree of confinement.

Two of the most relevant physical phenomena studied in relation to the final properties of a polymer in confinement are crystallization and polymer dynamics. Moreover, crystalline regions can significantly modify the relaxation behavior of polymer chains in the amorphous regions and consequently affect many important physical properties. Confinement effects on polymer crystallinity and crystal structure and molecular dynamics of semicrystalline polymers, such as, poly(ethylene) oxide (PEO) [14-15], poly(ε-caprolactone) (PCL) [16-17], poly(vinylidene fluoride) (PVDF) [18-20], poly(L-lactide) (PLLA) [21], polypropylene(PP) [16], poly(3-hydroxybutyrate)(PHB) [22], poly(ethylene)(PE) [23] , syndiotactic polystyrene (sPS) [24], poly(3-dodecylthiophene) (P3DDT) [25], Nylon-6 [26], and even block copolymers with PEO and PE crystallizable blocks [23], just to name a few examples, have been studied in the past.

Recent reviews on polymer crystallization discuss AAO infiltrated systems, as well as, polymer confined in droplets, ultrathin films or nanolayers.[2-3, 5, 27] One of the main conclusions of these works is that, as confinement increases, the crystallization temperature can experience large decreases, reflecting a change from heterogeneous nucleation in the bulk polymer to surface or homogeneous nucleation for polymers infiltrated inside nanopores. In some cases, fractionated crystallization has been reported (see references 2 and 3 and references therein). Recently, some of us reported[17] that if a proper removal of the polymer layer that typically remains after infiltration is not achieved, this leads to pore connection at the surface of the AAO. In this case, such percolation of pores by a polymer layer can cause the appearance of fractionated crystallization. It has also been reported, that the crystallization of homogeneously nucleated crystals decreases as pore volume decreases (i.e., increasing confinement) since the probability of nucleation also decreases and if the pore volume is below a critical size (around 10 nm), crystallization can be totally inhibited.

In summary, nanoconfinement plays a significant role in two main factors of crystallization: (a) a change in nucleation mechanism, from heterogeneous nucleation to surface or homogeneous nucleation and (b) the dependence of the crystallization temperature on the volume or the surface (or interphase) of the crystallizable micro or nanodomains. Moreover, the melting point also decreases with confinement but to a much lesser degree than the crystallization temperature. Also, Su et al. reported a preferential orientation of polymeric crystals generally induced by one or two-dimensional confinement [28]. Avrami indexes decrease with confinement until values of 1 (or even lower) are achieved in the limit of isolated domains, as the material approaches a first-order (or lower) crystallization kinetics. This type of kinetics reflects that nucleation is the rate-determining step in the overall crystallization of ideally confined polymers [2-3, 5, 27, 29].

The molecular motions in polymer systems can be easily investigated using neutron diffraction and relaxation techniques [30-31]. Both techniques allow monitoring glass transition changes in confined situations in comparison to the bulk material. Confinement effects are of two types, pure confinement effects due to the hindering of a molecular motion, as a consequence of restricted space, and associated confinement effects, i.e., they are not a direct consequence of a confined molecular motion but related to surface interaction effects and, therefore, also related to low dimensionality, although they can often be masked. Nevertheless, this effect cannot be underestimated since, in many nanomaterials applications, the polymer is close to a surface which effectively confines it. In this kind of materials, surfaces are usually attractive, so interactions take place.

Recently, it has been shown that confinement not only affects segmental dynamics but also the chain dynamics of polymers, where an unexpected enhancement of the flow and a reduction in intermolecular entanglements has been found. Only to cite some examples, the influence of polymer confinement within templates of cylindrical nanopores on the single-chain dynamics of PEO has been studied by neutron scattering techniques [14-15, 32], and the segmental dynamics

and the relaxation behavior of PVDF [18], PHB [22] and PMMA by broad dielectric spectroscopy [33]. Results showed that the properties of the infiltrated polymers largely differ from those of the respective bulk polymer. However, the influence of confinement on the dynamic properties of polymer nanostructures is far from generalized and needs to be studied for each particular case, i.e., for PBS and PBA, among other biopolymers.

Taking into account previous results for semicrystalline polymers[18, 32], this chapter aims to elucidate the influence of confinement effects on the thermal properties of PBS and PBA infiltrated within nanoporous AAO templates. Both PBA and PBS are biodegradable aliphatic polyesters with a crystallization ability in the range 35–45% and a glass transition temperature $T_g$ around -55 °C and -35 °C, respectively. The samples were studied by Differential Scanning Calorimetry (DSC), Grazing Incidence Wide Angle X-Ray Scattering (GIWAXS), Scanning Electron Microscope (SEM), Broadband Dielectric Spectroscopy (BDS), Infrared (IR) and Raman spectroscopy. Very large differences were found in the nucleation and crystallization of the infiltrated materials with respect to the polymers in bulk. The dielectric relaxation results indicated that molecular relaxations of the amorphous parts of both PBS and PBA were also significantly affected by confinement.

## 8.2. RESULTS AND DISCUSSION

### 8.2.1. SEM observations

SEM allows observing the surface of the AAO templates and the obtained nanofibers, after the partial dissolution of the alumina template with 1 M NaOH solution. The AAO templates are opened on one side only. The other side is closed and also contains the original aluminum base employed for the preparation of the template.Figure 8.1a shows a representative image of the manufactured AAO templates, which confirms the size of the nanopores of the obtained templates. The pore size distribution on the sample surface is uniform with very well-defined geometry. Figures 8.1b and 8.1c are representative images of PBS and PBA

nanofibers with around 70 nm diameter, respectively. As it can be seen, we have obtained nanofibers with good quality and high aspect ratio.

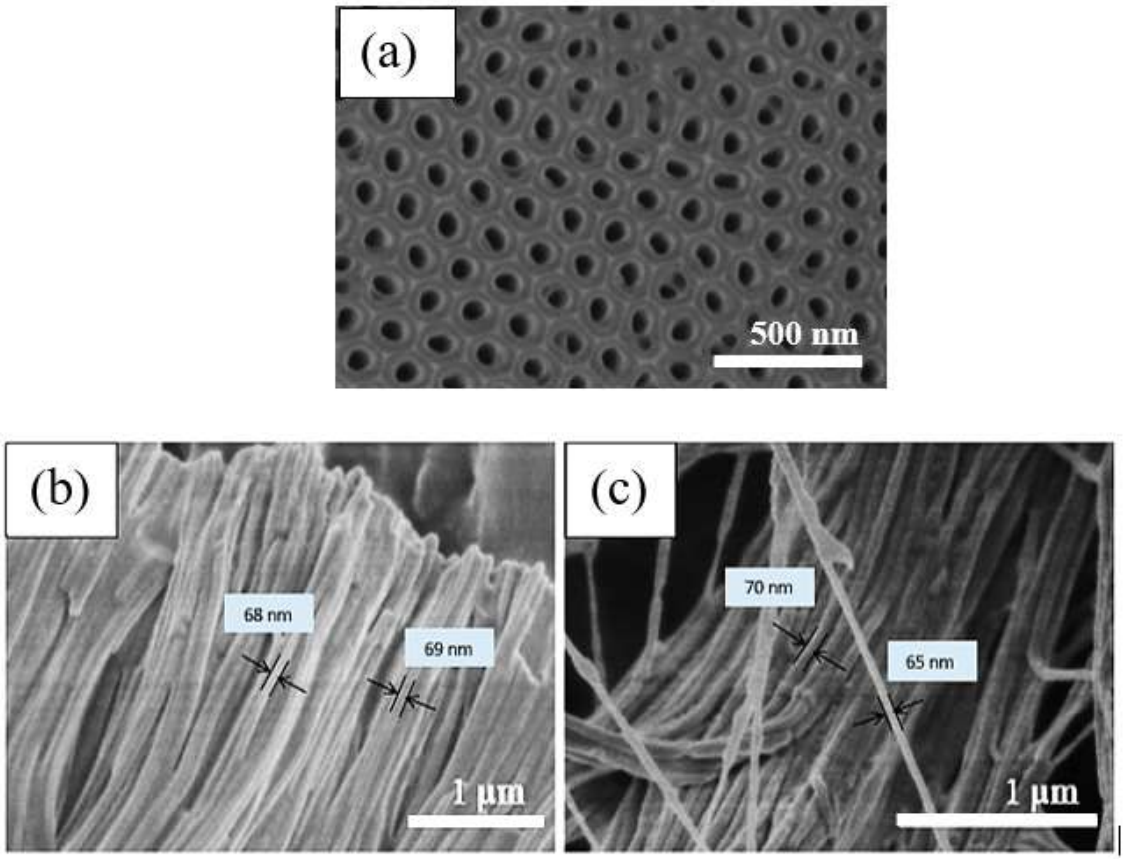


***Figure 8.1.*** *(a) SEM micrograph of the top view of the prepared AAO template with 70 nm pore size and 30 µm length, (b) PBS and (c) PBA nanofibers grown in the AAO template (after the dissolution of the template in 1 M NaOH solution for 1 h).*

### 8.2.2. Raman and FTIR spectroscopies

AAO templates filled with PBS and PBA nanofibers were analyzed by Raman spectroscopy to corroborate that the infiltration of the polymers had been carried out successfully. PBS and PBA in bulk were also studied to compare their spectra with those of the infiltrated materials. For the characterization of Raman spectroscopy, first, the different main bands are assigned to each of the bonds that make up the PBS and PBA, respectively. The PBS and PBA spectra in bulk present less noise than confined samples and the bands are very well-defined, so these spectra will be used to compare with the spectra of infiltrated materials and to verify with their characteristic bands that the polymer has infiltrated correctly.

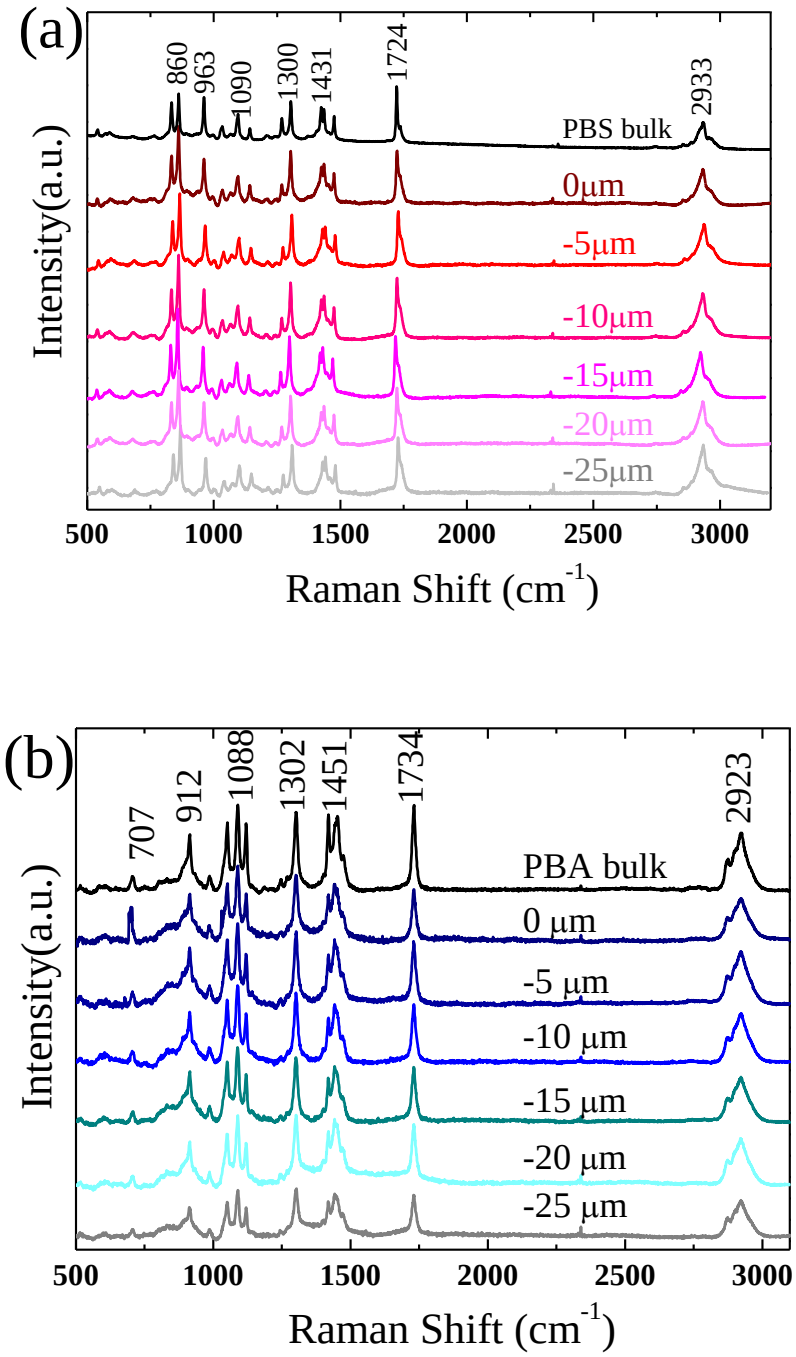


***Figure 8.2***. *Depth profile Raman spectra of PBS (a) and PBA (b) in bulk, as references, and infiltrated within AAO templates with 70 nm pore size and 30 μm length. Inserted numbers show the depth from the AAO surface.*

For both polymers, the signals identified with specific bond vibrations according to the literature[34-36] are the following: around 2958 $cm^{-1}$, asymmetric stretching mode of the $CH_2$ groups; around 2875 $cm^{-1}$, symmetric stretching mode of the $CH_2$ groups; around 1724 $cm^{-1}$, stretching mode of the C = O bonds; around 1457 $cm^{-1}$, bending in the plane of the $CH_2$; and around 1121 $cm^{-1}$, stretching mode of the C-O bonds.

Figure 8.2a and 2b show the normalized Raman spectra of infiltrated PBS and PBA inside AAO templates, with pinhole placement at different depths. Despite the noise due to the fluorescence of the alumina, it is possible to observe all characteristic bands of PBS and PBA up to 25 µm, respectively. As observed, all the bands remain constant along the depth for both polymers, so, it confirms that both polymers penetrated homogeneously into the nanocavities.

Taking into consideration the SEM images of the nanofibers together with the Raman results and weight calculations of polymer infiltration, we can assume that the polymers were completely infiltrated into the full length of the nanopores (30 µm).

Figure 8.3 shows FTIR spectra for PBS (a) and for PBA (b). Based on the literature[36-41], characteristic absorption bands in the range 3100−2800 $cm^{-1}$ are identified as C−H vibrations of $CH_2$ and $CH_3$ groups. The strong bands at 1712 and 1725 $cm^{-1}$ are due to the carbonyl group of the PBS and PBA ester groups, respectively. The other important bands are: C−H bending at 1460 $cm^{-1}$ and C=O stretching at 1160-1170 $cm^{-1}$. The signal at 1154 $cm^{-1}$ is a characteristic of C–O–C stretching vibration in the repeated $–OCH_2CH_2$ unit.

The most important differences in FTIR spectra between bulk and infiltrated samples are located at two regions that are labeled as *a* and *b* in Figure 8.3. In the dashed square labeled "*a*" in Figure 8.3, i.e., region from 1100–850 $cm^{-1}$, three

strong absorption bands corresponding to the C–O single bonds can be observed. For both polyesters, the band at 915 $cm^{-1}$ (marked as dashed vertical line I) corresponds to the C–OH bending vibration of the carboxylic acid groups and the band at 953 $cm^{-1}$ (marked as dashed vertical line II) is due to the O–$CH_3$ stretching. Peaks at 1063 $cm^{-1}$ for PBA and at 1045 $cm^{-1}$ for PBS (marked as dashed vertical line III) correspond to C−C−O stretching vibration. The ratio of the intensity of the C−O stretching and C–OH bending peaks to the intensity of the O−$CH_3$ stretching peaks (III/II and I/II) increases in the nanofibers, as compared to the bulk. Also, the ratio of the intensity of the C−O stretching band to the intensity of the C−OH bending band (III/I) decreases in the nanofibers with respect to the bulk. These changes prove that nano-structuration affects the FTIR spectra. In fact, we can observe a smaller share of O−$CH_3$ bonds in the spectra, which could result from the interaction of PBS and PBA chains with the walls of the AAO templates. The differences between infiltrated and neat PBS spectra seem higher than those present in the case of neat and infiltrated PBA, but quantification of these signals is difficult.

In addition, for both PBA and PBS, we observed a new intense band at 1571 $cm^{-1}$ (see dashed square labeled “b” in Figure 8.3), which is characteristic of carboxylic acid salt stretching vibrations ($COO^-$), probably formed inside the AAO pores were small amounts of water moisture produced the hydrolysis of ester groups due to the hydrophilic character of the AAO template [42-44]. From the obtained results, it can be concluded that with nano-structuration of PBA and PBS, there is a decrease of interactions between the polymer chains and new interactions appear between the polymer chains and the walls of the AAO templates (i.e., C−O on O−$CH_3$). Similar results were found for infiltrated PMMA as a function of the degree of confinement, by Raman spectroscopy. The Raman results helped to understand the effect of confinement on dielectric relaxation behavior of the PMMA [33].

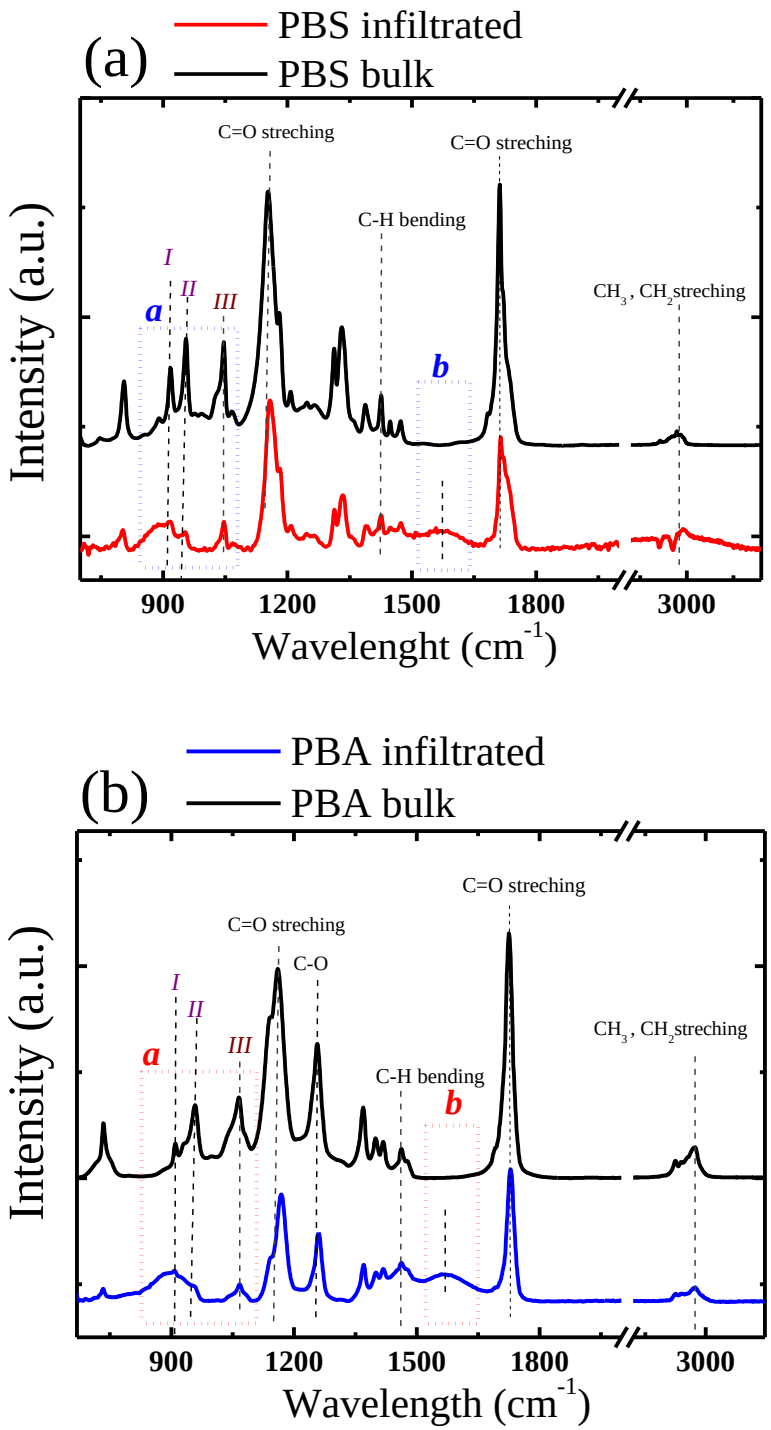


**Figure *8.3.*** *FT-IR spectra of PBS (a) and PBA (b) in bulk, as reference, and infiltrated in AAO templates with 70 nm nanopore size and 100 µm length.*

### 8.2.3. Non-isothermal Crystallization

DSC scans of PBS-bulk, PBA-bulk, PBS-nanofibers, and PBA-nanofibers inside 70 nm AAO templates are shown in Figure 8.4. The extracted data from DSC curves are summarized in Table 8.1. Figure 8.4a shows that during the cooling scan, PBA-bulk exhibits a crystallization peak at around 306 K that it is shifted drastically to 241 K when the PBA is confined within the alumina nanopores. The subsequent heating scans show that the melting point of confined PBA is slightly lower as compared to bulk PBA, 330 K, and 326 K, respectively. Moreover, Figure 8.4b shows that the crystallization peak of PBS-bulk decreased from 355 K to 291 K in confined PBS and the peak melting temperature of PBS-bulk is 388 K, whereas it is 385 K for infiltrated PBS.

Both infiltrated PBS and PBA show only a single crystallization exotherm at temperatures much lower than those in bulk (between 64 and 66 K lower respectively). The total absence of a crystallization peak at crystallization temperatures similar to those in bulk PBS or PBA indicates that the number of nanopores is much higher (possibly by several orders of magnitude) than the number of active heterogeneities capable of nucleating these polyesters in bulk at much lower supercooling. In other words, the nanopores are statistically clean, and they are also completely isolated and in no way interconnected [16,24]. If after the infiltration process a polymer layer would have remained on top of AAO template, such layer could have interconnected pores and then spread heterogeneous nucleation by percolation. In this work, we have applied very careful cleaning procedures (see experimental section) to make sure that no remaining film is left after cleaning the surface of the AAO nanocavities following the recommendations of Shi et al.[17], so heterogeneous nucleation can be ruled out.

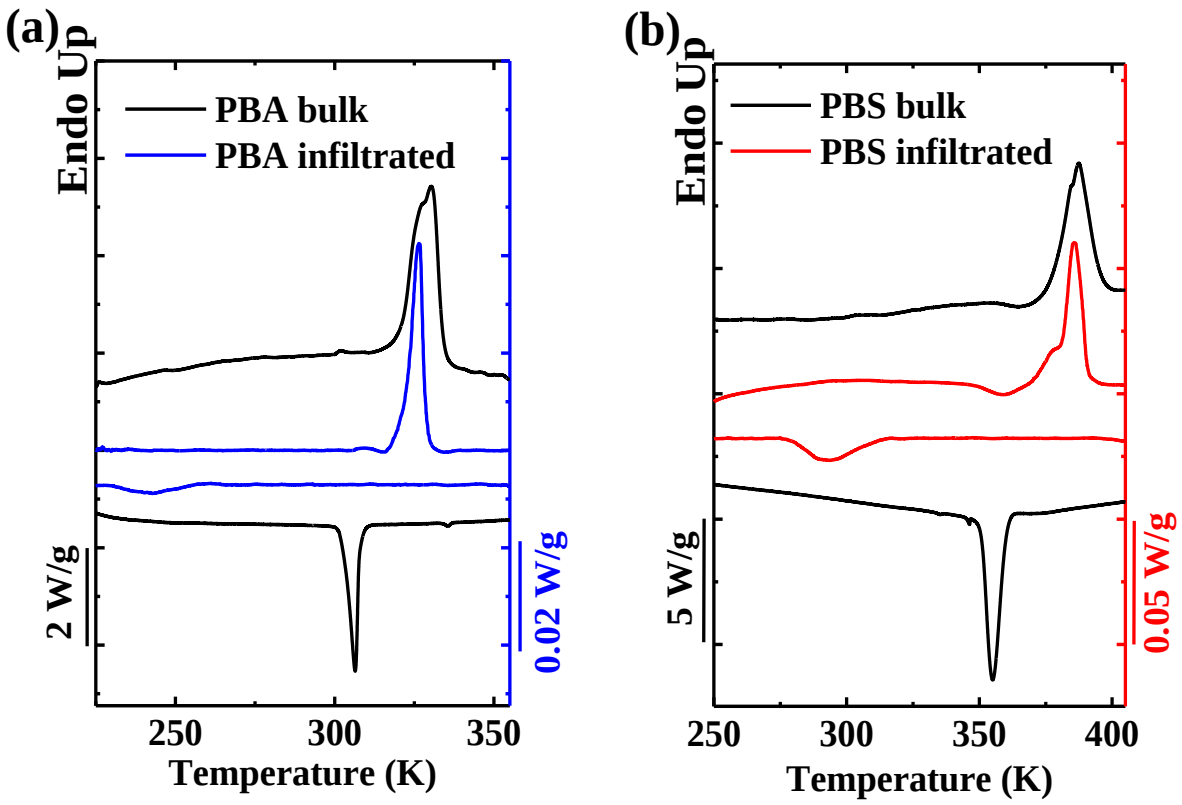


***Figure 8.4**. DSC curves for bulk and infiltrated samples of (a) PBA and (b) PBS.*

Mi et al. [45] studied how PBA nanotubes in alumina templates with 100 and 200 nm pore diameters crystallized, and they observed a very small shift of the non-isothermal crystallization temperature. This either indicates that all nanotubes contain similar heterogeneities as those of PBA in bulk, or that some PBA film remained on the surface of the AAO templates interconnecting the nanopores. However, our work is focused on how confinement affected phase transitions rather than in the nucleation of PBA.

***Table 8.1:*** *Data Summary of DSC Results*

| Sample | $T_m$ (K) | $T_c$ (K) |
|---|---|---|
| **PBS bulk** | 388 | 355 |
| **PBS Infiltrated** | 385 | 291 |
| **PBA bulk** | 330 | 306 |
| **PBA Infiltrated** | 326 | 241 |

The change in $T_c$ obtained upon infiltration in this work can be explained by a change in the nucleation mechanism of the polyesters, from heterogeneous to homogeneous or to surface nucleation. Infiltrated polymers can also nucleate at the AAO surface [2-3, 17, 27, 46-47]. It is difficult to distinguish between surface and homogeneous nucleation.[2-3, 27, 48] However, if the crystallization temperature is very close to the glass transition temperature (5-15 K above the $T_g$ value), the nucleation will be most likely homogeneous.[2, 3, 29, 48] If on the other hand, the crystallization occurs at higher supercooling as compared to the bulk polymer, but still at considerably higher temperatures than $T_g$, then surface nucleation probably dominates the nucleation process within the nanopores. However, it must also be remembered that the homogeneous nucleation temperature is a function of the volume of the isolated nano or micro-domains. [29]

Comparing the $T_g$ value for PBA (218 K) with the crystallization temperatures reported in Table 8.1, we can deduce that the nucleation must have

changed from heterogeneous for the bulk sample (with $T_c$ = 306 K) to homogeneous for the infiltrated sample (with a peak at $T_c$ = 241 K, notice that the exotherm is wide and ends at 228 K), as the infiltrated sample is crystallizing at temperatures very close to the glass transition temperature. Therefore, in the infiltrated PBA case, the crystallization occurs just before vitrification in a single exotherm, a clear sign of confined crystallization initiated by homogeneous nucleation [2, 3, 29, 48].

The situation differs for the PBS case, as the crystallization changes from a peak value of 355 K to 291 K upon infiltration. Even though the change in supercooling is large, the $T_g$ of PBS is located at around 243 K, hence still significantly much lower. Therefore, in the infiltrated PBS nanofibers, our DSC results indicate that the crystallization during cooling from the melt probably occurs by surface-induced nucleation caused by the AAO walls.

### 8.2.4. Crystalline Structure and chain orientations of PBS and PBA within nanopores

To investigate the orientation and crystal texture of the PBA and PBS crystals within the AAO nanopores, 2D WAXS experiments with Grazing incident mode were carried out at room temperature.

Figure 8.5a and 8.5b show GIWAXS patterns for PBS-bulk and PBS-nanofibers (i.e., infiltrated PBS), respectively. There are five distinct reflections for PBS-bulk at $q$ = 13.9, 15.5, 16.0, 18.4, 20.3 nm$^{-1}$. These reflections have $d$-spacing values of 4.52, 3.97, 3.93, 3.41, and 3.09 Å, which can be assigned to the following crystal planes: (020/$\bar{1}$11), (021), (110), (12$\bar{1}$) and (111), respectively. Similar diffraction features can be found for the infiltrated PBS. Two major peaks with $q$ =13.8 and 15.9 nm$^{-1}$ can be indexed as the (020/$\bar{1}$11) and (021/110) reflections. Compared with the bulk PBS, the (021) and (110) reflections are not well resolved in the infiltrated sample. As shown in Figure Apnx.8.1 (see Appendix), the peak centered at 15.9 nm$^{-1}$ can be fitted with two peaks. The small shoulder peak corresponds to the (021) reflection. Nevertheless, the difference is subtle, and we

would not like to emphasize too much about the (021) peak. Therefore, we assign this peak to a combination of (021) and (110) reflections. The (111) reflection at $q$ = 20.3 $nm^{-1}$ is also visible in the infiltrated PBS. The results show that both the bulk and the infiltrated PBS crystallized into the same α form.

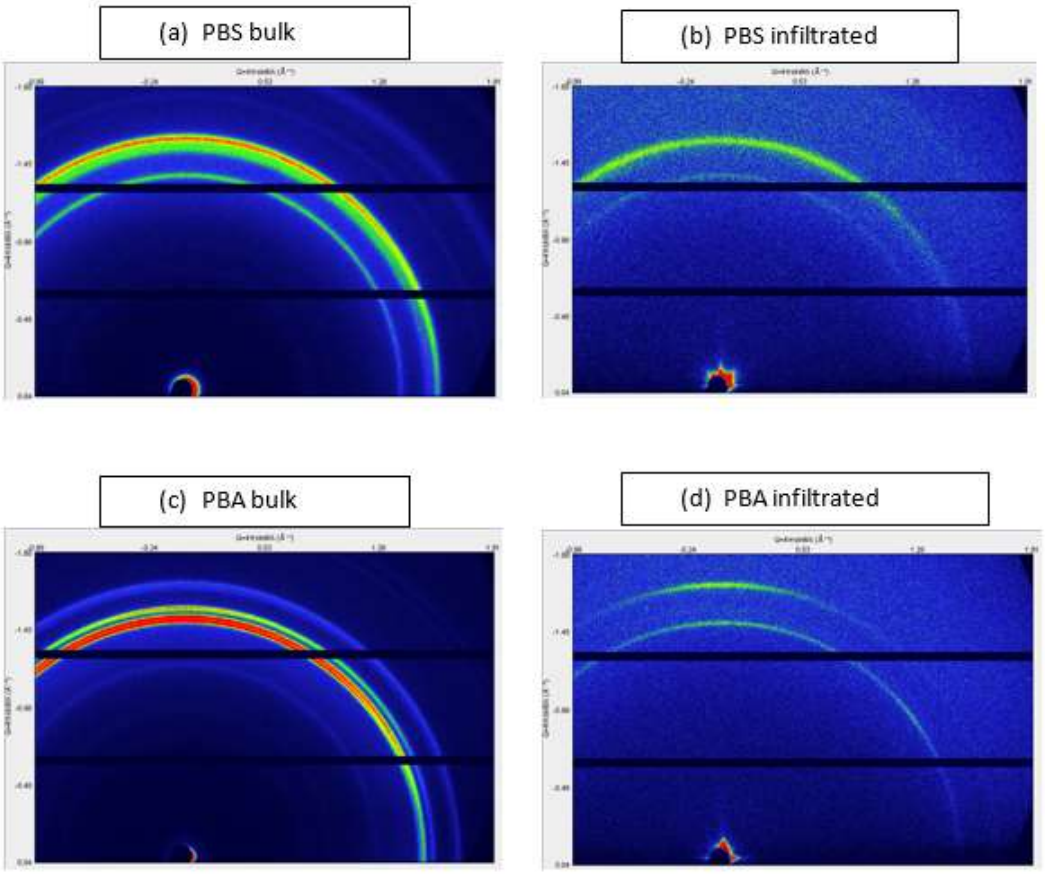


***Figure 8.5.*** *2D WAXS patterns of (a) PBS-bulk (b) PBS infiltrated (c) PBA-bulk, and (d) PBA-infiltrated within AAO template with pore depth of 30 μm and pore diameter of 70 nm. X-ray incident angle with respect to the template is 3°.*

Figure 8.5c and Figure 8.5d show the GIWAXS patterns of PBA-bulk and PBA-nanofibers, respectively. For PBA-bulk, main reflections were observed at $q$= 12.5, 15.1, 15.3, 15.8, 17.0, and 17.2 $nm^{-1}$. The reflections have $d$-spacing values of 5.03, 4.16, 4.10, 3.98, 3.69, and 3.65 Å, which can be assigned to the following crystallographic planes: $\alpha$ (002), $\beta$ (110), $\alpha$ (110), $\alpha$ (020), $\alpha$ (021), and $\beta$ (020) reflections[49-51], respectively. Hence, bulk PBA shows a mixture of two polymorphic phases, $\alpha$ and $\beta$.[52] On the other hand, the reflection patterns of the PBA-nanofibers show only two $\beta$-crystals reflections at $q$ = 15.1 and $q$ = 17.2 $nm^{-1}$, which can be assigned to $\beta$ (110), $\beta$ (020) reflections. Sun et al. have reported similar results, as they only found $\beta$-crystals reflections, for PBA infiltrated within AAO templates [45, 53].

In both polymers, the scattered intensity inside AAO is poorer than the scattered intensity in bulk. This could be associated with the reduced amount of polymer inside the AAO template, in conjunction with a decrease in the degree of crystallinity.

Another feature of confined crystallization of polymers within AAO is the usual orientation of crystals inside the nanopores. As shown in Figure 8.6a, the degree of anisotropy of the PBS nanofibers is quite low as compared with other polymers such as PCL[17], PEO[15], and iPP.[17] One possible reason is that the two major scattering arcs contain more than one reflection. If we assume the normal case of "*c* axis perpendicular to the pore axis"[20], the (020) and (110) should locate on the meridian, while the ($\bar{1}$11) and (021) should locate somewhere on the off-meridian position. Therefore, the mixed reflections could cause the broad azimuthal distribution of the two major arcs (see schematic illustration in Figure 8.6c).

On the other hand, infiltrated PBA exhibits a higher degree of anisotropy, as it is clear that the (020) reflection locates predominately on the meridian (see figure 8.6b). Azimuthal intensity profiles (see Figure 8.7) show that the intensity of the (020) peak is strongest on the meridian (azimuth = 90°). Two peaks are

observed for the (110) reflection at azimuth = 90° and 36°. The β form of PBA has an orthorhombic unit cell with lattice parameters of *a* = 0.505 nm, *b* = 0.736 nm, and *c* = 1.47 nm[54-55], resembling crystalline structures of poly(tetramethylene adipate) [56].

The Polanyi equation is given by [57]:

$$\cos(\varphi) = \cos(\theta)\cos(\phi) \qquad \text{Eq.8.1}$$

where $\vartheta$ is the half Bragg angle and $\phi$ the azimuthal angle with respect to the meridian. Plugging $\vartheta$ = 10.7° and $\phi$ = 54° (90°-36°) into the equation yields a $\varphi$ value of 55°, which agrees with the angle between the (110) plane and the (020) plane for PBA infiltrated crystals. The meridional (020) and the (110) shoulder peak at azimuth = 36° correspond to the orientation mode of *b*-axis parallel to the pore axis (see schematic illustration in Figure 8.6d).

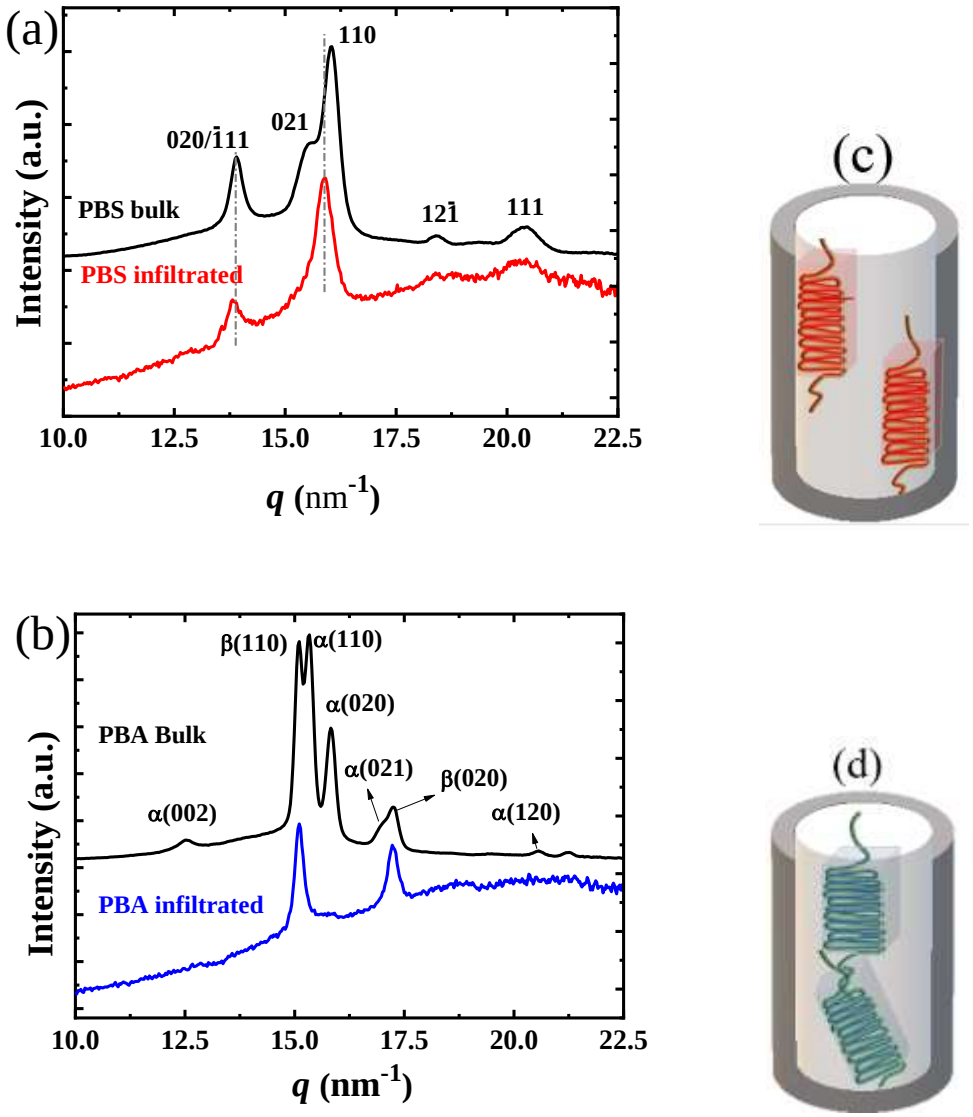


***Figure 8.6.*** *Corresponding 1D intensity profile of PBS (a) and PBA (b) samples, obtained by averaging the intensity along the azimuthal angle. Schematic illustration showing the cross section of a PBS (c) and PBA (d) nanofibers embedded in an AAO template with chain-folded lamellar crystals inside the nanopores.*

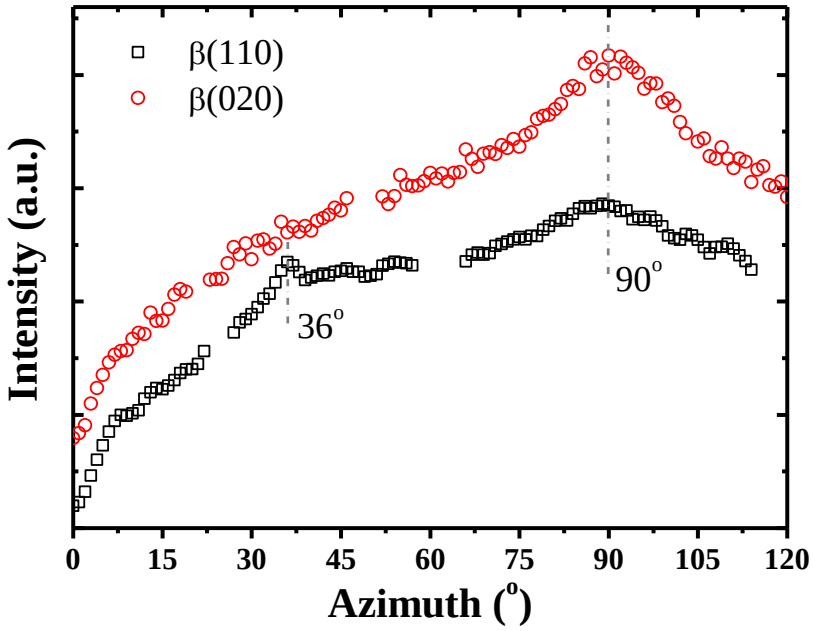


***Figure 8.7****. Azimuthal intensity profiles of the two major reflections of the infiltrated PBA sample.*

On the other hand, the (110) reflection for infiltrated PBA crystals has a broad peak at azimuth = 90°, which may indicate another possible orientation mode with the (110) plane normal parallel to the pore axis. We thus conclude that the PBA crystals within AAO templates exhibit a mixed orientation of *b*-axis or the (110) plane normal, parallel to the pore axis. Sun et al. reported an orientation mode of *b*-axis parallel to the pore axis for infiltrated PBA [45]. However, the crystallization temperatures of their infiltrated PBA samples are 301 K (200 nm) and 299 K (100 nm), much higher than that of our sample (241 K, 70 nm).

Our recent study showed that the orientation of crystals within AAO is determined by the fastest growth direction of crystals [28]. Therefore, the frequently observed mixed orientation in infiltrated polymers within AAO templates is rationalized by the comparable growth rates along several different crystal planes.

This scenario works for PBA as well, because the (110) and (010) growth planes are the two fastest growth planes of PBA, as shown by the morphology of solution crystallized single crystals [58].

### 8.2.5. Broadband Dielectric Spectroscopy for bulk and confined polymers

The dielectric loss, $\varepsilon''$, measured as a function of temperature is presented for bulk and infiltrated PBA and PBS samples in Figures 8.8a and 8.8b.

In both cases, two relaxation regions are observed: β and α in the order of increasing temperature. The relaxation processes appear as a peak in the dielectric loss spectra, moving towards higher temperatures as frequency increases. Two frequencies were plotted for comparison purposes, $10^1$ and $10^3$ Hz. At high temperatures, both polymers show the so-called α-relaxation (or long-range segmental relaxation) which is the dielectric manifestation of the glass transition. In this relaxation process, the relaxation time strongly increases as temperature decreases.

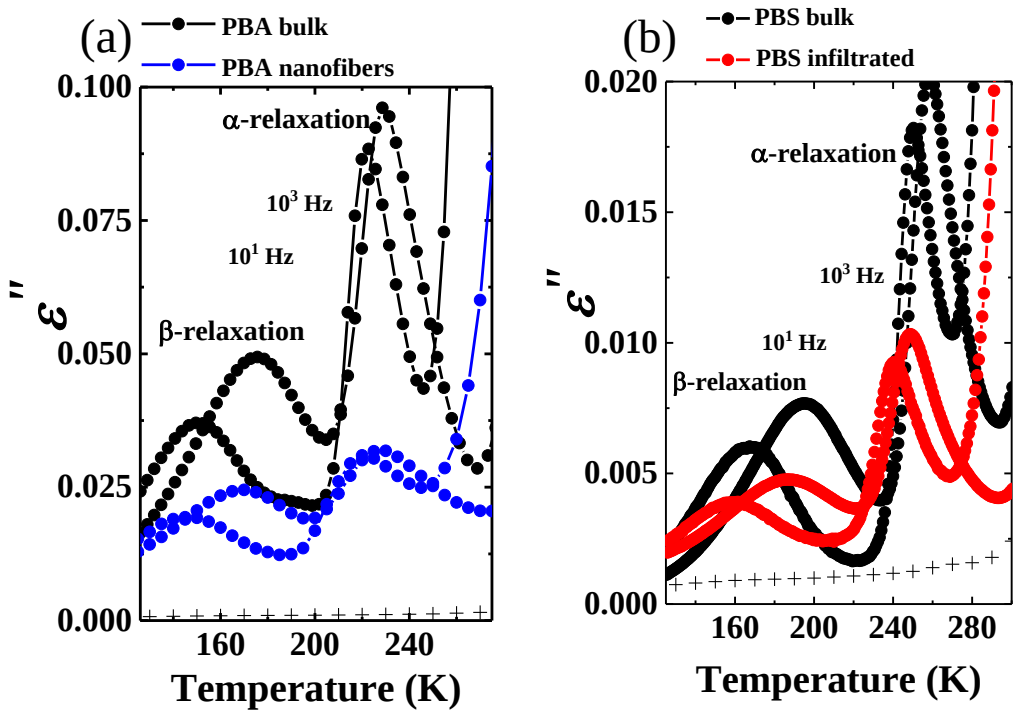


***Figure 8.8.*** *Isochronal plots of ε´´ for (a) PBA bulk and PBA infiltrated in 70 nm alumina template, and (b) PBS bulk and PBS infiltrated in 70 nm alumina template at $10^1$ and $10^3$ Hz. Loss curves of empty AAO templates (+) at $10^3$ Hz are included in both Figures for comparison purposes.*

A secondary *β*-relaxation is also detected in Figure 8.8. The *β*-relaxation is due to the short-range motions of lateral or short-chain segments, which occur below the glass transition temperature [59]. For this kind of semicrystalline polyesters, where the dielectric relaxations are related with reorientations of the dipole moments in the ester groups, a single *β*-relaxation component is observed, as Arandia et al. recently reported.[60] To get this single *β*-relaxation peak, the samples have to be carefully dried before the dielectric experiments are performed [61].

Figure 8.8 also shows data for PBA and PBS infiltrated within 70 nm pore AAO templates. For these samples, the dielectric losses have a lower contribution than the bulk samples (due to the reduction of the volume of the sample capacitor filled by the polymer) and an additional background-like signal from the alumina template that is weakly dependent on frequency and temperature. Relaxation processes (i.e., $\alpha$ and $\beta$) move to lower temperatures at given frequencies when the polymers are confined within the alumina nanopores.

Representative isothermal experiments in the temperature range relevant for the $\beta$-relaxation were carried out to analyze in detail the changes observed. The isothermal permittivity loss versus frequency for all samples at different temperatures is presented in Figure 8.9. In this figure, the main peaks observed correspond to the $\beta$-relaxation, and it is possible to compare quantitatively the differences in relaxation rates between bulk polymers and infiltrated samples better than in the isochronal plots case (Figure 8.9).

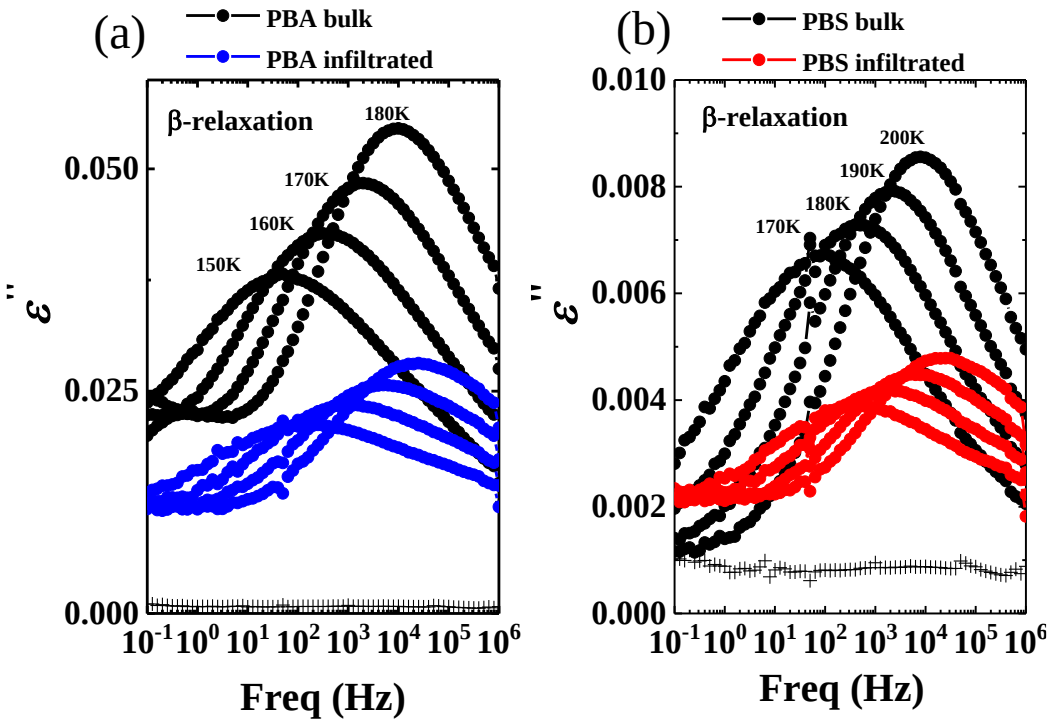


***Figure 8.9.*** *Isothermal plots of ε´´ for (a) PBA bulk and PBA infiltrated in 70 nm alumina template at 150, 160, 170 and 180K, and (b) PBS bulk and PBS infiltrated in 70 nm alumina template at 170, 180, 190 and 200K. Loss curves of empty AAO templates (+) at 160K for Figure 9a and at 180K for Figure 9b are included for comparison purposes.*

In the *β*-relaxation region, the peak frequency, $f_{max}$, of confined polymers occurs at higher frequencies than those of bulk samples, indicating a faster local dynamics (see Figure Apnx.8.2). Some conformational changes also explained and observed above by FTIR can cause these faster dynamics in the *β*-relaxation when the samples are infiltrated into alumina nanopores. Confined effects can be due to the limited small spaces within the alumina nanocavities or to surface nucleated alumina walls. To quantify these differences, the relaxation time from each isothermal plot has been calculated as:

$$\tau = (2\pi f_{max})^{-1} \qquad \text{Eq.8.2}$$

For both systems, a clear Arrhenius behavior is found, and consequently, the data have been fitted to the Arrhenius equation:

$$\tau\,(T) = \tau_\infty \exp\left[\frac{E_a}{k_B\,T}\right] \qquad \text{Eq.8.3}$$

The resulting values are presented in Table 8.2. The activation energies for both bulk samples, PBA and PBS, are about 10% higher than those obtained for infiltrated samples.

***Table 8.2.*** *Parameters describing the temperature dependence of the β-relaxation and α-relaxation.*

| Sample | β-relaxation | | | | α-relaxation | | | |
|---|---|---|---|---|---|---|---|---|
| | $E_a$ (kJ/mol) | $\tau_\infty$ (s) | $\Delta H$ (kJ/mol) | $\Delta S$ (kJ K/mol) | B (K) | $T_0$ (K) | $F_\infty$ (Hz) | $T_g$ * (K) |
| **PBA bulk** | 41 | $1.7\times10^{-17}$ | 40 | 0.072 | 1186 | 183 | $1\times10^{14}$ | 214 |
| **PBA Infiltrated** | 37 | $1.0\times10^{-16}$ | 6 | 0.058 | 1018 | 185 | $1\times10^{14}$ | 215 |
| **PBS bulk** | 43 | $1.4\times10^{-16}$ | 41 | 0.054 | 1393 | 204 | $1\times10^{14}$ | 238 |
| **PBS Infiltrated** | 38 | $4.3\times10^{-16}$ | 37 | 0.045 | 1387 | 195 | $1\times10^{14}$ | 229 |

** $T_g$ value for the bulk is taken equal to that one obtained from DSC data. The extrapolation to the infiltrated one is taken when log f (Hz) = a) -2.4 for PBA and b) -3.5 for PBS from Figure 8.11.*

The extremely low values obtained for $\tau_\infty$ indicate that the molecular origin of the β-relaxation does not correspond to single activated jumps between two equivalent positions of molecular units over an energy barrier, and therefore a more complex situation should be considered. One way of describing such behavior is by using the Eyring equation, where the relaxation time is expressed in terms of the difference in the Gibbs free energy, $\Delta G = \Delta H - T\Delta S$, between the equilibrium

and the activated state. This leads to an equation similar to the Arrhenius one, where an entropic term appears in addition to the enthalpic one, as follows:

$$\tau\,(T) = \frac{h}{k_B T} exp\left[\frac{\Delta G}{k_B T}\right] = \frac{h}{k_B T} exp\left[-\frac{\Delta S}{k_B}\right] exp\left[\frac{\Delta H}{k_B T}\right] \qquad \text{Eq.8.4}$$

where *h* is Planck´s constant and *ΔH* and *ΔS* are the enthalpic and entropic changes respectively corresponding to the activated state. The same data are plotted in Figure 8.10 but with a linear behavior corresponding to equation 8.4. The extracted parameters are shown in Table 8.2.

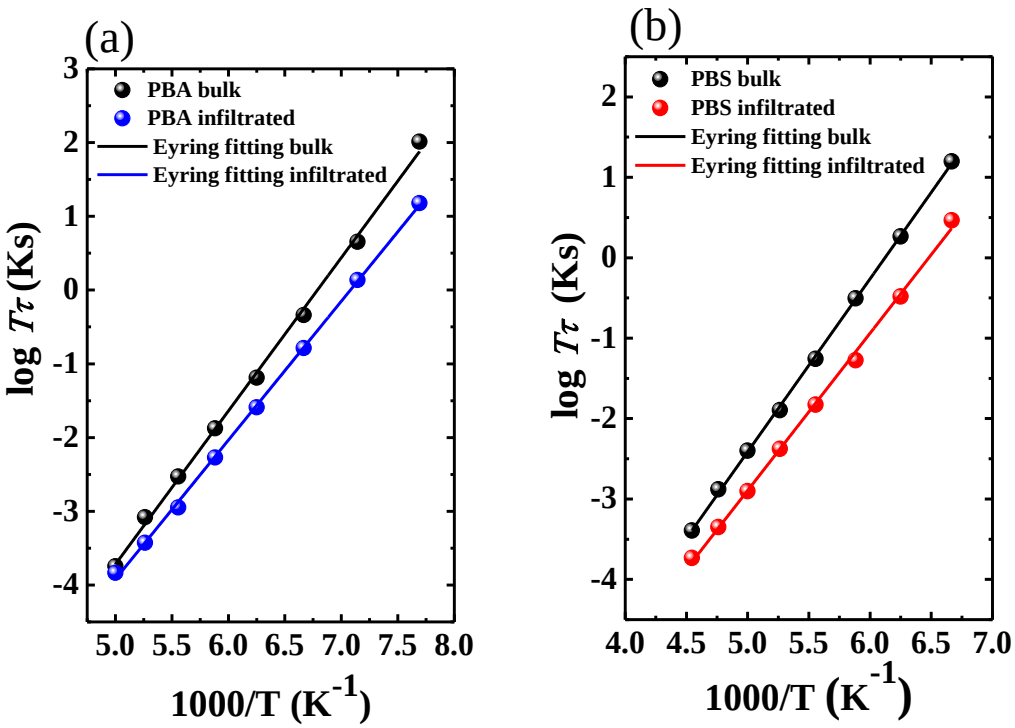


***Figure 8.10.*** *Arrhenius plots of β processes where solid lines represent the Eyring descriptions for (a) PBA bulk and infiltrated PBA, and (b) PBS bulk and infiltrated PBS.*

Both enthalpic and entropic terms observed for both bulk PBA and PBS take relatively large values as compared with the infiltrated samples. Accordingly, it seems that confinement in the nanopores not only reduce the energetic barriers

but also made the molecular mechanism for reorientation less complex (lower activation entropy).

Concerning the α-relaxation, it can be seen in Figure 8.6 that it is sharp and stronger as compared to the corresponding *β*-relaxation. The quantification of the *α*-relaxation has been made by using the isochronal representation shown in Figure 8.11, since the conductivity contributions difficult a reasonable analysis of the isothermal curves from the infiltrated polymers, mainly in the case of PBA.

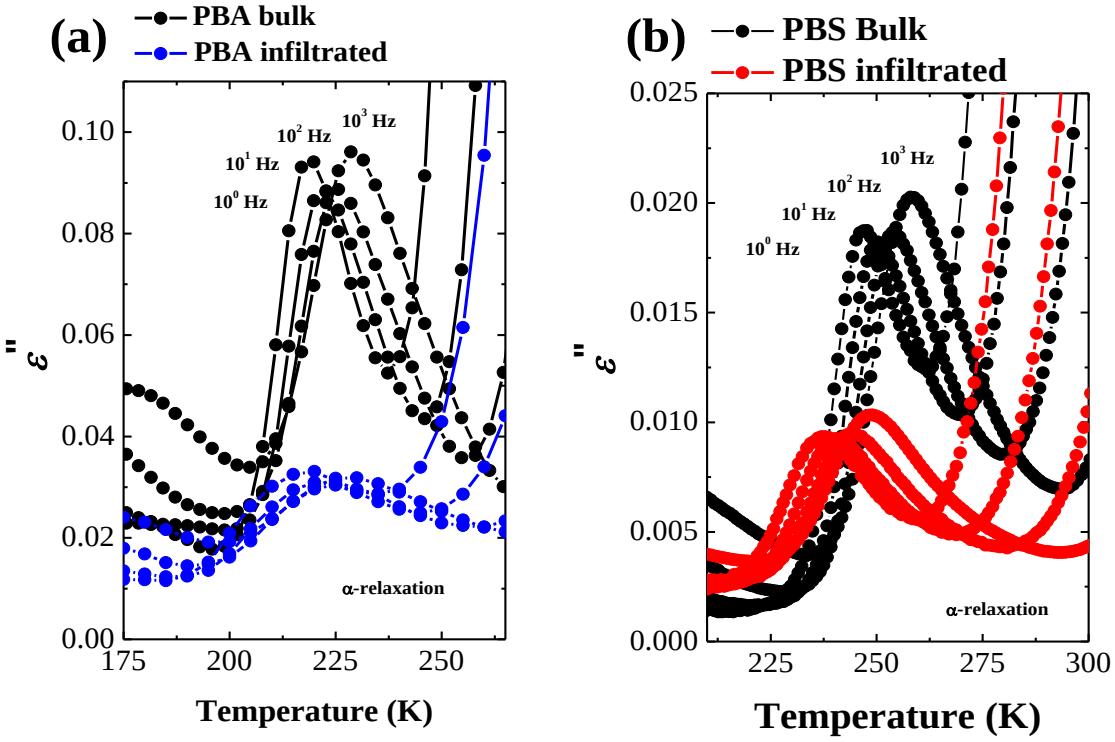


***Figure 8.11.*** *Isochronal plots of ε´´ (a) PBA bulk and infiltrated PBA, and (b) PBS bulk and infiltrated PBS for $10^0$, $10^1$, $10^2$ and $10^3$ Hz.*

Using the isochronal representation of the dielectric losses at different frequencies, the temperature ($T_{max}$) at which the *α*-relaxation loss peak occurs has

been determined for all samples. The temperature dependence of the peak frequencies corresponding to bulk and infiltrated samples are shown in Figure 8.12.

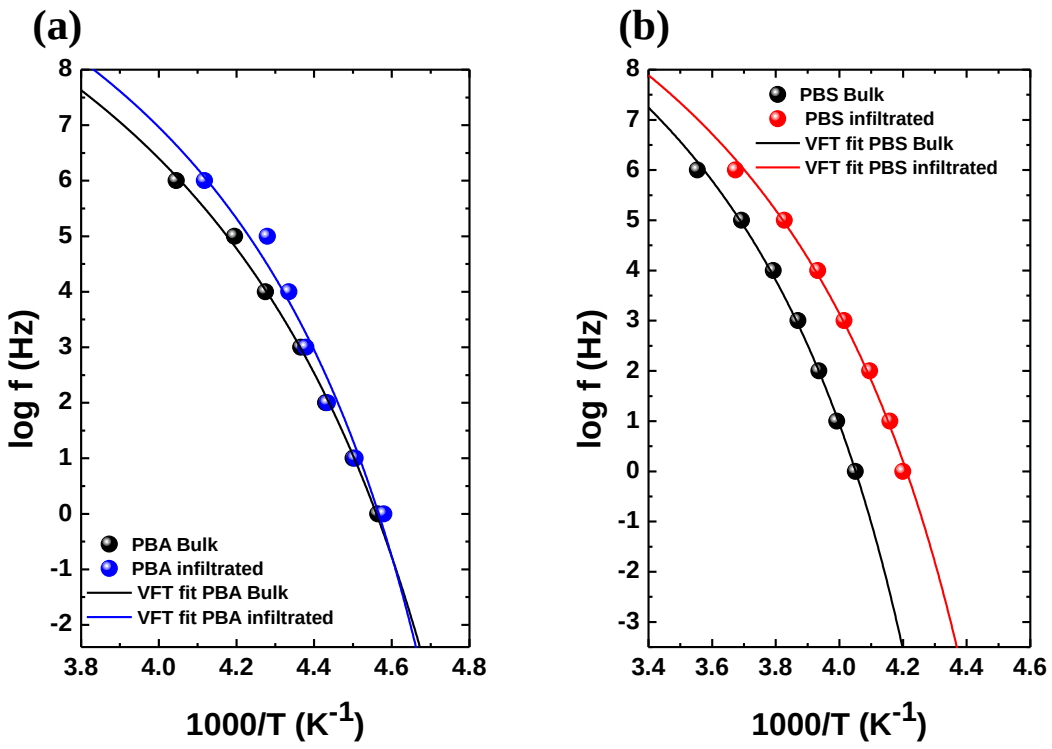


***Figure 8.12.*** *Arrhenius plot of the peak frequencies of (a) PBA bulk and infiltrated PBA, and (b) PBS bulk and infiltrated PBS. Solid lines represent the corresponding VFT fit of α relaxation.*

The data in Figure 8.12 were fitted to a usual Vogel-Fulcher-Tamman (VFT) equation

$$f\ (T_{max}) = f_{\infty} \exp\left(\frac{-B}{T_{max} - T_0}\right) \qquad \text{Eq.8.5}$$

where $T_0$ is the Vogel temperature, B is an energetic term, and $f_{\infty}$ would correspond to a typical vibration frequency. The obtained fitting lines are shown in Figure 8.12,

and the parameters are summarized in Table 8.2. To obtain accurate fits, and in accordance with the DSC $T_g$ values obtained for the bulk polymers, a value of $f_\infty$ of $1x10^6$ Hz was assumed.

The glass transition temperature obtained from the VFT fits is affected by confinement effects for both PBA and PBS samples. This glass transition temperature differences could be explained by taking into account the differences in the crystallinity between bulk and confined samples. However, the differences observed in α-relaxation peaks are also in accordance with the differences observed before in the $\beta$-relaxation peaks. Smaller differences are observed for the PBA than for the PBS polymer. However, there are also differences in the curvature of the VFT lines. In this case, the curvature increases for PBA but decreases for PBS. The behavior of PBA is quite unusual and could be due to a combination of two effects, one associated with faster local dynamics and the other hindering the cooperative motions involved in the glass transition. Consequently, it seems that these relaxations are quite dependent on the nature of the material used.

DSC experiments have also detected important differences in the crystallization of confined PBA and PBS, as in PBA the nucleation is probably homogeneous, but in the case of PBS, it is induced by the AAO walls (i.e., surface nucleation). Moreover, it is worth considering that confinement and surface effects of the nano-constraint polymers may not necessarily be identical over the entire frequency or temperature range of the relaxation response.

The results compiled in Table 8.2 suggest some correlation between the $\alpha$-relaxation and the $\beta$-relaxation, although both processes are located at different frequencies and temperature ranges. The different values obtained for $E_a$ ($\beta$-relaxation) and $T_0$ ($\alpha$-relaxation) reported for the confined samples in this manuscript, confirm that confinement effects are playing a large role in these samples, and that is why the dynamics of the PBA and PBS chains are different from those obtained for the bulk samples.

Furthermore, there are large differences in the trends experienced by the glass transition temperature (see Table 8.2) upon confinement. PBA either

experiences a very slight increase in $T_g$ upon infiltration (i.e., 1 K) or does not change with respect to the bulk if we consider the difference not significant. On the other hand, the $T_g$ of PBS decreases 9 K with confinement (see Table 8.2). These differences may be correlated with the different interactions that the polymer chains have with the AAO walls in addition to confinement effects.

In several infiltrated polymers, the detection of two $T_g$ transitions (or even 3 $T_g$ transitions) has been reported. This prompted researchers to interpret these two $T_g$ values, as arising from two different layers within the infiltrated material. Typically, one $T_g$ is much lower than the bulk $T_g$ value and the other one, either stays at temperatures close to the bulk value or is even higher. If we consider the pores as perfect cylinders, we can divide each pore into two concentric cylinders. One of them consists of chains with higher segmental long-range mobility in the amorphous regions (the part with the lower $T_g$ values), while the other has chains with more restricted mobility, comparable or even slower than those in the bulk material (the part with the higher $T_g$ values) [62-65-66].

In our case, only one $T_g$ relaxation process has been detected for both PBS and PBA. However, we speculate that in the PBS case, where the material is more likely to nucleate at the AAO walls, a rigid semi-crystalline layer could be produced around the pore walls that do not contribute to the α-process that we detect by dielectric experiments or DSC (maybe because the layer is thin and its mobility is compromised by the crystals present and by the interactions with the walls). Instead, the dominant mobile amorphous chains present in the core experience higher segmental mobility and concomitantly a lower $T_g$ value.

In the homogenously nucleated PBA case, the nucleation should occur within the volume of each nanopore (a characteristic of homogenous nucleation, see refs. 2-3) and away from the interface with the AAO walls. As the $T_g$ is similar than that of the bulk, we speculate that segmental mobility is in this case dominated by confinement within the pores and is less affected by the presence of the AAO walls [22].

## 8.3. CONCLUSIONS

Polybutylene succinate (PBS) and Polybutylene adipate (PBA) were successfully infiltrated within laboratory-made Anodic Aluminum Oxide (AAO) templates of 70 nm diameter. DSC results indicate that infiltrated PBA molecules nucleate homogeneously inside the pore volume while BDS measurements showed that $T_g$ values did not significantly change upon infiltration. On the other hand, PBS probably nucleates at the surface of AAO walls and the possible interactions with alumina were detected by FTIR. Such interaction with AAO walls influenced chain dynamics in such a way that BDS studies found a depression of approximately 9 K in the glass transition temperature upon infiltration. We conclude that PBS displays a higher affinity with AAO walls in comparison with PBA. Some differences were also found in terms of polymorphic behavior and crystal orientation between PBS and PBA by GIWAXS. Our study shows that the consequences of confinement in 70 nm diameter AAO templates are clearly different for PBA and PBS.

## 8.4. REFERENCES


1. Fujimaki, T., Processability and properties of aliphatic polyesters,'BIONOLLE', synthesized by polycondensation reaction. *Polymer degradation and stability* **1998,** *59* (1-3), 209-214.

2. Michell, R. M.; Blaszczyk-Lezak, I.; Mijangos, C.; Mueller, A. J., Confinement effects on polymer crystallization: From droplets to alumina nanopores. *Polymer* **2013,** *54* (16), 4059-4077.

3. Michell, R. M.; Mueller, A. J., Confined crystallization of polymeric materials. *Progress in Polymer Science* **2016,** *54*, 183-213.

4. Jiang, Q.; Ward, M. D., Crystallization under nanoscale confinement. *Chemical Society Reviews* **2014,** *43* (7), 2066-2079.

5. Wu, H.; Higaki, Y.; Takahara, A., Molecular self-assembly of one-dimensional polymer nanostructures in nanopores of anodic alumina oxide templates. *Progress in Polymer Science* **2018,** *77*, 95-117.

6. Mijangos, C.; Hernandez, R.; Martin, J., A review on the progress of polymer nanostructures with modulated morphologies and properties, using nanoporous AAO templates. *Progress in Polymer Science* **2016,** *54*, 148-182.

7. Alexandris, S.; Sakellariou, G.; Steinhart, M.; Floudas, G., Dynamics of unentangled cis-1, 4-polyisoprene confined to nanoporous alumina. *Macromolecules* **2014,** *47* (12), 3895-3900.

8. Politidis, C.; Alexandris, S.; Sakellariou, G.; Steinhart, M.; Floudas, G., Dynamics of Entangled cis-1, 4-Polyisoprene Confined to Nanoporous Alumina. *Macromolecules* **2019**.

9. Masuda, H.; Fukuda, K., Ordered metal nanohole arrays made by a two-step replication of honeycomb structures of anodic alumina. *science* **1995,** *268* (5216), 1466-1468.

10. Masuda, H.; Hasegwa, F.; Ono, S., Self-ordering of cell arrangement of anodic porous alumina formed in sulfuric acid solution. *Journal of the electrochemical society* **1997,** *144* (5), L127-L130.

11. Martín, J.; Manzano, C. V.; Martín-González, M., In-depth study of self-ordered porous alumina in the 140–400 nm pore diameter range. *Microporous and Mesoporous Materials* **2012,** *151*, 311-316.

12. Martín, J.; Manzano, C. V.; Caballero-Calero, O.; Martín-González, M., High-aspect-ratio and highly ordered 15-nm porous alumina templates. *ACS applied materials & interfaces* **2012,** *5* (1), 72-79.

13. Manzano, C. V.; Martín, J.; Martín-González, M. S., Ultra-narrow 12 nm pore diameter self-ordered anodic alumina templates. *Microporous and Mesoporous Materials* **2014,** *184*, 177-183.

14. Suzuki, Y.; Duran, H.; Steinhart, M.; Butt, H.-J.; Floudas, G., Homogeneous crystallization and local dynamics of poly (ethylene oxide)(PEO) confined to nanoporous alumina. *Soft Matter* **2013,** *9* (9), 2621-2628.

15. Guan, Y.; Liu, G.; Gao, P.; Li, L.; Ding, G.; Wang, D., Manipulating crystal orientation of poly (ethylene oxide) by nanopores. *ACS Macro Letters* **2013,** *2* (3), 181-184.

16. Suzuki, Y.; Duran, H.; Akram, W.; Steinhart, M.; Floudas, G.; Butt, H.-J., Multiple nucleation events and local dynamics of poly (ε-caprolactone)(PCL) confined to nanoporous alumina. *Soft Matter* **2013,** *9* (38), 9189-9198.

17. Shi, G.; Liu, G.; Su, C.; Chen, H.; Chen, Y.; Su, Y.; Müller, A. J.; Wang, D., Reexamining the crystallization of poly (ε-caprolactone) and isotactic polypropylene under hard confinement: nucleation and orientation. *Macromolecules* **2017,** *50* (22), 9015-9023.

18. Martín, J.; Mijangos, C.; Sanz, A.; Ezquerra, T. A.; Nogales, A., Segmental dynamics of semicrystalline poly (vinylidene fluoride) nanorods. *Macromolecules* **2009,** *42* (14), 5395-5401.

19. Steinhart, M.; Senz, S.; Wehrspohn, R. B.; Gösele, U.; Wendorff, J. H., Curvature-directed crystallization of poly (vinylidene difluoride) in nanotube walls. *Macromolecules* **2003,** *36* (10), 3646-3651.

20. Steinhart, M.; Göring, P.; Dernaika, H.; Prabhukaran, M.; Gösele, U.; Hempel, E.; Thurn-Albrecht, T., Coherent kinetic control over crystal orientation in macroscopic ensembles of polymer nanorods and nanotubes. *Physical review letters* **2006,** *97* (2), 027801.

21. Guan, Y.; Liu, G.; Ding, G.; Yang, T.; Müller, A. J.; Wang, D., Enhanced crystallization from the glassy state of poly (L-lactic acid) confined in anodic alumina oxide nanopores. *Macromolecules* **2015,** *48* (8), 2526-2533.

22. Dai, X.; Li, H.; Ren, Z.; Russell, T. P.; Yan, S.; Sun, X., Confinement Effects on the Crystallization of Poly (3-hydroxybutyrate). *Macromolecules* **2018,** *51* (15), 5732-5741.

23. Casas, M. T.; Michell, R. M.; Blaszczyk-Lezak, I.; Puiggali, J.; Mijangos, C.; Lorenzo, A. T.; Müller, A. J., Self-assembly of semicrystalline PE-b-PS diblock copolymers within AAO nanoporous templates. *Polymer* **2015,** *70*, 282-289.

24. Wu, H.; Wang, W.; Yang, H.; Su, Z., Crystallization and orientation of syndiotactic polystyrene in nanorods. *Macromolecules* **2007,** *40* (12), 4244-4249.

25. Wu, H.; Higaki, Y.; Nojima, S.; Takahara, A., Orientation and crystallization of regioregular poly (3-dodecylthiophene) in alumina nanopores. *Soft matter* **2017,** *13* (26), 4661-4666.

26. Yu, S.; Lai, Z.; Jinnai, H.; Zeng, X.; Ageishi, M.; Lotz, B.; Cheng, S. Z.; Zheng, N.; Zhang, S.; Feng, X., Adding Symmetry: Cylindrically Confined Crystallization of Nylon-6. *Macromolecules* **2019**.

27. Michell, R. M.; Blaszczyk-Lezak, I.; Mijangos, C.; Müller, A. J., Confined crystallization of polymers within anodic aluminum oxide templates. *Journal of Polymer Science Part B: Polymer Physics* **2014,** *52* (18), 1179-1194.

28. Su, C.; Shi, G.; Li, X.; Zhang, X.; Müller, A. J.; Wang, D.; Liu, G., Uniaxial and Mixed Orientations of Poly (ethylene oxide) in Nanoporous Alumina Studied by X-ray Pole Figure Analysis. *Macromolecules* **2018,** *51* (23), 9484-9493.

29. Müller, A. J.; Balsamo, V.; Arnal, M. L., Nucleation and crystallization in diblock and triblock copolymers. In *Block Copolymers II*, Springer: 2005; pp 1-63.

30. Hoffman, J. D., Anelastic and dielectric effects in polymeric solids. By NG McCrum, BE Read, and G. Williams, Wiley, 1967, pp. 617, $25.00, Lib. Congress Card 67: 29334. *Journal of Polymer Science B Polymer Physics* **1969,** *7*, 750-750.

31. Schönhals, A.; Kremer, F., Analysis of dielectric spectra. In *Broadband dielectric spectroscopy*, Springer: 2003; pp 59-98.

32. Martin, J.; Krutyeva, M.; Monkenbusch, M.; Arbe, A.; Allgaier, J.; Radulescu, A.; Falus, P.; Maiz, J.; Mijangos, C.; Colmenero, J., Direct observation of confined single chain dynamics by neutron scattering. *Physical review letters* **2010,** *104* (19), 197801.

33. Blaszczyk-Lezak, I.; Hernández, M.; Mijangos, C., One dimensional PMMA nanofibers from AAO templates. Evidence of confinement effects by dielectric and Raman analysis. *Macromolecules* **2013,** *46* (12), 4995-5002.

34. Socrates, G., *Infrared and Raman characteristic group frequencies: tables and charts*. John Wiley & Sons: 2004.

35. Tammer, M., G. Sokrates: Infrared and Raman characteristic group frequencies: tables and charts. Springer: 2004.

36. Zhao, J. B.; Li, K. Y.; Yang, W. T., Chain extension of polybutylene adipate and polybutylene succinate with adipoyl-and terephthaloyl-biscaprolactamate. *Journal of applied polymer science* **2007,** *106* (1), 590-598.

37. Abderrahim, B.; Abderrahman, E.; Mohamed, A.; Fatima, T.; Abdesselam, T.; Krim, O., Kinetic thermal degradation of cellulose, polybutylene succinate and a green composite: comparative study. *World Journal of Environmental Engineering* **2015,** *3* (4), 95.

38. Wang, H.; Ji, J.; Zhang, W.; Zhang, Y.; Jiang, J.; Wu, Z.; Pu, S.; Chu, P. K., Biocompatibility and bioactivity of plasma-treated biodegradable poly (butylene succinate). *Acta biomaterialia* **2009,** *5* (1), 279-287.

39. Yan, C.; Zhang, Y.; Hu, Y.; Ozaki, Y.; Shen, D.; Gan, Z.; Yan, S.; Takahashi, I., Melt crystallization and crystal transition of poly (butylene adipate) revealed by infrared spectroscopy. *The Journal of Physical Chemistry B* **2008,** *112* (11), 3311-3314.

40. Debuissy, T.; Pollet, E.; Avérous, L., Synthesis and characterization of biobased poly (butylene succinate-ran-butylene adipate). Analysis of the composition-dependent physicochemical properties. *European Polymer Journal* **2017,** *87*, 84-98.

41. Huang, C. Q.; Luo, S. Y.; Xu, S. Y.; Zhao, J. B.; Jiang, S. L.; Yang, W. T., Catalyzed chain extension of poly (butylene adipate) and poly (butylene succinate) with 2, 2'-(1, 4-phenylene)-bis (2-oxazoline). *Journal of applied polymer science* **2010,** *115* (3), 1555-1565.

42. Partini, M.; Pantani, R., FTIR analysis of hydrolysis in aliphatic polyesters. *Polymer degradation and stability* **2007,** *92* (8), 1491-1497.

43. Li, F.; Zhang, L.; Metzger, R. M., On the growth of highly ordered pores in anodized aluminum oxide. *Chemistry of materials* **1998,** *10* (9), 2470-2480.

44. Sousa, C.; Leitao, D.; Proenca, M.; Ventura, J.; Pereira, A.; Araujo, J., Nanoporous alumina as templates for multifunctional applications. *Applied Physics Reviews* **2014,** *1* (3), 031102.

45. Mi, C.; Zhou, J.; Ren, Z.; Li, H.; Sun, X.; Yan, S., The phase transition behavior of poly (butylene adipate) in the nanoporous anodic alumina oxide. *Polymer Chemistry* **2016,** *7* (2), 410-417.

46. Shimizu, T., *Self-assembled nanomaterials II: nanotubes*. Springer: 2008; Vol. 220.

47. Duran, H.; Steinhart, M.; Butt, H.-J. r.; Floudas, G., From heterogeneous to homogeneous nucleation of isotactic poly (propylene) confined to nanoporous alumina. *Nano letters* **2011,** *11* (4), 1671-1675.

48. Di Lorenzo, M. L.; Androsch, R.; Righetti, M. C., Low-temperature crystallization of poly (butylene succinate). *European Polymer Journal* **2017,** *94*, 384-391.

49. Yoo, E.; Im, S., Melting behavior of poly (butylene succinate) during heating scan by DSC. *Journal of Polymer Science Part B: Polymer Physics* **1999,** *37* (13), 1357-1366.

50. Liu, G.; Zheng, L.; Zhang, X.; Li, C.; Jiang, S.; Wang, D., Reversible lamellar thickening induced by crystal transition in poly (butylene succinate). *Macromolecules* **2012,** *45* (13), 5487-5493.

51. Yang, J.; Pan, P.; Hua, L.; Xie, Y.; Dong, T.; Zhu, B.; Inoue, Y.; Feng, X., Fractionated crystallization, polymorphic crystalline structure, and spherulite morphology of poly (butylene adipate) in its miscible blend with poly (butylene succinate). *Polymer* **2011,** *52* (15), 3460-3468.

52. Wang, M.; Tashiro, K.; Ozaki, Y., Reinvestigation of the β-to-α Crystal Phase Transition of Poly (butylene adipate) by the Time-Resolved X-ray Scattering and FTIR Spectral Measurements in the Temperature-Jump Process. *Macromolecules* **2017,** *50* (10), 3883-3889.

53. Sun, X.; Fang, Q.; Li, H.; Ren, Z.; Yan, S., Effect of anodic alumina oxide pore diameter on the crystallization of poly (butylene adipate). *Langmuir* **2016,** *32* (13), 3269-3275.

54. Minke, R.; Blackwell, J., Single crystals of poly (tetramethylene adipate). *Journal of Macromolecular Science, Part B: Physics* **1980,** *18* (2), 233-255.

55. Minke, R.; Blackwell, J., Polymorphic structures of poly (tetramethylene adipate). *Journal of Macromolecular Science, Part B: Physics* **1979,** *16* (3), 407-417.

56. Pouget, E.; Almontassir, A.; Casas, M. T.; Puiggalí, J., On the crystalline structures of poly (tetramethylene adipate). *Macromolecules* **2003,** *36* (3), 698-705.

57. Polanyi, M., The X-ray fiber diagram. *Z Phys* **1921,** *7*, 149-180.

58. Iwata, T.; Kobayashi, S.; Tabata, K.; Yonezawa, N.; Doi, Y., Crystal Structure, Thermal Behavior and Enzymatic Degradation of Poly (tetramethylene adipate) Solution-Grown Chain-Folded Lamellar Crystals. *Macromolecular bioscience* **2004,** *4* (3), 296-307.

59. Kremer, F.; Schönhals, A., Broadband dielectric spectroscopy. *Springer* **2003**.

60. Arandia, I.; Mugica, A.; Zubitur, M.; Mincheva, R.; Dubois, P.; Müller, A. J.; Alegría, A., The complex amorphous phase in poly (butylene succinate-ran-butylene azelate) isodimorphic copolyesters. *Macromolecules* **2017,** *50* (4), 1569-1578.

61. Charlon, S.; Delbreilh, L.; Dargent, E.; Follain, N.; Soulestin, J.; Marais, S., Influence of crystallinity on the dielectric relaxations of poly (butylene succinate) and poly [(butylene succinate)-co-(butylene adipate)]. *European Polymer Journal* **2016,** *84*, 366-376.

62. Tarnacka, M.; Talik, A.; Kamińska, E.; Geppert-Rybczyńska, M.; Kaminski, K.; Paluch, M., The Impact of Molecular Weight on the Behavior of Poly(propylene glycol) Derivatives Confined within Alumina Templates. *Macromolecules* **2019,** *52* (9), 3516-3529.

63. Li, L.; Zhou, D.; Huang, D.; Xue, G., Double glass transition temperatures of poly (methyl methacrylate) confined in alumina nanotube templates. *Macromolecules* **2013,** *47* (1), 297-303.

64. Li, L.; Chen, J.; Deng, W.; Zhang, C.; Sha, Y.; Cheng, Z.; Xue, G.; Zhou, D., Glass transitions of poly (methyl methacrylate) confined in nanopores: conversion of three-and two-layer models. *The Journal of Physical Chemistry B* **2015,** *119* (15), 5047-5054.

65. Talik, A.; Tarnacka, M.; Grudzka-Flak, I.; Maksym, P.; Geppert-Rybczynska, M.; Wolnica, K.; Kaminska, E.; Kaminski, K.; Paluch, M., The Role of Interfacial Energy and Specific Interactions on the Behavior of Poly (propylene glycol) Derivatives under 2D Confinement. *Macromolecules* **2018,** *51* (13), 4840-4852.

66. Tarnacka, M.; Kaminski, K.; Mapesa, E. U.; Kaminska, E.; Paluch, M., Studies on the Temperature and Time Induced Variation in the Segmental and Chain Dynamics in Poly (propylene glycol) Confined at the Nanoscale. *Macromolecules* **2016,** *49* (17), 6678-6686.

# *Chapter IX:*

# *The Nucleation and Crystallization of PBS-ran-PCL copolyesters Infiltrated within AAO Templates*

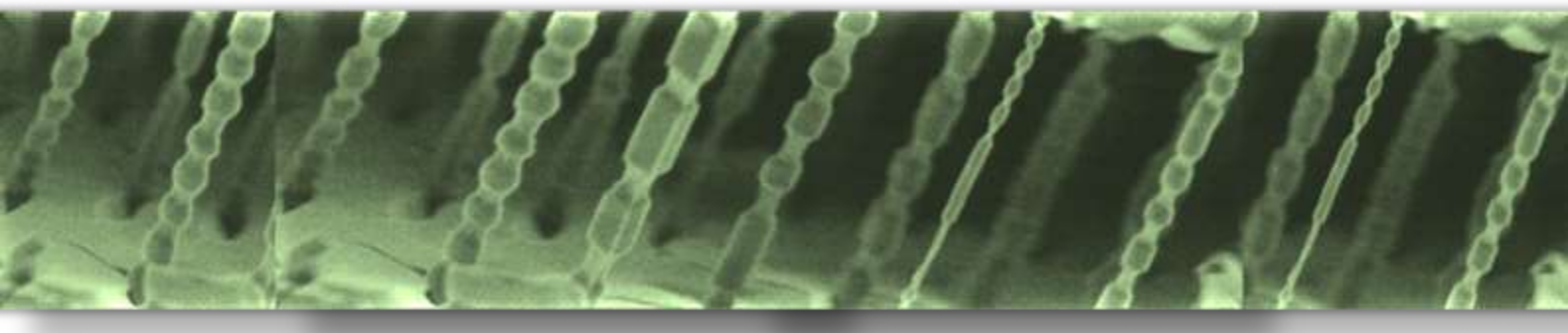

# Table of Contents

## ABSTRACT

Melt nanomolding of a random copolyester employing anodic aluminum oxide (AAO) templates, is reported here for the first time. In this chapter, the study of the structure and crystallization of infiltrated isodimorphic PBS-*ran*-PCL copolyesters within 100 nm diameter AAO template was investigated by scanning electron microscopy (SEM), Raman spectroscopy, differential scanning calorimetry (DSC) and wide-angle X-ray diffraction (GIWAXD).

SEM micrographs and Raman spectra presented a successful infiltrated BS-*ran*-CL copolyester. DSC exposed a pseudo-eutectic behavior for the infiltrated BS-*ran*-CL copolyesters as well as the bulk copolyesters. In addition, DSC revealed that a change in the nucleation process occurred from the heterogeneous or surface nucleation to the homogeneous nucleation. Comparing $T_c$ -$T_g$ values show that when getting closer to the pseudo-eutectic point, a clear change from heterogeneous or surface to homogeneous nucleation after infiltration within 100 nm pore size AAO template. Finally, GIWAXS results indicate that PBS and PBS-rich nanofibers crystallize in the α-phase, as well as their bulk samples and CL-rich compositions crystals initiated by homogeneous nucleation.

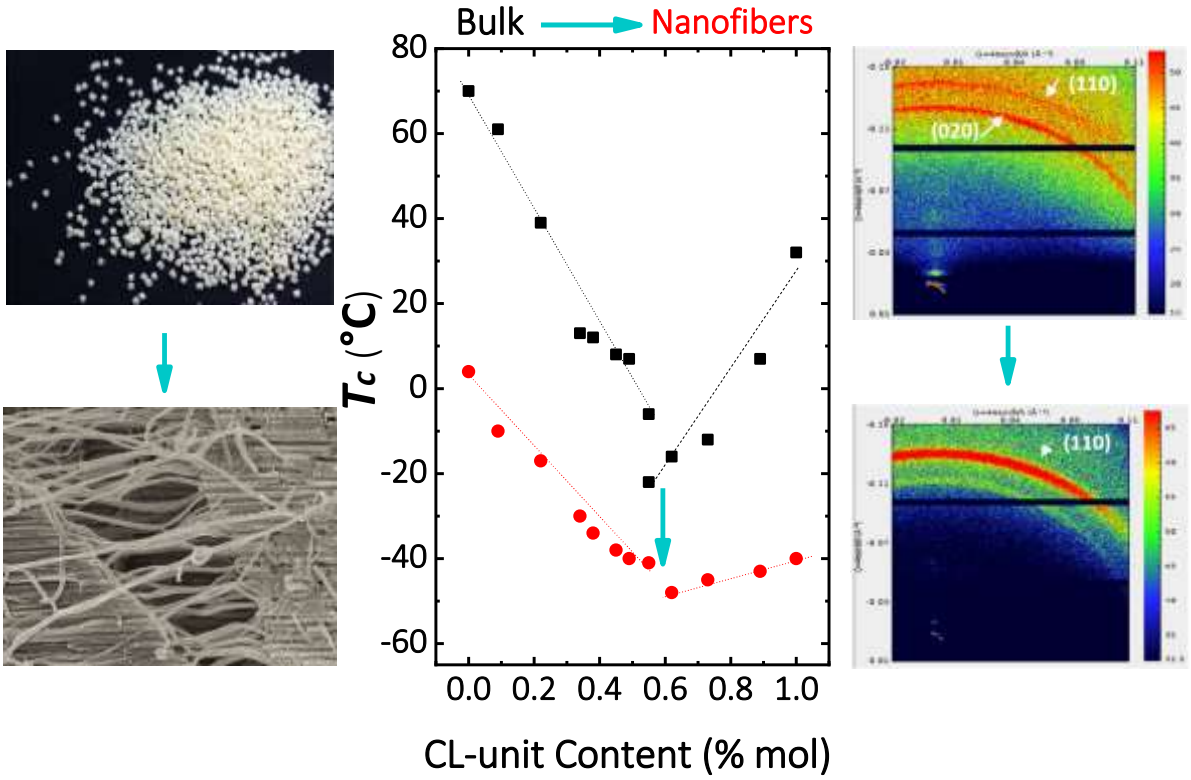
Bulk
Nanofibers
80
60
40
20
0
-20
-40
-60
$T_c$ (°C)
0.0
0.2
0.4
0.6
0.8
1.0
CL-unit Content (% mol)
(110)
(020)
(110)

## 9.1. **INTRODUCTION**

During the past decade, nanotechnology has become an active field of research because of its tremendous potential in all technical disciplines [1-4]. In the large field of nanotechnology, 1D polymers have turned a prominent area of current research and development [5-7]. Several strategies have been developed to prepare 1D nanostructures, and among them, one of the most successful, inexpensive, fast and promising fabrication methods is the confinement of crystallizable polymers into inorganic templates represents. As a result, the investigation of biodegradable polymer confinement has become a research hotspot [8-15].

The interest in employing semicrystalline polymers in nanotechnology applications has been growing in the last decades. With the purpose of obtaining nanostructured semicrystalline polymers, either blends or block copolymers, the strategy used nowadays is the confinement of these materials [8, 16-27]. The main goal of this confinement is to create very small and isolated microdomains of the polymer that is able to crystallize. These microdomains can be created employing inorganic templates, such as porous anodic aluminum oxide (AAO), which has been developed to fabricate novel nanostructured hybrid materials. Scalability, low fabrication cost and easy control over its nano-scale morphology, make AAO patterning methods an intriguing candidate for nanopatterning [5, 28].

On the other hand, Random biodegradable copolymers have been recently studied in the literature not only for their biodegradation but also for their interesting crystallization behaviors [29]. Random copolymers with crystallizable components show multiple crystallization behaviors. In the isodimorphic random copolymers, two crystal structures could be formed depending on the composition. Moreover, the thermal properties show a eutectic region, in which the two comonomers have the same chance to crystallize. It is worth noting that the crystallization in all the composition range, which leads to different properties, allow to conclude that the properties of this kind of copolymers could be tailored just by changing the composition or even the thermal history of some compositions (e.g., changing the thermal history at the

eutectic point) [30-35]. Therefore, a better understanding of the crystallization into confined spaces could be achieved from the study of random isodimorphic copolymers.

In the previous chapters (Chapter 3-7), we have synthesized and studied in details the morphological and thermal characterization of HMw PBS-*ran*-PCL copolyesters in bulk state. We found that this random copolyester plays an isodimorphic behavior; and it means that: (1) has two crystalline structures that resemble that of the rich phase depending on composition; (2) shows a pseudo-eutectic behavior depending on molecular weight and composition; (3) shows changes in the unit cell of the dominant crystalline phases that proof the comonomer inclusion; and finally (4) by changing the composition, molecular weight or even the thermal history of these copolymers, their properties can be tailored [36-37].

In this chapter, we proposed for the first time to study random copolymers with being infiltrated in AAO template with closed pore bottoms (the porous alumina layer was attached to a primary aluminum substrate). Taking into account that the properties of random copolymers either in bulk or into templates are closely associated with their structure, in this research, we applied DSC, SEM, Raman, and GIWAXS techniques in order to study the crystallization of the infiltrated random isodimorphic HMw-BS-*ran*-CL copolymer.

## 9.2. RESULTS

### 9.2.1. SEM Observations

AAO commercial templates were used as closed end-pore templates with 100 nm diameter and 100 µm length size. Figure 9.1 corresponds to SEM images of a cracked AAO template after infiltration of PBS homopolymer (a), $BS_{78}CL_{22}$ copolyester (b) and PCL homopolymer (c). The SEM images clearly demonstrate a nanofiber structures for PBS and PCL homopolymers, and $BS_{78}CL_{22}$ copolyester. The results confirmed the formation of PBS-*ran*-PCL copolymers nanofibers with a diameter about 100 nm. Figure A.9.2 shows that the PBS nanofibers have 100 nm diameter.

We should note that due to the lesser rigidity of nanofibers in the compositions close to the pseudo-eutectic point, it was hard to physically bring out nanofibers outside of AAO template by cracking the template in liquid nitrogen. As an example, Figure 9.2.a and 9.2.b show $BS_{45}CL_{55}$ sample the top and cross-section views that present the fully filled pores with the copolymer in all the nanocavities. In addition, a good copolymer distribution along the pores is noticed from the bottom to the surface (see Figure 9.2.b).

Figure A.9.1 shows another example of infiltrated copolymer close to the pseudo-eutectic point, $BS_{51}CL_{49}$ sample, which successfully infiltrated through the alumina nanotube.

### 9.2.3. Raman

AAO templates filled with PBS and selected PBS-rich phase copolymers bulk and nanofibers were analyzed by Raman spectroscopy to verify that the infiltration of the polymers had been carried out successfully. For the characterization of Raman spectroscopy, first, the different main bands are assigned to each of the bonds that make up the PBS and BS-rich copolymers, respectively. In general, the spectra in bulk present less noise than confined samples and the bands are very well-defined, so these spectra will be used to compare with the spectra of infiltrated copolyester and to verify with their characteristic bands that the copolymer has infiltrated correctly.

Figure 9.3a, 9.3.b and 9.3c show the normalized Raman spectra of infiltrated the selected samples, neat PBS, $BS_{78}CL_{22}$ and $BS_{45}CL_{55}$ compositions inside AAO templates, respectively, at different depths up to 70 µm. As detected, all the bands remain constant along the depth for all copolymers, thus it confirms that PBS homopolymer and both copolymers penetrated homogeneously within the nanocylinders.

Rama spectra of neat infiltrated PBS, $BS_{78}CL_{22}$ $BS_{45}CL_{55}$ samples shows the main specific bond vibration of PBS homopolymer according to the literature as following [38-39] : around 1723 $cm^{-1}$ stretching mode of the C=O bonds; around 1447 $cm^{-1}$, bending in

the plane of the $CH_2$; around 1256 $cm^{-1}$, asymmetric stretching mode of the $CH_2$ groups; and around 1080 $cm^{-1}$, stretching mode of the C-O bonds.

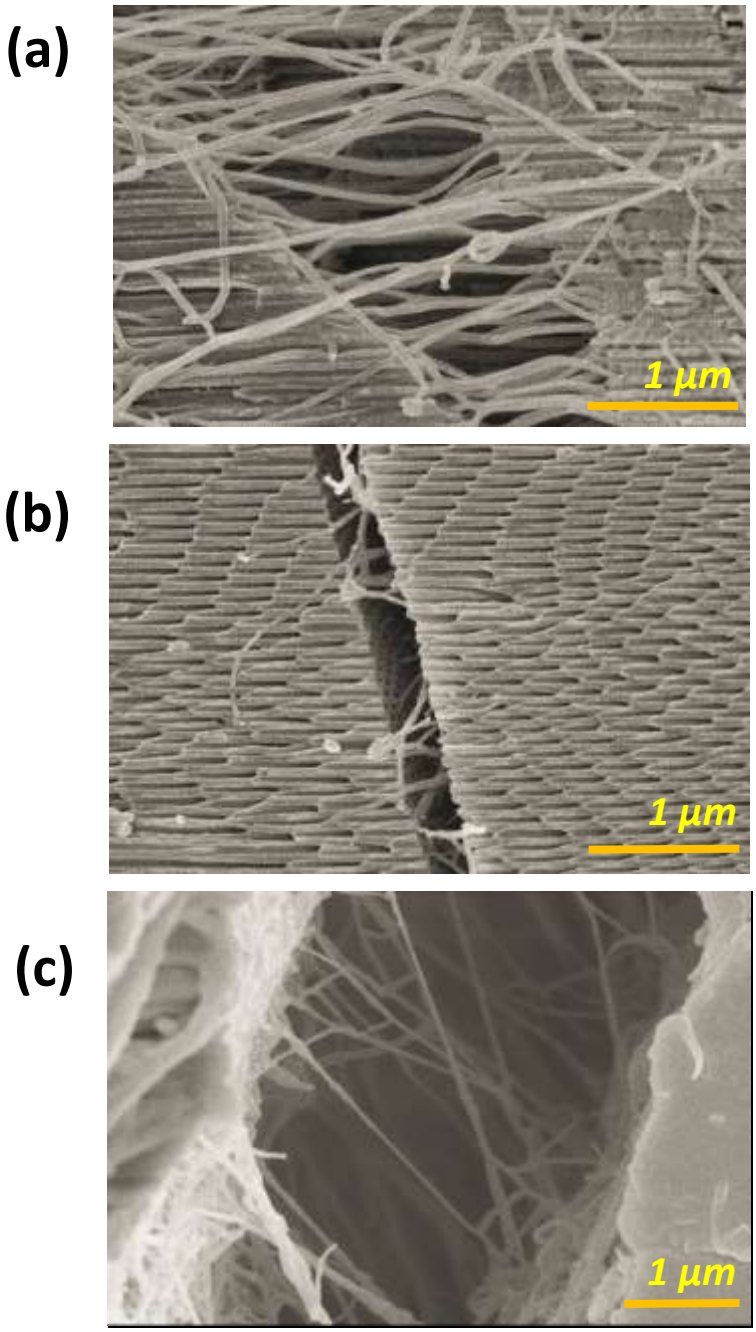


***Figure 9.1.*** *SEM micrograph of the (a) PBS, (b) $BS_{78}CL_{22}$ and (c) PCL nanofibers produced inside the AAO templates after the breaking the template using liquid nitrogen.*

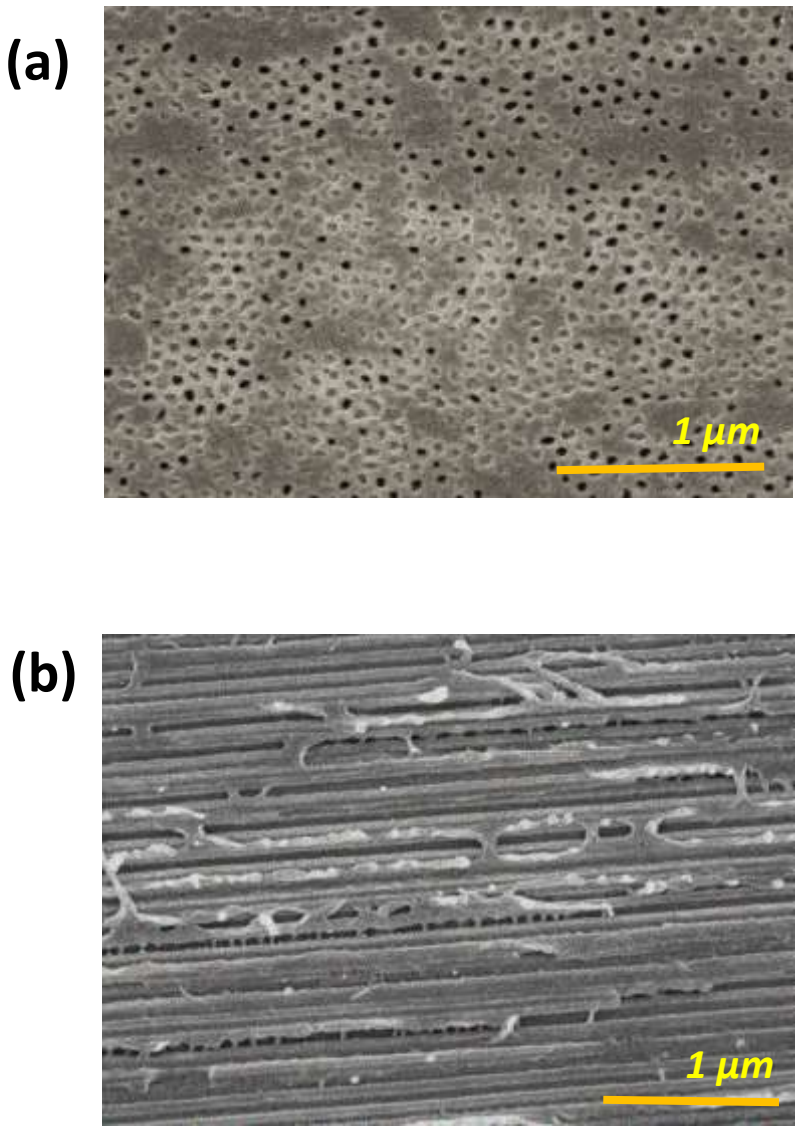


***Figure 9.2.** SEM micrograph of (a) the top view of the infiltrated $BS_{45}CL_{55}$ copolymer inside the AAO template and (b) the cross-section view of the infiltrated $BS_{45}CL_{55}$ inside AAO template.*

Concerning the SEM images of the nanofibers together with the Raman results, we can assume that the polymers were completely infiltrated into the full length of the nanopores up to 100 µm.

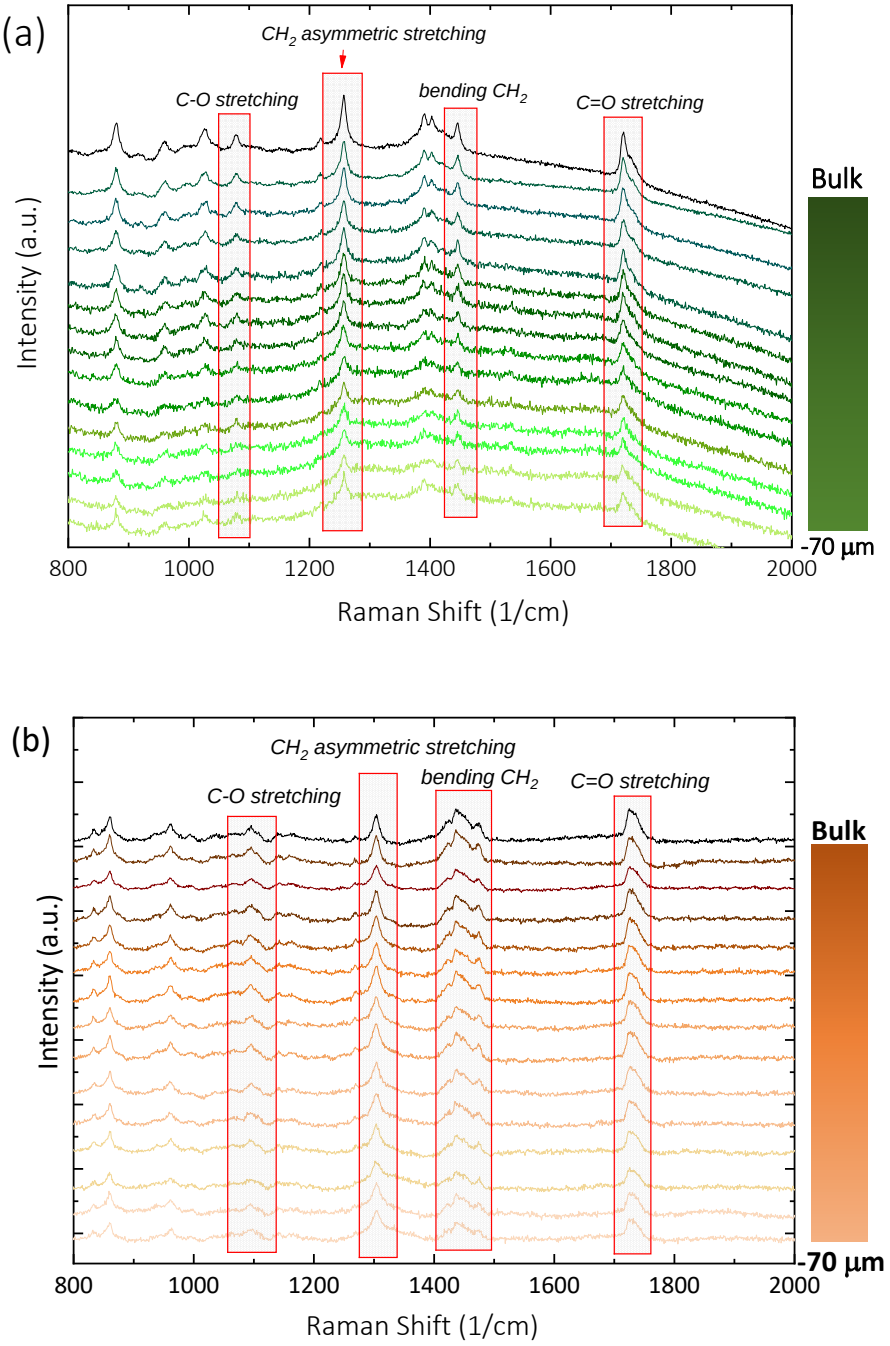


***Figure 9.3.*** *Depth profile Raman spectra of $BS_{78}CL_{22}$ (a) and $BS_{45}CL_{55}$ (b) in bulk, as references, and infiltrated within AAO templates with 100 nm pore size and 100 µm length at room temperature. Inserted numbers show the depth from the AAO surface.*

### 9.2.4. Non-isothermal characterization

DSC scans of BS-rich phase and CL-rich phase bulk and infiltrated inside 100 nm AAO templates are shown in Figure 9.4 and Figure 9.5, respectively. The extracted data from DSC curves are summarized in Table A.9.1.

Figure 9.4 and 9.5 show that during the cooling scan, copolyesters exhibit a crystallization peak depend on composition that it is shifted drastically to the lower temperature when the composition is confined within the alumina nanopores. Furthermore, all infiltrated compositions show only a single crystallization exotherm at temperatures much lower than those in bulky state. The total absence of a crystallization peak at crystallization temperatures similar to those in bulk PBS or PCL homopolymers indicates that the surface of nanopores are clean, and polyesters are also completely isolated and in no way interconnected [16,24].

As it is reported before, it is difficult to distinguish between surface and homogeneous nucleation [23, 40-42]. Nevertheless, if the crystallization temperature is 5-15 °C above the $T_g$ value, the nucleation will be most likely homogeneous [40, 42-43]. On the other hand, if the crystallization occurs at higher supercooling as compared to the bulk polymer, but still at noticeably higher temperatures than $T_g$, then surface nucleation probably controls the nucleation process within the nanopores. The $T_c$–$T_g$ difference value in this work may be relevant to the variations of the nucleation mechanism. Herein, BS-rich and CL-rich compositions exhibit two different nucleation mechanism.

In Figure 9.6a, $T_c$ values of infiltrated and bulk compositions are plotted as a function of CL-unit content. As it can be seen, the infiltrated copolyesters display a pseudo-eutectic behavior as well as the bulk copolyesters. Remarkably, BS-rich and CL-rich compositions indicate different trend by adding the comonomer content to their composition. At the left-hand side of the pseudo-eutectic point, where BS-rich compositions stand, the nucleation mechanism varies from heterogonous or surface for PBS homopolymer to homogenous for $BS_{45}CL_{55}$ composition. In fact, the amount of difference between the crystallization and the glass transition temperatures of BS-rich

compositions shows that by adding CL-comonomer content, the nucleation mechanism turns to the homogenous nucleation progressively. For instance, the $T_c$ value of infiltrated PBS homopolymer is 38 °C above its $T_g$ temperature, however, the $T_c$ value of infiltrated composition with 32% CL content is about 13 °C and for the composition at the pseudo-eutectic point with 55% CL content is only 7 °C above their corresponding $T_g$ temperature.

On the right-hand side of the pseudo-eutectic point, where there are only CL-rich compositions, all infiltrated samples exhibit homogenous nucleation mechanism, nevertheless, with a similar trend to composition for the BS-rich cases, $T_c$ value of infiltrated compositions are getting closer to their corresponding $T_g$ values by reaching to the pseudo-eutectic point.

The subsequent heating scans in Figure 9.6b show that the melting point of confined copolyesters for all compositions are slightly lower as compared to the bulk values ( around 3-7 °C) due to the smaller crystal size caused by the nanopores.

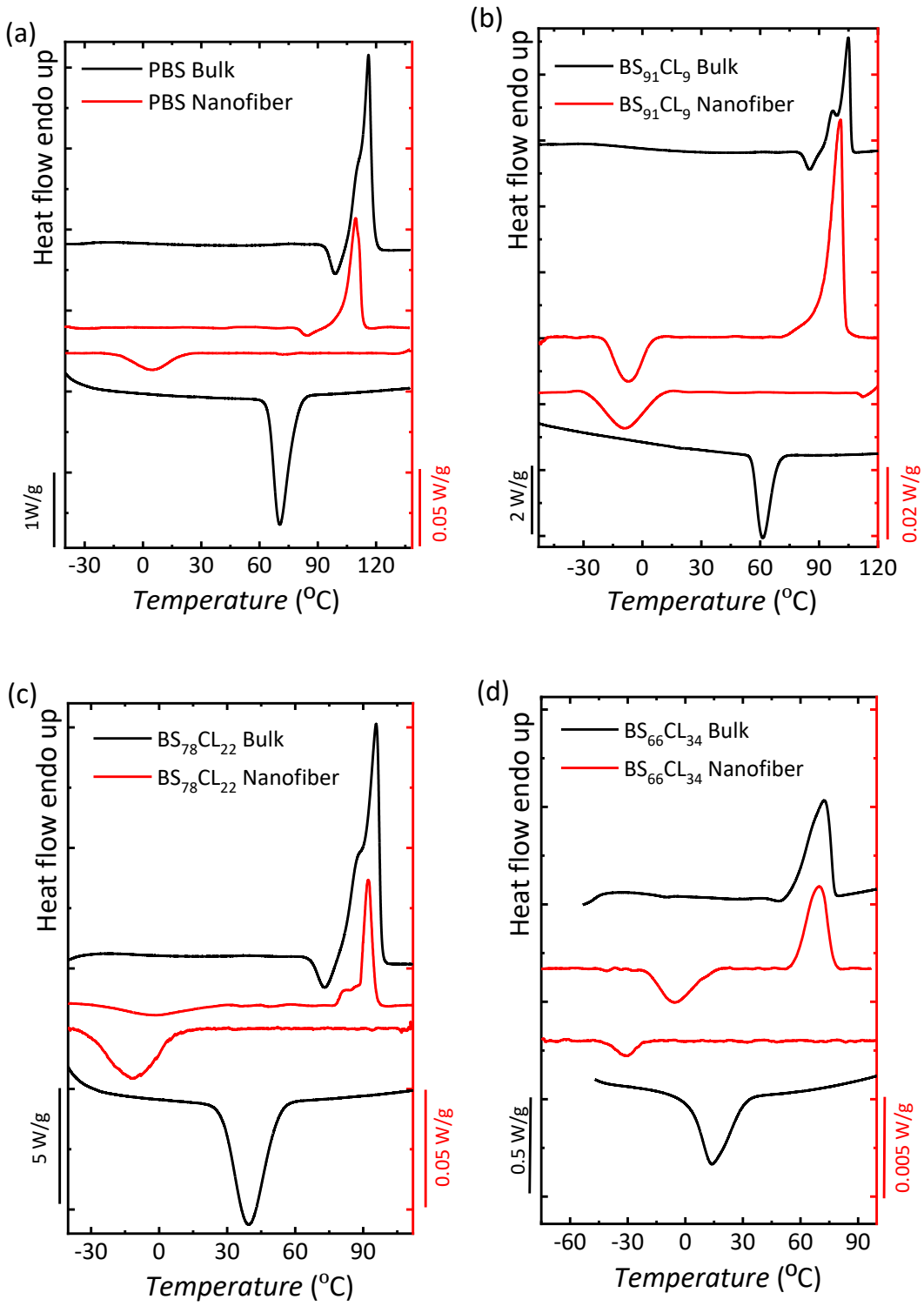
(a)
PBS Bulk
PBS Nanofiber
Heat flow endo up
1W/g
0.05 W/g
-30 0 30 60 90 120
Temperature (°C)
(b)
BS91CL9 Bulk
BS91CL9 Nanofiber
Heat flow endo up
2 W/g
0.02 W/g
-30 0 30 60 90 120
Temperature (°C)
(c)
BS78CL22 Bulk
BS78CL22 Nanofiber
Heat flow endo up
5 W/g
0.05 W/g
-30 0 30 60 90
Temperature (°C)
(d)
BS66CL34 Bulk
BS66CL34 Nanofiber
Heat flow endo up
0.5 W/g
0.005 W/g
-60 -30 0 30 60 90
Temperature (°C)

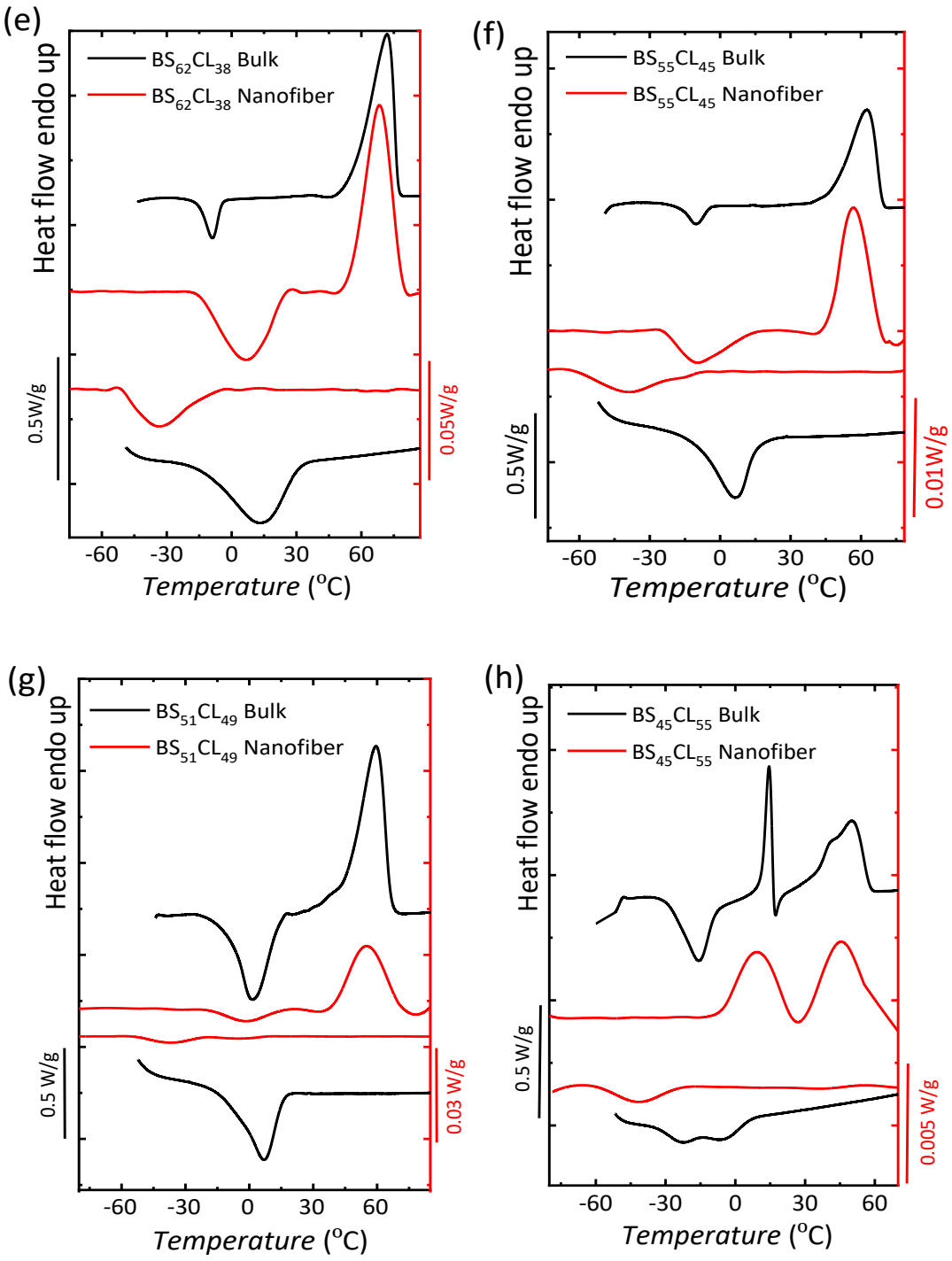


***Figure 9.4.*** *DSC curves for bulk and infiltrated PBS homopolymer and PBS-rich phase copolyesters.*

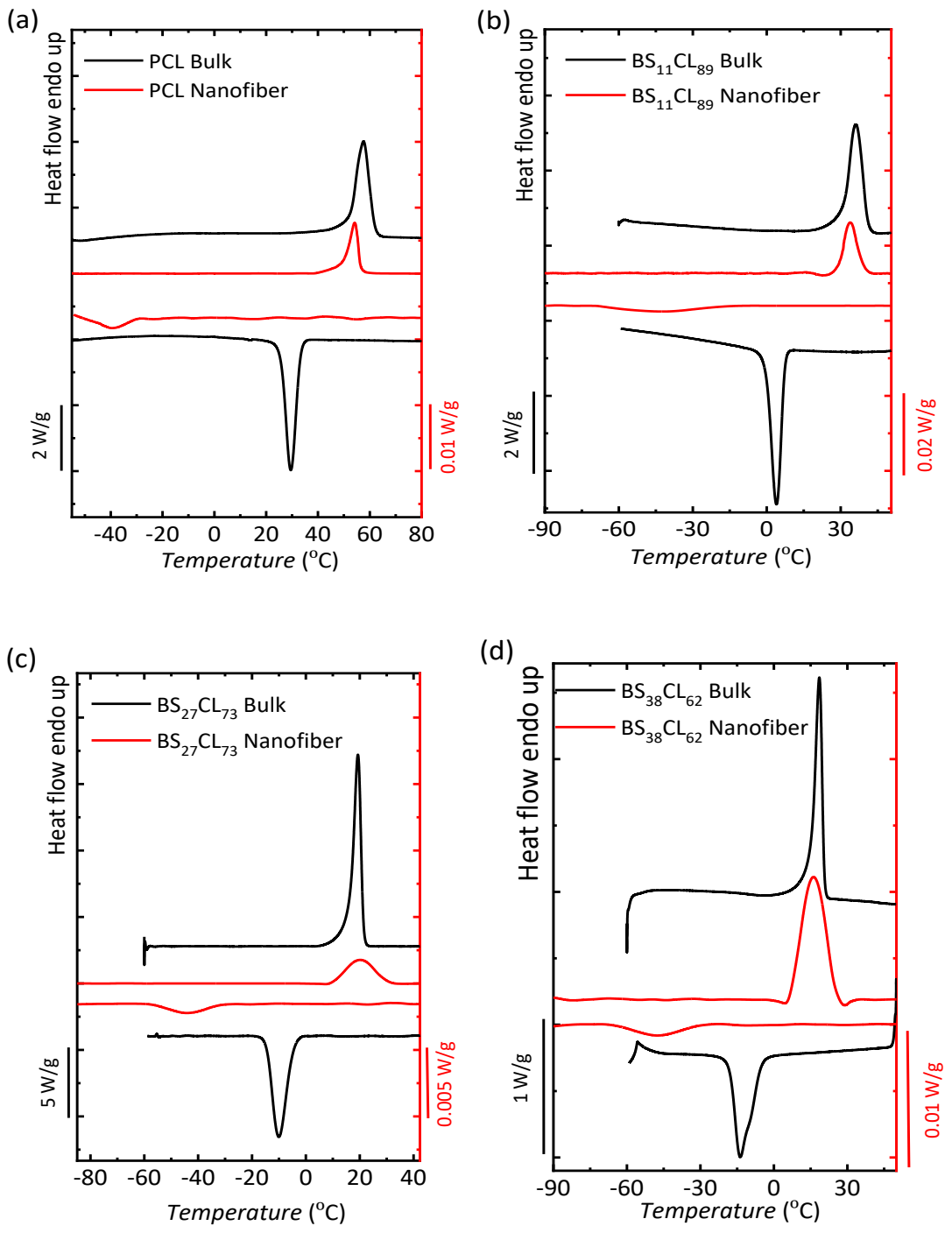


***Figure 9.5.*** *DSC curves for bulk and infiltrated PCL homopolymer and PCL-rich phase copolyesters.*

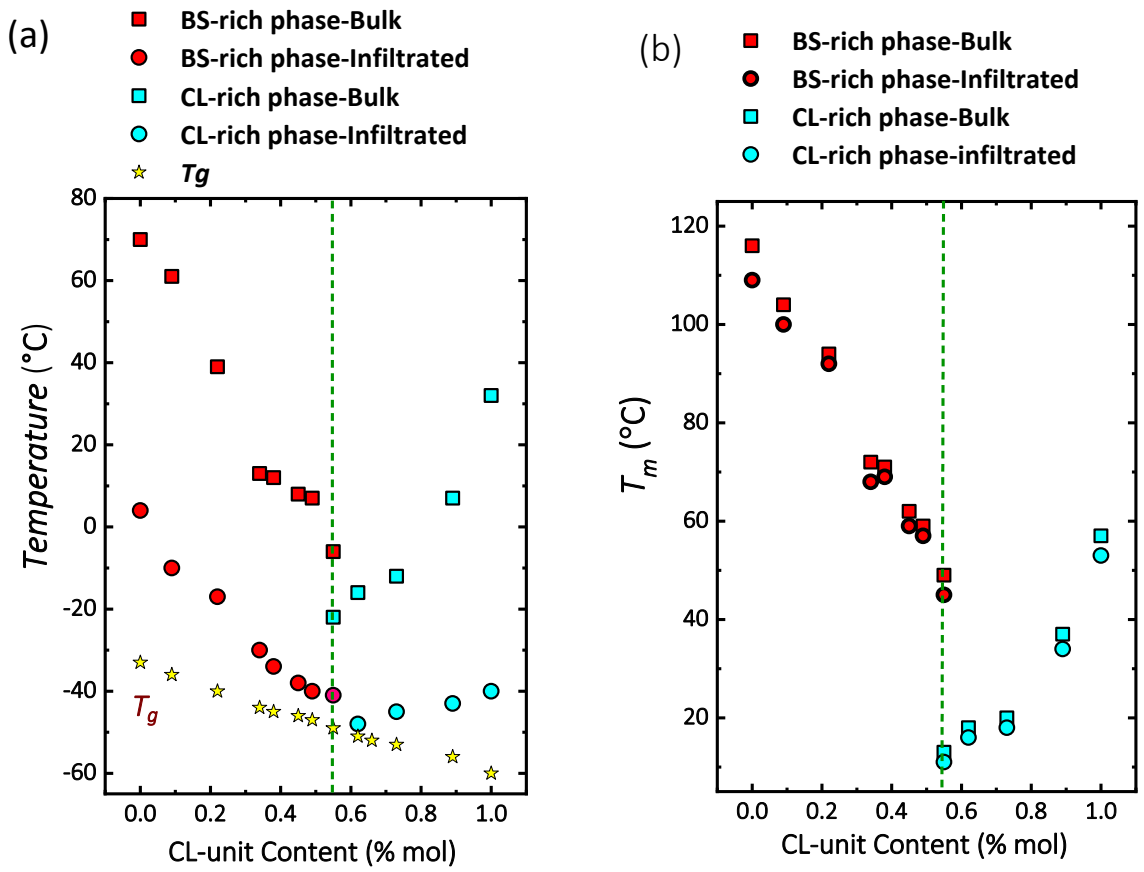


***Figure 9.6.*** *Composition dependence of (a) peak crystallization temperature $T_c$ of bulk (squares), peak crystallization temperature $T_c$ of infiltrated (circles) and glass transition temperature $T_g$ of bulk (stars) samples (b) peak melting temperature $T_m$ of the bulk and infiltrated samples.*

### 9.2.5. Crystalline Structure of PBS-*ran*-PCL within nanopores

To investigate the orientation and crystal texture of the PBS-*ran*-PCL crystals within the AAO nanopores, 2D WAXS experiments with Grazing incident mode were carried out at room temperature. The samples for WAXS measurements were first heated above their corresponding melting temperatures and then cooled slowly to crystallize at a cooling rate of 5 °C/min.

Figure 9.7a-b show GIWAXS patterns for BS-rich phase bulk and infiltrated samples, respectivily. There are three distinct reflections for PBS homopolymer

bulk at $q$ = 13.9, 15.3 and 15.9 $nm^{-1}$. These reflections have $d$-spacing values of 4.52, 3.98 and 3.95 Å, which can be assigned to the following crystal planes: (020), (021), and (110), respectively. For the infiltrated PBS-rich phase with two major peaks at $q$ = 13.8 and 15.9 $nm^{-1}$ were found that can be indexed as the (020) and (110) reflections. The results show that both bulk and infiltrated homopolymer and BS-rich copolymers crystallized into the same α form, see Figure 9.7. The same results were observed in our periviouse work for infiltrated PBS in 70 nm AAO template

Figure 9.9a-d show the GIWAXS patterns of CL-rich phase bulk and infiltrated at room temperature. For PCL homopolymer bulk, main reflections were observed at $q$ = 15.1, 15.6, and 16.7 $nm^{-1}$, which correspond to and the reflections have $d$-spacing values of 4.16, 4.02, and 3.77 Å. The 1D intensity profiles are plotted in Figure 9.10 and the *β* (110), (111), and (200) reflections can be observed, which correspond to the PCL orthorhombic unit cell , respectively, as reported by Chatani *et al*.[44]. We can conclude that the crystal form of PCL does not change upon confinement within 100nm nanopores as previously reported by Shi *et al*. [45]. Among the CL-rich compositions, we could measure GIWAXS of $BS_{11}CL_{89}$ sample due to this composition is the only composition that is not molten at room temperature and shows the similar reflections as PCL homopolymer reflections (see Figure 9.9c-d and 9.10).

The reduced amount of polymer inside the AAO template with a decrease in the degree of crystallinity in all cases, led to a poorer scattered intensity inside AAO than the scattered intensity in bulk.

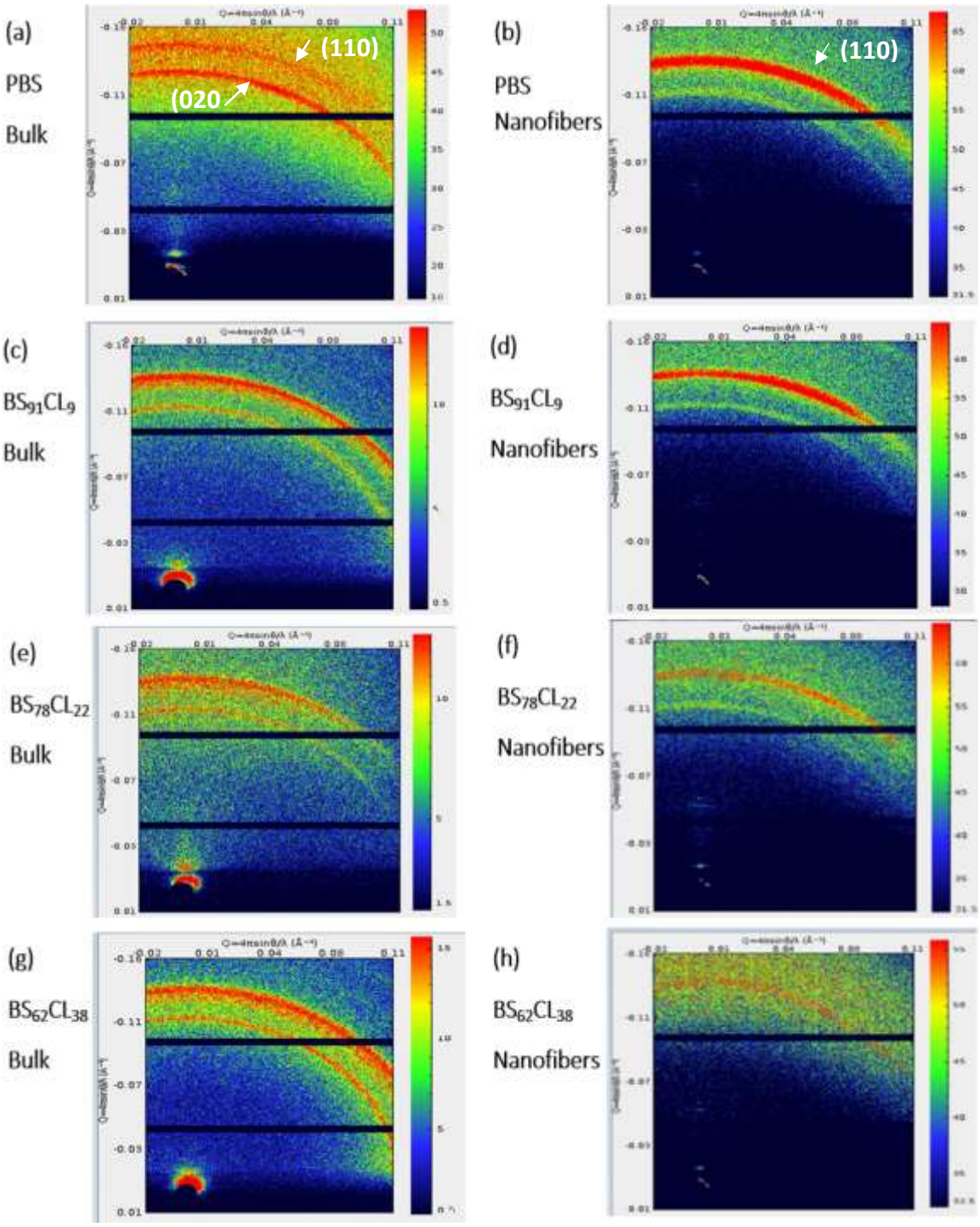


***Figure 9.7.*** *2D WAXS patterns of (a) PBS bulk, (b) PBS infiltrated, (c) $BS_{91}CL_9$ bulk, (d) $BS_{91}CL_9$ infiltrated, (e) $BS_{78}CL_{22}$ Bulk and (f) $BS_{78}CL_{22}$ infiltrated within AAO template with pore depth of 100 µm and pore diameter of 100 nm. X-ray incident angle with respect to the template is 3°.*

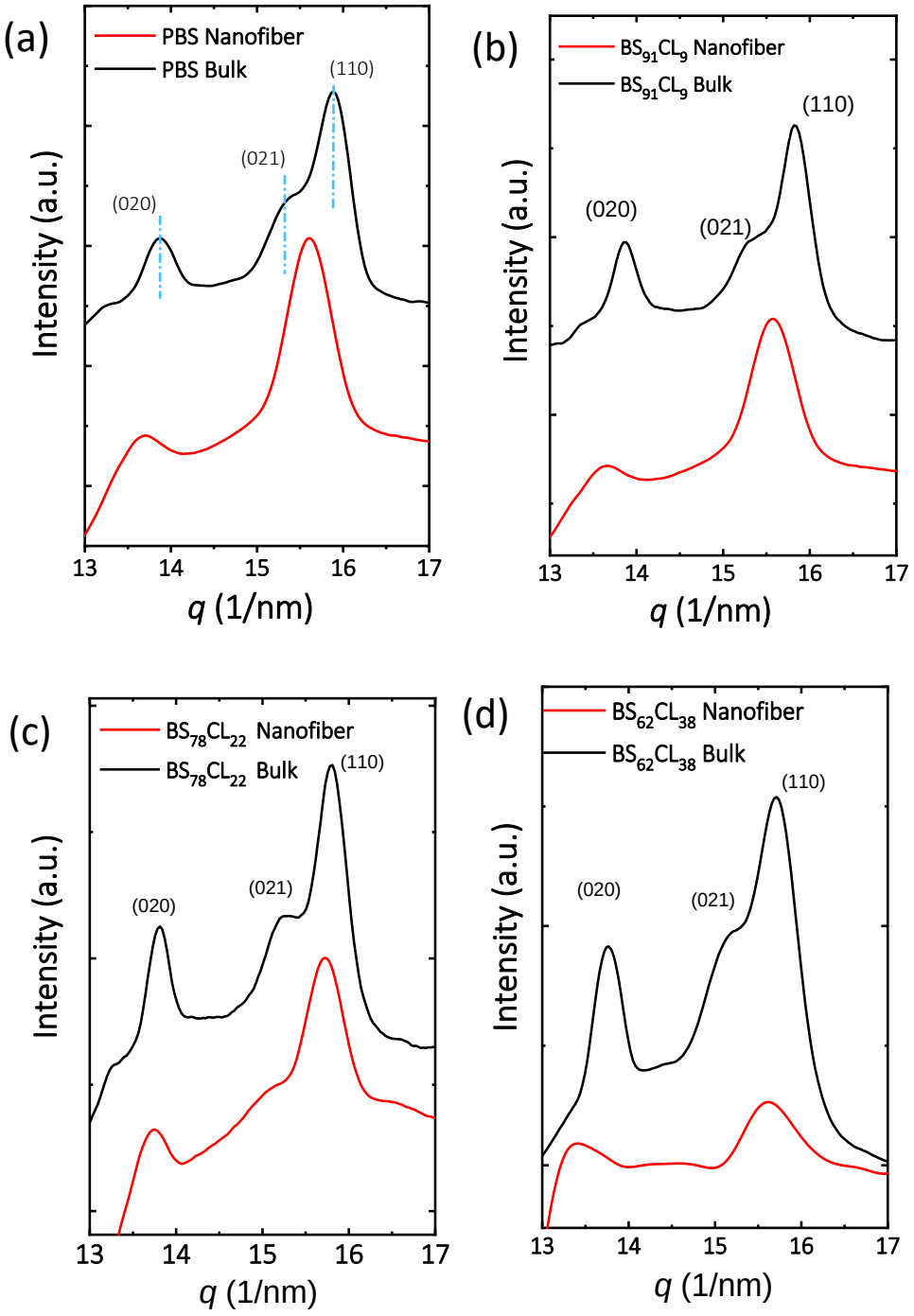


***Figure 9.8.*** *Corresponding 1D intensity profile of PBS (a), $BS_{91}CL_9$ (b) $BS_{78}CL_{22}$ (c) $BS_{66}CL_{34}$ (d) samples, obtained by averaging the intensity along the azimuthal angle.*

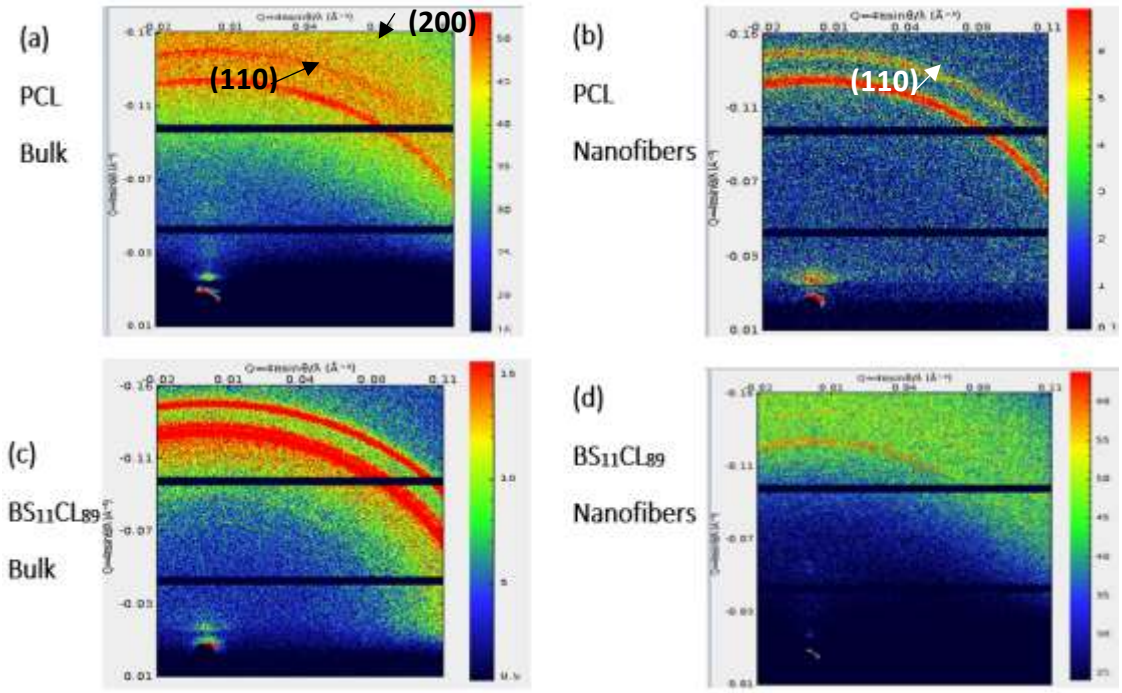


***Figure 9.9.*** *2D WAXS patterns of (a) PCL bulk (b) PCL infiltrated (c) $BS_{11}CL_{89}$ bulk, and (d) $BS_{11}CL_{89}$ infiltrated within AAO template with pore depth of 100 µm and pore diameter of 100 nm. X-ray incident angle with respect to the template is 3°.*

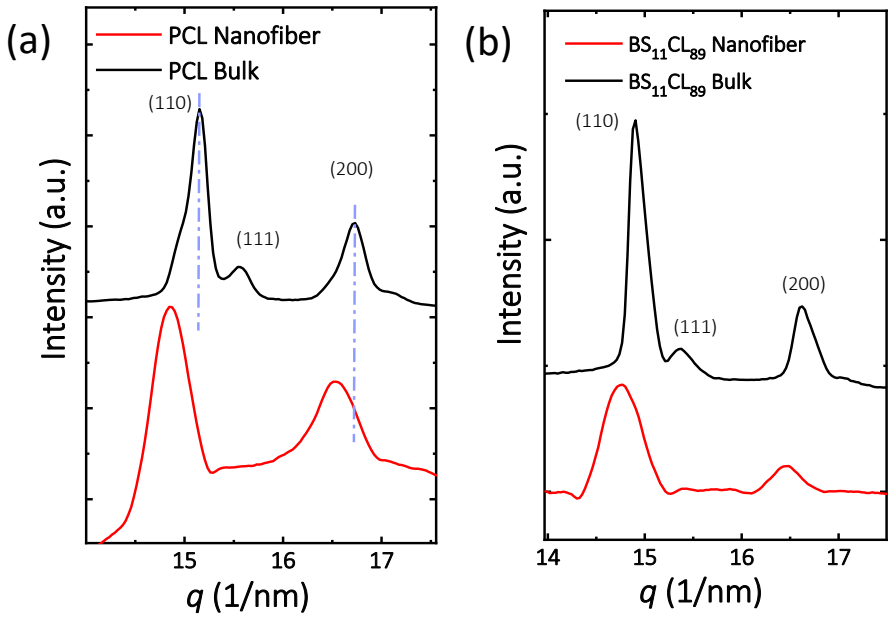


***Figure 9.10.*** *Corresponding 1D intensity profile of PCL (a) and $BS_{11}CL_{89}$ (b) samples, obtained by averaging the intensity along the azimuthal angle.*

## 9.3. CONCLUSION

The results shown in this study demonstrate that nanofibers successfully made from PBS-*ran*-PCL random copolyesters in all composition range. The crystallization temperature decreases significantly within AAO template and a pseudo-eutectic behavior for the infiltrated copolyesters as well as the bulk copolyesters. For the BS-rich compositions, the nucleation mechanism strongly is depended on composition and a change from heterogeneous or surface nucleation, for the PBS, to homogeneous nucleation (for compositions near to the eutectic point) within the nanopores was confirmed. On the contrary, for the PCL and CL-rich compositions that were infiltrated in the AAO templates, a homogenous nucleation mechanism is more reliable for all infiltrated CL-rich compositions with the results obtained.

## 9.4. REFERENCES

1. Timp, G., Nanotechnology Springer. *New York* **1999**.

2. Andrews, D.; Nann, T.; Lipson, R. H., *Comprehensive Nanoscience and Nanotechnology*. Academic Press: 2019.

3. Zhang, L.; Webster, T. J., Nanotechnology and nanomaterials: promises for improved tissue regeneration. *Nano today* **2009,** *4* (1), 66-80.

4. Wilson, M.; Kannangara, K.; Smith, G.; Simmons, M.; Raguse, B., *Nanotechnology: basic science and emerging technologies*. Chapman and Hall/CRC: 2002.

5. Martin, J.; Maiz, J.; Sacristan, J.; Mijangos, C., Tailored polymer-based nanorods and nanotubes by" template synthesis": From preparation to applications. *Polymer* **2012,** *53* (6), 1149-1166.

6. Müller, A. J.; Hu, W., Introduction to the "The effects of confinement on polymeric thermal transitions and nanostructuring" Special Volume. *Progress in Polymer Science* **2016,** *100* (54-55), 1-2.

7. O'Brien, G. A.; Quinn, A. J.; Tanner, D. A.; Redmond, G., A single polymer nanowire photodetector. *Advanced Materials* **2006,** *18* (18), 2379-2383.

8. Hernández, J. J.; Puente-Orench, I.; Ezquerra, T. A.; Gutiérrez-Fernández, E.; García-Gutiérrez, M.-C., Confinement effects in one-dimensional nanoarrays of polymer semiconductors and their photovoltaic blends. *Polymer* **2019,** *163*, 13-19.

9. Adrjanowicz, K.; Winkler, R.; Dzienia, A.; Paluch, M.; Napolitano, S., Connecting 1D and 2D Confined Polymer Dynamics to Its Bulk Behavior via Density Scaling. *ACS macro letters* **2019,** *8* (3), 304-309.

10. Sayin, S.; Ozdemir, E.; Acar, E.; Ince, G. O., Multifunctional one-dimensional polymeric nanostructures for drug delivery and biosensor applications. *Nanotechnology* **2019,** *30* (41), 412001.

11. Xu, Q.; Meng, G.; Han, F., Porous AAO template-assisted rational synthesis of large-scale 1D hybrid and hierarchically branched nanoarchitectures. *Progress in Materials Science* **2018,** *95*, 243-285.

12. Martin, J.; Krutyeva, M.; Monkenbusch, M.; Arbe, A.; Allgaier, J.; Radulescu, A.; Falus, P.; Maiz, J.; Mijangos, C.; Colmenero, J., Direct observation of confined single chain dynamics by neutron scattering. *Physical review letters* **2010,** *104* (19), 197801.

13. Zhang, X.; Liu, H.; Jiang, L., Wettability and applications of nanochannels. *Advanced Materials* **2019,** *31* (5), 1804508.

14. Rath, A.; Theato, P., Advanced AAO Templating of Nanostructured Stimuli-Responsive Polymers: Hype or Hope? *Advanced Functional Materials* **2019**.

15. Tao, S. L.; Desai, T. A., Aligned arrays of biodegradable poly (ϵ-caprolactone) nanowires and nanofibers by template synthesis. *Nano letters* **2007,** *7* (6), 1463-1468.

16. Müller, A. J.; Arnal, M. L.; Trujillo, M.; Lorenzo, A. T., Super-nucleation in nanocomposites and confinement effects on the crystallizable components within block copolymers, miktoarm star copolymers and nanocomposites. *European Polymer Journal* **2011,** *47* (4), 614-629.

17. Frensch, H.; Harnischfeger, P.; Jungnickel, B., Fractionated crystallization in incompatible polymer blends. *Multiphase polymers: blends and ionomers* **1989,** *395*, 101.

18. Hamley, I., Crystallization in block copolymers. In *Interfaces Crystallization Viscoelasticity*, Springer: 1999; pp 113-137.

19. Hamley, I. W., *Developments in block copolymer science and technology*. John Wiley & Sons: 2004.

20. Loo, Y. L.; Register, R. A., Crystallization within block copolymer mesophases. *Developments in block copolymer science and technology* **2004,** *213*.

21. Müller, A. J.; Arnal, M. L.; Balsamo, V., Crystallization in block copolymers with more than one crystallizable block. In *Progress in understanding of polymer crystallization*, Springer: 2007; pp 229-259.

22. Müller, A. J.; Arnal, M. L.; Lorenzo, A. T., Crystallization in nano-confined polymeric systems. *Handbook of polymer crystallization* **2013,** *1*.

23. Michell, R. M.; Blaszczyk-Lezak, I.; Mijangos, C.; Mueller, A. J., Confinement effects on polymer crystallization: From droplets to alumina nanopores. *Polymer* **2013,** *54* (16), 4059-4077.

24. Michell, R. M.; Lorenzo, A. T.; Müller, A. J.; Lin, M.-C.; Chen, H.-L.; Blaszczyk-Lezak, I.; Martin, J.; Mijangos, C., The crystallization of confined polymers and block copolymers infiltrated within alumina nanotube templates. *Macromolecules* **2012,** *45* (3), 1517-1528.

25. Casas, M. T.; Michell, R. M.; Blaszczyk-Lezak, I.; Puiggali, J.; Mijangos, C.; Lorenzo, A. T.; Mueller, A. J., Self-assembly of semicrystalline PE-b-PS diblock copolymers within AAO nanoporous templates. *Polymer* **2015,** *70*, 282-289.

26. Chen, D.; Chen, J. T.; Glogowski, E.; Emrick, T.; Russell, T. P., Thin film instabilities in blends under cylindrical confinement. *Macromolecular rapid communications* **2009,** *30* (4-5), 377-383.

27. Xu, J.; Wang, K.; Liang, R.; Yang, Y.; Zhou, H.; Xie, X.; Zhu, J., Structural transformation of diblock copolymer/homopolymer assemblies by tuning cylindrical confinement and interfacial interactions. *Langmuir* **2015,** *31* (45), 12354-12361.

28. Sanz, B.; Ballard, N.; Marcos-Fernandez, A.; Asua, J. M.; Mijangos, C., Confinement effects in the step-growth polymerization within AAO templates and modeling. *Polymer* **2018,** *140*, 131-139.

29. Li, L.; Raghupathi, K.; Song, C.; Prasad, P.; Thayumanavan, S., Self-assembly of random copolymers. *Chemical Communications* **2014,** *50* (88), 13417-13432.

30. Papageorgiou, G. Z.; Bikiaris, D. N., Synthesis and Properties of Novel Biodegradable/Biocompatible Poly [propylene-co-(ethylene succinate)] Random Copolyesters. *Macromolecular Chemistry and Physics* **2009,** *210* (17), 1408-1421.

31. Pérez-Camargo, R. A.; Fernández-d'Arlas, B.; Cavallo, D.; Debuissy, T.; Pollet, E.; Avérous, L.; Müller, A. J., Tailoring the structure, morphology, and crystallization of isodimorphic poly (butylene succinate-ran-butylene adipate) random copolymers by changing composition and thermal history. *Macromolecules* **2017,** *50* (2), 597-608.

32. Yu, Y.; Sang, L.; Wei, Z.; Leng, X.; Li, Y., Unique isodimorphism and isomorphism behaviors of even-odd poly (hexamethylene dicarboxylate) aliphatic copolyesters. *Polymer* **2017,** *115*, 106-117.

33. Arandia, I.; Mugica, A.; Zubitur, M.; Arbe, A.; Liu, G.; Wang, D.; Mincheva, R.; Dubois, P.; Müller, A. J., How composition determines the properties of isodimorphic poly (butylene succinate-ran-butylene azelate) random biobased copolymers: from single to double crystalline random copolymers. *Macromolecules* **2014,** *48* (1), 43-57.

34. Yu, Y.; Wei, Z.; Liu, Y.; Hua, Z.; Leng, X.; Li, Y., Effect of chain length of comonomeric diols on competition and miscibility of isodimorphism: A comparative study of poly (butylene glutarate-co-butylene azelate) and poly (octylene glutarate-co-octylene azelate). *European Polymer Journal* **2018,** *105*, 274-285.

35. Jeong, Y. G.; Jo, W. H.; Lee, S. C., Cocrystallization behavior of poly (butylene terephthalate-co-butylene 2, 6-naphthalate) random copolymers. *Macromolecules* **2000,** *33* (26), 9705-9711.

36. Pérez-Camargo, R. A.; Arandia, I.; Safari, M.; Cavallo, D.; Lotti, N.; Soccio, M.; Müller, A. J., Crystallization of isodimorphic aliphatic random copolyesters: Pseudo-eutectic behavior and double-crystalline materials. *European Polymer Journal* **2018,** *101*, 233-247.

37. Safari, M.; Martínez de Ilarduya, A.; Mugica, A.; Zubitur, M.; Muñoz-Guerra, S. n.; Müller, A. J., Tuning the Thermal Properties and Morphology of Isodimorphic Poly [(butylene succinate)-ran-(ε-caprolactone)] Copolyesters by Changing Composition, Molecular Weight, and Thermal History. *Macromolecules* **2018,** *51* (23), 9589-9601.

38. Socrates, G., *Infrared and Raman characteristic group frequencies: tables and charts*. John Wiley & Sons: 2004.

39. Tammer, M., G. Sokrates: Infrared and Raman characteristic group frequencies: tables and charts. Springer: 2004.

40. Michell, R. M.; Mueller, A. J., Confined crystallization of polymeric materials. *Progress in Polymer Science* **2016,** *54*, 183-213.

41. Michell, R. M.; Blaszczyk-Lezak, I.; Mijangos, C.; Müller, A. J., Confined crystallization of polymers within anodic aluminum oxide templates. *Journal of Polymer Science Part B: Polymer Physics* **2014,** *52* (18), 1179-1194.

42. Di Lorenzo, M. L.; Androsch, R.; Righetti, M. C., Low-temperature crystallization of poly (butylene succinate). *European Polymer Journal* **2017,** *94*, 384-391.

43. Müller, A. J.; Balsamo, V.; Arnal, M. L., Nucleation and crystallization in diblock and triblock copolymers. In *Block Copolymers II*, Springer: 2005; pp 1-63.

44. Chatani, Y.; Okita, Y.; Tadokoro, H.; Yamashita, Y., Structural studies of polyesters. III. Crystal structure of poly-ε-caprolactone. *Polymer Journal* **1970,** *1* (5), 555.

45. Shi, G.; Liu, G.; Su, C.; Chen, H.; Chen, Y.; Su, Y.; Muller, A. J.; Wang, D., Reexamining the crystallization of poly (ε-caprolactone) and isotactic polypropylene under hard confinement: nucleation and orientation. *Macromolecules* **2017,** *50* (22), 9015-9023.

# *Chapter X*

# *Appendix*

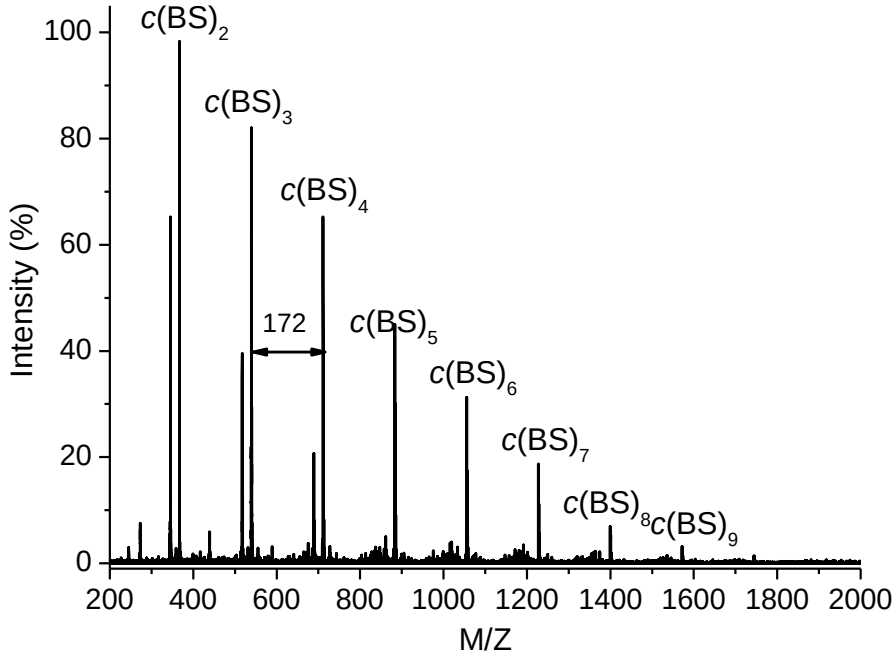


***Figure A.4.1****. MALDI-Toff MS spectrum of the crude oligomeric c(BS)$_n$ mixture. The MALDI-Tof MS spectrum of the crude c(BS)n mixture revealed that it was composed of species with sizes going from dimer to nonamer whereas those containing ten or more units are practically negligible.*

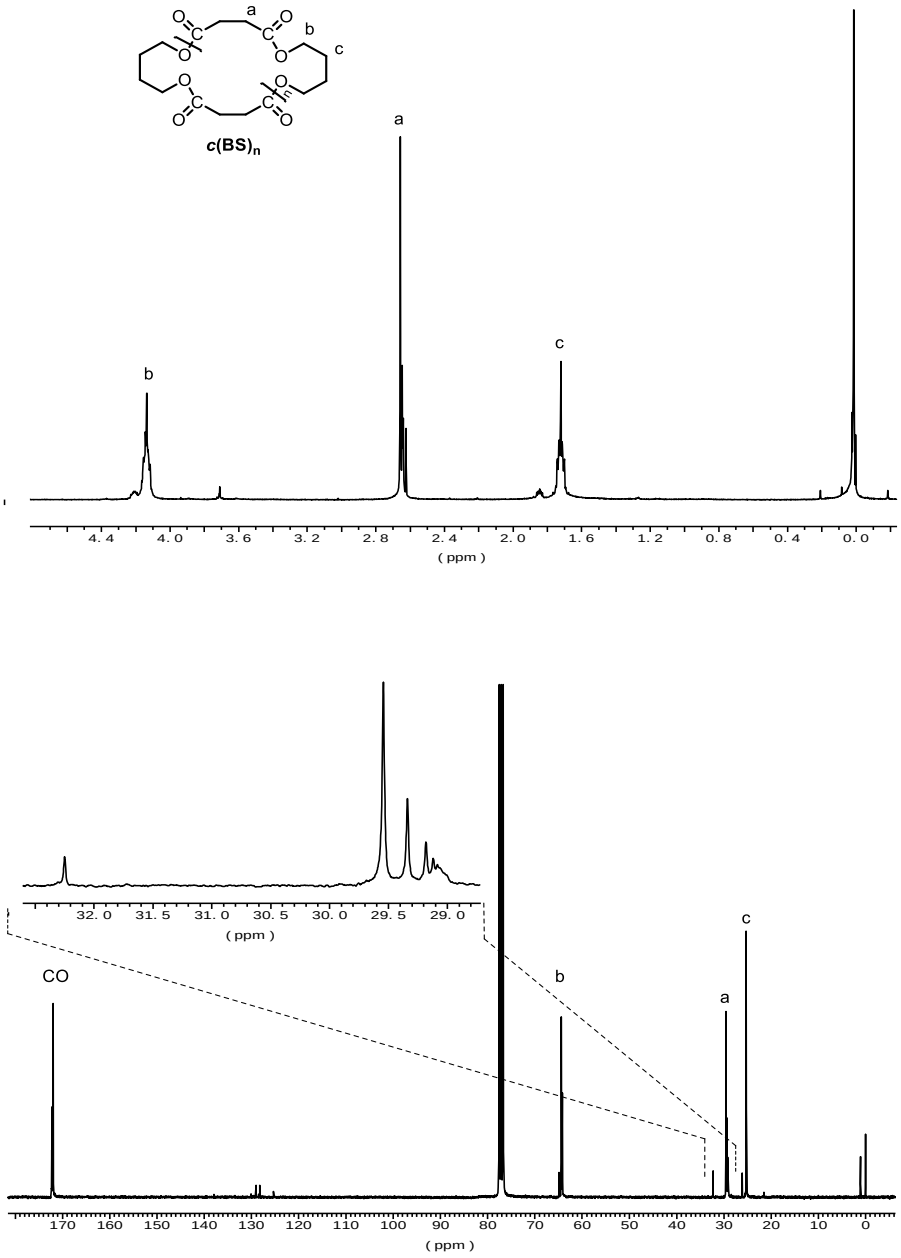


***Figure A.4.2****. [1]H (top) and [13]C (bottom) NMR spectra of the oligomeric c(BS)n mixture recorded in* $CDCl_3$*. Both [1]H and [13]C NMR spectra of the oligomer mixture strongly supported the results afforded by MALDI-Tof. The three conspicuous signals observed in the [1]H NMR spectrum were attributable to the three different protons present in the butylene succinate unit whereas that arising from the terminal methyl ester proton at δ 3.7 ppm appeared with insignificant intensity ( δ 1.66 - 1.76 (m, 4H,* $–CH_2CH_2CH_2CH_2–$*), δ 2.60 - 2.69 (m, 4H,* $–(C=O)(CH_2)_2(C=O)–$*), δ 4.05 - 4.20 (m, 4H,* $–OCH_2(CH_2)_2CH_2O–$*).*

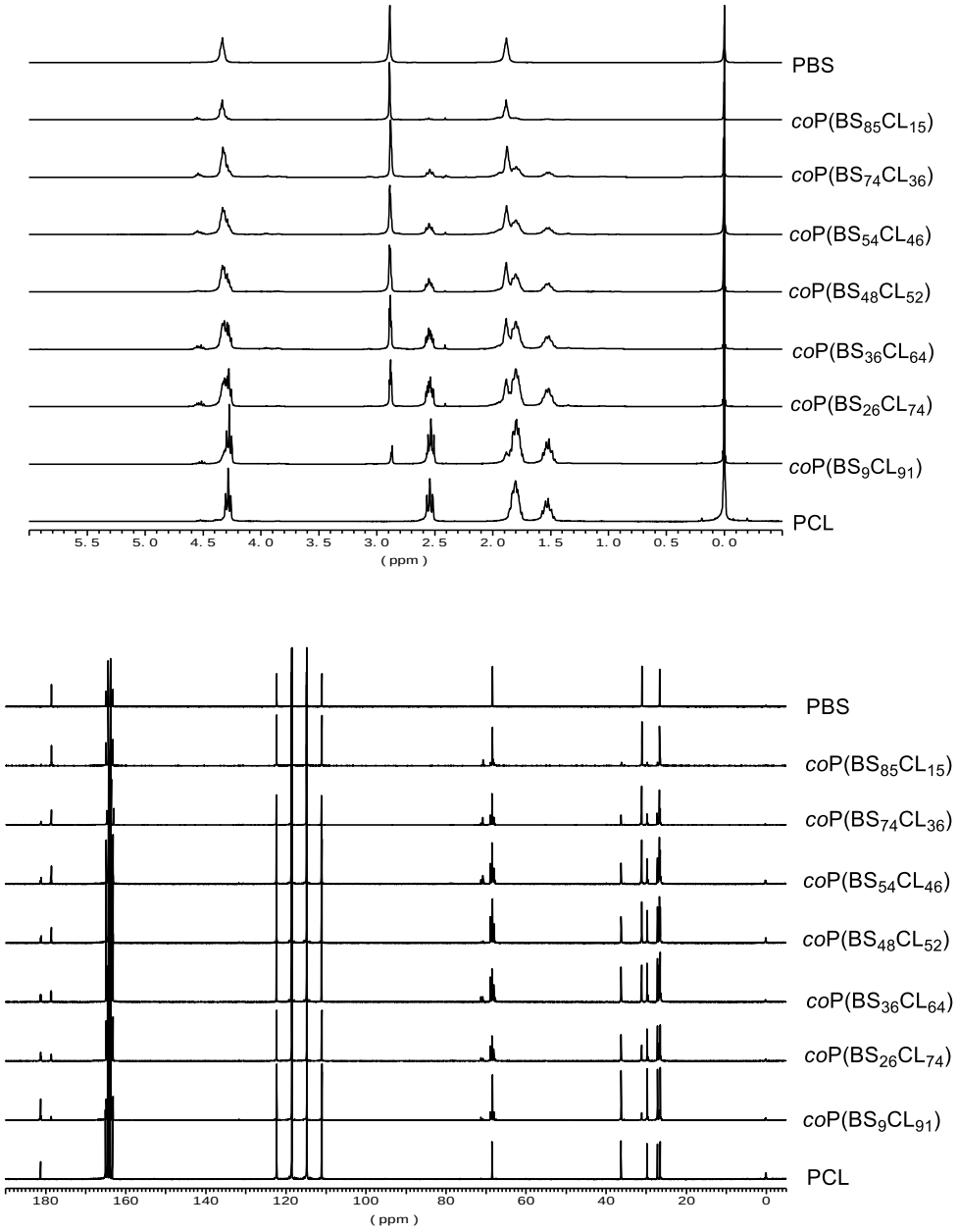


***Figure A.4.3.*** *$^{1}H$ (top) and $^{13}C$ (bottom) NMR spectra of the coP($BS_xCL_y$) series including the homopolyesters PBS and PCL as references. Spectra recorded in TFA-d.*

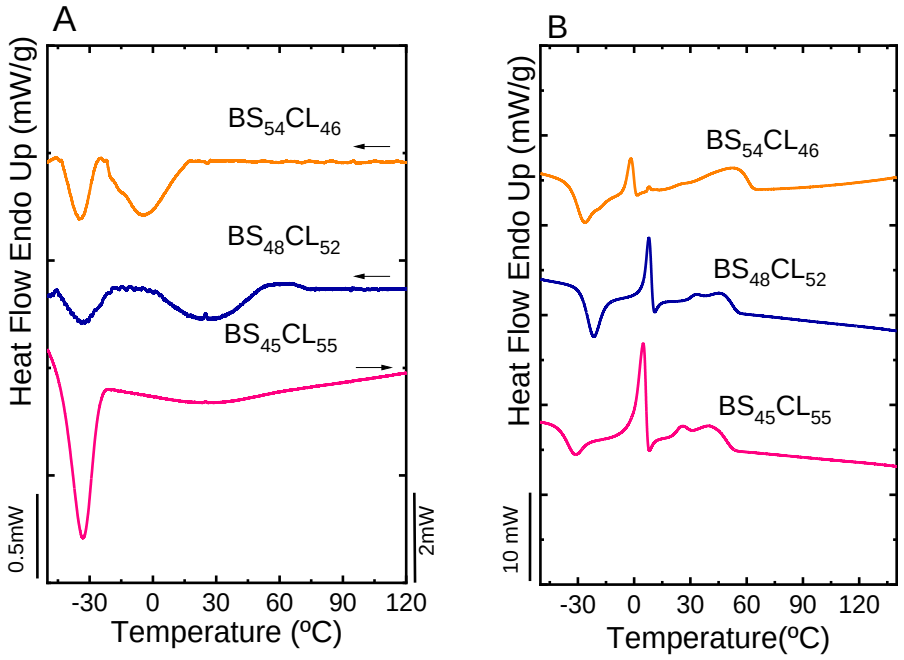


***Figure Apnx.4.4.*** *(A) Cooling DSC scans from the melt and (B) subsequent heating scans for those samples that indicate both homopolymers phases.*

**Table A.4.1:** Observed diffraction Bragg spacing (*d*) using extracted data from WAXS.

| Copolyester | -60 °C | | | 25 °C | | |
|---|---|---|---|---|---|---|
| | *2ϑ(deg)* | *Crystalline Plane (hkl)* | *d(nm)* | *2ϑ(deg)* | *Crystalline Plane (hkl)* | *d(nm)* |
| PBS | 19.61 | (020) | 0.452 | 19.55 | (020) | 0.453 |
| | 21.96 | (021) | 0.404 | 21.91 | (021) | 0.405 |
| | 22.75 | (110) | 0.390 | 22.63 | (110) | 0.392 |
| $BS_{85}CL_{15}$ | 19.58 | (020) | 0.453 | 19.51 | (020) | 0.454 |
| | 21.84 | (021) | 0.406 | 21.81 | (021) | 0.407 |
| | 22.80 | (110) | 0.389 | 22.63 | (110) | 0.392 |
| $BS_{64}CL_{36}$ | 19.50 | (020) | 0.455 | 19.47 | (020) | 0.455 |
| | 21.66 | (021) | 0.410 | 21.65 | (021) | 0.410 |
| | 22.81 | (110) | 0.390 | 22.59 | (110) | 0.393 |
| $BS_{54}CL_{46}$ | 19.47 | (020) | 0.456 | 19.44 | (020) | 0.456 |
| | 21.39 | (110) | 0.415 | 21.61 | (021) | 0.411 |
| | 22.81 | (110) | 0.389 | 22.59 | (110) | 0.393 |
| | 24.43 | (200) | 0.364 | | | |
| $BS_{36}CL_{64}$ | 21.39 | (110) | 0.415 | | | |
| | 22.21 | (111) | 0.400 | - | - | - |
| | 24.50 | (200) | 0.363 | | | |
| $BS_{32}CL_{68}$ | 21.39 | (110) | 0.415 | | | |
| | 22.21 | (111) | 0.400 | - | | - |
| | 24.47 | (200) | 0.363 | | - | |
| $BS_{26}CL_{74}$ | 21.39 | (110) | 0.415 | 21.31 | (110) | 0.416 |
| | 22.21 | (111) | 0.400 | 21.95 | (111) | 0.404 |
| | 24.43 | (200) | 0.364 | 23.83 | (200) | 0.373 |
| $BS_{9}CL_{91}$ | 21.46 | (110) | 0.414 | 21.31 | (110) | 0.416 |
| | 22.10 | (111) | 0.402 | 21.95 | (111) | 0.404 |
| | 24.01 | (200) | 0.370 | 23.75 | (200) | 0.374 |
| PCL | 21.46 | (110) | 0.414 | 21.35 | (110) | 0.416 |
| | 22.06 | (111) | 0.402 | 21.95 | (111) | 0.404 |
| | 23.86 | (200) | 0.372 | 23.83 | (200) | 0.374 |

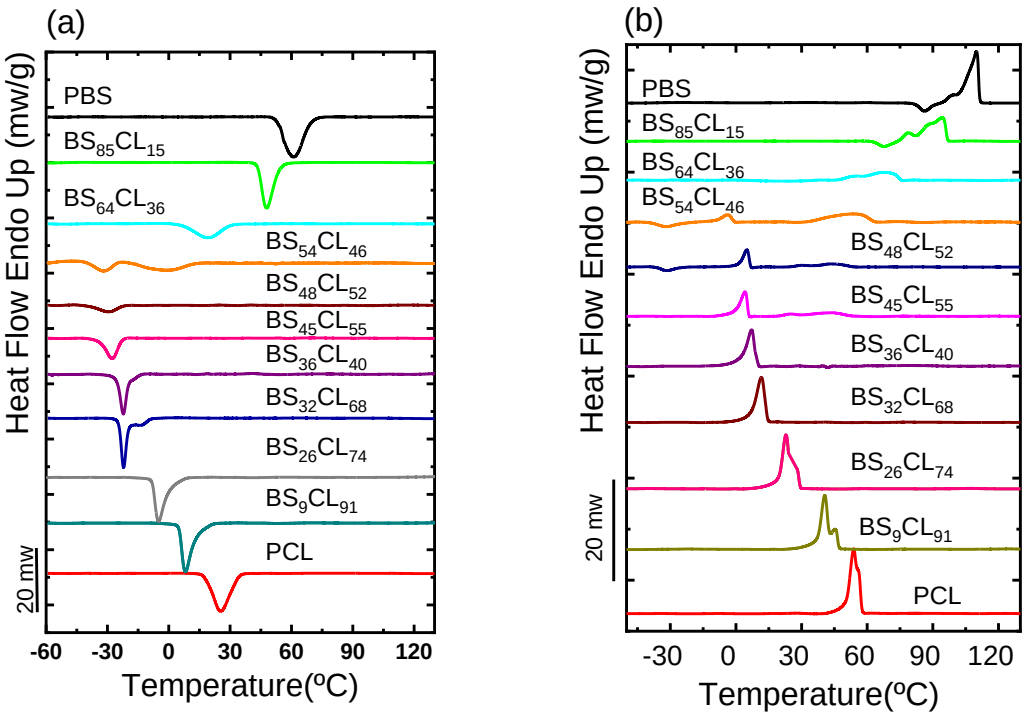


***Figure A.4.5.*** *DSC scans of the $BS_xCL_y$ copolyester series and the parent homopolyesters PBS and PCL. Traces recorded during cooling from the melt (a) and subsequent heating (b) at 10 °C/min.*

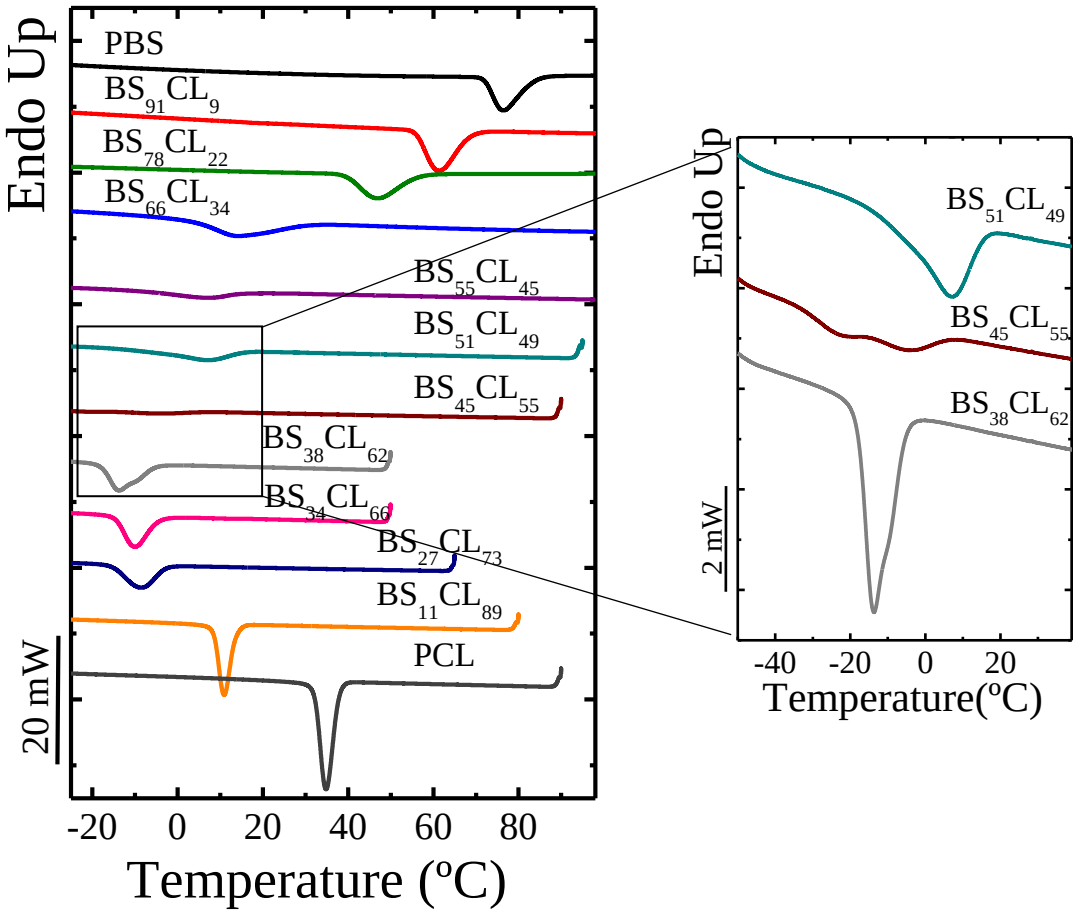


***Figure A.5.1.*** *DSC cooling scans from the melt at 10 °C/min for the indicated samples.*

**Table A.5.1**. Extracted data from DSC measurement at a rate of 10 ºC/min for $HM_w$ $\mathbf{BS_xCL_y}$ .

| # | Copolyester | $T_g$ (°C) | $T_c$ (°C) | $\Delta H_c$ | $T_{cc}$ (°C) | $\Delta H_{cc}$ | $T_m$ (°C) | $\Delta H_m$ | $Xc$ (%) |
|---|---|---|---|---|---|---|---|---|---|
| 1 | PBS | -33 | 76 | 66 | 97 | -9 | 114 | 66 | 62 |
| 2 | $BS_{91}CL_9$ | -36 | 61 | 55 | 85 | -8 | 104 | 54 | 50 |
| 3 | $BS_{78}CL_{22}$ | -40 | 46 | 41 | 72 | -1 | 93 | 41 | 37 |
| 4 | $BS_{66}CL_{34}$ | -44 | 14 | 30 | -9 | -2 | 73 | 30 | 27 |
| 5 | $BS_{62}CL_{38}$ | -45 | 12 | 24 | -10 | -5 | 70 | 25 | 22 |
| 6 | $BS_{55}CL_{45}$ | -46 | 7 | 16 | -10 | -5 | 62 | 18 | 15 |
| 7 | $BS_{51}CL_{49}$ | -47 | 4 | 14 | -12 | -2 | 58 | 15 | 13 |
| 8 | $BS_{45}CL_{55}$ | -48 | -5,-22 | 2, 3 | -17 | -16 | 13,49 | 7,17 | 2, 3 |
| 9 | $BS_{38}CL_{62}$ | -50 | -13 | 24 | - | - | 17 | 26 | 18 |
| 10 | $BS_{34}CL_{66}$ | -51 | -10 | 28 | - | - | 18 | 31 | 21 |
| 11 | $BS_{27}CL_{73}$ | -53 | -8 | 37 | - | - | 19 | 38 | 28 |
| 12 | $BS_{11}CL_{89}$ | -56 | 10 | 57 | - | - | 36 | 58 | 41 |
| 13 | PCL | -60 | 34 | 74 | - | - | 55 | 75 | 54 |

**Table A.5.2.** Extracted data from DSC measurement at a rate of 20 ºC/min for $HM_w$ $\mathbf{BS_xCL_y}$.

| # | Copolyester | $T_g$ (°C) | $T_c$ (°C) | $\Delta H_c$ | $T_{cc}$ (°C) | $\Delta H_{cc}$ | $T_m$ (°C) | $\Delta H_m$ | $Xc$ (%) |
|---|---|---|---|---|---|---|---|---|---|
| 1 | PBS | -33 | 70 | 65 | 98 | -9 | 116 | 63 | 61 |
| 2 | $BS_{91}CL_9$ | -36 | 54 | 55 | 85 | -10 | 104 | 50 | 46 |
| 3 | $BS_{78}CL_{22}$ | -40 | 39 | 40 | 71 | -10 | 93 | 40 | 35 |
| 4 | $BS_{66}CL_{34}$ | -44 | 10 | 15 | -2 | -14 | 72 | 27 | 13 |
| 5 | $BS_{62}CL_{38}$ | -45.8 | 8 | 10 | -1 | -22 | 72 | 23 | 10 |
| 6 | $BS_{55}CL_{45}$ | -46.3 | 0 | 7 | 0 | -17 | 63 | 17 | 6 |
| 7 | $BS_{51}CL_{49}$ | -47 | -4 | 5 | 2 | -15 | 59 | 14 | 5 |
| 8 | $BS_{45}CL_{55}$ | -48.2 | -21 | 3 | -7 | -22 | 50,16 | 14, 6 | 2 |
| 9 | $BS_{38}CL_{62}$ | -50 | -19 | 14 | -19 | -5 | 19 | 25 | 10 |
| 10 | $BS_{34}CL_{66}$ | -51 | -16 | 23 | - | - | 20 | 30 | 17 |
| 11 | $BS_{27}CL_{73}$ | -53 | -11 | 31 | - | - | 24 | 37 | 22 |
| 12 | $BS_{11}CL_{89}$ | -56 | 7 | 49 | - | - | 37 | 54 | 36 |
| 13 | PCL | -60 | 32 | 70 | - | - | 56 | 70 | 50 |

**Table A.5.3**. *d*-spacing , Extracted data from WAXS measurements at -60 °C

| Copolyester | d(nm) [020] | d(nm) [110] | d(nm) [110] | d(nm) [200] |
|---|---|---|---|---|
| PBS | 4.48 | | 3.87 | |
| $BS_{91}CL_9$ | 4.51 | | 3.88 | |
| $BS_{78}CL_{22}$ | 4.51 | | 3.90 | |
| $BS_{66}CL_{34}$ | 4.53 | | 3.91 | |
| $BS_{62}CL_{38}$ | 4.53 | | 3.93 | |
| $BS_{55}CL_{45}$ | 4.56 | | 3.94 | |
| $BS_{51}CL_{49}$ | 4.56 | | 3.95 | |
| $BS_{45}CL_{55}$ | | 4.13 | | 3.61 |
| $BS_{38}CL_{62}$ | | 4.13 | | 3.62 |
| $BS_{27}CL_{73}$ | | 4.13 | | 3.63 |
| $BS_{11}CL_{89}$ | | 4.12 | | 3.62 |
| PCL | | 4.10 | | 3.68 |

**Table A.5.4**. *d*-spacing, Extracted data from WAXS measurements at 25 °C

| Copolyester | d(nm) [020] | d(nm) [110] | d(nm) [110] | d(nm) [200] |
|---|---|---|---|---|
| PBS | 4.51 | | 3.91 | |
| $BS_{91}CL_9$ | 4.54 | | 3.94 | |
| $BS_{78}CL_{22}$ | 4.54 | | 3.95 | |
| $BS_{66}CL_{34}$ | 4.54 | | 3.95 | |
| $BS_{62}CL_{38}$ | 4.54 | | 3.95 | |
| $BS_{55}CL_{45}$ | 4.54 | | 3.96 | |
| $BS_{51}CL_{49}$ | 4.54 | | 3.96 | |
| $BS_{45}CL_{55}$ | 4.54 | | 3.96 | |
| $BS_{11}CL_{89}$ | | 4.16 | | 3.71 |
| PCL | | 4.13 | | 3.74 |

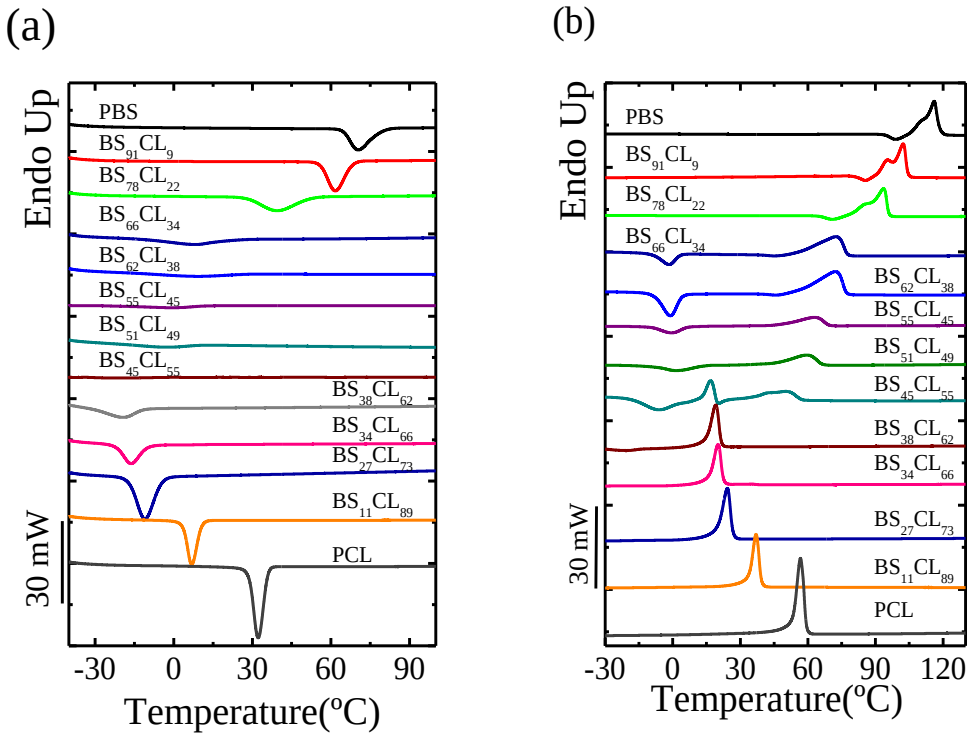


***Figure A.5.2.*** *(**a**) DSC cooling scans and (b) DCS subsequent heating scans at 20 °C/min for the indicated samples.*

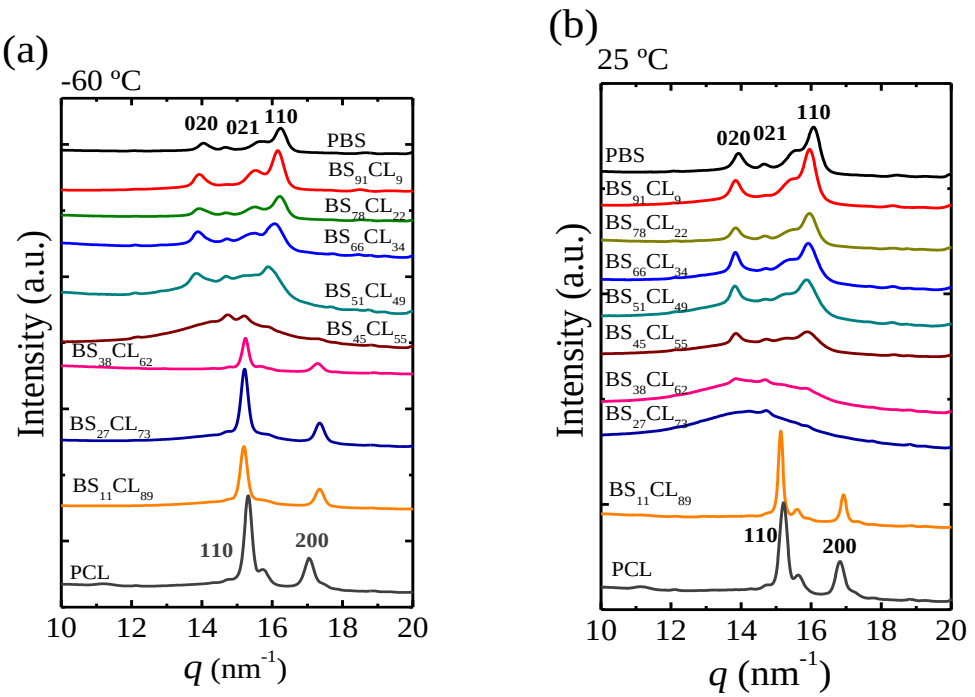


***Figure A.5.3.*** *WAXS diffraction patterns of $HM_w$ $BS_xCL_y$ registered at -60 °C (a) and 25 °C, after heating from -60 °C to 25 °C at 10 °C/min (b).*

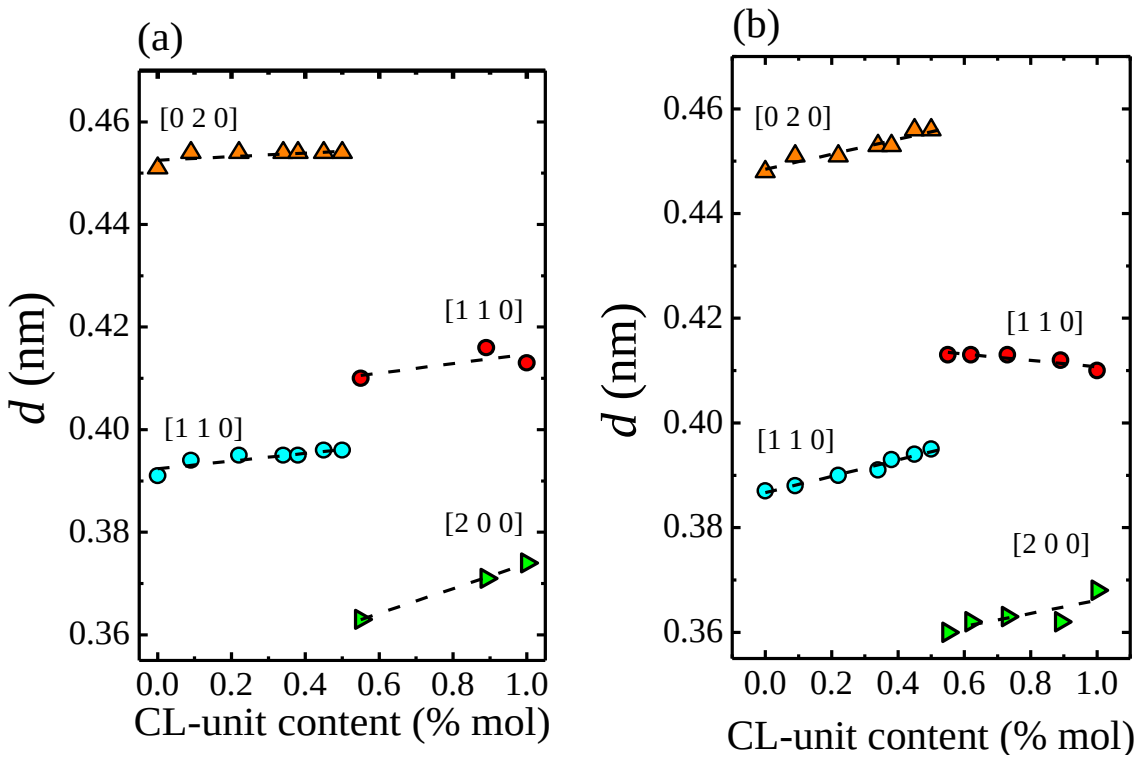


***Figure A.5.4****. Plot of d-spacings determined by WAXS at 25 °C (a) and at -60 °C, after cooling from the melt at 10 °C/min (b). Indexing has been made based on the monoclinic and orthorhombic unit cells reported for PBS and PCL respectively.*

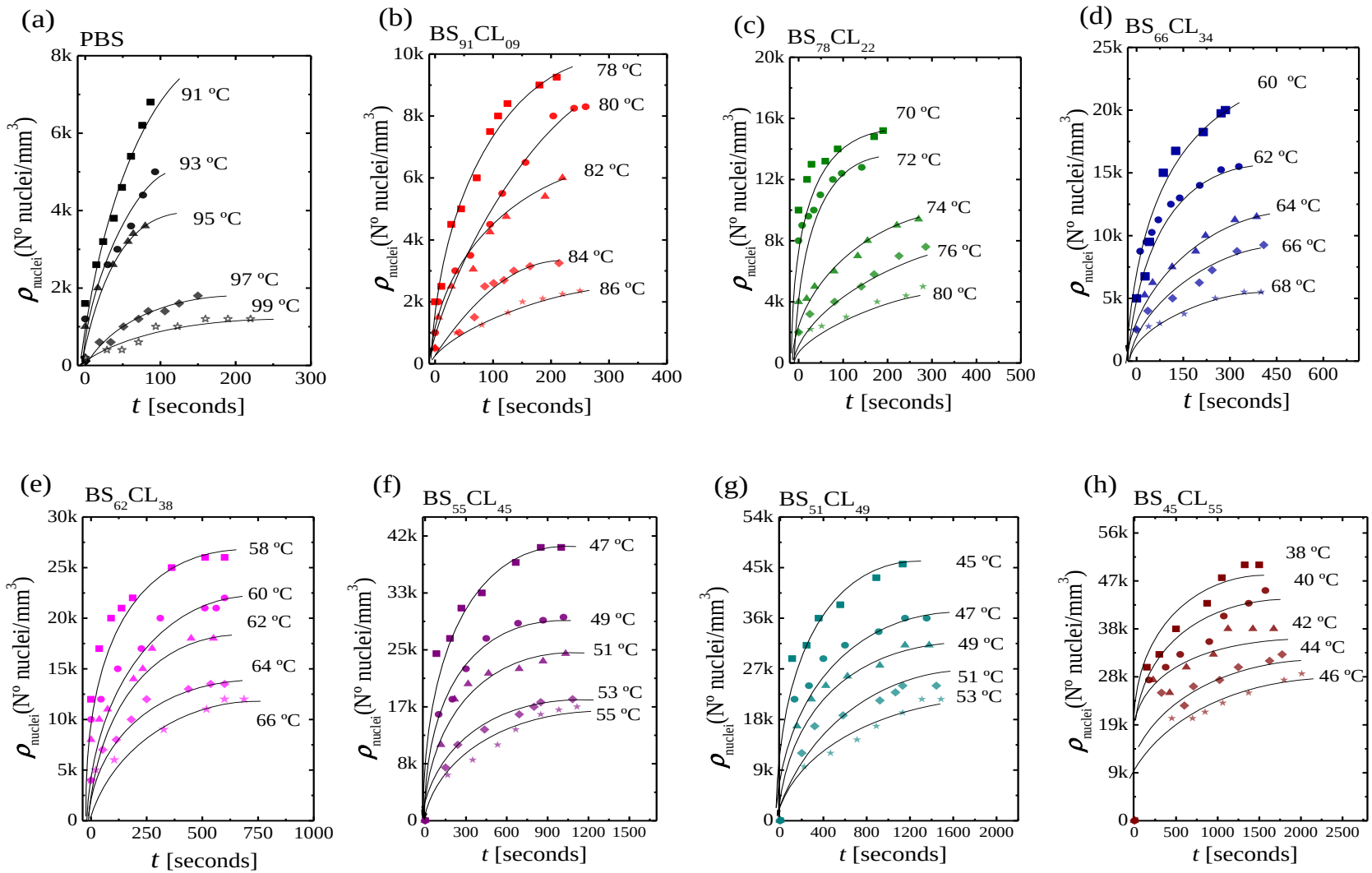


***Figure A.6.1.*** *Nucleation kinetics studies by PLOM. Nuclei density as a function of time at different crystallization temperature for PBS-rich phase samples: (a) PBS, (b) BS91CL9, (c) BS78CL22, (d) BS66CL34, (e) BS62CL38, (f) BS55CL45, (g) BS51CL49, and (h) BS45CL55. TC are at ΔT = 40, 38, 36, 34, 32 °C for all samples.*

**Table A.6.1.** $T_m$ equilibrium values for CoP(BSxCLy) compositions and their corresponding homopolymers.

| Copolyester | $T_m^0$ (°C) |
|---|---|
| **PBS** | 131 |
| **$BS_{91}CL_9$** | 118 |
| **$BS_{78}CL_{22}$** | 110 |
| **$BS_{66}CL_{34}$** | 100 |
| **$BS_{62}CL_38$** | 98 |
| **$BS_{55}CL_45$** | 87 |
| **$BS_{51}CL_{49}$** | 85 |
| **$BS_{45}CL_{55}$(BS-rich)** | 78 |
| **$BS_{45}CL_{55}$(CL-rich)** | 35 |
| **$BS_{38}CL_{62}$** | 38 |
| **$BS_{34}CL_{66}$** | 42 |
| **$BS_{27}CL_{73}$** | 47 |
| **$BS_{11}CL_{89}$** | 63 |
| **PCL** | 88 |

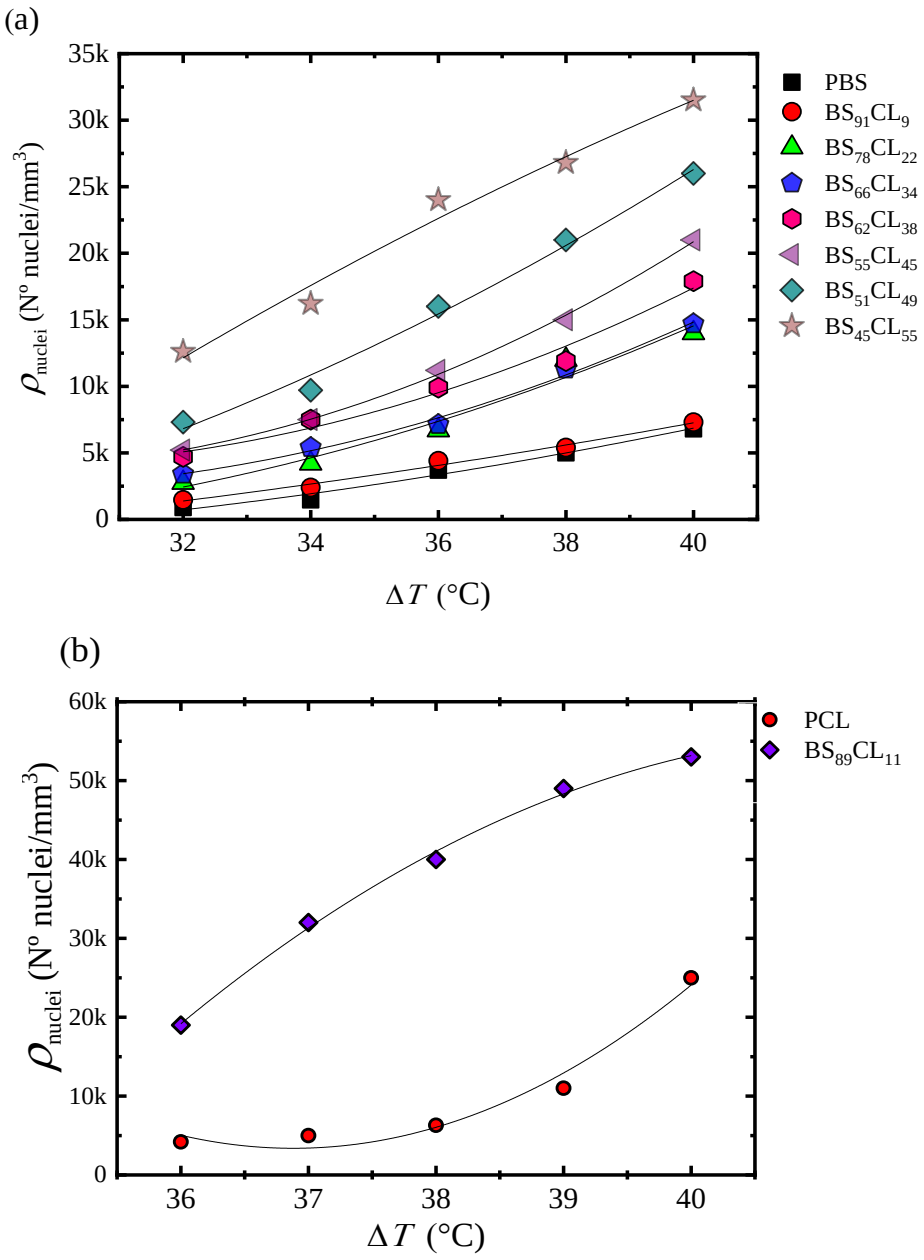


***Figure A.6.2****. Nuclei density during isothermal crystallization as a function of ΔT for PBS-rich phase (a) and for PCL-rich phase (b) copolyesters.*

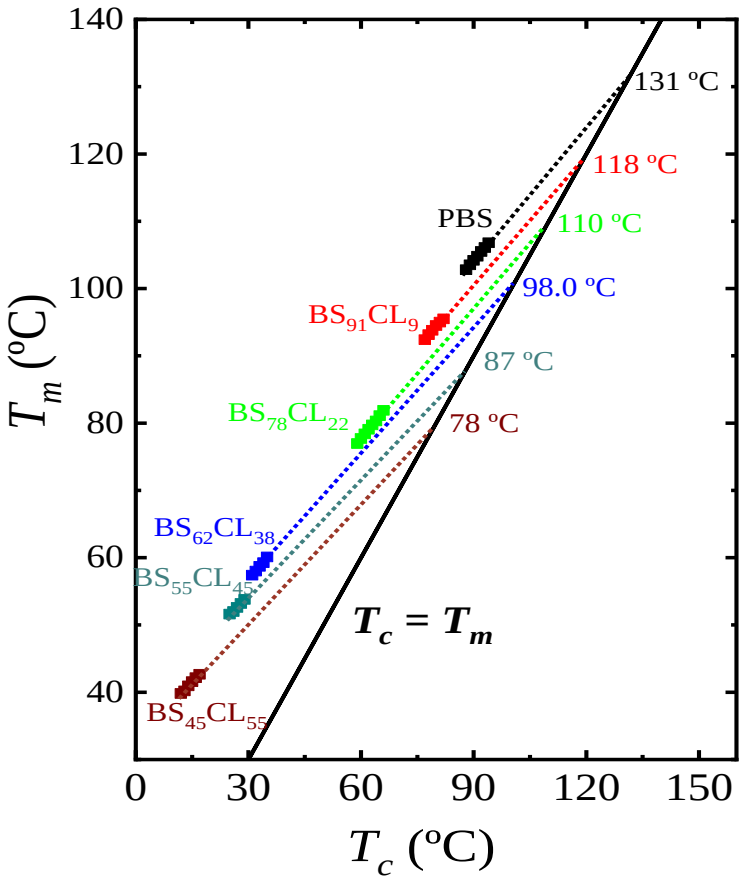


***Figure A.6.3.*** *Hoffman–Weeks plots for PBS-ran-PCL compositions. The black solid line represents the thermodynamic equilibrium line $T_m = T_c$.*

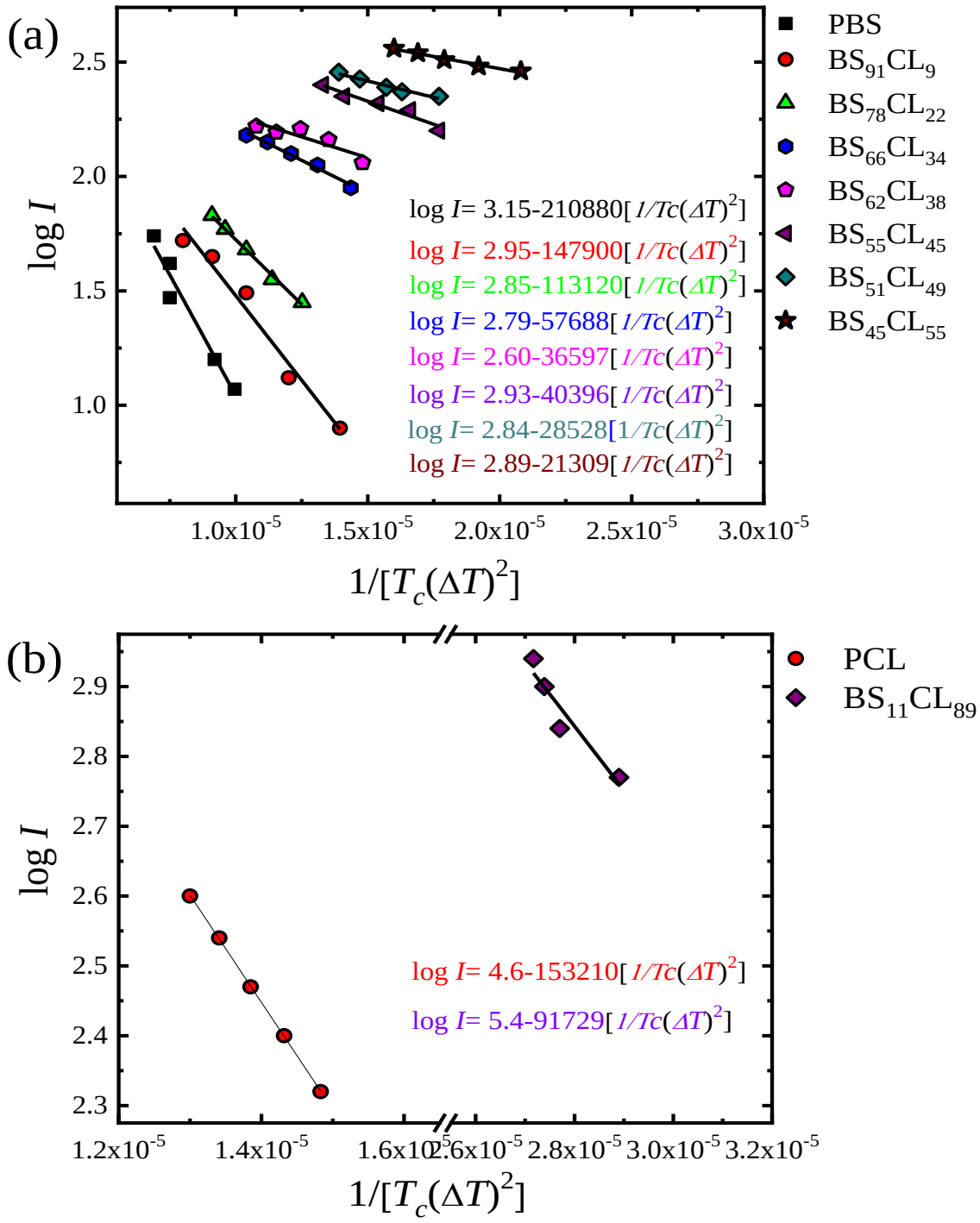


***Figure A.6.4.*** *Plot of log I versus 1/T(ΔT)² and fitting to Turnbull–Fisher equation (Eq. 1) for PBS-rich (a) and PCL-rich (b) compositions.*

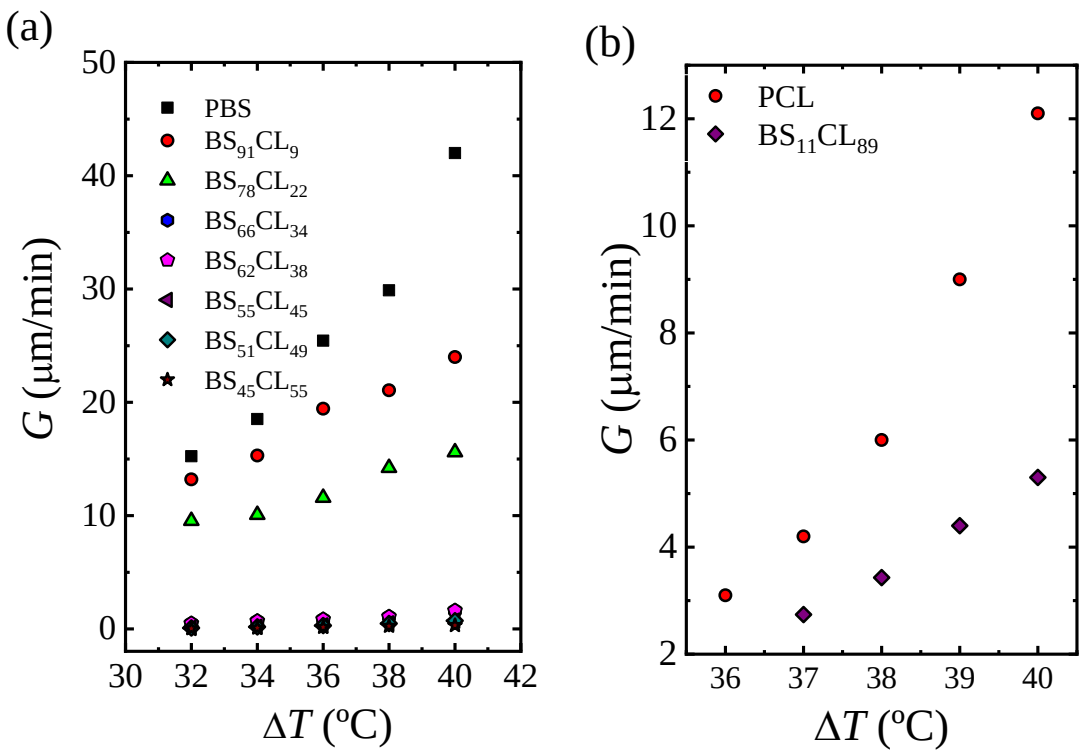


***Figures A.6.5****. Spherulitic growth rates G determined by PLOM for neat PBS and PBS-rich (a) and for neat PCL and PCL-rich (b) copolymers as a function of supercooling.*

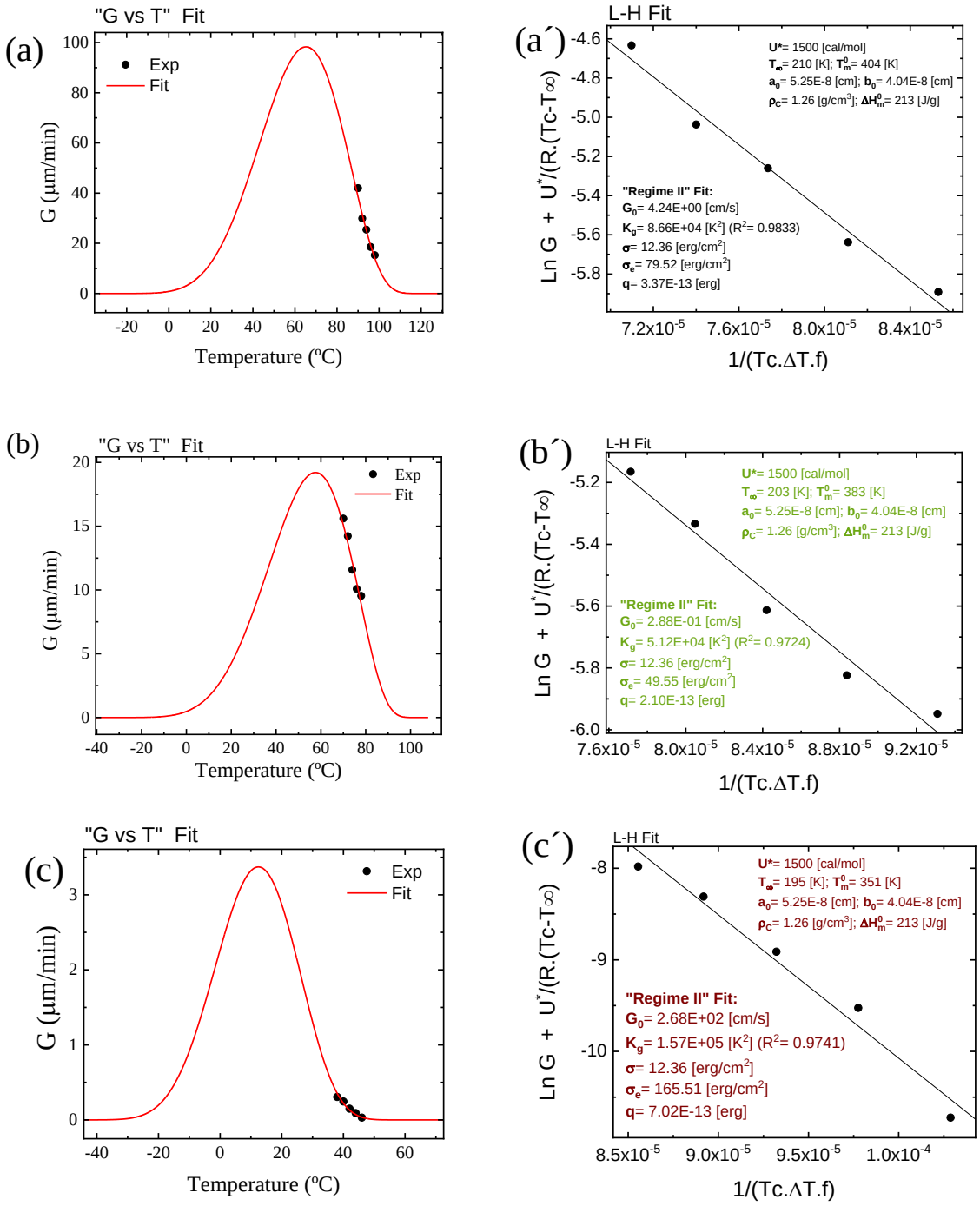


***Figure A.6.6.*** *The fits to the Lauritzen-Hoffman equation using the free Origin plug-in developed by Lorenzo et al.and the experimental data for the (a-a´) PBS, (b-b´) $BS_{78}CL_{22}$, and (c-c´) $BS_{45}CL_{55}$.*

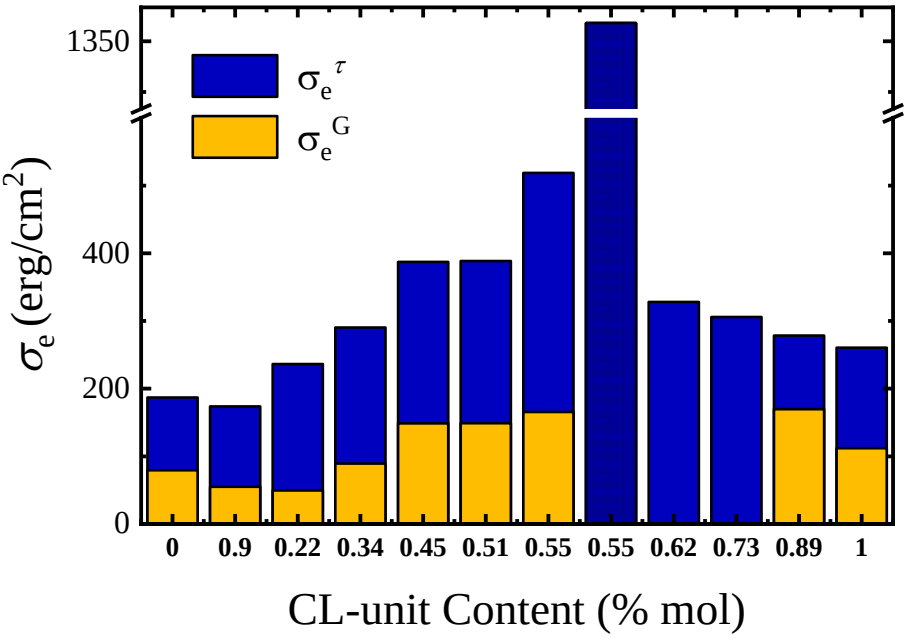


***Figure A.6.7.*** *The σe value versus CL-unit molar fraction that obtained for PLOM experiments ($\sigma_g^G$) and DSC experiments ($\sigma_g^\tau$).*

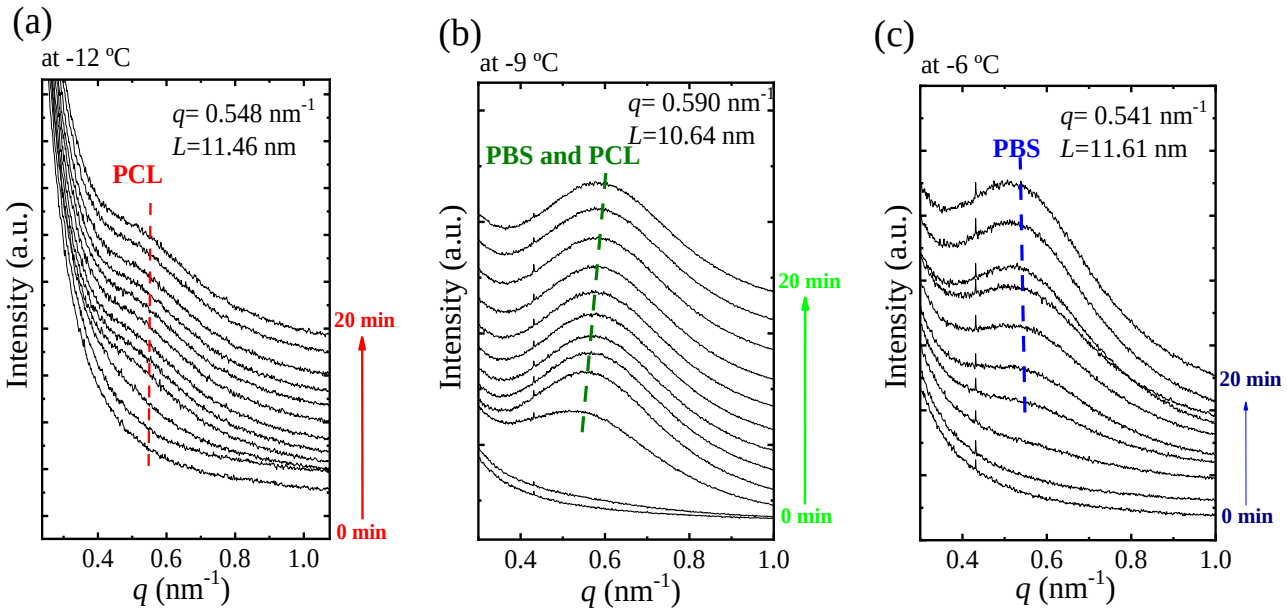


***Figure A.6.8.*** *SAXS diffraction patterns of $BS_{45}CL_{55}$ registered during isothermal crystallization at -12 °C (a), -9 °C (b) and -6 °C (c).*

***Table A.6.2.*** *Overall crystallization kinetic data for PBS-ran-PCL copolyesters based on the Avrami model.*

| **PBS** | | | | | | | | |
|---|---|---|---|---|---|---|---|---|
| $T_C$ (ºC) | $1/\tau_{ao}$ (1/min) | $T_o$ (min) | $n$ | $K\ (min^{-n})$ | $K_n$ | $R^2$ | $t_{50\%}$ Experimental (min) | $t_{50\%}$ Theoritical (min) |
| 90 | 2.89855 | 0.345 | 2.58 | 8.00E-02 | 0.3757 | 1.0000 | 2.45 | 2.307 |
| 91 | 2.64550 | 0.378 | 2.54 | 4.93E-02 | 0.305754 | 1.0000 | 2.97 | 2.835 |
| 92 | 1.98020 | 0.505 | 2.46 | 2.85E-02 | 0.235444 | 1.0000 | 3.813 | 3.655 |
| 93 | 1.55521 | 0.643 | 2.45 | 1.61E-02 | 0.185393 | 1.0000 | 4.853 | 4.649 |
| 94 | 1.10254 | 0.907 | 2.45 | 8.99E-03 | 0.14615 | 1.0000 | 6.137 | 5.879 |
| 95 | 0.85690 | 1.167 | 2.37 | 5.14E-03 | 0.108184 | 1.0000 | 8.218 | 7.897 |
| **$BS_{91}CL_9$** | | | | | | | | |
| 77 | 2.28328 | 0.353 | 2.70 | 1.56E-02 | 0.214184 | 1.0000 | 4.092 | 4.07 |
| 78 | 2.25733 | 0.443 | 2.62 | 1.01E-02 | 0.173097 | 1.0000 | 5.012 | 5.029 |
| 79 | 1.74825 | 0.572 | 2.65 | 4.89E-03 | 0.134289 | 1.0000 | 6.524 | 6.504 |
| 80 | 1.16550 | 0.858 | 2.56 | 3.45E-03 | 0.109197 | 1.0000 | 7.918 | 7.918 |
| 81 | 0.76628 | 1.305 | 2.47 | 2.35E-03 | 0.086229 | 1.0000 | 9.88 | 10.002 |
| 82 | 0.61275 | 1.632 | 2.51 | 1.17E-03 | 0.067912 | 1.0000 | 12.678 | 12.684 |
| 83 | 0.42105 | 2.37 | 2.41 | 8.67E-04 | 0.053637 | 1.0000 | 15.977 | 15.702 |
| **$BS_{78}CL_{22}$** | | | | | | | | |
| 61 | 2.57732 | 0.388 | 2.45 | 1.17E-01 | 0.4165506 | 0.9999 | 2.128 | 2.065 |
| 62 | 2.48756 | 0.400 | 2.45 | 1.00E-01 | 0.3906940 | 0.9999 | 2.255 | 2.202 |
| 63 | 2.23714 | 0.487 | 2.32 | 9.56E-02 | 0.3635317 | 1.0000 | 2.363 | 2.351 |
| 64 | 2.05339 | 0.447 | 2.42 | 6.75E-02 | 0.3282776 | 1.0000 | 2.658 | 2.619 |
| 65 | 1.78571 | 0.560 | 2.33 | 6.48E-02 | 0.3089914 | 1.0000 | 2.765 | 2.788 |
| 66 | 1.66389 | 0.610 | 2.34 | 5.25E-02 | 0.2838309 | 1.0000 | 3.002 | 3.013 |
| **$BS_{66}CL_{34}$** | | | | | | | | |
| 31 | 2.39808 | 0.417 | 2.26 | 9.64E-02 | 0.355203 | 1.0000 | 2.38 | 2.395 |
| 32 | 2.10526 | 0.475 | 2.25 | 6.92E-02 | 0.305135 | 1.0000 | 2.765 | 2.788 |
| 33 | 2.07469 | 0.535 | 2.27 | 4.64E-02 | 0.258561 | 1.0000 | 3.287 | 3.294 |
| 34 | 1.86916 | 0.482 | 2.39 | 2.54E-02 | 0.215063 | 1.0000 | 4.027 | 3.996 |
| 35 | 1.73010 | 0.578 | 2.38 | 1.71E-02 | 0.180951 | 1.0000 | 4.743 | 4.743 |
| 36 | 1.48148 | 0.675 | 2.40 | 1.06E-02 | 0.150387 | 1.0000 | 5.763 | 5.718 |
| **$BS_{55}CL_{45}$** | | | | | | | | |
| 25 | 2.34192 | 0.427 | 2.54 | 2.01E-02 | 0.2147667 | 0.9999 | 4.228 | 4.032 |
| 26 | 2.18818 | 0.457 | 2.46 | 1.70E-02 | 0.1908404 | 0.9999 | 4.783 | 4.53 |
| 27 | 1.28534 | 0.778 | 2.16 | 2.38E-02 | 0.1771802 | 1.0000 | 4.862 | 4.779 |
| 28 | 1.02888 | 0.972 | 2.13 | 2.04E-02 | 0.160842 | 1.0000 | 5.335 | 5.26 |
| 29 | 0.72046 | 1.388 | 2.02 | 2.13E-02 | 0.14875 | 1.0000 | 5.577 | 5.593 |
| 30 | 0.70028 | 1.428 | 2.18 | 8.69E-03 | 0.1133957 | 1.0000 | 7.545 | 7.429 |
| **$BS_{51}CL_{49}$** | | | | | | | | |
| 23 | 1.27226 | 0.767 | 2.36 | 1.09E-01 | 0.3909578 | 0.9999 | 2.495 | 2.191 |
| 24 | 1.29366 | 0.773 | 2.44 | 6.76E-02 | 0.3314896 | 0.9999 | 3.008 | 2.598 |
| 25 | 1.01121 | 0.988 | 2.28 | 5.98E-02 | 0.2907137 | 0.9998 | 3.372 | 2.93 |
| 26 | 0.81103 | 1.233 | 2.20 | 5.67E-02 | 0.2712982 | 0.9998 | 3.483 | 3.118 |
| 27 | 0.62972 | 1.588 | 2.10 | 4.59E-02 | 0.2305515 | 0.9999 | 4.06 | 3.66 |
| 28 | 0.54200 | 1.845 | 2.13 | 2.97E-02 | 0.1918600 | 0.9998 | 4.837 | 4.378 |

| | | | | | | | | |
|---|---|---|---|---|---|---|---|---|
| 29 | 0.52083 | 1.92 | 2.25 | 1.24E-02 | 0.1421123 | 0.9998 | 6.777 | 5.961 |
| **$BS_{45}CL_{55}$ (BS-rich phase)** | | | | | | | | |
| 12 | 1.27714 | 0.783 | 1.80 | 3.63E-02 | 0.1584704 | 0.9998 | 5.985 | 5.166 |
| 13 | 1.10254 | 0.907 | 1.80 | 3.25E-02 | 0.1477501 | 0.9996 | 5.962 | 5.407 |
| 14 | 0.75301 | 1.328 | 1.77 | 2.29E-02 | 0.1396186 | 0.9996 | 7.112 | 6.850 |
| 15 | 0.62034 | 1.612 | 1.96 | 2.57E-02 | 0.1341501 | 1.0000 | 5.357 | 5.359 |
| 16 | 0.47461 | 2.197 | 2.07 | 1.86E-02 | 0.1363818 | 1.0000 | 5.675 | 5.726 |
| 17 | 0.45106 | 2.217 | 2.10 | 6.79E-03 | 0.0928020 | 1.0000 | 9.073 | 9.014 |
| **$BS_{45}CL_{55}$ (CL-rich phase)** | | | | | | | | |
| -14 | 1.980 | 0.505 | 3.63 | 1.94E-01 | 0.636505 | 0.9996 | 1.513 | 1.541 |
| -13 | 1.695 | 0.590 | 3.32 | 1.75E-01 | 0.591561 | 0.9996 | 1.477 | 1.513 |
| -12 | 1.349 | 0.736 | 3.30 | 1.31E-01 | 0.54014 | 0.9997 | 1.325 | 1.401 |
| -11 | 1.265 | 0.790 | 3.15 | 1.01E-01 | 0.48296 | 0.9996 | 1.250 | 1.322 |
| -10 | 1.120 | 0.892 | 3.25 | 9.89E-02 | 0.490715 | 0.9997 | 1.020 | 1.103 |
| **$BS_{38}CL_{62}$** | | | | | | | | |
| -1 | 1.61010 | 0.621 | 2.62 | 2.66E-01 | 0.603239 | 1.0000 | 1.441 | 1.443 |
| 0 | 1.41843 | 0.750 | 2.55 | 1.90E-01 | 0.510089 | 1.0000 | 1.781 | 1.800 |
| 1 | 1.17650 | 0.805 | 2.44 | 1.22E-01 | 0.422238 | 1.0000 | 2.036 | 2.143 |
| 2 | 1.09292 | 0.895 | 2.44 | 7.8E-02 | 0.351512 | 1.0000 | 2.447 | 2.773 |
| 3 | 0.89291 | 1.120 | 2.34 | 6.7E-02 | 0.315009 | 1.0000 | 2.835 | 3.303 |
| **$BS_{27}CL_{73}$** | | | | | | | | |
| 3 | 1.63398 | 0.612 | 2.61 | 7.35E-02 | 0.367813 | 1.0000 | 2.36 | 2.43 |
| 4 | 1.41843 | 0.705 | 2.33 | 4.99 E-02 | 0.276213 | 0.9999 | 2.899 | 3.038 |
| 5 | 0.91743 | 1.09 | 2.29 | 3.86 E-02 | 0.241429 | 0.9998 | 3.534 | 3.813 |
| 6 | 0.78125 | 1.043 | 2.42 | 1.48 E-02 | 0.175352 | 0.9999 | 4.903 | 5.432 |
| 7 | 0.39526 | 2.53 | 1.96 | 3.15 E-02 | 0.171329 | 0.9999 | 4.842 | 5.11 |
| 8 | 0.28090 | 2.56 | 1.95 | 3.22 E-02 | 0.171711 | 0.9998 | 4.850 | 5.09 |
| **$BS_{11}CL_{89}$** | | | | | | | | |
| 19 | 2.0490 | 0.488 | 2.59 | 3.58 | 1.636268 | 1.0000 | 1.291 | 1.302 |
| 20 | 1.6340 | 0.612 | 2.58 | 1.75 | 1.242227 | 1.0000 | 1.706 | 1.723 |
| 21 | 1.0235 | 0.777 | 2.60 | 8E-02 | 0.37854 | 1.0000 | 2.296 | 2.33 |
| 23 | 0.6180 | 1.618 | 2.40 | 1.98E-02 | 0.195109 | 1.0000 | 4.387 | 4.15 |
| 25 | 0.2503 | 3.995 | 2.20 | 5.75E-03 | 0.095867 | 0.9999 | 8.857 | 8.772 |
| **PCL** | | | | | | | | |
| 40 | 3.27869 | 0.305 | 2.98 | 1.45E+00 | 1.1327924 | 1.0000 | 0.808 | 0.781 |
| 41 | 2.98507 | 0.335 | 3.16 | 4.13E-01 | 0.7559015 | 1.0000 | 1.223 | 1.167 |
| 42 | 2.09644 | 0.477 | 3.15 | 1.12E-01 | 0.4990734 | 1.0000 | 1.84 | 1.781 |
| 43 | 0.95420 | 1.048 | 2.82 | 3.97E-02 | 0.3053861 | 1.0000 | 2.893 | 2.865 |
| 44 | 0.74516 | 1.342 | 3.08 | 3.17E-03 | 0.1544029 | 1.0000 | 5.86 | 5.734 |

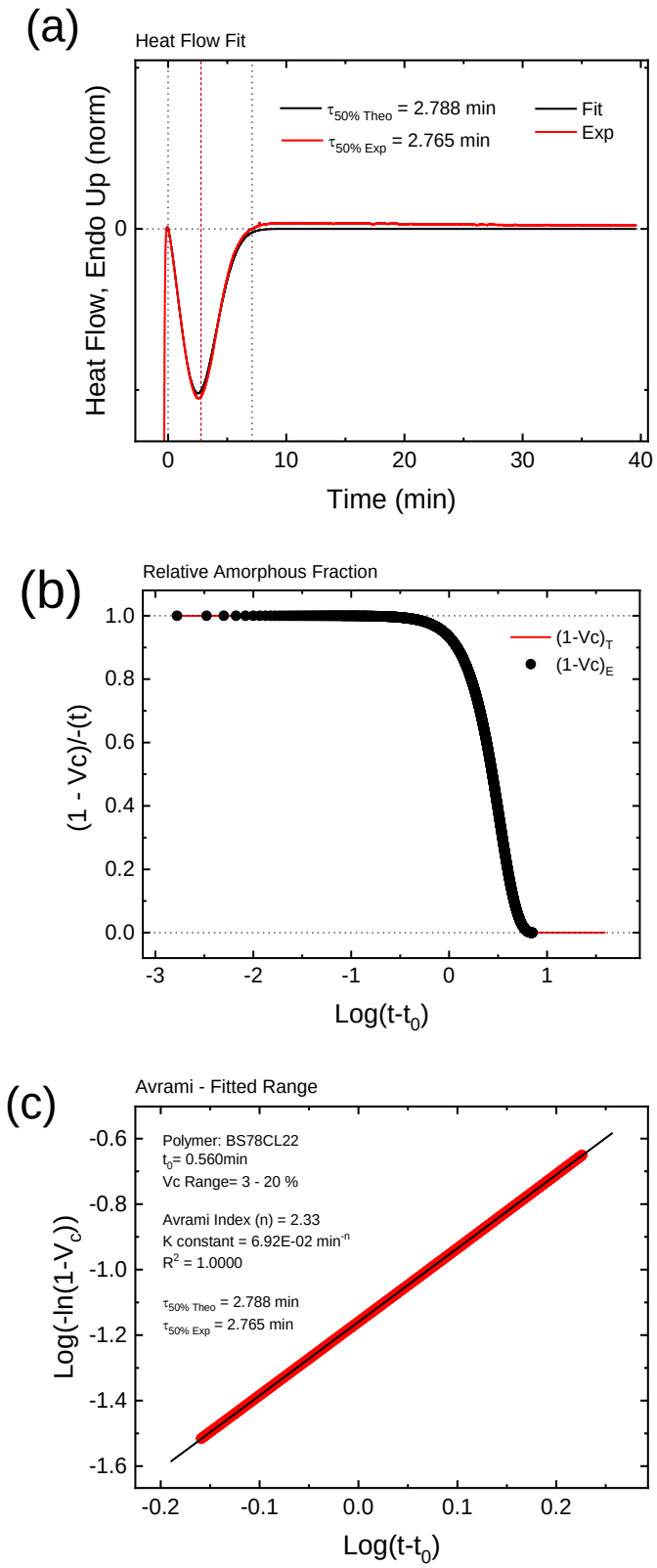


***Figure A.6.9.*** *(a–c) The fits to the Avrami equation using the Origin plug-in developed by Lorenzo et al.7 and the experimental data for the* $BS_{78}CL_{22}$ *copolymer sample.*

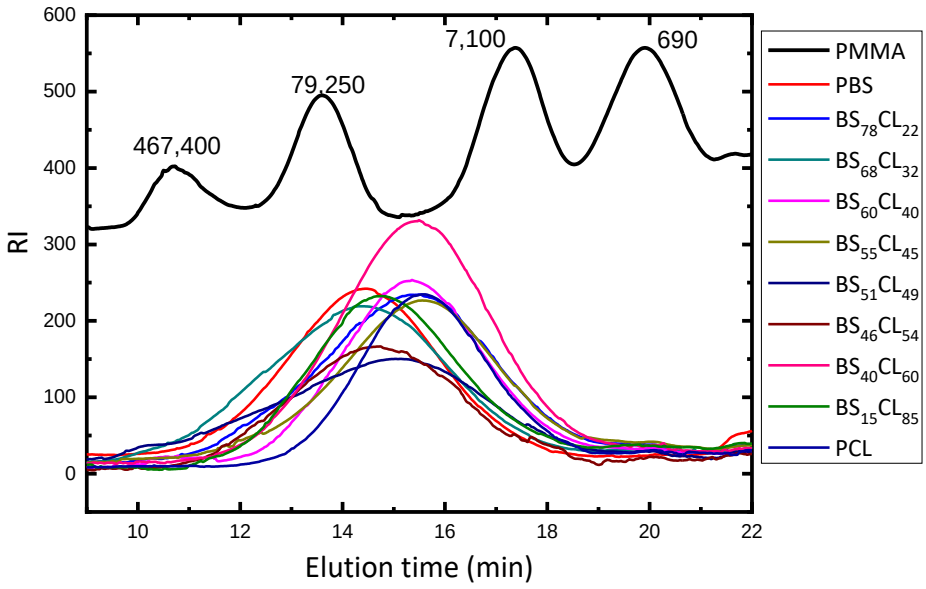


***Figure A.7.1.*** *GPS results of VHMw-PBS-ran-PCL copolyesters*

***Table A.7.1.*** *Extracted data from the Tensile tests.*

| Copolyester | E (MPa) | $\sigma_b$ (MPa) | $\varepsilon_b$ (%) |
|---|---|---|---|
| PBS | 579 | 27.9 | 7.80 |
| $BS_{68}CL_{32}$ | 219 | 11.9 | 10.9 |
| $BS_{51}CL_{49}$ | 80.9 | 3.72 | 11.2 |
| $BS_{46}CL_{54}$ | 42.7 | 2.19 | 15.5 |
| $BS_{15}CL_{85}$ | 112 | 4.21 | 213 |
| PCL | 219±15 | 11.9±1.1 | 111±60 |

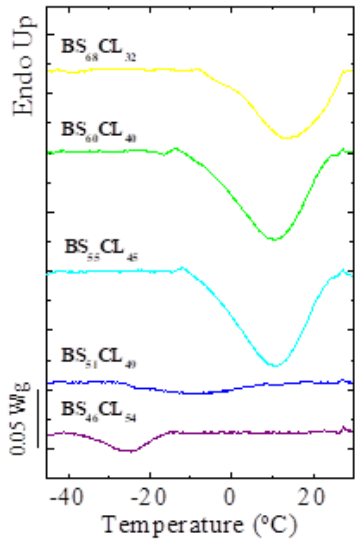


***Figure A.7.2. .*** *Cooling DSC scans from the melt for those samples that indicate both homopolymers phases*

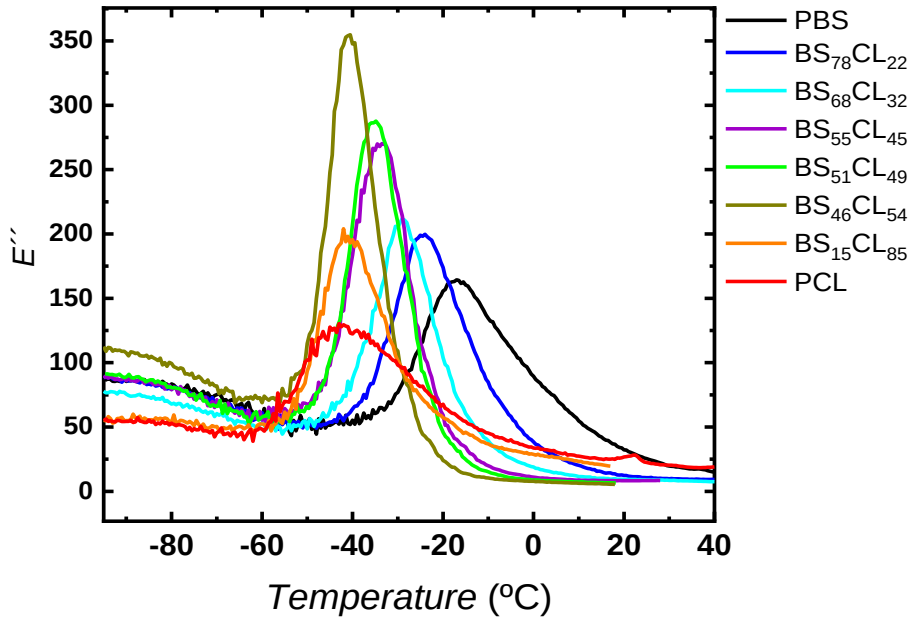


***Figure A.7.3.*** *The loss modulus of the copolyesters as a function of temperature at a constant heating rate of 4 °C/min and frequency of 1 Hz.*

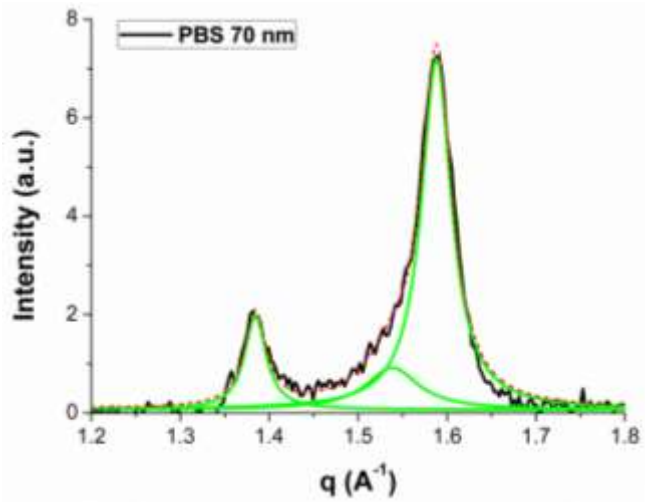


***Figure A.8.1.*** *1D intensity profile of PBS 70 nm sample obtained by averaging the intensity along the azimuthal angle.*

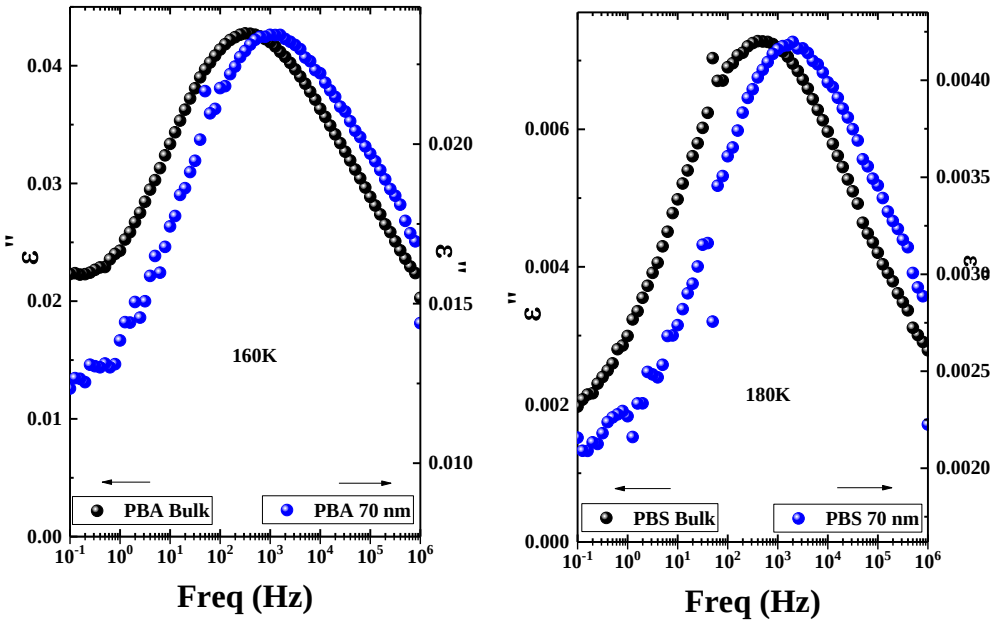


***Figure A.8.2.*** *Isothermal plots of ε´´ for a) PBA homopolymer and PBA infiltrated in 70nm alumina template at 160K, and b) PBS homopolymer and PBS infiltrated in 70nm alumina template at 180K.*

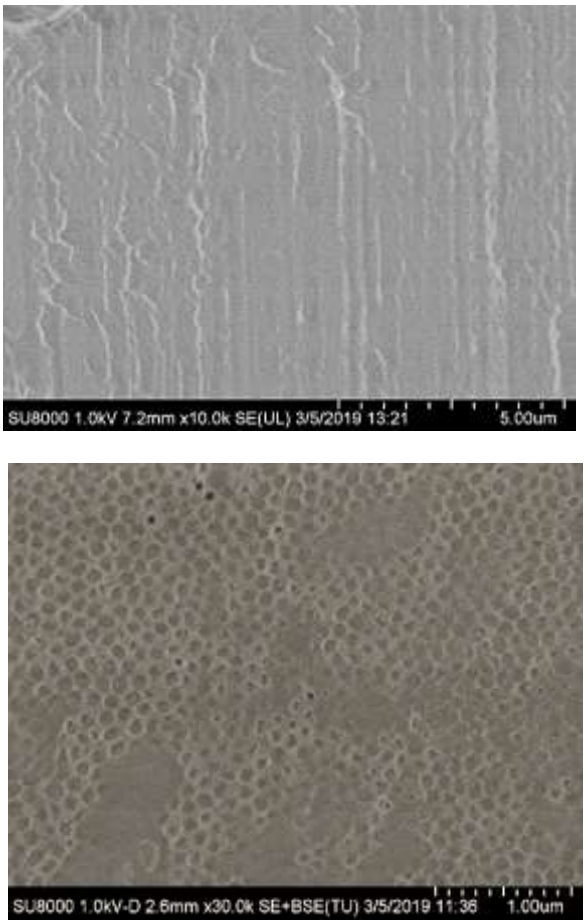


***Figure A.9.1.*** *SEM micrograph from $BS_{55}CL_{45}$ composition (a) cross-sectional view and (b) top view.*

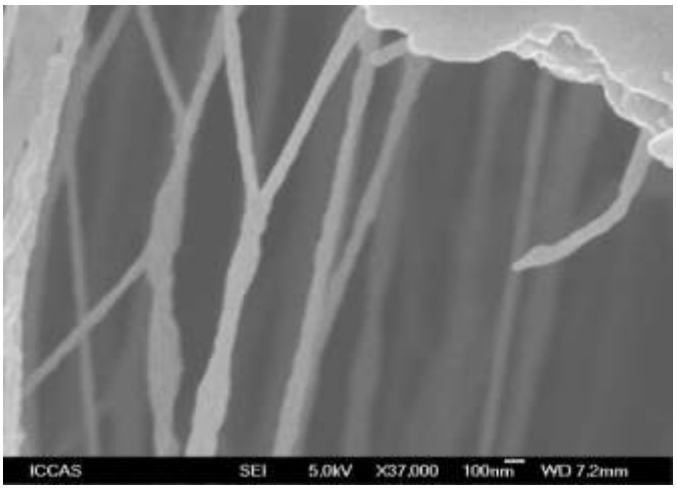


***Figure A.9.2.*** *SEM micrograph from PBS homopolymer nafibers within AAO template with 100 nm diameter.*

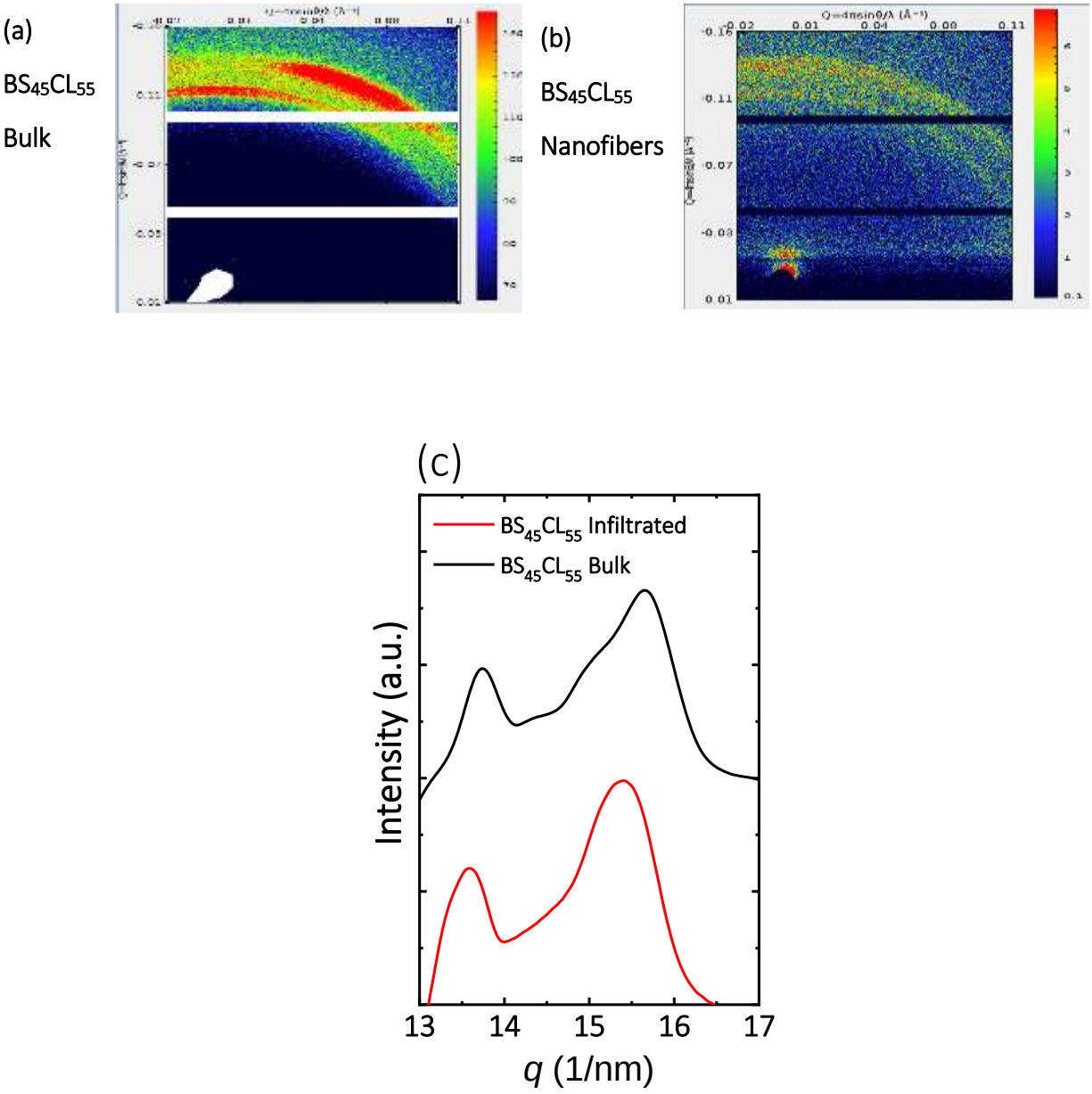


***Figure A.9.3.*** *2D WAXS patterns of (a) $BS_{45}CL_{55}$ bulk (b) $BS_{45}CL_{55}$ infiltrated. Corresponding 1D intensity profile of $BS_{45}CL_{55}$ sample (c) obtained by averaging the intensity along the azimuthal angle.*

**Table A.9.1.**

| Copolyester | *Tm* ( °C) | *Tc* ( °C) | *Tcc* ( °C) |
|---|---|---|---|
| **PBS Bulk** | 116 | 70 | - |
| **PBS Infiltrated** | 109 | 4 | - |
| **$BS_{91}CL_9$ Bulk** | 104 | 61 | - |
| **$BS_{91}CL_9$ Infiltrated** | 100 | -10 | -10 |
| **$BS_{78}CL_{22}$ Bulk** | 94 | 39 | - |
| **$BS_{78}CL_{22}$ Infiltrated** | 92 | -17 | -12 |
| **$BS_{66}CL_{34}$ Bulk** | 72 | 13 | - |
| **$BS_{66}CL_{34}$ Infiltrated** | 68 | -30 | -6 |
| **$BS_{62}CL_{38}$ Bulk** | 71 | 12 | -8 |
| **$BS_{62}CL_{38}$ Infiltrated** | 69 | -34 | -5 |
| **$BS_{55}CL_{45}$ Bulk** | 62 | 8 | -10 |
| **$BS_{55}CL_{45}$ Infiltrated** | 59 | -38 | -13 |
| **$BS_{51}CL_{49}$ Bulk** | 59 | 7 | 1.5 |
| **$BS_{51}CL_{49}$ Infiltrated** | 57 | -40 | - |
| **$BS_{45}CL_{55}$ Bulk** | 13, 49 | -6, -22 | -16 |
| **$BS_{45}CL_{55}$ Infiltrated** | 10, 45 | -41 | - |
| **$BS_{38}CL_{62}$ Bulk** | 18 | -16 | - |
| **$BS_{38}CL_{62}$Infiltrated** | 16 | -48 | - |
| **$BS_{27}CL_{73}$ Bulk** | 20 | -12 | - |
| **$BS_{27}CL_{73}$Infiltrated** | 18 | -45 | - |
| **$BS_{11}CL_{89}$ Bulk** | 37 | 7 | - |
| **$BS_{11}CL_{89}$ Infiltrated** | 34 | -43 | - |
| **PCL Bulk** | 57 | 32 | - |
| **PCL Infiltrated** | 53 | -40 | - |